R-04-69

Neutron data for accelerator-driven transmutation technologies

Annual Report 2003/2004

J Blomgren, A Hildebrand, L Nilsson,
P Mermod, N Olsson, S Pomp, M Österlund
Department of Neutron Research, Uppsala University

August 2004

Svensk Kärnbränslehantering AB
Swedish Nuclear Fuel
and Waste Management Co
Box 5864
SE-102 40 Stockholm Sweden
Tel 08-459 84 00
+46 8 459 84 00
Fax 08-661 57 19
+46 8 661 57 19

ISSN 1402-3091
SKB Rapport R-04-69

Neutron data for accelerator-driven transmutation technologies

Annual Report 2003/2004

J Blomgren, A Hildebrand, L Nilsson,
P Mermod, N Olsson, S Pomp, M Österlund
Department of Neutron Research, Uppsala University

August 2004

Summary

The project NATT, Neutron data for Accelerator-driven Transmutation Technology, is performed within the nuclear reactions group of the Department of neutron research, Uppsala university. The activities of the group are directed towards experimental studies of nuclear reaction probabilities of importance for various applications, like transmutation of nuclear waste, biomedical effects and electronics reliability. The experimental work is primarily undertaken at the The Svedberg Laboratory (TSL) in Uppsala, where the group has previously developed two world-unique instruments, MEDLEY and SCANDAL.

Highlights from the past year:

- Analysis and documentation has been finalized of previously performed measurements of elastic neutron scattering from hydrogen at 96 MeV. The results corroborate the normalization of previously obtained data at TSL, which have been under debate. This is of importance since this reaction serves as reference for many other measurements.
- Compelling evidence of the existence of three-body forces in nuclei has been obtained.
- Within the project, one PhD exam and one licentiate exam has been awarded. One PhD exam and one licentiate exam has been awarded for work closely related to the project.
- A new neutron beam facility with significantly improved performance has been built and commissioned at TSL.

Sammanfattning

Projektet NATT, Neutrondata för Acceleratordriven Transmutationsteknik, bedrivs inom kärnreaktionsgruppen vid institutionen för neutronforskning, Uppsala universitet. Gruppens verksamhet är inriktad mot experimentella studier av kärnfysikaliska reaktionssannolikheter för olika tillämpningsområden, som transmutation av kärnavfall, biomedicinska effekter och tillförlitlighet hos elektronik. Den experimentella verksamheten bedrivs huvudsakligen vid Svedberglaboratoriet (TSL) i Uppsala, där gruppen tidigare utvecklat två världsunika instrument, MEDLEY och SCANDAL.

Höjdpunkter från det gångna verksamhetsåret:

- Analys och dokumentation har färdigställts av tidigare utförda mätningar av elastisk neutronspridning mot väte vid 96 MeV. Resultaten av dessa mätningar styrker att tidigare mätningar vid TSL varit korrekt absolutnormerade, vilket varit under debatt. Detta är av stor betydelse eftersom denna reaktion utgör ”kalibrering” av många andra mätningar.
- Tydliga experimentella stöd för existensen av trekropparkrafter i kärnor har erhållits.
- Inom projektet har en doktorand disputerat för doktorsexamen och en för licentiatexamen. Ytterligare en licentiat- och en doktorsexamen har avlagts inom näraliggande verksamhet.
- En ny, radikalt förbättrad neutronfacilitet har byggts och tagits i drift vid Svedberglaboratoriet.

Contents

1 Background

1.1 The NATT project

The present project, Neutron data for Accelerator-driven Transmutation Technology (NATT), supported as a research task agreement by Statens Kärnkraftinspektion (SKI), Svensk Kärnbränslehantering AB (SKB), Ringhalsverket AB and Totalförsvarets forskningsinstitut (FOI), started 2002-07-01. The primary objective from the supporting organizations is to promote research and research education of relevance for development of the national competence within nuclear energy.

The aim of the project is in short to:

- promote development of the competence within nuclear physics and nuclear technology by supporting licenciate and PhD students,
- advance the international research front regarding fundamental nuclear data within the presently highlighted research area accelerator-driven transmutation,
- strengthen the Swedish influence within the mentioned research area by expanding the international contact network,
- provide a platform for Swedish participation in relevant EU projects,
- monitor the international development for the supporting organizations,
- constitute a basis for Swedish participation in the nuclear data activities at IAEA and OECD/NEA.

The project is operated by the Department of Neutron Research (INF) at Uppsala University, and is utilizing the unique neutron beam facility at the national The Svedberg Laboratory (TSL) at Uppsala University.

In this document, we give a status report after the second year (2003-07-01 – 2004-06-30) of the project.

1.2 The former KAT project

Project NATT was preceded by the project KAT (Kärndata för Acceleratorbaserad Transmutation, i.e. nuclear data for accelerator-driven transmutation). The contract on financial support to the KAT project was for four calendar years, during the period 1998-07-01 – 2002-06-30. Two students were supposed to be educated to PhD exam within the project. Because PhD students cannot be accepted at Uppsala university until full funding has been guaranteed, they were accepted September 1, 1998 (Joakim Klug) and March 1, 1999 (Cecilia Johansson). In addition, they have been involved on a minor fraction of their time in teaching and outreaching activities, paid from other sources.

Thereby, they still had some time left until dissertation for the PhD level at the time when the financial support was terminated. Funding for the remaining time had, however, been reserved, i.e. the total funding was adequate for completing the task. These modifications of the agenda have been presented to and agreed upon by the reference group.

Joakim Klug defended his PhD thesis “Elastic neutron scattering at 96 MeV” at June 6, 2003. Opponent was Dr Arjan Plompen, EU-JRC Institute for Reference Materials and Measurements, Geel, Belgium. Cecilia Johansson defended her PhD thesis “High-Sensitivity Radioactive Xenon Monitoring and High-Accuracy Neutron-Proton Scattering Measurements” at June 4, 2004. Opponent was Prof Allena Opper, Ohio University. Thereby, the deliverables of project KAT have been fulfilled, and the project is completed in all its aspects.

2 Introduction

Transmutation techniques in accelerator-driven systems (ADS) involve high-energy neutrons, created in the proton-induced spallation of a heavy target nucleus. The existing nuclear data libraries developed for reactors of today go up to about 20 MeV, which covers all available energies for that application; but with a spallator coupled to a core, neutrons with energies up to 1–2 GeV will be present. Although a large majority of the neutrons will be below 20 MeV, the relatively small fraction at higher energies still has to be characterized. Above about 200 MeV, direct reaction models work reasonably well, while at lower energies nuclear distortion plays a non-trivial role. This makes the 20–200 MeV region most important for new experimental cross section data /Blomgren, 2002/.

Ten years ago, very little high-quality neutron-induced data existed in this energy domain. Only the total cross section /Finlay et al. 1993/ and the np scattering cross section had been investigated extensively. Besides this, there were data on neutron elastic scattering from UC Davis at 65 MeV on a few nuclei /Hjort et al. 1994/. Programmes to measure neutron elastic scattering had been proposed or begun at Los Alamos /Rapaport and Osborne/ and IUCF /Finlay, 1992/, with the former resulting in a thesis on data on a few nuclei.

The situation was similar for (n,xp) reactions, where programmes have been run at UC Davis /Ford et al. 1989/, Los Alamos /Rapaport and Sugarbaker, 1994/, TRIUMF /Alford and Spicer, 1998/ and TSL Uppsala /Olsson, 1995; Blomgren, 1997/, but with limited coverage in secondary particle energy and angle. Better coverage had been obtained by the Louvain-la-Neuve group up to 70 MeV /Slypen et al. 1994/.

Thus, there was an urgent need for neutron-induced cross section data in the region around 100 MeV, which is an area where very few facilities in the world can give contributions. By international collaboration within an EU supported Concerted Action, which has been followed by the full scale project HINDAS, the level of ambition for the present project has been increased, and the potential of the unique neutron beam facility at The Svedberg Laboratory in Uppsala can be fully exploited.

During the last few years, the situation has improved dramatically, especially due to the HINDAS activities. At present, the nuclear data situation for ADS applications is relatively satisfactory up to 100 MeV. At 100 MeV, the hitherto most common energy at TSL, there are elastic neutron scattering data, neutron-induced light ion production data, neutron-induced activation, and fission cross sections available, in all cases on a series of nuclei. Some results have been published already, and there is a wealth of data under analysis and documentation. The present report will present some glimpses of this ongoing work.

Looking into the future, it can be envisioned that the coming 5–10 years will be devoted to similar activities at higher energies, i.e. up to 180 MeV, which is the highest neutron energy available at TSL.

3 Experimental setup and techniques

3.1 The TSL neutron beam facility

At TSL, quasi-monoenergetic neutrons are produced by the reaction ^{7}Li(p,n)^{7}Be in a ^{7}Li target bombarded by 50–180 MeV protons from the cyclotron, as is illustrated in Figure 3-1. /Condé et al. 1990; Klug et al. 2002/. After the target, the proton beam is bent by two dipole magnets into an 8 m long concrete tunnel, where it is focused and stopped in a well-shielded Faraday cup, used to measure the proton beam current. A narrow neutron beam is formed in the forward direction by a system of three collimators, with a total thickness of more than four metres.

The energy spectrum of the neutron beam consists of a high-energy peak, having approximately the same energy as the incident proton beam, and a low-energy tail. About half of all neutrons appear in the high-energy peak, while the rest are roughly equally distributed in energy, from the maximum energy and down to zero. The thermal contribution is small. The low-energy tail of the neutron beam can be reduced using time-of-flight (TOF) techniques over the long distance between the neutron source and the reaction target (about 8 m).

The relative neutron beam intensity is monitored by integrating the charge of the primary proton beam, as well as by using thin film breakdown counters, placed in the neutron beam, measuring the number of neutron-induced fissions in ^{238}U /Prokofiev et al. 1999/.

Two multi-purpose experimental setups are semi-permanently installed at the neutron beam line, namely MEDLEY and SCANDAL. These were described in detail in the annual report 1999/2000, and only a brief presentation is given here.

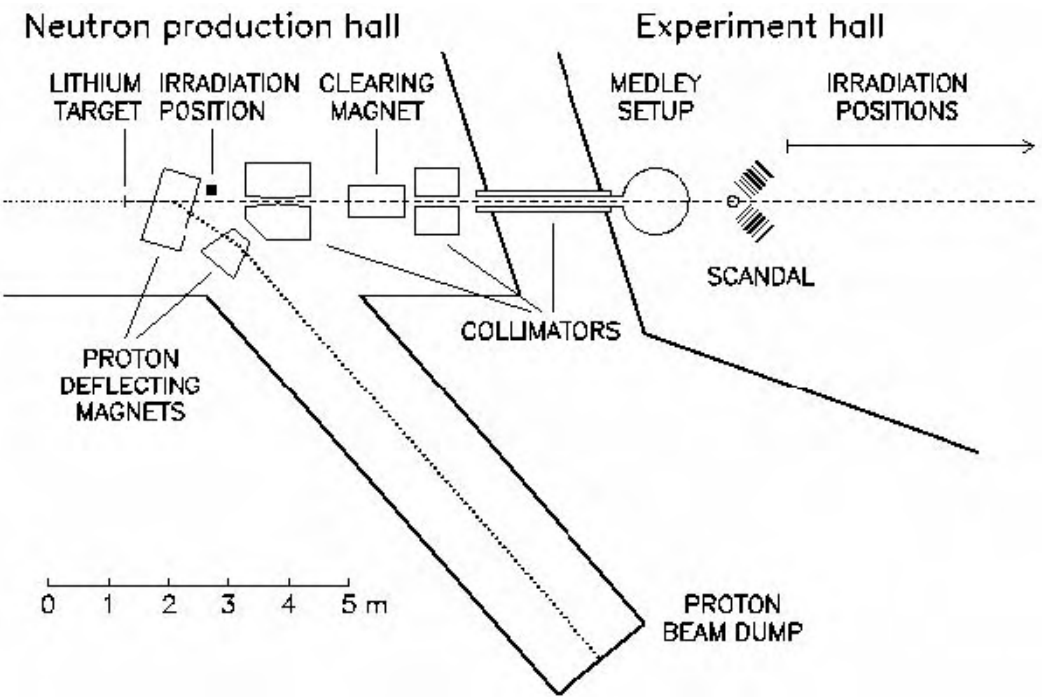

Figure 3-1. *The old TSL neutron beam facility.*

3.2 The MEDLEY setup

The MEDLEY detector array /Dangtip et al. 2000/, shown in Figure 3-2, is designed for measurements of neutron-induced light-ion production cross sections of relevance for applications within ADS and fast-neutron cancer therapy and related dosimetry. It consists of eight particle telescopes, installed at emission angles of 20–160 degrees with 20 degrees separation, in a 1 m diameter scattering chamber, positioned directly after the last neutron collimator. All the telescopes are fixed on a turnable plate at the bottom of the chamber, which can be rotated without breaking the vacuum.

Each telescope is a ΔE–ΔE–E detector combination, where the ΔE detectors are silicon surface barrier detectors with thicknesses of 50 or 60 μm and 400 or 500 μm, respectively, while the E detector is a 50 mm long inorganic CsI(Tl) crystal. ΔE-ΔE or ΔE-E techniques are used to identify light charged particles (p, d, t, 3He, α). The chosen design gives a sufficient dynamic range to distinguish all charged particles from a few MeV up to more than 100 MeV.

The solid angle of the telescopes is defined by active collimators, designed as thin hollow plastic scintillator detectors, mounted on small photomultiplier tubes. A signal from such a detector is used to veto the corresponding event, thereby ensuring that only particles that pass inside the collimator are registered.

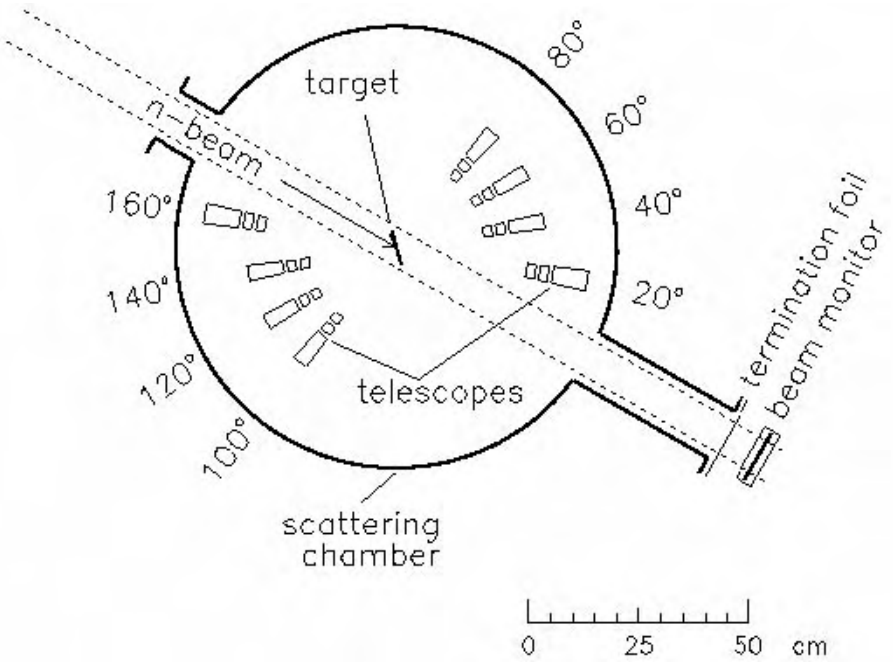

Figure 3-2. *The MEDLEY setup.*

3.3 The SCANDAL setup

The SCANDAL setup /Klug et al. 2002/ is primarily intended for studies of elastic neutron scattering, i.e. (n,n) reactions. Neutron detection is accomplished via conversion to protons by the H(n,p) reaction. In addition, (n,xp) reactions in nuclei can be studied by direct detection of protons. This feature is also used for calibration, and the setup has therefore been designed for a quick and simple change from one mode to the other.

The device is illustrated in Figure 3-3. It consists of two identical systems, in most cases located on each side of the neutron beam. The design allows the neutron beam to pass through the drift chambers of the right-side setup, making low-background measurements close to zero degrees feasible.

In neutron detection mode, each arm consists of a 2 mm thick veto scintillator for fast charged-particle rejection, a neutron-to-proton converter which is a 10 mm thick plastic scintillator, a 2 mm thick plastic scintillator for triggering, two drift chambers for proton tracking, a 2 mm thick ΔE plastic scintillator, which is also part of the trigger, and an array of 12 large CsI detectors for energy determination. The trigger is provided by a coincidence of the two trigger scintillators, vetoed by the front scintillator. The compact geometry allows a large solid angle for protons emitted from the converter. Recoil protons are selected using the ΔE and E information from the plastic scintillators and the CsI detectors, respectively. The energy resolution is about 3.7 MeV (FWHM), which is sufficient to resolve elastic and inelastic scattering in several nuclei. The angular resolution is calculated to be about 1.4 degrees (rms) when using a cylindrical scattering sample of 5 cm diameter.

When SCANDAL is used for (n,xp) studies, the veto and converter scintillators are removed. A multitarget arrangement can be used to increase the target content without impairing the energy resolution, which is typically 3.0 MeV (FWHM). This multitarget box allows up to seven targets to be mounted simultaneously, interspaced with multi-wire proportional counters (MWPC). In this way it is possible to determine in which target layer the reaction took place, and corrections for energy loss in the subsequent targets can be applied. In addition, different target materials can be studied simultaneously, thus facilitating absolute cross section normalization by filling a few of the multitarget slots with CH2 targets. The first two slots are normally kept empty, and used to identify charged particles contaminating the neutron beam.

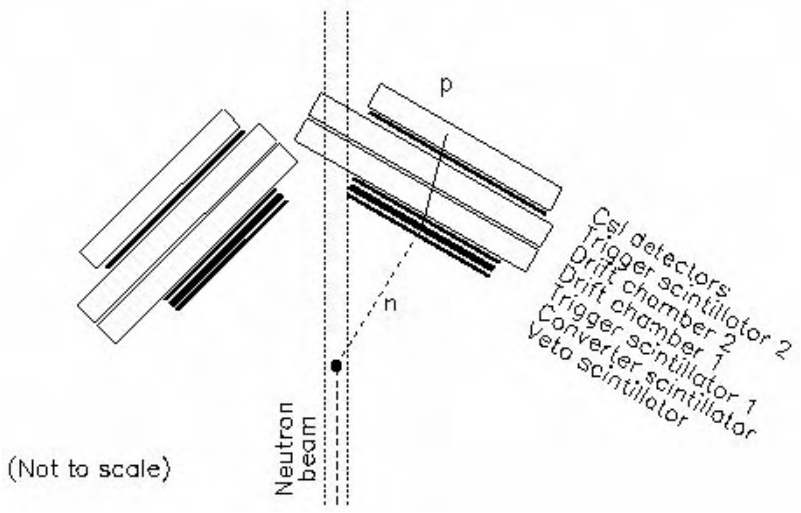

Figure 3-3. *The SCANDAL setup.*

3.4 New neutron beam facility at TSL

The rapidly increasing number of neutron beam users has motivated a new facility to be built. Practical work begun in spring 2002, which included re-building of beam line magnets, removal of obsolete heavy equipment and procurement of concrete for the new shielding walls. Major installations were undertaken in autumn 2003, during which the experimental program was resting. First beam was delivered early January 2004. During the first half of spring 2004, a series of commissioning runs were undertaken to characterize the beam, i.e. to measure beam energy spectra, intensity profiles, etc. First beam to commercial customers was delivered in May 2004, and the first physics experiment has been scheduled for late August 2004.

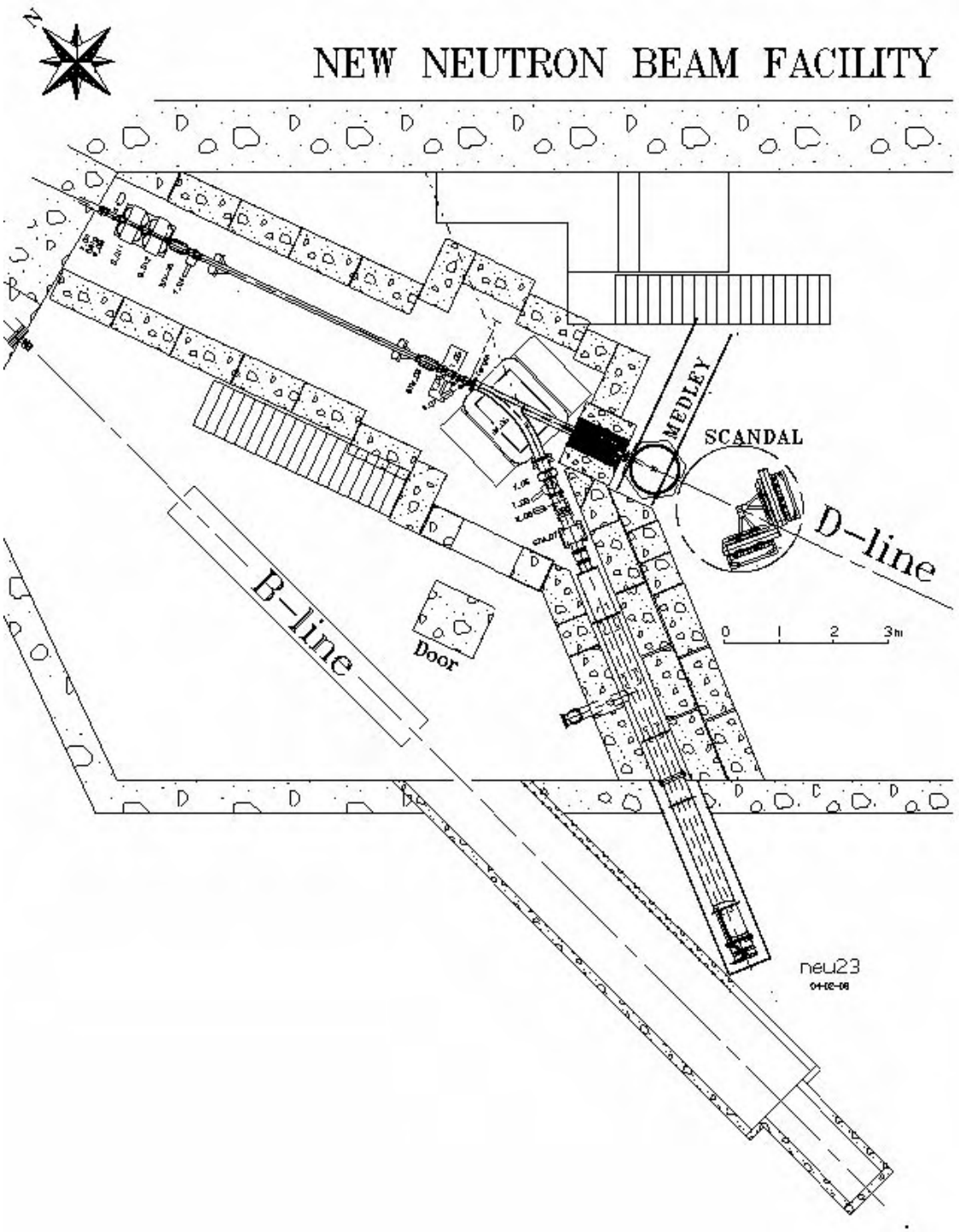

Figure 3-4. *The new neutron beam facility at TSL.*

4 Results

4.1 Elastic scattering

The analysis of the data on elastic scattering from ^{1}H, i.e. *np* scattering, has now resulted in final data. A preliminary angular distribution is shown in Figure 4-1. A paper has been submitted to Phys. Rev. C (appendix XV).

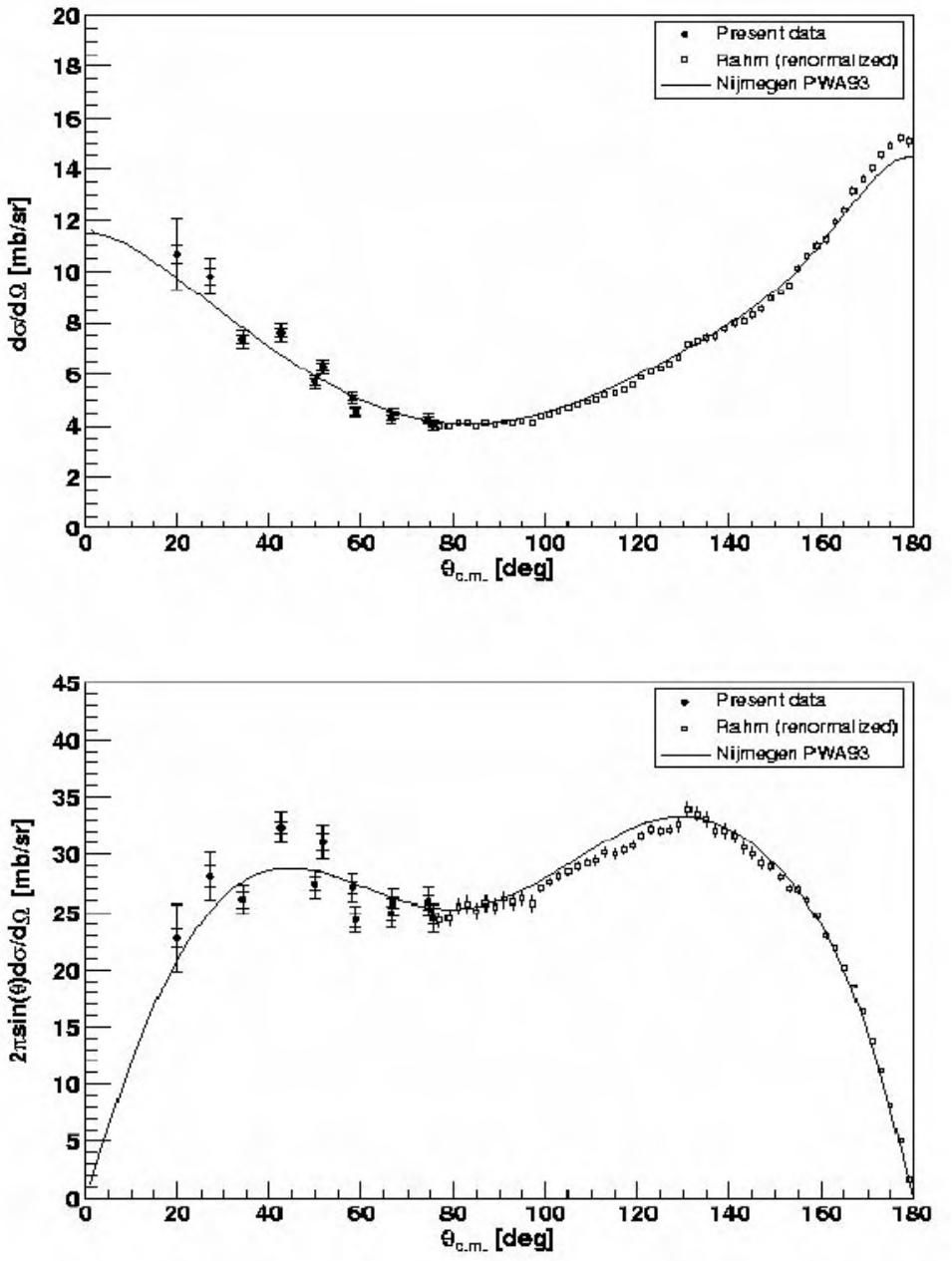

Figure 4-1. *The elastic neutron-proton scattering cross sections at 96 MeV. For details, see appendix XV.*

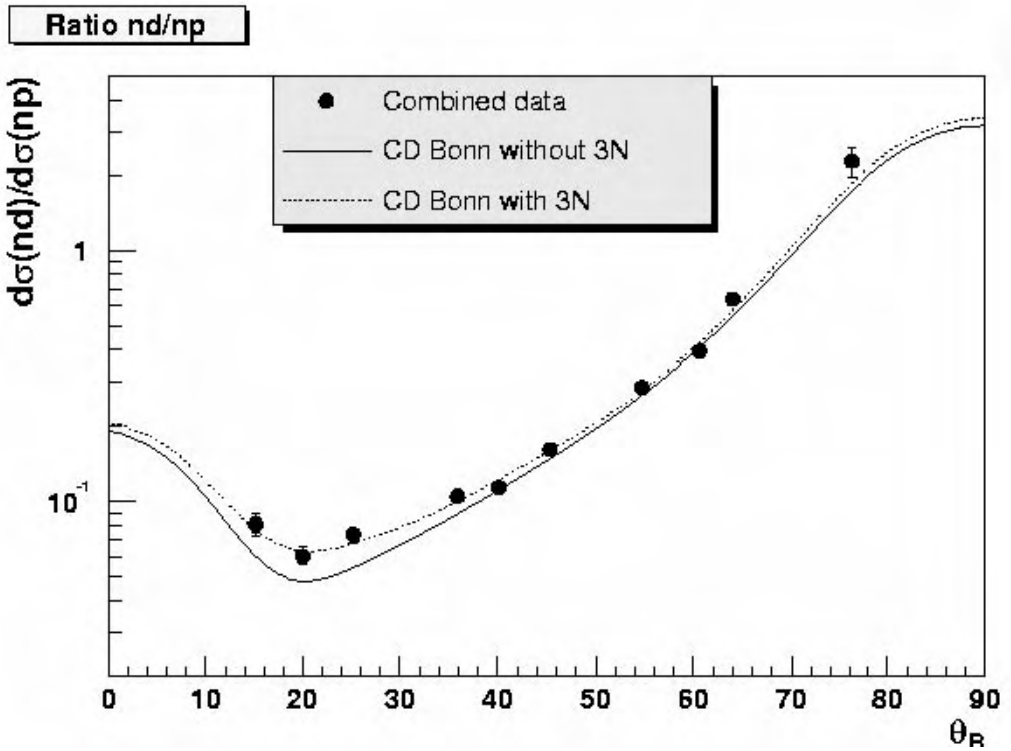

Figure 4-2. *The ratio of the neutron-deuteron and neutron-proton scattering cross sections at 95 MeV. The solid line is a theory prediction based on two-body forces only, while the dotted line includes three-body forces. For details, see appendix IV.*

Previously, our group has published results at backward angles, i.e. by detecting the emitted proton recoil /Rahm et al. 2001/. At forward angles, neutron detection has to be employed, which presents significantly increased experimental difficulties. With the present data, an essentially complete angular distribution has been obtained. This extended data set has been normalized to the experimental total *np* cross section, resulting in a renormalization of the earlier data of 0.7%, which is well within the reported normalization uncertainty for that experiment. In the elastic scattering measurements on carbon and lead /Klug et al. 2003/, a novel normalization technique was reported. This technique has also been investigated in the present experiment, but it turns out that it has a total uncertainty of about 7%, which is insufficient to allow for a reduction of the overall experimental accuracy. The results on forward *np* scattering are in reasonable agreement with theory models and partial wave analyses.

A number of experimental observations seem to indicate that three-body forces exist in nuclei. Recent calculations /Witala et al. 1998/ have indicated that measurements of the differential cross section for elastic neutron-deuteron (*nd*) scattering in the 60–200 MeV range should be useful in searches for three-nucleon (*3N*) force effects. The *nd* elastic scattering differential cross section has been measured using both MEDLEY and SCANDAL at 95 MeV incident neutron energy. Up to now, the MEDLEY data have been analyzed, and are presented in Figure 4-2 as the ratio between proton and deuteron production. It is evident that models based on inclusion of *3N* forces describe *nd* data in the angular region of the cross-section minimum very well, while models without 3N forces cannot account for the data. Additional data obtained with SCANDAL are under analysis. Preliminary, the results corroborate the MEDLEY results. A large publication is underway.

4.2 (n,xlcp) reactions

In parallel with the other experiments mentioned above and below, data were taken with the MEDLEY setup on light-ion production reactions (see Figure 4-3). During the last year, data analysis has been completed and the first papers (appendix I and III) have been published. Additional publications are underway.

4.3 (n,xn') reactions

We have a collaboration project with a group from Caen, France, on (n,xn') reactions. For these studies, a modified SCANDAL converter (CLODIA) has been designed and built in Caen. A series of test runs have lead to a final design, which was commissioned in beam in March 2003. A large experiment on lead and iron targets has been scheduled for August 2004. This experiment is our deliverable in the EU 6th FWP EUROTRANS.

4.4 Tagged neutron-proton scattering

Neutron-proton scattering is the reference cross section for fast-neutron reactions, i.e. it is the standard which all other cross sections are measured relative to. Besides our activities at TSL, we have been involved in a similar experiment at Indiana University Cyclotron Facility (IUCF), Bloomington, Indiana, USA. A large paper on the technical aspects of the project has been published in Nuclear Instruments and Methods A (appendix II), and the results have been presented at an international conference (appendix VIII).

4.5 Fission

We are working on the development of a setup for fission studies, based on MEDLEY in a revised geometric configuration. In November 2002, this facility was tested and in April 2003, data for publication were taken on fission cross sections and fragment angular distributions. One interesting feature of the new setup is that it allows a precise determination of the absolute cross section by measuring *np* scattering simultaneously. This is important, since only one previous experiment on high-energy fission has been performed with a reasonably good control of the absolute scale. The first results have been presented at international conferences (appendices X and XIV).

In addition, we have a long-term collaboration with a fission experiment group at Khlopin Radium Institute (KRI) in St Petersburg, Russia. Results from this collaboration has been presented in a journal publication (appendix VII), and additional publications are underway.

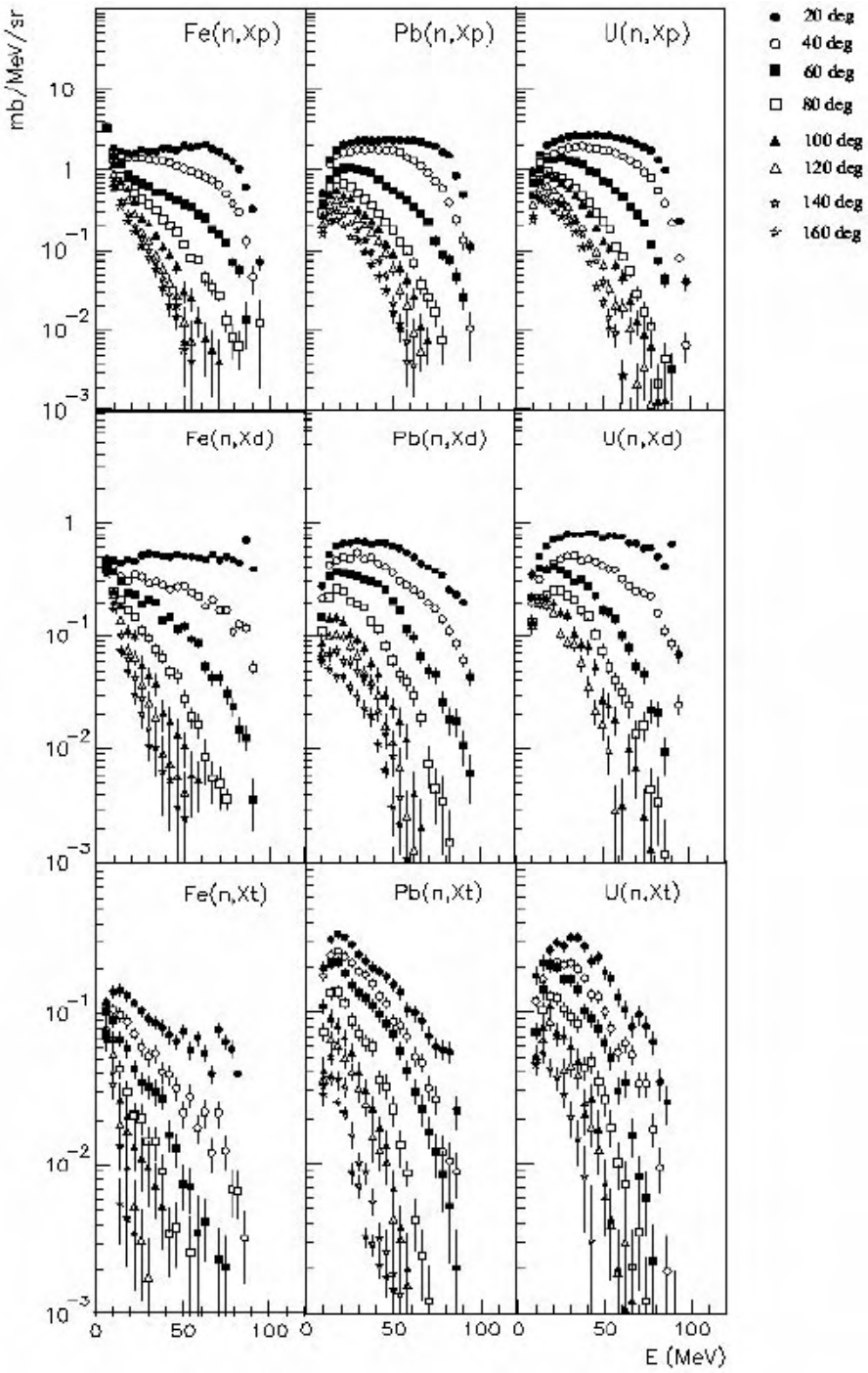

Figure 4-3. *The production of hydrogen ions at 96 MeV on iron, lead and uranium. For details, see appendix III.*

5 International activities

5.1 Collaboration

INF has participated in the EU project HINDAS (High- and Intermediate Energy Nuclear Data for Accelerator-Driven Systems), which involved 16 European institutions from Belgium, France, Germany, The Netherlands, Spain, Sweden and Switzerland. The experimental work was performed at six European laboratories (UCL in Louvain-la-Neuve, TSL in Uppsala, KVI in Groningen, PSI in Villigen, COSY at Jülich and GSI in Darmstadt). Work on the theoretical interpretation of the experimental results was also included. The project, which started 2000-09-01 and ended 2003-11-30, was coordinated by Prof Jean-Pierre Meulders, Louvain-la-Neuve, Belgium.

HINDAS had a total budget of 2.1 MEUR, whereof 210 kEUR fell on the Uppsala partner, while the collaborators that used the TSL neutron facility received in total about 500 kEUR. Most of the money was spent on PhD students or postdocs. Thus, the involvement in HINDAS resulted in an increased European focus on the activities at TSL.

To our judgment, HINDAS was very well organized and focused. It involved a major part of the competence and equipment available in Europe, and did significantly contribute to the development of nuclear data activities in Europe by bringing new scientists into this area.

At present, the organization of nuclear data activities in the upcoming 6th framework program EUROTRANS is being negotiated. It is already clear that the total nuclear data frame will be significantly smaller than in the 5th FWP. Our group and our long-term collaborators from LPC Caen, France, have merged our activities in EUROTRANS, and we have a joint deliverable concerning (n,xn') reactions (see above).

The enlargement of the European union has motivated a process of merging nuclear data activities in the EU and the candidate countries. Jan Blomgren has participated in this process, exemplified by contributions to a recent enlargement workshop (appendix V and VI). Additional workshops are planned for next project year.

5.2 Meetings and conferences

Nils Olsson is Swedish representative in the OECD/NEA Nuclear Science Committee (NSC) and its Executive Group. Notes from the meetings are enclosed in appendix XVIII.

6 Administrative matters

6.1 Staff and students

During the project year, Jan Blomgren has been project leader, active on a 25–50% basis within the project. His other major activities are teaching and duties as director of studies, both at INF and the Swedish Nuclear Technology Center (SKC). November 1, 2003, Blomgren was promoted to full professor. Assistant professor (forskarassistent) Stephan Pomp has worked essentially full time within the project with research and student supervision. Adjunct professor Nils Olsson, former project leader and now research director at FOI, is active within the project on a part-time basis (20%). Michael Österlund started July 1, 2003 as associate professor (universitetslektor). His main duty is teaching of nuclear power engineering for the Swedish Nuclear Safety Center (KSU), and he is involved in part-time research within the group. Leif Nilsson, retired professor, has been employed on about 10% time for student supervision.

Two PhD students are directly connected to and financed by the present project, Angelica Hildebrand and Philippe Mermod, which both are connected to the research school AIM (Advanced Instrumentation and Measurements). The KAT PhD students, Cecilia Johansson and Joakim Klug, have now both graduated, as discussed in the introduction. Udomrat Tippawan, employed at Chiang Mai University, Thailand, has been semi-permanently based in Uppsala during 2000–2004, financed with a scholarship from Thailand. He has had tasks strongly related to the present project, and especially to the line of development emerging from the collaboration with the French groups within HINDAS. Tippawan graduated for both licentiate and PhD degree during the present project year.

6.2 Reference group

The reference group consists of Per-Eric Ahlström (SKB), Benny Sundström (SKI), Thomas Lefvert (Vattenfall AB), Katarina Wilhelmsen (FOI) and Fredrik Winge (BKAB). A reference group meeting was held in Uppsala 2003-10-16. Scientific and administrative reports on the progress of the project were given at the meeting.

In addition to this meeting, the progress of the work has continuously been communicated to the reference group members by short, written, quarterly reports.

References

Alford W P, Spicer B M, 1998. Nucleon charge-exchange reactions at intermediate energy, Advances in Nuclear Physics 24, 1.

Blomgren J, 1997. The (n,p) reaction – Not So Boring After All? Proceedings from International Symposium on New Facet of Spin Giant Resonances in Nuclei, Tokyo, p 70. (Invited talk)

Blomgren J, 2002. Experimental activities at high energies, Proceedings from an international symposium on Accelerator Driven Systems for Energy production and Waste Incineration: Physics, Design and Related Nuclear Data, Trieste, p 327. (Invited talk)

Condé H, Hultqvist S, Olsson N, Rönnqvist T, Zorro R, Blomgren J, Tibell G, Håkansson A, Jonsson O, Lindholm A, Nilsson L, Renberg P-U, Brockstedt A, Ekström P, Österlund M, Brady P, Szeflinski Z, 1990. A facility for studies of neutron induced reactions in the 50 – 200 MeV range, Nucl. Instr. Meth. A292, 121.

Dangtip S, Atac A, Bergenwall B, Blomgren J, Elmgren K, Johansson C, Klug J, Olsson N, Alm Carlsson G, Söderberg J, Jonsson O, Nilsson L, Renberg P-U, Nadel-Turonski P, Le Brun C, Lecolley F-R, Lecolley J-F, Varignon C, Eudes Ph, Haddad F, Kerveno M, Kirchner T, Lebrun C, 2000. A facility for measurements of nuclear cross sections for fast neutron cancer therapy, Nucl. Instr. Meth. A452, 484.

Finlay R, Abfalterer W P, Fink G, Montei E, Adami T, Lisowski P W, Morgan G L, Haight R C, 1993. Neutron total cross sections at intermediate energies, Phys. Rev. C 47, 237.

Finlay R, 1992. Proposal to the NSF for support of CHICANE/Spectrometer System for the IUCF Cooler Ring.

Ford T D, Brady F P, Castaneda C M, Drummond J R, McEachern B, Romero J L, Sorenson D S, 1989. A large dynamic range detector for measurement of neutron-induced charged particle spectra down to zero degrees, Nucl. Instr. Meth. A274, 253.

Hjort E L, Brady F P, Romero J L, Drummond J R, Sorenson D S, Osborne J H, McEachern B, 1994. Measurements and analysis of neutron elastic scattering at 65 MeV, Phys. Rev. C 50, 275.

Klug J, Blomgren J, Atac A, Bergenwall B, Dangtip S, Elmgren K, Johansson C, Olsson N, Rahm J, Jonsson O, Nilsson L, Renberg P-U, Nadel-Turonski P, Ringbom A, Oberstedt A, Tovesson F, Le Brun C, Lecolley J-F, Lecolley F-R, Louvel M, Marie N, Schweitzer C, Varignon C, Eudes Ph, Haddad F, Kerveno M, Kirchner T, Lebrun C, Stuttgé L, Slypen I, Prokofiev A, Smirnov A, Michel R, Neumann S, Herpers U, 2002. SCANDAL – A facility for elastic neutron scattering studies in the 50–130 MeV range, Nucl. Instr. Meth. A489, 282.

Klug J, Blomgren J, Atac A, Bergenwall B, Hildebrand A, Johansson C, Mermod P, Nilsson L, Pomp S, Tippawan U, Elmgren K, Olsson N, Jonsson O, Prokofiev A V, Renberg P-U, Nadel-Turonski P, Dangtip S, Phansuke P, Österlund M, Le Brun C, Lecolley J F, Lecolley F R, Louvel M, Marie-Noury N, Schweitzer C, Eudes Ph, Haddad F, Lebrun C, Koning A J, Ledoux X, 2003. Elastic neutron scattering at 96 MeV from ^{12}C and ^{208}Pb, Phys. Rev. C 68, 064605.

Olsson N, 1995. Studies of spin-isospin excitations at TSL in Uppsala, Nucl. Phys. News 5, no. 2, 28.

Prokofiev A V, Smirnov A N, Renberg P-U, 1999. A monitor for intermediate-energy neutrons based on thin film breakdown counters, Report TSL/ISV-99-0203, Uppsala University.

Rahm J, Blomgren J, Condé H, Dangtip S, Elmgren K, Olsson N, Rönnqvist T, Zorro R, Jonsson O, Nilsson L, Renberg P-U, Ringbom A, Tibell G, van der Werf S Y, Ericson T E O, Loiseau B, 2001. np scattering measurements at 96 MeV, Phys. Rev. C 63, 044001.

Rapaport J, Sugarbaker E, 1994. Isovector excitations in nuclei, Ann. Rev. Nucl. Part. Sci. 44, 109.

Rapaport J, private communication, and **Osborne J**, thesis, unpublished.

Slypen I, Corcalciuc V, Ninane A, Meulders J P, 1994. Charged particles produced in fast neutron induced reactions ^{12}C in the 45–80 MeV energy range, Nucl. Instr. Meth. A337, 431.

Witala H, Glöckle W, Hüber D, Golak J, Kamada H, 1998. Cross section minima in elastic Nd scattering: Possible evidence for three-nucleon force effects, Phys. Rev. Lett. 81, 1183.

Appendix I

PHYSICAL REVIEW C **69**, 064609 (2004)

Light-ion production in the interaction of 96 MeV neutrons with silicon

U. Tippawan,[1,2] S. Pomp,[1,*] A. Ataç,[1] B. Bergenwall,[1] J. Blomgren,[1] S. Dangtip,[1,2] A. Hildebrand,[1] C. Johansson,[1] J. Klug,[1] P. Mermod,[1] L. Nilsson,[1,4] M. Österlund,[1] N. Olsson,[1,3] K. Elmgren,[3] O. Jonsson,[4] A. V. Prokofiev,[4] P.-U. Renberg,[4] P. Nadel-Turonski,[5] V. Corcalciuc,[6] Y. Watanabe,[7] and A. J. Koning[8]

[1]*Department of Neutron Research, Uppsala University, Uppsala, Sweden*

[2]*Fast Neutron Research Facility, Chiang Mai University, Chiang Mai, Thailand*

[3]*Swedish Defence Research Agency, Stockholm, Uppsala, Sweden*

[4]*The Svedberg Laboratory, Uppsala University, Uppsala, Sweden*

[5]*Department of Radiation Sciences, Uppsala University, Uppsala, Sweden*

[6]*Institute of Atomic Physics, Heavy Ion Department, Bucharest, Romania*

[7]*Department of Advanced Energy Engineering Science, Kyushu University, Kasuga, Japan*

[8]*Nuclear Research and Consultancy Group, Petten, The Netherlands*

(Received 16 January 2004; published 16 June 2004)

Double-differential cross sections for light-ion (p, d, t, ^{3}He, and α) production in silicon, induced by 96 MeV neutrons, are reported. Energy spectra are measured at eight laboratory angles from 20° to 160° in steps of 20°. Procedures for data taking and data reduction are presented. Deduced energy-differential, angle-differential, and production cross sections are reported. Experimental cross sections are compared to theoretical reaction model calculations and experimental data in the literature.

DOI: 10.1103/PhysRevC.69.064609 PACS number(s): 25.40.Hs, 25.40.Kv, 24.10.−i, 28.20.−v

I. INTRODUCTION

In the past few years, there has been an increasing request for experimental studies of fast-neutron-induced reactions, especially at higher incident neutron energies. For basic physics, nucleon-induced reactions provide useful means to investigate nuclear structure, to characterize reaction mechanisms and to impose stringent constraints on nuclear model calculations. The silicon nucleus is sufficiently heavy for many of the statistical assumptions to hold (high density of excited states), yet not so heavy to give a strong suppression of charged particle emission due to Coulomb barrier effects. Therefore, nuclear reaction models for equilibrium and pre-equilibrium decay can be tested and benchmarked. Experimental data in the literature at incident neutron energies from reaction thresholds up to 60 MeV [1] and between 25 and 65 MeV [2] offer possibilities to test the predictions of reaction models.

In recent years, an increasing number of applications involving fast neutrons have been developed or are under consideration, e.g., radiation treatment of cancer [3–5], soft-error effects in computer memories [6], accelerator-driven transmutation of nuclear waste and energy production [7], and determination of the response of neutron detectors [8]. Silicon data are particularly important for detailed soft-error simulation in electronic devices [6,9].

In this paper, we present experimental double-differential cross sections (inclusive yields) for protons, deuterons, tritons, ^{3}He, and alpha particles produced by 96 MeV neutrons incident on silicon. Measurements have been performed at the cyclotron of The Svedberg Laboratory (TSL), Uppsala, using the dedicated MEDLEY experimental setup [10]. Spectra have been measured at eight laboratory angles, ranging from 20° to 160° in 20° steps. Extrapolation procedures are used to obtain coverage of the full angular distribution and consequently energy-differential and production cross sections are deduced, the latter by integrating over energy and angle. The experimental data are compared to results of calculations with nuclear reaction codes and to existing experimental data.

The experimental methods are briefly discussed in Sec. II and data reduction and correction procedures are presented in Secs. III and IV, respectively. The theoretical framework is presented in Sec. V. In Sec. VI, experimental results are reported and compared with theoretical and previous experimental data. Conclusions and an outlook are given in Sec. VII.

II. EXPERIMENTAL SETUP AND METHODS

The neutron beam facility at TSL uses the ^{7}Li$(p,n)^7$Be reaction (Q=−1.64 MeV) to produce a quasimonoenergetic neutron beam [11]. The lithium target was 26 mm in diameter and 8 mm thick in the present experiment and enriched to 99.98% in ^{7}Li. The 98.5±0.3 MeV protons from the cyclotron impinge on the lithium target, producing a full-energy peak of neutrons at 95.6±0.5 MeV with a width of 1.6 MeV (FWHM) and containing 40% of the neutrons, and an almost constant low-energy tail containing 60% of the neutrons. The neutron beam is shaped by a collimator system, and delivered to the experimental area. After passage of the target, the proton beam is deflected by two magnets into a well-shielded beam dump, where the beam current is integrated in a Faraday cup. The integrated charge serves as one neutron beam monitor. With a beam intensity of about 5 μA, the neutron flux at the target location is about 5

*Corresponding author. Electronic address: stephan.pomp@tsl.uu.se

$\times 10^4$ neutrons/(s cm^2). The collimated neutron beam has a diameter of 80 mm at the location of the target. A thin-film breakdown counter (TFBC) [12] installed after the reaction chamber is used as another beam monitor. The two beam monitor readings were in agreement during the measurements.

The charged particles are detected by the MEDLEY setup [10]. It consists of eight three-element telescopes mounted inside a 100-cm-diam evacuated reaction chamber. Each telescope consists of two fully depleted ΔE silicon surface barrier detectors and a CsI(Tl) crystal. The thickness of the first ΔE detector (ΔE_1) is either 50 or 60 μm, while the second one (ΔE_2) is either 400 or 500 μm. They are all 23.9 mm in diameter (nominal). The cylindrical CsI(Tl) crystal, 50 mm long and 40 mm in diameter, serves as the E detector. The back-end part of the crystal, 20 mm long, has a conical shape, tapered off to 18 mm diameter, to fit the size of a readout diode.

To obtain a well-defined acceptance, a plastic scintillator collimator is placed in front of each telescope. The active collimators have an opening of 19 mm diameter and a thickness of 1 mm.

A passivated implanted planar silicon (PIPS) detector is used as an active target. It has a 32×32 mm^2 quadratic shape and a thickness of 303 μm. It is suspended in a thin aluminum frame using threads and small springs. The dimensions of the frame have been chosen in such a way so that it does not interfere with the incident neutron beam. Besides the energy deposited by the detected light ion, the active target recorded the energy deposition due to other products, like recoils, of the same event. This information was, however, not used in the present analysis.

For absolute cross-section normalization, a 25-mm-diam and 1.0-mm-thick polyethylene $(CH_2)_n$ target is used. The np cross section at 20° laboratory angle provides the reference cross section [13].

The background is measured by removing the target from the neutron beam. It is dominated by protons produced by neutron beam interaction with the beam tube and reaction chamber material, especially at the entrance and exit of the reaction chamber and in the telescope housings. Therefore, the telescopes at 20° and 160° are most affected. Since the protons in the background originated not from the target but came from different directions, they can be misidentified-leading to a large background even for the other particles. For the 160° telescope, i.e., the worst case, the signal-to-background ratios are 2.5, 1, and 0.1 for protons, deuterons, and tritons, respectively, whereas the corresponding numbers for the 40° telescope, i.e., the best case, are 8, 12, and 5. In the case of ^{3}He and alpha particles, the background is negligible.

The time of flight (TOF), obtained from the radio frequency of the cyclotron (stop signal for the TDC) and the timing signal from each of the eight telescopes (start signal), is measured for each charged-particle event. The raw data are stored event by event for online monitoring and subsequent offline analysis. Typical count rates for target-in and target-out runs were 10 and 2 Hz, respectively. The dead time of the system was typically 1–2 % and never exceeding 10%.

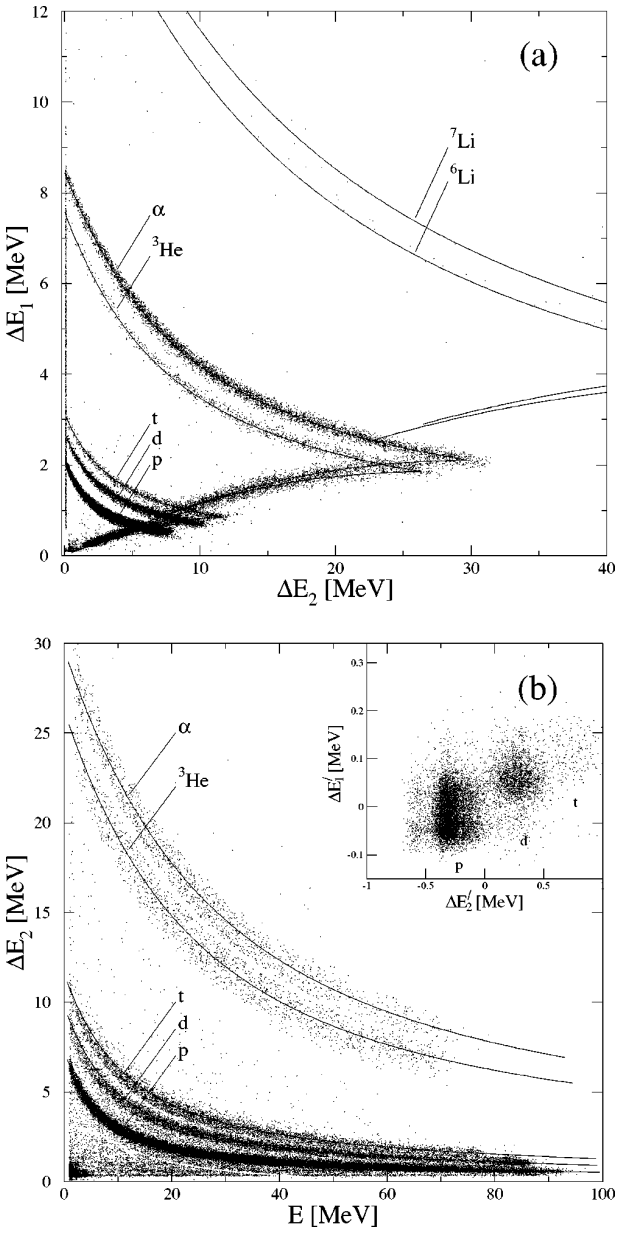

FIG. 1. (a) Particle identification spectra at 20° for the (a) $\Delta E_1 - \Delta E_2$ and (b) $\Delta E_2 - E$ detector combinations. The solid lines represent tabulated energy loss values in silicon [14]. The insert in (b) illustrates the separation of high-energy protons, deuterons, and tritons discussed in Sec. III A.

III. DATA REDUCTION PROCEDURES

A. Particle identification and energy calibration

The $\Delta E - E$ technique is used to identify light charged particles ranging from protons to lithium ions, which is illustrated in Fig. 1(a). Good separation of all particles is btained over their entire energy range. Since the energy resolution of each individual detector varies with the particle type, the particle identification cuts are defined to cover 3σ, where σ is the standard deviation of the energy resolution of each

particle type. Typical energy resolutions of the thin ΔE detectors are between 40 and 80 keV, increasing with particle mass. The corresponding values are between 150 and 550 keV for the thick ΔE detectors and between 900 and 1200 keV for the E detectors. For energy depositions in the E detector above 70 MeV in Fig. 1(b), the two-dimensional cuts for protons, deuterons, and tritons overlap slightly since the energy loss of the hydrogen isotopes in the ΔE_2 detector is rather small. This ambiguity is resolved by a two-dimensional plot [inset of Fig. 1(b)] of the deviations of the ΔE_1 and ΔE_2 signals from tabulated energy loss values in silicon [14] [solid lines in Fig. 1(a)]. Particle identification is done by cutting along the minimum contour line, and thus possible misidentification should even out. This technique is also used to improve the separation between ^{3}He and alpha particles in some telescopes where the energy resolution is poor.

Energy calibration of all detectors is obtained from the data itself [15]. Events in the $\Delta E-E$ bands are fitted with respect to the energy deposited in the three detectors (solid lines in Fig. 1). This energy is determined from the detector thicknesses and tabulated energy loss values in silicon [14]. The ΔE_1 detectors are further calibrated and checked using a 5.48 MeV alpha source. For the energy calibration of the CsI(Tl) detectors, two parameterizations of the light output versus energy of the detected particle [10] are used, one for hydrogen isotopes and another one for helium isotopes. Supplementary calibration points are provided by the $H(n,p)$ reaction, as well as transitions to the ground state and low-lying states in the $^{12}C(n,d)^{11}B$ and $^{28}Si(n,d)^{27}Al$ reactions. The energy of each particle type is obtained by adding the energy deposited in each element of the telescope.

Low-energy charged particles are stopped in the ΔE_1 detector, leading to a low-energy cutoff for particle identification of about 3 MeV for hydrogen isotopes and about 8 MeV for helium isotopes [see Fig. 1(a)]. The helium isotopes stopped in the ΔE_1 detector are nevertheless analyzed and a remarkably low cutoff, about 4 MeV, can be achieved for the experimental alpha-particle spectra. These alpha-particle events could obviously not be separated from ^{3}He events in the same energy region, but the yield of ^{3}He is much smaller than the alpha-particle yield in the region just above 8 MeV, where the particle identification works properly. That the relative yield of ^{3}He is small is also supported by the theoretical calculations in the evaporation peak region. In conclusion, the ^{3}He yield is within the statistical uncertainties of the alpha-particle yield for alpha energies between 4 and 8 MeV. A consequence of this procedure is that the ^{3}He spectra have a low-energy cutoff of about 8 MeV.

B. Low-energy neutron rejection and background subtraction

Knowing the energy calibration and the flight distances, the flight time for each charged particle from target to detector can be calculated and subtracted from the registered total TOF. The resulting neutron TOF is used for selection of charged-particle events induced by neutrons in the main peak of the incident neutron spectrum. The TOF cut reduces the background of charged particles produced by peak neutrons hitting the chamber and telescope housing since the flight paths are different, especially for the backward telescopes. The widths of the TOF cuts in all detectors are fixed to 3σ, where σ is the standard deviation of the $H(n,p)$ peak in the 20° telescope. Figure 2(a) illustrates the selection procedure for deuterons at 20° laboratory angle. The solid line is a

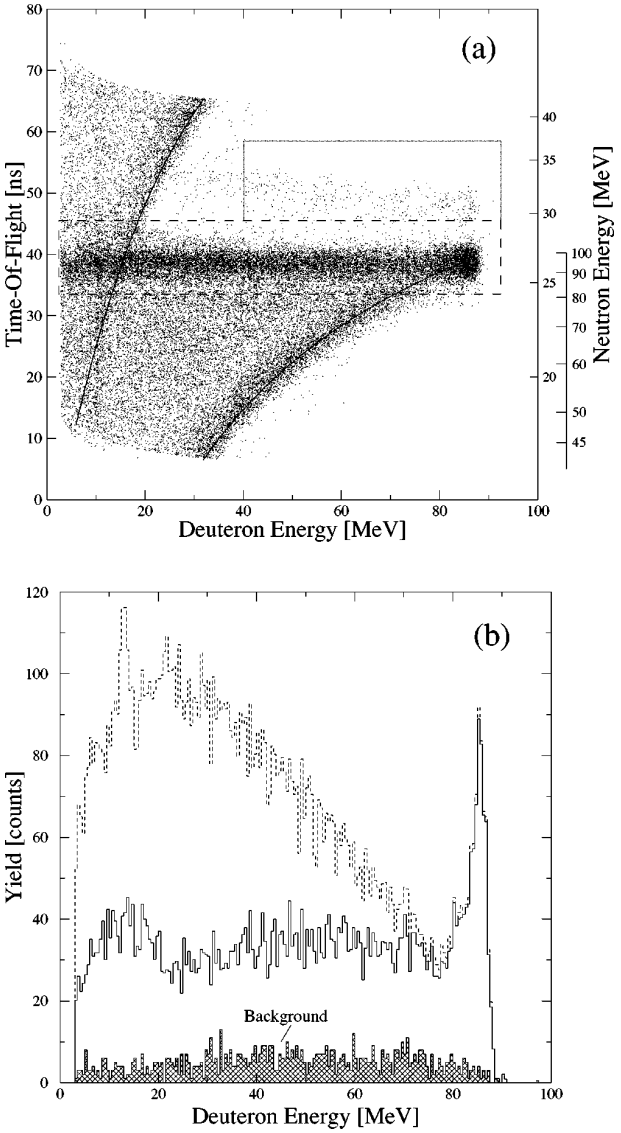

FIG. 2. (a) Neutron TOF spectrum vs deuteron energy for the $Si(n,dx)$ reaction at 20° and the selection of deuterons associated with the full-energy neutron peak. The neutron-energy scale is given to the right. The solid line is a kinematic calculation of the ground-state deuteron energy as a function of the neutron energy. The lower rectangular cut is associated with neutrons in the full-energy peak, whereas the adjacent rectangular cut is used when correcting for the observed timing shift discussed in Sec. IV C. (b) Deuteron energy spectrum at 20° with (solid histogram) and without (dashed histogram) the full-energy neutron cut. The cross-hatched histogram shows the target-out background. The bump below 20 MeV in the solid histogram is due to wraparound effects discussed in Sec. IV C.

kinematic calculation of the ground-state peak in the deuteron spectra for each corresponding neutron energy. It provides a cross check of the energy and time calibration of the whole energy spectrum.

Background events, measured in target-out runs and analyzed in the same way as target-in events, are subtracted from the corresponding target-in runs after normalization to the same neutron fluence. Figure 2(b) shows the resulting spectrum of deuteron events at 20° induced by the main neutron peak. For comparison, the same spectrum without TOF cut is presented. Finally, the target-out background obtained with the same TOF cut is shown. The signal-to-background ratio is about 4.

C. Absolute cross-section normalization

Absolute double-differential cross sections are obtained by normalizing the silicon data to the number of recoil protons emerging from the CH_2 target. After selection of events in the main neutron peak and proper subtraction of the target-out and $^{12}C(n,p)$ background contributions, the latter taken from a previous experiment, the cross section can be determined from the recoil proton peak, using *np* scattering data [13]. All data have been normalized using the *np* scattering peak in the 20° telescope. As a cross check, $Si(n,px)$ spectra have also been normalized using the *np* scattering peak in the 40° and 60° telescopes, resulting in spectra in agreement with those normalized to the 20° telescope.

IV. CORRECTIONS

A. Thick target correction

Due to the thickness of the target and to the low-energy cutoffs in the particle identification, the measured low-energy charged particles are produced in fractions of the entire thickness of the target. Therefore, not only energy-loss corrections are needed but also particle-loss corrections. Charged particles with the initial kinetic energy E_{init} have a well-defined range R in the target material. If $R(E_{init})$ is equal to or larger than the target thickness, all produced particles can escape from the target and no particle loss correction is required. If, on the other hand, $R(E_{init})$ is smaller than the target thickness, a correction for particles stopped inside the target is needed.

The adopted correction method employs an initial energy (E_{init}) distribution called the inverse response function for each measured energy. For the 303 μm silicon target used in the present experiment, a measured alpha particle of 4 MeV could either be due to a 4 MeV particle from the front surface of the target, a 27 MeV particle from the back surface of the target, or anything in between. Therefore, the content of the measured energy bin should be redistributed over the initial energy region from 4 to 27 MeV. A FORTRAN program, TCORR [16], has been developed which calculates the inverse response functions, initially assuming an energy-independent cross section. These inverse response functions are normalized to the corresponding bin content in the measured spectrum and summed to get the true initial energy spectrum. Finally, the particle loss correction is applied. The resulting spectrum is folded with the primary inverse response functions to get improved inverse response functions, and the procedure is repeated. Resulting spectra from two successive iterations are compared by a Kolmogorov test [17] to judge the convergence.

Results from the correction method have been verified with an independent Monte Carlo program called TARGSIM, based on the GEANT code [18]. This program simulates the measured spectra using the corrected spectra and the MEDLEY geometry as the input. The simulation results are in agreement with the experimental data within the statistical errors over the whole energy region.

Obviously, the simulated spectra have much better statistics than the original experimental spectra and, therefore, the statistical fluctuations between neighboring energy bins are much smaller. In a sense, they are fits to the experimental spectra. In order to estimate the systematic uncertainty introduced by the thick target correction, these simulated spectra are corrected with TCORR again and compared with the result of the first correction. The observed differences for individual energy bins are typically 5% and less than 10% in general. An extreme value of 40% was found in the lowest bin of the alpha spectrum at 140°. However, in all cases, except for protons where the statistical errors are very small, the deviations are within the statistical uncertainties of the original corrected data.

In conclusion, the systematic error of the target correction comes essentially from the statistical uncertainties. For protons and deuterons we estimate that this error is about 10% in the lowest two energy bins decreasing to a few percent from 15 MeV and upwards. Due to less statistics and the increasing width of the inverse response functions, the uncertainty is larger for tritons, ^{3}He and alpha particles, where it is 20% in the lowest two bins, decreasing to 10% above 25 MeV.

In addition, evaluated data [19] were used as input to check the reliability of our programs, obviously because validation with known realistic data is desirable. The latter have been simulated with the TARGSIM program to get pseudoexperimental data and have subsequently been corrected with the TCORR program using the same conditions as in the experiment. The corrected results appear to reproduce the known realistic data well.

B. Collimator correction

As mentioned in Sec. II, active collimators have been placed in front of the telescope in order to define the solid angle. However, due to malfunctioning in the present experiment, the signal from these collimators could not be used to suppress events hitting them. Therefore, although the collimators actually work as passive collimators for helium particles below 35 MeV, their effect when particles punch through them has to be corrected for. To this end, a FORTRAN program has been developed that, based on the measured spectrum of particles and an iteration procedure, estimates the shape and fraction of the energy spectrum of particles hitting the collimator. It has been found that the corrections in shape are rather small and under control in all cases. The

systematic error related to this correction comes from the uncertainty in the solid angle subtended by the silicon detectors for high-energy protons relative to the solid angle subtended by the collimator opening. This uncertainty is estimated to be 5% and, due to the normalization procedure, only affects the helium spectra and the low-energy part of the hydrogen spectra.

C. Other corrections

The 17 MHz repetition rate of the cyclotron beam pulse, which limits the TOF window to 58 ns, causes wraparound problems. Thus, it is not possible to distinguish 96 MeV neutrons from those of 26 MeV created by the previous beam burst, since the latter have the same apparent TOF. This can be seen in Fig. 2(a), where the bent band from the low-energy neutron tail crosses the straight band of the full-energy neutrons. Since the Q value for the ^{28}Si(n,d) reaction is −9.4 MeV, this interference shows up as a bump below 20 MeV in Fig. 2(b). A correction for this effected is applied, using tabulated values from Ref. [23] and a ratio of the neutron fluence in the wraparound region and at 96 MeV of 6.3%. For the neutron-energy spectrum in the wraparound region, a square distribution ranging from 24 to 29 MeV is assumed. Thus, the cross sections at 24, 26, and 28 MeV as given in Ref. [23] are used, with the 24 MeV values entering at half weight. The data for 80°, 100°, 120°, 140°, and 160° are obtained by linear interpolation. Only the spectra for proton, deuteron, and alpha particles are corrected. The effect of this correction is a reduction of about 5% in the production cross section. In the (n,d) spectra presented in Fig. 4, some structure at 20° and 40° around 15 MeV might be attributed to deficiencies in the correction. The triton production cross sections given in Ref. [23] (Q value=−16.2 MeV) indicate, that the correction would be about an order of magnitude lower and is therefore negligible. For ^{3}He production (Q value=−12.1 MeV), the correction is also negligible due to the high-energy cutoff of 8 MeV.

There is a TOF shift problem, seen as a band parallel with the main band in Fig. 2(a). The reason for this is probably that the electronic timing module has not worked properly. This is corrected by extending the TOF cut with the dotted rectangle in the same figure to include these events. This method could be applied only in the energy region where there is no interference from the low-energy neutron tail. Therefore, the ratio of the number of events between the parallel and the main band is determined and then applied to the low-energy region as well. This ratio is 1.3% in the worst case.

Albeit a majority of the neutrons appears in the narrow full-energy peak at 95.6% MeV, a significant fraction (about 25%) belongs to a tail extending towards lower energies, remaining also after the TOF cut. The average neutron energy with these tail neutrons included is 92.4 MeV. This effect has been taken into account in the normalization of the data. Minor corrections of a few percent are applied to the experimental spectra for the CsI(Tl) intrinsic efficiency [11] and for the dead time in the data acquisition system.

V. THEORETICAL MODELS

Data have been compared with nclear theory predictions, computed with the two nuclear reaction codes GNASH [20,21] and TALYS [22]. While GNASH has been widely used during the last years, TALYS is a new code still under development. Two sets of GNASH calculations are presented, one with parameters as presented in a recent evaluation [23], and another set with modified parameters [19] as described in Sec. V B. The latter parameter set is developed as part of another data evaluation [24]. Since the latter work and TALYS are not published, they are described in some detail below.

Both GNASH and TALYS integrate direct, preequilibrium, and statistical nuclear reaction models into one calculation scheme and thereby give predictions for all the open reaction channels. Both codes use the Hauser-Feshbach model for sequential equilibrium decay and the exciton model for preequilibrium emission. The angular distributions are obtained using the Kalbach systematics [25].

A. TALYS calculations

The purpose of TALYS is to simulate nuclear reactions that involve neutrons, photons, protons, deuterons, tritons, ^{3}He, and alpha particles, in the 1 keV–200 MeV energy range. Predicted quantities include integrated, single- and double-differential cross sections, for both the continuum and discrete states, residue production and fission cross sections, gamma-ray production cross sections, etc. For the present work, single- and double-differential cross sections are of interest. To predict these, a calculation scheme is invoked which consists of a direct direct+preequilibrium reaction calculation followed by subsequent compound nucleus decay of all possible residual nuclides calculated by means of the Hauser-Feshbach model.

First, dedicated optical model potentials (OMP) were developed for both neutrons and protons on ^{28}Si up to 200 MeV. The used parameters are from the OMP collection of Ref. [26]. These potentials provide the necessary reaction cross sections and transmission coefficients for the statistical model calculations. For complex particles, the optical potentials were directly derived from the nucleon potentials using the folding approach of Watanabe [27].

Preequilibrium emission takes place after the first stage of the reaction but long before statistical equilibrium of the compound nucleus is attained. It is imagined that the incident particle step-by-step creates more complex states in the compound system and gradually loses its memory of the initial energy and direction. The default preequilibrium model of TALYS is the two-component exciton model of Kalbach [28]. In the exciton model (see Refs. [29,30] for extensive reviews), at any moment during the reaction, the nuclear state is characterized by the total energy E_{tot} and the total number of particles above and holes below the Fermi surface. Particles (p) and holes (h) are indiscriminately referred to as excitons. Furthermore, it is assumed that all possible ways of sharing the excitation energy between different particle-hole configurations with the same exciton number $n=p+h$ have equal probability. To keep track of the evolution of the scattering process, one merely traces the development of the exciton number, which changes in time as a result of intranuclear two-body collisions.

The basic starting point of the exciton model is a time-dependent master equation, which describes the probability

of transitions to more and less complex particle-hole states as well as transitions to the continuum, i.e., emission. Upon integration over time, the energy-averaged emission spectrum is obtained. The assumptions above make the exciton model amenable to practical calculations. This, however, requires the introduction of a free parameter, namely the average matrix element of the residual two-body interaction, occurring in the transition rates between two exciton states. Without going into details, the basic formulas are given for the two-component exciton model. The created particles and holes of proton and neutron type are explicitly followed throughout the reaction. A notation is used in which $p_\pi(p_\nu)$ is the proton (neutron) particle number and $h_\pi(h_\nu)$ the proton (neutron) hole number. Following Kalbach [28], the exciton model cross section is now given by

$$\frac{d\sigma_k^{EM}}{dE_k} = \sigma^{CF} \sum_{p_\pi=p_\pi^0}^{p_\pi^{eq}} \sum_{p_\nu=p_\nu^0}^{p_\nu^{eq}} w_k(p_\pi,h_\pi,p_\nu,h_\nu,E_k) S_{pre}(p_\pi,h_\pi,p_\nu,h_\nu), \tag{1}$$

where σ^{CF} is the compound formation cross section and S_{pre} the time-integrated strength that determines how long the system remains in a certain exciton configuration [28]. The initial proton and neutron particle numbers are denoted $p_\pi^0 = Z_p$ and $p_\nu^0 = N_p$, with $Z_p(N_p)$ being the proton (neutron) number of the projectile. In general, $h_\pi = p_\pi - p_\pi^0$ and $h_\nu = p_\nu - p_\nu^0$, so that the initial hole numbers are zero, i.e., $h_\pi^0 = h_\nu^0 = 0$, for primary preequilibrium emission. The preequilibrium part is calculated by Eq. (1), using $p_\pi^{eq} = p_\nu^{eq} = 6$, whereas the remainder of the reaction flux is distributed through the Hauser-Feshbach model. In addition, the never-come-back approximation is adopted.

The emission rate w_k for ejectile k with spin s_k is given by

$$w_k(p_\pi,h_\pi,p_\nu,h_\nu,E_k) = \frac{2s_k+1}{\pi^2\hbar^3}\mu_k E_k \sigma_{k,inv}(E_k) \times \frac{\omega(p_\pi - Z_k, h_\pi, p_\nu - N_k, h_\nu, E_x)}{\omega(p_\pi,h_\pi,p_\nu,h_\nu,E^{tot})}, \tag{2}$$

where $\sigma_{k,inv}(E_k)$ is the inverse reaction cross section as calculated from the optical model and ω is the two-component particle-hole state density. The expression for S_{pre} contains the adjustable transition matrix element M^2 for each possible transition between neutron-proton exciton configurations. A proton-neutron ratio of 1.6 for the squared internal transition matrix elements was adopted to give the best overall agreement with experiment, i.e., $M^2_{\pi\nu} = M^2_{\nu\pi} = 1.6M^2_{\pi\pi} = 1.6M^2_{\nu\nu}$. Partial level density parameters $g_\pi = Z/15$ and $g_\nu = N/15$ were used in the equidistant spacing model for the partial level densities.

At incident energies above several tens of MeV, the residual nuclides formed after binary emission may have so large excitation energy that the presence of additional fast particles inside the nucleus becomes possible. The latter can be imagined as strongly excited particle-hole pairs resulting from the first binary interaction with the projectile. The residual system is then clearly nonequilibrated and the excited particle that is high in the continuum may, in addition to the first emitted particle, also be emitted on a short time scale. This so-called multiple preequilibrium emission forms an alternative theoretical picture of the intranuclear cascade process, whereby the exact location and momentum of the particles are not followed, but instead the total energy of the system and the number of particle-hole excitations (exciton number).

In actual calculations, the particle-hole configuration of the residual nucleus after emission of the ejectile is reentered as initial condition in Eq. (1). When looping over all possible residual configurations, the multiple preequilibrium contribution is obtained. In TALYS, multiple preequilibrium emission is followed up to arbitrary order, though for 96 MeV only secondary preequilibrium emission is significant.

It is well known that semiclassical models, such as the exciton model, have always had some problems to describe angular distributions (essentially because it is based on a compoundlike concept instead of a direct one). Therefore, as mentioned previously, the double-differential cross sections are obtained from the calculated energy spectra using the Kalbach systematics [25].

To account for the evaporation peaks in the charged-particle spectra, multiple compound emission was treated with the Hauser-Feshbach model. In this scheme, all reaction chains are followed until all emission channels are closed. The Ignatyuk model [31] has been adopted for the total level density to account for the damping of shell effects at high excitation energies.

For preequilibrium reactions involving deuterons, tritons, ^{3}He, and alpha particles, a contribution from the exciton model is automatically calculated with the formalism described above. It is, however, well known that for nuclear reactions involving projectiles and ejectiles with different particle numbers, mechanisms like stripping, pickup, and knockout play an important role and these directlike reactions are not covered by the exciton model. Therefore, Kalbach developed a phenomenological contribution for these mechanisms [32], which is included in TALYS. It has recently been shown (see Table I of Ref. [33]) that this method gives a considerable improvement over the older methods. The latter seemed to consistently underpredict neutron-induced reaction cross sections.

B. GNASH calculations

For the present work, GNASH calculations have been performed with a modified parameter set. The calculation procedure is outlined in Ref. [24]. Transmission coefficients needed for the GNASH input were calculated using the optical potential parameters by Sun *et al.* [34] for neutrons and protons, Daehnick, Childs, and Vrcelj [35] for deuterons, Becchetti-Greenlees [36] for tritons and ^{3}He particles, and Avrigeanu, Hodgson, and Avrigeanu [37] for alpha particles.

Like in the TALYS case, default level density parameters were used with the Ignatyuk level density formula [31]. The normalization factor used in the preequilibrium model calculation was determined by analyses of proton-induced reactions. The calculated result of preequilibrium deuteron and

alpha emission is different from that of the original GNASH code calculation [23]. In the deuteron emission, the component with the exciton number 3 was ignored. The direct pickup component was calculated using a phenomenological approach [38] with a normalization that is independent of the incident energy. This normalization was determined from analysis of experimental (n,dx) energy spectra up to 60 MeV [1]. The alpha knockout component given by the same phenomenology [38] was ignored.

The results are given in the laboratory system. Like in the TALYS case, angular distributions are obtained using the Kalbach systematics [25]. The required preequilibrium fraction is taken from the GNASH output. The c.m.-to-lab transformation is performed using the kinematics of one-particle emission as described in Refs. [20,21].

The exciton model implemented in GNASH is a one-component exciton model developed by Kalbach [39], with a parameterization for the energy dependence of the squared internal transition matrix element that has been validated at relatively low incident energies (below 40 MeV). There are indications that at higher incident energies, this energy dependence is no longer appropriate and that a more general form, covering a wider energy range, is needed. Such a smooth form has been implemented in TALYS, on the basis of a collection of double-differential (nucleon-in, nucleon-out) cross-section measurements [22].

VI. RESULTS AND DISCUSSION

Double-differential cross sections at laboratory angles of 20°, 40°, 100°, and 140° for protons, deuterons, tritons, ^{3}He, and alpha particles are shown in Figs. 3–7, respectively. All spectra for each particle type are plotted on the same cross-section scale to facilitate the comparison of their magnitude. The choice of the energy bin width is a compromise between the energy resolution in the experiment, the width of the inverse response functions, and acceptable statistics in each energy bin. The error bars represent statistical uncertainties only.

The overall relative statistical uncertainties of individual points in the double-differential energy spectra at 20° are typically 3% for protons, 7% for deuterons, 20% for tritons, 20% for ^{3}He, and 15% for alpha particles. As the angular distributions are forward-peaked, these values increase with angle. The systematic uncertainty contributions are due to thick target correction (1–20%), collimated solid angle (1–5%), beam monitoring (2–3%), the number of silicon nuclei (1%), CsI(Tl) intrinsic efficiency (1%), particle identification (1%), and dead time (<0.1%). The uncertainty in the absolute cross section is about 5%, which is due to uncertainties in the *np* scattering angle, the contribution from the low-energy continuum of the ^{7}Li(p,n) spectrum to the *np* scattering proton peak (3%), the reference *np* cross sections (2%) [13], statistics in the *np* scattering proton peak (2%), the carbon contribution (0.1%), and the number of hydrogen nuclei (0.1%).

From Figs. 3–7 it is obvious that the charged-particle emission from 96 MeV neutron irradiation of silicon is dominated by proton, deuteron, and alpha-particle channels.

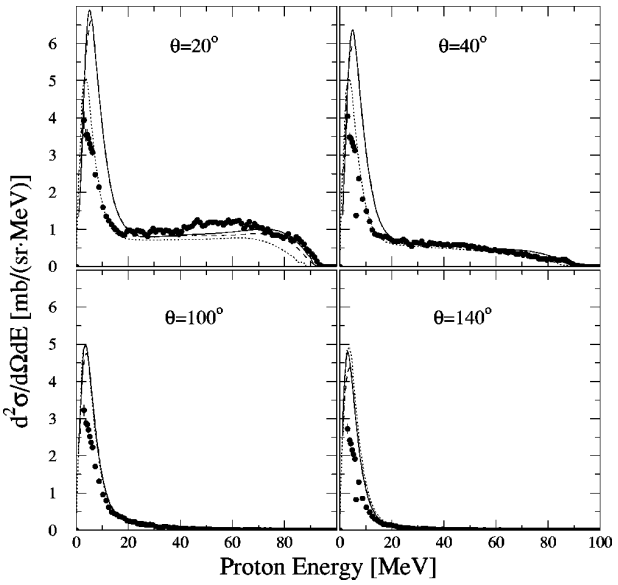

FIG. 3. Experimental double-differential cross sections (filled circles) of the Si(n,px) reaction at 96 MeV at four laboratory angles. The curves indicate theoretical calculations based on GNASH (Ref. [23]) (dashed), TALYS (present work) (dotted), and GNASH (present work) (solid). The TALYS result is in the c.m. system and the GNASH results are in the lab system.

The spectra of the two other particle types studied in this work (tritons and ^{3}He) are more than an order of magnitude weaker. All the spectra have more or less pronounced peaks at low energies (below 10–15 MeV), the angular distribu-

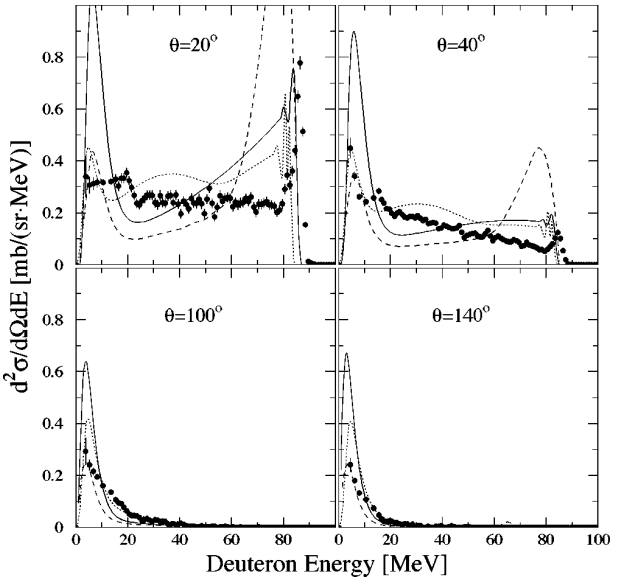

FIG. 4. Experimental double-differential cross sections (filled circles) of the Si(n,dx) reaction at 96 MeV at four laboratory angles. The curves indicate theoretical calculations based on GNASH (Ref. [23]) (dashed), TALYS (present work) (dotted), and GNASH (present work) (solid). The TALYS result is in the c.m. system and the GNASH results are in the lab system.

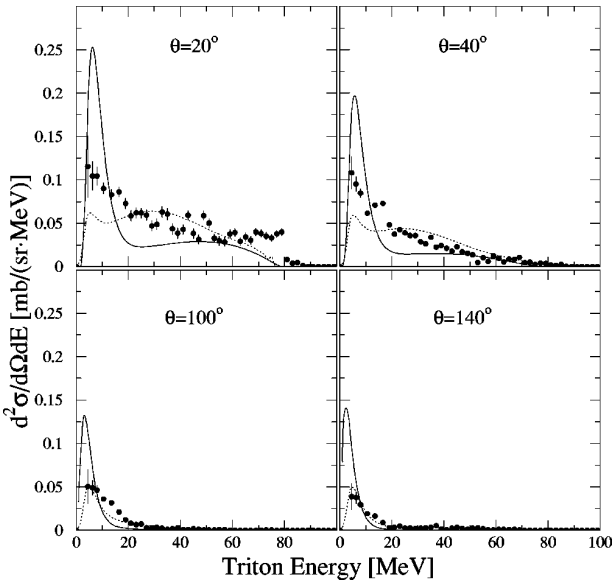

FIG. 5. Experimental double-differential cross sections (filled circles) of the Si(n,tx) reaction at 96 MeV four laboratory angles. The curves indicate theoretical calculations based on TALYS (present work) (dotted) and GNASH (present work) (solid). The TALYS result is in the c.m. system and the GNASH result is in the lab system.

tions of which are not too far from isotropy. This low-energy peak is not observed in the ^{3}He spectra due to the 8 MeV low-energy cutoff discussed in Sec. III A.

All the particle spectra at forward angles show relatively large yields at medium-to-high energies. The emission of high-energy particles is strongly forward-peaked and hardly

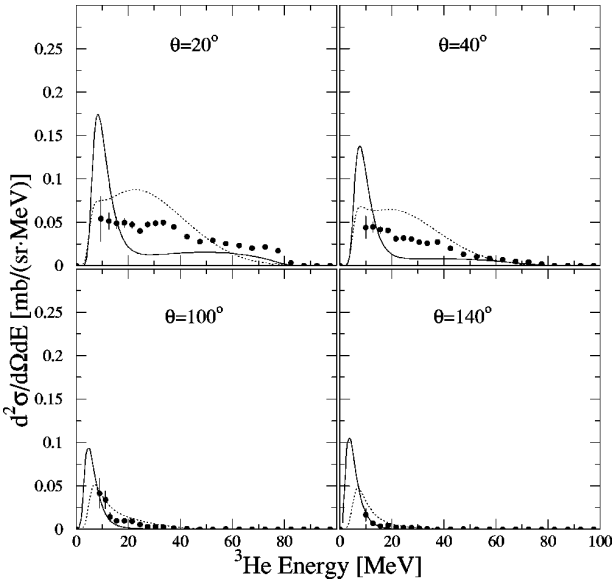

FIG. 6. Experimental double-differential cross sections (filled circles) of the Si$(n,{}^3\mathrm{He}x)$ reaction at 96 MeV at four laboratory angles. The curves indicate theoretical calculations based on TALYS (present work) (dotted) and GNASH (present work) (solid). The TALYS result is in the c.m. system and the GNASH result is in the lab system.

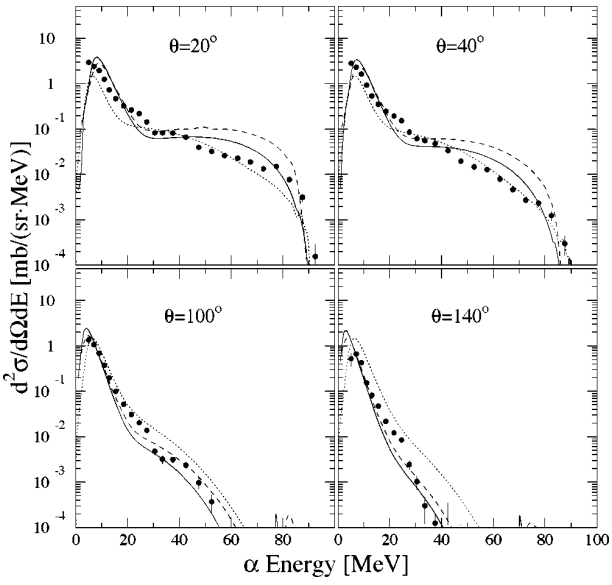

FIG. 7. Experimental double-differential cross sections (filled circles) of the Si$(n,\alpha x)$ reaction at 96 MeV at four laboratory angles. The curves indicate theoretical calculations based on GNASH (Ref. [23]) (dashed), TALYS (present work) (dotted), and GNASH (present work) (solid). The TALYS result is in the c.m. system and the GNASH results are in the lab system. Note the logarithmic scale.

visible in the backward hemisphere. It is a sign of particle emission before statistical equilibrium has been reached in the reaction process. In addition to this broad distribution of emitted particles, the deuteron spectra at forward angles show narrow peaks corresponding to transitions to the ground state and low-lying states in the final nucleus, ^{27}Al. These transitions are most likely due to pickup of weakly bound protons in the target nucleus, ^{28}Si.

A. Comparison with theoretical model calculations

In Figs. 3–8 the experimental results are presented together with theoretical model calculations. The GNASH calculations of Ref. [23] have been done for protons, deuterons, and alpha particles, whereas the other two calculations have been performed for all five particle types.

Figure 3 shows a comparison between the double-differential (n,px) experimental spectra and the calculations based on the TALYS and GNASH models. For protons above 25 MeV, all calculations give a good description of the spectra. Below this energy, some differences can be observed, e.g., at forward angles TALYS gives a better description of the statistical peak than the GNASH calculations.

The situation is quite different for the deuteron spectra (Fig. 4). None of the predictions do account for the data. At all angles deviations of a factor of 2 or more are present. At forward angles the high-energy part is strongly overestimated, indicating problems in the hole-strength treatment. There is a large difference in the spectral shapes calculated with the two versions of GNASH [19,23]. This difference is due to the fact that emission from the configurations with exciton number 3 is neglected in the present GNASH calcula-

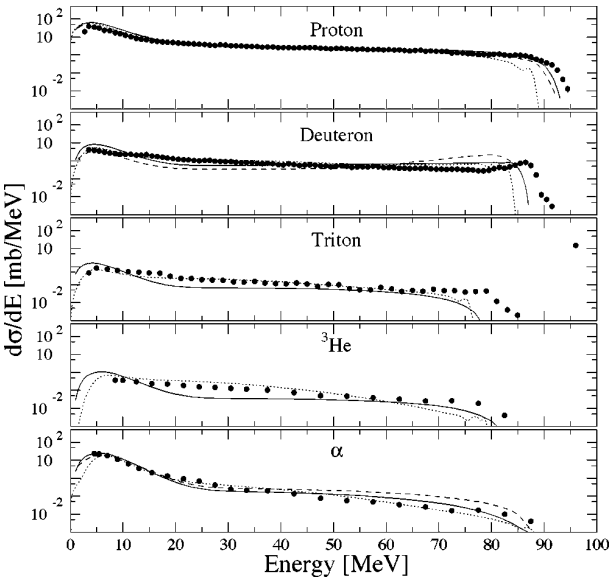

FIG. 8. Experimental energy-differential cross sections (filled circles) for neutron-induced p, d, t, ^{3}He, and α production at 96 MeV. The curves indicate theoretical calculations based on GNASH (Ref. [23]) (dashed), TALYS (present work) (dotted), and GNASH (present work) (solid). The TALYS result is in the c.m. system and the GNASH results are in the lab system.

tions. This component is taken into account as a direct pickup component calculated with an empirical formula due to Kalbach [38].

For tritons (Fig. 5), the TALYS calculations give a slightly better description of the experimental data, whereas for ^{3}He (Fig. 6) some large deviations can be observed. The TALYS calculations seem to account better for the spectrum shapes.

The overall description of the alpha-particle spectra (Fig. 7) is fair. The GNASH calculations overpredict the high-energy data at forward angles, whereas the TALYS predictions are too large at backward angles.

The ability of the models to account for the low-energy peak caused by evaporation processes is not impressive. In general, the models tend to overpredict the cross sections. It should, however, be kept in mind that the peak maximum is close to (for ^{3}He below) the low-energy cutoff, which complicates the comparison. Another complication in this context is that the c.m.-to-lab transformation of the calculated TALYS spectra could, at least in some cases, make a considerable difference. The GNASH cross sections are given in the lab system, but the c.m.-to-lab transformation is performed using the kinematics of one-particle emission [20,21], which obviously is an approximation.

B. Integrated spectra

For each energy bin of the light-ion spectra, the experimental angular distribution is fitted by a simple two-parameter functional form, $a \exp(b \cos\theta)$ [25]. This allows extrapolation of double-differential cross sections to very forward and very backward angles. In this way coverage of the full angular range is obtained. By integration of the angular distribution, energy-differential cross sections ($d\sigma/dE$) are obtained for each ejectile. These are shown in Fig. 8 together with the theoretical calculations. All calculations are in good agreement with the proton experimental data over the whole energy range. In the cases of deuterons and alpha particles, the models overpredict the high-energy parts of the spectra.

TABLE I. Experimental production cross sections for protons, deuterons, tritons, ^{3}He, and alpha particles from the present work. Theoretical values resulting from GNASH and TALYS calculations are given as well. The experimental data in the second column have been obtained with cutoff energies of 2.5, 3.0, 3.5, 8.0, and 4.0 MeV for p, d, t, ^{3}He, and alpha particles, respectively. The third column shows data corrected for these cutoffs, using the GNASH calculation of the present work.

σ_{prod}	Experiment (mb)	Experiment (cutoff corr.)	GNASH ([23])	GNASH (present)	TALYS (present)
(n,px)	436±22	507	670.3	701.9	558.3
(n,dx)	81±4	89.5	77.0	109.6	107.6
(n,tx)	15.2±0.8	17.9	-	15.0	13.1
$(n,^3\mathrm{He}x)$	7.8±0.5	13.0	-	10.6	14.5
$(n,\alpha x)$	144±7	183	175.8	202.4	146.8

The production cross sections are deduced by integration of the energy-differential spectra (see Table I). As explained above, the experimental values in Table I have to be corrected for the undetected particles below the low-energy cutoff. This is particularly important for ^{3}He because of the high cutoff.

The proton and deuteron production cross sections are compared with previous data at lower energies [2] in Figs. 9 and 10. There seems to be general agreement between the trend of the previous data and the present data point. The curves in these figures are based on a GNASH calculation [23].

VII. CONCLUSIONS AND OUTLOOK

In the present paper, we report an experimental data set on light-ion production induced by 96 MeV neutrons on silicon. Experimental double-differential cross sections ($d^2\sigma/d\Omega\, dE$) are measured at eight angles between 20° and 160°. Energy-differential ($d\sigma/dE$) and production cross sections are obtained for the five types of outgoing particles. Theoretical calculations based on nuclear reaction codes including direct, preequilibrium, and statistical calculations give generally a good account of the magnitude of the experimental cross sections. For proton emission, the shape of the spectra for the double-differential and energy-differential cross sections are well described. The calculated and the experimental alpha-particle spectra are also in fair agreement with the exception of the high-energy part, where the theory predicts higher yields than experimentally observed. For the other complex ejectiles (deuteron, triton, and ^{3}He) there are important differences between theory and experiment in what concerns the shape of the spectra.

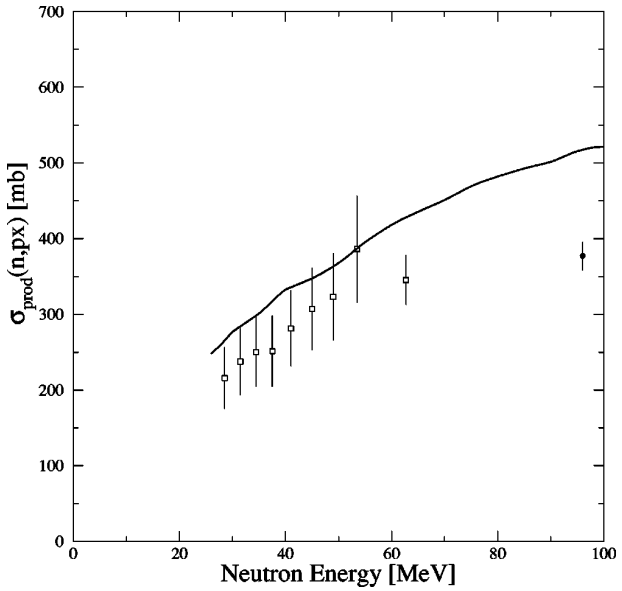

FIG. 9. Neutron-induced proton production cross section as a function of neutron energy. The full circle is from the present work, whereas the open squares are from previous work [2]. The curve is based on a GNASH calculation [23]. The data as well as the calculations correspond to a cutoff energy of 4 MeV. Note that the cutoff energy is different from that in Table I.

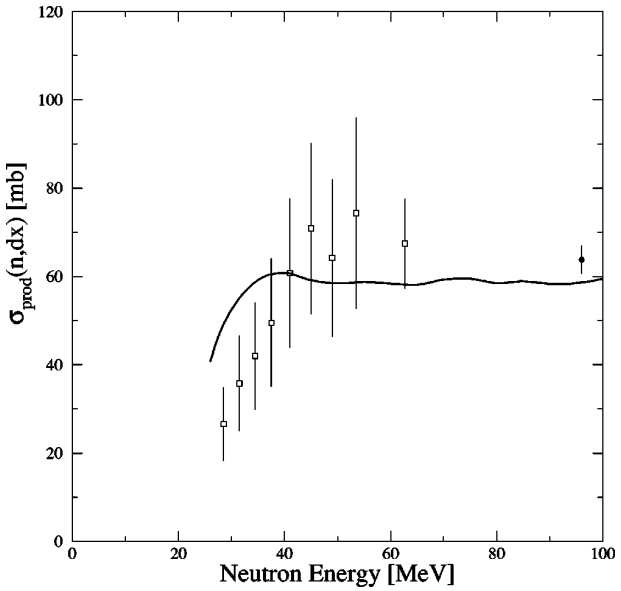

FIG. 10. Same as Fig. 9 for deuteron production, with a cutoff energy of 8 MeV.

For the further development of the field, data at even higher energies are requested. The results suggest that the MEDLEY facility, which was used for the present work, should be upgraded to work also at 180 MeV, i.e., the maximum energy of the TSL neutron beam facility. At present, a new neutron beam facility is under commission at TSL, covering the same energy range, but with a projected intensity increase of a factor 5. This will facilitate measurements at higher energies than in the present work.

The setup described in this paper comprises an active target, the information of which was not used in the analysis here but can provide valuable information on the kinetic energy transferred to the residual nucleus. This information might be crucial for soft-error studies and therefore it is of interest to compare this measurement with theoretical calculations. Work along this line is in progress.

ACKNOWLEDGMENTS

This work was supported by the Swedish Natural Science Research Council, the Swedish Nuclear Fuel and Waste Management Company, the Swedish Nuclear Power Inspectorate, Ringhals AB, and the Swedish Defence Research Agency. The authors wish to thank the The Svedberg Laboratory for excellent support. U.T. wishes to express his gratitude to the Thai Ministry of University Affairs and to the International Program in the Physical Sciences at Uppsala University. Y.W. is grateful to the scientific exchange program between the Japan Society for the Promotion of Science and the Royal Swedish Academy of Sciences.

[1] F. B. Bateman, R. C. Haight, M. B. Chadwick, S. M. Sterbenz, S. M. Grimes, and H. Vonach, Phys. Rev. C **60**, 064609 (1999).
[2] S. Benck, I. Slypen, J. P. Meulders, and V. Corcalciuc, Nucl. Sci. Eng. **141**, 55 (2002).
[3] R. Orecchia, A. Zurlo, A. Loasses, M. Krengli, G. Tosi, S. Zurrida, P. Zucali, and U. Veronesi, Eur. J. Cancer **34**, 459 (1998).
[4] D. L. Schwartz, J. Einck, J. Bellon, and G. E. Laramore, Int. J. Radiat. Oncol., Biol., Phys. **50**, 449 (2001).
[5] G. E. Laramore and T. W. Griffin, Int. J. Radiat. Oncol., Biol., Phys. **32**, 879 (1995).
[6] Single-Event Upsets in Microelectronics, topical issue, edited by H. H. K. Tang and N. Olsson [Mater. Res. Soc. Bull. **28** (2003)].
[7] High and Intermediate energy Nuclear Data for Accelerator-driven Systems (HINDAS), European Contract No. FIKW-CT-2000-00031, coordinated by J. P. Meulders; A. Koning, H. Beijers, J. Benlliure, O. Bersillon, J. Blomgren, J. Cugnon, M. Duijvestijn, Ph. Eudes, D. Filges, F. Haddad, S. Hilaire, C. Lebrun, F.-R. Lecolley, S. Leray, J.-P. Meulders, R. Michel, R.-D. Neef, R. Nolte, N. Olsson, E. Ostendorf, E. Ramström, K.-H. Schmidt, H. Schuhmacher, I. Slypen, H.-A. Synal, and R. Weinreich, J. Nucl. Sci. Technol. **2**, 1161 (2002).
[8] R. A. Cecil, B. D. Anderson, and R. Madey, Nucl. Instrum. Methods **161**, 439 (1979).
[9] M. B. Chadwick and E. Normand, IEEE Trans. Nucl. Sci. **46**, 1386 (1999).
[10] S. Dangtip, A. Ataç, B. Bergenwall, J. Blomgren, K. Elmgren, C. Johansson, J. Klug, N. Olsson, G. Alm Carlsson, J. Söder-

berg, O. Jonsson, L. Nilsson, P.-U. Renberg, P. Nadel-Turonski, C. Le Brun, F. R. Lecolley, J. F. Lecolley, C. Varignon, Ph. Eudes, F. Haddad, M. Kerveno, T. Kirchner, and C. Lebrun, Nucl. Instrum. Methods Phys. Res. A **452**, 484 (2000).

[11] J. Klug, J. Blomgren, A. Ataç, B. Bergenwall, S. Dangtip, K. Elmgren, C. Johansson, N. Olsson, S. Pomp, A. V. Prokofiev, J. Rahm, U. Tippawan, O. Jonsson, L. Nilsson, P.-U. Renberg, P. Nadel-Turonski, A. Ringbom, A. Oberstedt, F. Tovesson, V. Blideanu, C. Le Brun, J. F. Lecolley, F. R. Lecolley, M. Louvel, N. Marie, C. Schweitzer, C. Varignon, Ph. Eudes, F. Haddad, M. Kerveno, T. Kirchner, C. Lebrun, L. Stuttgé, I. Slypen, A. Smirnov, R. Michel, S. Neumann, and U. Herpers, Nucl. Instrum. Methods Phys. Res. A **489**, 282 (2002).

[12] A. N. Smirnov, V. P. Eismont, and A. V. Prokofiev, Radiat. Meas. **25**, 151 (1995).

[13] J. Rahm, J. Blomgren, H. Condé, S. Dangtip, K. Elmgren, N. Olsson, T. Rönnqvist, R. Zorro, O. Jonsson, L. Nilsson, P.-U. Renberg, A. Ringbom, G. Tibell, S. Y. van der Werf, T. E. O. Ericson, and B. Loiseau, Phys. Rev. C **63**, 044001 (2001).

[14] J. F. Ziegler, TRIM code, version 95.4, IBM-Research, 1995.

[15] U. Tippawan, B. Bergenwall, S. Dangtip, A. Ataç, J. Blomgren, K. Elmgren, C. Johansson, J. Klug, N. Olsson, S. Pomp, O. Jonsson, L. Nilsson, P.-U. Renberg, and P. Nadel-Turonski, J. Nucl. Sci. Technol. **2**, 1330 (2002).

[16] S. Pomp (unpublished).

[17] HBOOK, CERN Program Library Long Writeup Y250, Reference Manual, 1993.

[18] GEANT, CERN Program Library Long Writeup W5013, Detector Description and Simulation Tool, 1993.

[19] Y. Watanabe (unpublished).

[20] P. G. Young, E. D. Arthur, and M. B. Chadwick, Los Alamos National Laboratory Report No LA-12343-MS, 1992, GNASH-FKK version gn9cp0, PSR-0125.

[21] M. B. Chadwick, P. G. Young, R. E. MacFarlane, and A. J. Koning, in *Proceedings of the 2nd International Conference on Accelerator-Driven Transmutation Technologies and Applications, Kalmar, Sweden, 1996*, edited by H. Condé (Gotab, Stockholm, Sweden, 1997), p. 483.

[22] A. J. Koning, S. Hilaire, and M. C. Duijvestijn (unpublished).

[23] ICRU Report No. 63, International Commission on Radiation Units and Measurements, Bethesda MD, March, 2000.

[24] W. Sun, Y. Watanabe, E. S. Sukhovitskii, O. Iwamoto, and S. Chiba, J. Nucl. Sci. Technol. **2**, 120 (2002).

[25] C. Kalbach, Phys. Rev. C **37**, 2350 (1988).

[26] A. J. Koning and J. P. Delaroche, Nucl. Phys. **A713**, 231 (2003).

[27] S. Watanabe, Nucl. Phys. **8**, 484 (1958).

[28] C. Kalbach, Phys. Rev. C **33**, 818 (1986).

[29] H. Gruppelaar, P. Nagel, and P. E. Hodgson, Riv. Nuovo Cimento **7**, 1 (1986).

[30] E. Gadioli and P. E. Hodgson, *Preequilibrium Nuclear Reactions* (Oxford University Press, Oxford, 1992).

[31] A. V. Ignatyuk, G. N. Smirenkin, and A. S. Tishin, Sov. J. Nucl. Phys. **21**, 255 (1975).

[32] C. Kalbach, users manual for PRECO-2000, Duke University, 2001.

[33] M. Kerveno, F. Haddad, Ph. Eudes, T. Kirchner, C. Lebrun, I. Slypen, J. P. Meulders, C. Le Brun, F. R. Lecolley, J. F. Lecolley, M. Louvel, F. Lefèbvres, S. Hilaire, and A. J. Koning, Phys. Rev. C **66**, 014601 (2002).

[34] W. Sun, Y. Watanabe, E. S. Sukhovitskii, O. Iwamoto, and S. Chiba, J. Nucl. Sci. Technol. **40**, 635 (2003).

[35] W. W. Daehnick, J. D. Childs, and Z. Vrcelj, Phys. Rev. C **21**, 2253 (1980).

[36] F. D. Bechhetti and G. W. Greenless, in *Proceedings of the Conference on Polarization Phenomena in Nuclear Reactions, Madison, 1970*, edited by H. H. Barschall and W. Haeberli (University of Wisconsin Press, Madison, 1971), p. 682.

[37] V. Avrigeanu, P. E. Hodgson, and M. Avrigeanu, Phys. Rev. C **49**, 2136 (1994).

[38] C. Kalbach, Z. Phys. A **283**, 401 (1977).

[39] C. Kalbach, Phys. Rev. C **32**, 1157 (1985).

Appendix II

Available online at www.sciencedirect.com
SCIENCE DIRECT®
ELSEVIER
Nuclear Instruments and Methods in Physics Research A 527 (2004) 432–461
NUCLEAR INSTRUMENTS & METHODS IN PHYSICS RESEARCH Section A
www.elsevier.com/locate/nima

Development of a tagged neutron facility at intermediate energies

T. Peterson[a,1], S.E. Vigdor[a,*], C. Allgower[a], B. Bergenwall[b], L.C. Bland[a], J. Blomgren[b], J. Doskow[a], T. Hossbach[a], W.W. Jacobs[a], C. Johansson[b], T. Kinashi[a], J. Klug[b], A.V. Klyachko[a], P. Nadel-Turonski[b], L. Nilsson[b], N. Olsson[b], M. Planinic[a,2], S. Pomp[b], J. Rapaport[c], T. Rinckel[a], E.J. Stephenson[a], U. Tippawan[b], S.W. Wissink[a], Y. Zhou[a]

[a] *Department of Physics, Cyclotron Facility, Indiana University, 2401 Milo B. Sampson Lane, Bloomington, IN 47408, USA*
[b] *Uppsala University, Uppsala, Sweden*
[c] *Ohio University, Athens, OH 45701, USA*

Received 3 February 2003; received in revised form 8 March 2004; accepted 11 March 2004

Abstract

A unique experimental facility has been developed to measure absolute neutron scattering cross-sections through the use of tagged intermediate-energy neutrons. The neutrons are produced via the reaction $p + d \rightarrow n + 2p$ with an electron-cooled circulating proton beam of 200 MeV bombarding energy incident on a deuterium gas jet target. The "tagging" of the neutrons is accomplished by detection of the associated recoil protons in an array of silicon microstrip detectors located in vacuum. The detection of two protons in coincidence signals the production of a neutron, while energy and position measurements on the recoil protons allow for reconstruction of the four-momentum of the neutron, and its impact position on a secondary target, on an event-by-event basis. Performance characteristics of this facility are presented, and its future application to an absolute measurement of the np elastic scattering cross-section is described.

PACS: 25.40.Dn; 29.25.Dz; 29.40.Gx; 29.40.Wk

Keywords: Tagged neutron source; Double-sided silicon strip detectors; Neutron scattering

1. Introduction

An important open question in the field of nucleon–nucleon scattering is the proper normalization for the np elastic scattering differential cross-section. While total neutron cross-sections have been measured precisely [1], many np

*Corresponding author. Tel.: +1-812-855-9369; fax: +1-812-855-6645.
E-mail address: vigdor@iucf.indiana.edu (S.E. Vigdor).
[1] Present address: Department of Radiology and Radiological Sciences, Vanderbilt University, Nashville, TN 37232, USA.
[2] Present address: University of Zagreb, HR-10000 Zagreb, Croatia.

0168-9002/$ - see front matter © 2004 Elsevier B.V. All rights reserved.
doi:10.1016/j.nima.2004.03.194

differential cross-section data have been reported as relative measurements only, and the normalization methods used to quote absolute cross-sections in other cases are not entirely reliable or have large uncertainties. The primary difficulty in determining the normalization in these experiments stems from the problem of accurately determining the absolute neutron flux. Beyond the normalization question, there are inconsistencies in the np database at intermediate energies which a high-precision differential cross-section measurement might also address. For example, there are existing datasets that differ in the shape of the angular distribution at backward angles [2,3], and those who perform analyses of *NN* data often use controversial criteria in selecting which data to include [4–6]. The experimental discrepancies in both normalization and shape of the differential cross-section could in principle be resolved by a measurement of np elastic scattering using a "tagged" neutron beam. Such a measurement would also have considerable bearing on the controversy over the proper value for the pion–nucleon coupling constant [2,6,7], one of the basic parameters of nuclear physics.

This work describes the development and commissioning of a tagged neutron facility at the Indiana University Cyclotron Facility using the Cooler, the laboratory's electron-cooled light ion storage ring [8]. The term "tagged neutrons" indicates that the neutrons used as a beam for a scattering experiment each have their production marked by the detection of the other final-state particles emerging from the initiating reaction. The production of tagged neutrons in this manner presents the possibility of measuring absolute neutron cross-sections with unprecedented precision via direct counting of the neutron flux through the scattering target. The key to this endeavor is to determine the path of each produced neutron with sufficient precision to discern reliably whether and where the neutron passes through a secondary scattering target. Previous attempts [9,10] to tag intermediate-energy neutrons for the purpose of calibrating neutron detector efficiencies have not focused on preparing a secondary beam useful for neutron-scattering experiments.

2. Experimental setup

2.1. Basic concept

A storage ring with a cooled beam and internal target, such as the IUCF Cooler [8], possesses many of the attributes necessary for a tagged medium-energy neutron facility. First, a windowless gas target makes possible detection of low-energy recoil particles associated with the production of a neutron, while the storage ring environment provides reasonable luminosities even with such thin production targets. Electron cooling results in beams of well-defined energy with very narrow energy spread ($\Delta T_p \lesssim 20$ keV for $T_p = 200$ MeV), so that the energy of a neutron can be accurately determined from energy measurements of the low-energy recoil particles associated with its production. Furthermore, the small emittance of a cooled beam results in a tight constraint for both the lateral event origin (due to the small beam size) and initial momentum direction (due to the small divergence) of the neutron. As will be explained further below, both of these constraints facilitate kinematic reconstruction of an outgoing neutron with good resolution.

The production reaction chosen is $p + d \rightarrow n + 2p$ using a circulating proton beam of bombarding energy near 200 MeV incident on a deuterium gas jet target (GJT) [11]. This reaction is one which has been used to produce neutron beams for other experiments, such as in the Polarized Neutron Facility (PNF) at IUCF [12]. A favorable aspect of this production reaction is that the strength of the $^1S_0$ final state interaction for the two outgoing protons results in a neutron beam of relatively small intrinsic energy spread (~ 10 MeV) at small angles [13]. To tag a neutron using this reaction, it is necessary to detect two protons of low energy (~ 0.5–15 MeV) in coincidence in a detector array (the "tagger") located in vacuum. Energy and position measurements of the recoil protons allow reconstruction of the four-momentum of the neutron, making it possible to determine whether and where the neutron is incident on the secondary target. A side benefit to use of this system is that a tagged secondary proton beam can be defined and used simultaneously with the tagged neutrons, by

detecting recoil deuterons in the tagger from elastic $p + d$ scattering events in the GJT. The simultaneous acquisition of secondary np and pp scattering events permits careful crosschecks to be performed on the target thickness and detector acceptances relevant to the secondary scattering.

Due to the three-body $n + 2p$ final state, even for neutrons of a fixed energy at a particular angle, the recoil protons emerge with a distribution spread both in energy and angle. Consequently, the tagging efficiency (the fraction of neutrons incident on the target that are tagged) attained depends on both the solid angle covered by the recoil detectors and the triggering efficiency for pairs of protons with small spatial separation. A tagging efficiency well-below unity can be accommodated because we require a tag to be associated with all neutron scattering events analyzed, so that the untagged neutrons incident on target do not enter into the analysis. It is also important to exclude the substantial fraction of *tagged* neutrons that miss the secondary target, placing a premium on good energy and position resolution for the recoil protons. These two classes of uninteresting neutrons do not complicate absolute cross-section measurements as long as the associated rates are not too high. That is to say, the rates in the forward detector array from the scattering of *untagged* neutrons must be small enough that accidental coincidences with tags not become a problem. Likewise, the rate of tagged neutrons that do not pass through the target must be small enough that it does not dominate the tagged neutron flux sample. In practice, the tagged neutron beam is defined by the size and placement of the secondary scattering target. Likewise, the neutron energy distribution, as well as the upper limit on the tagged neutron yield (given by the actual neutron production cross-section), is set by the range in outgoing neutron angle defined by the placement of the secondary target. Finally, the operating luminosity is limited by the rate of false neutron tags arising from accidental coincidences in the recoil detector.

One issue that must be dealt with is the extended nature of the gas jet target. Because only one [(x', y'), where x' is horizontal and y' vertical within the plane of the tagger] position measurement is made on each recoil proton (they are generally too low in energy to traverse two position-sensitive detectors), the event origin must be known to determine the angles at which the protons emerged, and, therefore, the outgoing angle of the neutron. The longitudinal coordinate (z—see Fig. 1) of the event vertex along the central beam axis is determined by comparing the magnitude of the outgoing neutron's momentum calculated using conservation of energy,

$$p_E c = \sqrt{(E_i - E_{p1} - E_{p2})^2 - m_n^2 c^4} \quad (1)$$

to that calculated using conservation of momentum

$$p_M(z) = |\vec{p}_i - \vec{p}_{p1}(z) - \vec{p}_{p2}(z)|. \quad (2)$$

In Eqs. (1) and (2) E_i is the initial total relativistic energy of the system (beam proton plus target deuteron) and $\vec{p}_i$ is the incident proton momentum vector; $(E_{p1}/c, \vec{p}_{p1}(z))$ and $(E_{p2}/c, \vec{p}_{p2}(z))$ denote the four-momenta of the two detected recoil protons;

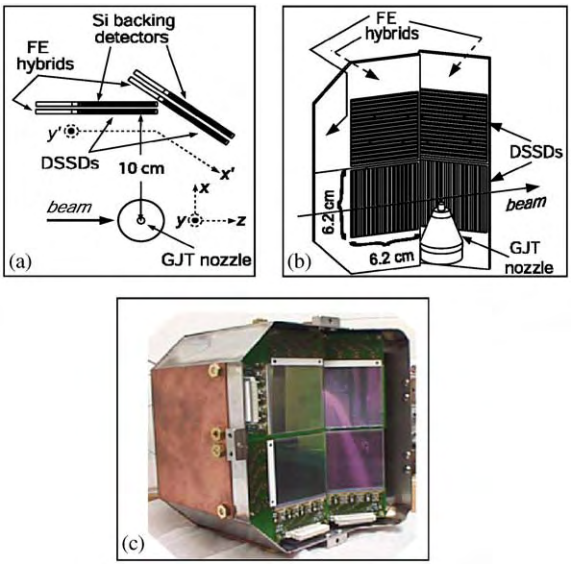

Fig. 1. Top (a) and perspective (b) views showing the arrangement of the neutron tagging silicon detectors with respect to the gas jet target (GJT). The beam coordinate system x, y, z and the detector-fixed coordinates x', y' are indicated in frame (a), and distances to set the length scale are given in frames (a) and (b). The photograph in (c) shows the tagger detectors in their steel and copper housing, to which a thin aluminized mylar entrance window is added before insertion of the housing into the Cooler vacuum.

and m_n is the neutron rest mass. Note that evaluation of Eq. (1) is independent of z, while the recoil proton three-momenta in Eq. (2) are not. By forming the quantity,

$$\Delta p(z) \equiv p_E - p_M(z) \quad (3)$$

we determine the event origin by using a bisection method to find where $\Delta p(z) = 0$. Simulations suggest that the quantity $\Delta p(z)$ is single-valued, and permits determination of z with a resolution σ_z better than 1 mm (for more detail, see Ref. [14]). With the event origin thus determined, the four-momentum of the neutron is reconstructed based on the kinematics of the two recoil protons.

2.2. Tagger

The tagger comprises an array of four silicon double-sided strip detectors (DSSDs), each backed by a silicon pad detector to form a $\Delta E - E$ telescope, as indicated in Fig. 1. The DSSDs provide energy and two-dimensional position information, while the pad detectors yield energy information for particles with sufficient energy to punch through a DSSD. Accurate neutron tagging requires that the full energy be measured for both recoil protons. By placing pad detectors behind the DSSDs, the maximum proton energy that can be used for tagged neutron reconstruction is increased. It further allows for discrimination against protons that punch through both a DSSD and pad detector and against accidental tags involving a deuteron, via the placement of a gate on the $\Delta E - E$ plot formed by the energy signals from the two detectors.

The DSSDs are AC-coupled detectors manufactured by SINTEF[3] using the Imager-'97 mask design. Detectors of both 500 and 300 μm thickness have been used, but the measurements reported here were all made using 300 μm thick detectors. The active area of each DSSD is 6.2×6.2 cm^2. The strips on the two sides of a DSSD are orthogonal, yielding an (x, y) measurement based on which strips on each side have signals induced. The strip pitch of these detectors is 80 μm, but because the needed position resolution is only ~ 0.5 mm, groups of six adjacent strips have been grouped together using a fan-in on the printed circuit board and read out via a single electronics channel. The resulting readout pitch is 480 μm, giving a total of 128 channels per detector side and 1024 DSSD channels for the entire tagger. The pad detectors closely match the DSSDs in active area and are 300 μm thick. Readout of the pad detectors is done using conventional, remote electronics.

The front-end electronics for a single DSSD side consist of four pairs of 32-channel Application-Specific Integrated Circuits (ASICs) provided by Integrated Detectors and Electronics (IDEAS of Norway).[4] The basic design principle of these ASICs is shown in Fig. 2. These readout chips are mounted on hybrids with the DSSD in the vacuum chamber. The first ASIC of each pair is the VA32_HDR2, a high-dynamic range version of the well-known VA chip [15], which provides a preamplifier, slow signal shaper, and sample and hold circuit for each channel, along with a multiplexed analog readout. The nominal shaping time for the amplifiers is 1.2 μs.

The second chip is the TA32C (hereafter referred to as TA), developed by IDEAS for use in this facility, which has a fast amplifier (~ 70 ns rise time) and leading-edge discriminator for each channel, with the corresponding preamp output from the VA chip serving as input. A wired OR of the 32 discriminator outputs provides a single fast logic signal per chip indicating at least one channel over threshold. The TAs also have a 33-bit serial shift register that allows for the disabling of individual channels via the download of a mask, in order to prevent individual noisy channels from dominating the trigger rate. The last bit of the shift register is used to select the signal polarity on which to trigger. A common discriminator threshold is set externally for each set of four TA chips attached to a detector side. The addition of the TA chips provides a *self-triggering* capability for the DSSDs that is critical for tagging operation, since counting the neutron flux requires recording

[3] SINTEF Electronics and Cybernetics, P.O. Box 124, Blindern, N-0314 Oslo, Norway.

[4] Integrated Detectors & Electronics AS, Veritasveien 9, N-1322 Hovik, Norway.

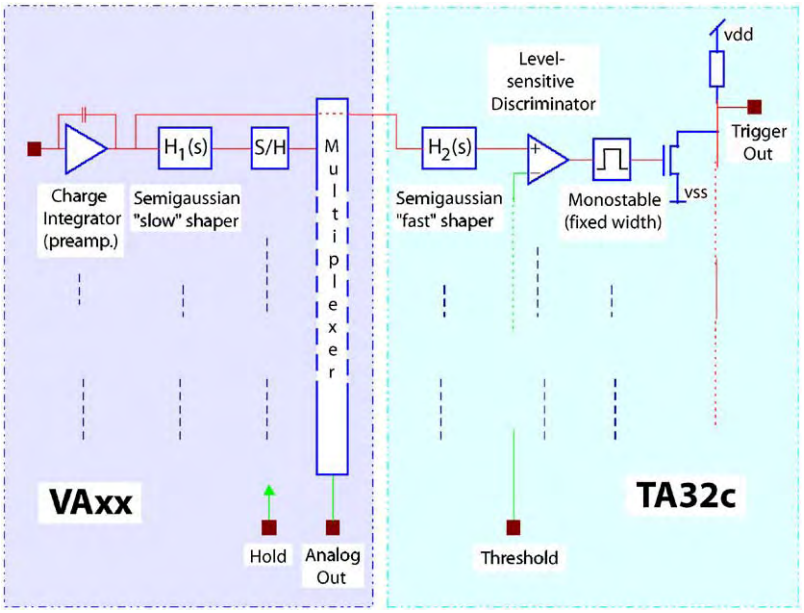

Fig. 2. An illustration of the basic electronics scheme for the VA-TA ASIC combination (courtesy of IDEAS, Norway).

events in which no detectors *other* than the DSSDs are fired.

Each detector hybrid is wired to provide a single set of differential VA outputs per detector side, yielding groups of 128 multiplexed analog signals for digitization. A separate output is provided for each TA chip, so that each detector side provides four logic signals for trigger decisions and timing information. In this way, one can trigger on a two-proton coincidence, as expected for the tagged neutron events, so long as both protons do not fall within the same x–y TA chip (15.5 mm × 15.5 mm) pixel.

One auxiliary (AUX) card located just outside the vacuum chamber is connected to each side of each detector hybrid to provide the necessary buffering and routing of all control, sequencer, analog, and trigger signals. The first three of these signal types are optocoupled so that the hybrids can be referenced to the bias voltage of the detectors, thereby minimizing the electrical stress on the capacitors integrated on both sides of the detectors. The local ground for the detector n-side hybrid is at the bias voltage ($\sim$50 V), while the p-side hybrid is referenced to the system ground. An external capacitive coupling was introduced between the two auxiliary boards for each detector quadrant in order to reduce noise.

The portion of the neutron tagger trigger logic based on silicon detector information (see Fig. 3) is centered around LRS4508 programmable lookup units (PLUs). Each channel of these CAMAC modules allows the user to map any 8-bit input word onto any eight-bit output word. This flexibility is suited to the need in this experiment to trigger for some events on the coincidence of two particles in the DSSDs, and for other (monitor) events on a single particle in the DSSDs.

The use of four TA chips per detector side results in the logical division of each detector into a four-by-four pixel array for triggering purposes. Any combination of a single hit on the p-side and a single hit on the n-side of the same detector, within the coincidence timing window, corresponds to a single PLU output state, labeled as a single particle hit. Two particles incident on a single detector can result in four TA signals (two from each side), three signals (two from one side, one from the other), or two (if the two particles are incident on the same logical detector pixel). The small fraction of two-particle coincidences falling in the latter class are unavoidably misidentified in

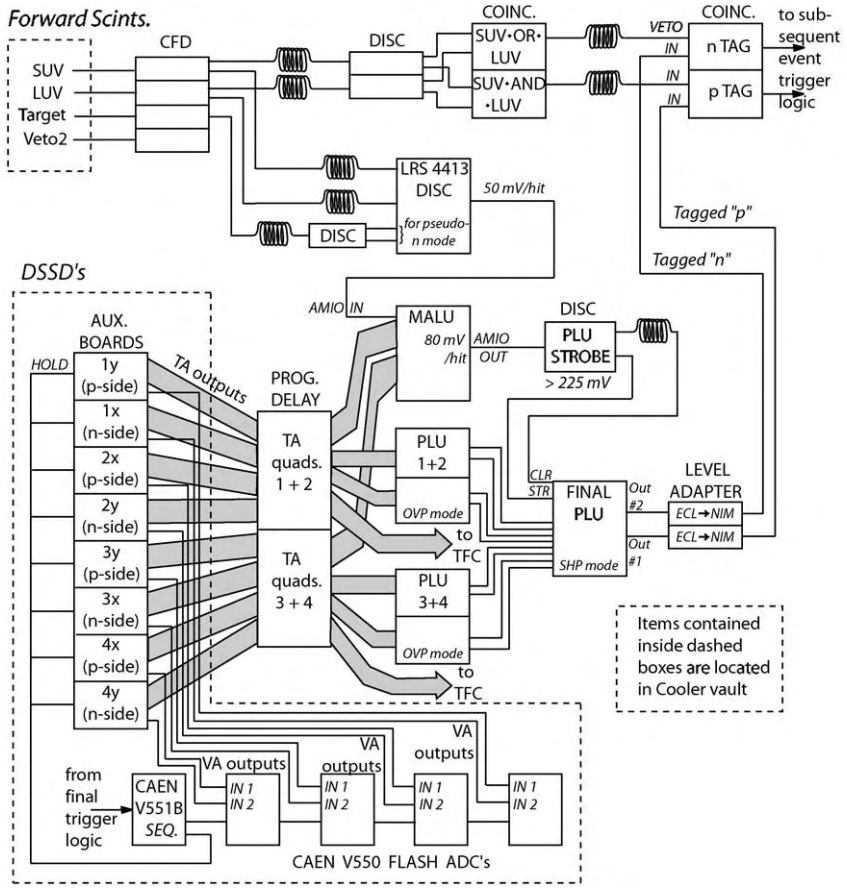

Fig. 3. Schematic electronics diagram of the tagger portion of the trigger logic. The programmable lookup units (PLUs) are programmed to distinguish events consistent with detection of two recoil particles (tagged "n") from those with only a single recoil (tagged "p").

the PLU logic as a single-particle hit, and hence are lost to the tagged neutron event streams. Events that satisfy either of the first two TA patterns above produce a single PLU output state, corresponding to a two-particle hit in that counter. For the events with four TA signals from a single detector, the proper pairing of p-side and n-side chips for most can be reconstructed in software by examination of pulse height and timing correlations, while reconstruction of events with three TA signals from a single detector must rely on pulse height information alone. Those events for which three TA signals result from a single charged particle incident near a chip boundary on one side of the DSSD can be easily distinguished in event reconstruction, because only a single hit cluster is reconstructed from the pulse-height signals for each detector side. Events in which three or four TA chips on the *same DSSD side* fire simultaneously arise mostly from noise, and the PLU logic therefore is set to reject them.

The two PLU outputs (one-particle vs. two-particle) for each DSSD are fed as input to a second-level PLU, which is programmed such that one output state ("tagged n") selects any combination of two hits in the detector array (single hits in two detectors or two hits in one detector). Another output state ("tagged p") of this second-level PLU is set to select single hits in the detector array (one TA signal from each side of the same

detector) to monitor pd elastic scattering events or to collect calibration data from a radioactive source. A coincidence is defined by the overlap of the signals entering into it; therefore, the effective resolving time for a coincidence is governed by the sum of the widths of the two TA outputs involved in the coincidence, typically $\simeq 140$ ns. A two-particle coincidence is likely to satisfy the one-hit logic prior to the arrival of the later hit, as well as after the end of the earlier one. The distinction is therefore made on the basis of the overlap of PLU inputs at the time of arrival of a strobe signal at the second-level PLU. The strobe is generated by the output of a Majority Logic Unit (LRS4532 MALU in Fig. 3) whenever 3 or more TA chips have fired or, alternatively, when at least two TA chips have fired in coincidence with two charged-particle veto scintillators in the forward detector array (to be described below). The outputs of the PLU logic are used as input to additional trigger logic to look for coincidence/anti-coincidence with the forward detector array. The final trigger signal, incorporating information from the forward detectors, is sent to a CAEN V551B sequencer to initiate the VA chip analog readout through CAEN V550 flash analog-to-digital converters (ADCs).

Fig. 4 summarizes the elements that go into operating a single tagger detector module. The four DSSDs, their associated hybrids, and their backing detectors are mounted together in a stainless-steel detector housing (see Fig. 1). The particles to be detected pass through a thin entrance window (1.5 μm aluminized mylar) on the detector box that provides separation from the inner pumping stage of the target region and completes the Faraday cage formed by the box to shield against noise pickup.

The location of the detectors with respect to the gas jet target is also shown in Fig. 1. Not shown in this figure is the GJT catcher, a conical metal cavity situated just above the beam for the purpose of extracting most of the gas in the jet. The pair of DSSDs that are parallel to the proton beam are located 10 cm from the GJT. The forward DSSDs are at a perpendicular distance of 9.7 cm from the GJT, and their plane is tilted by 36° with respect to that of the backward DSSDs. The full tagger array

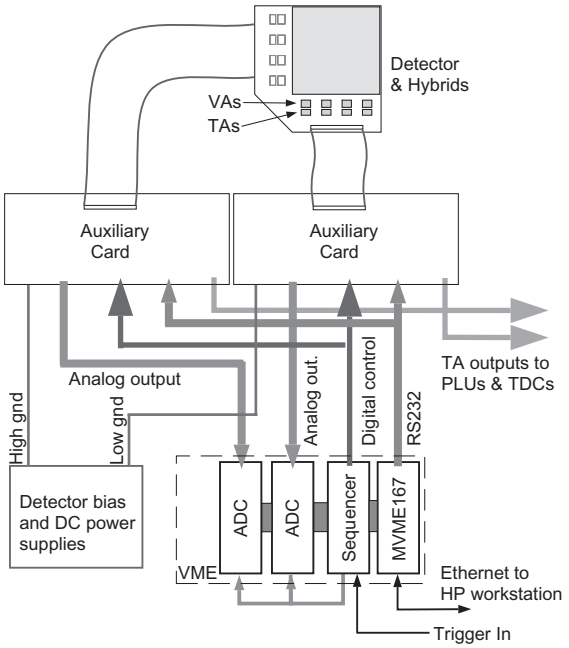

Fig. 4. Layout of the elements used in operation of a single DSSD.

subtends a solid angle of approximately 1.4 sr and covers scattering angles between 50° and 120° measured from the center of the GJT in the horizontal plane. The distance between a DSSD and its backing detector is approximately 3 mm. The DSSDs are oriented such that particles always enter a detector through the p-side, regardless of whether that side then measures the x or y position. This choice is made to ensure that all aspects of the signal generation that depend on the detector structure (e.g., dead layers, implant depth, oxide charge) are as similar as possible regardless of the detector hit. Such considerations could be of particular importance in this application, given that a large fraction of the particles stop within the DSSD volume.

The channel-to-channel gain variations within a VA chip are generally quite small, and the chip-to-chip variations in gain for the VAs on a detector side are also mostly small. However, the pedestal variations, even within the channels of a single chip, can be quite large. In some cases, it was found that the variation on a detector side was

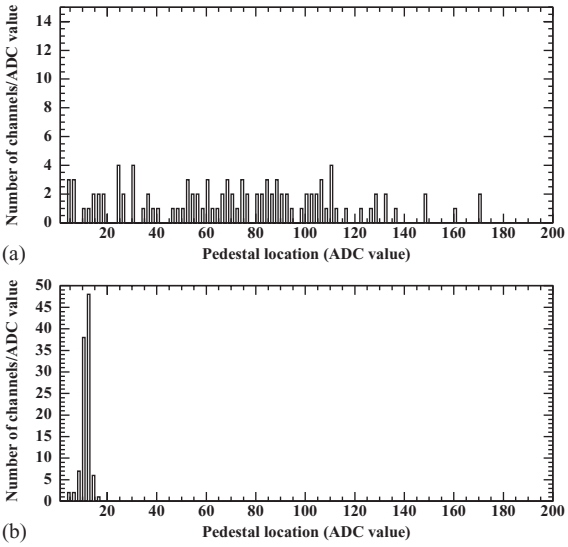

Fig. 5. Distribution of pedestal values for one detector side (a) before and (b) after setting of individual channel DAC values in the pedestal memory of the auxiliary card.

equivalent to more than a quarter of the amplitude range available with the ADC. Circuitry was therefore added to the AUX cards to reduce this offset spread to retain as much of the ADC dynamic range as possible. Fig. 5 shows the effect of this offset compensation circuitry, essentially eliminating a spread in channel pedestal values equivalent to 2 MeV energy deposition in the detector.

2.3. Forward detectors

The measurement of np backscattering is achieved via the detection of the forward-scattered proton emerging from a secondary target placed $\sim$1 m downstream of the GJT, and subtending neutron production angles from about 10° to 18° in the laboratory frame. The secondary target used during the facility commissioning runs was an active plastic scintillator of 20 cm × 20 cm square cross-section transverse to the neutron beam direction and 1.9 cm thickness. The scintillator target was read out by a single phototube mounted well above the active area. The design of the forward detector stack is based on plastic scintillators to provide triggering and energy information, along with a set of multi-wire proportional counters (MWPCs) to give position information for tracking. A schematic top view of the entire experimental setup in the Cooler T-region, including the forward detector array, is shown in Fig. 6. The sizes, locations and other specifications for the forward detectors are summarized in Table 1.

The two charged-particle veto detectors positioned upstream of the secondary target served somewhat different primary purposes: the large-area scintillator (labeled LUV in Fig. 6) was intended to discard tagged neutron events where the neutron subsequently interacted in the exit flange from the vacuum chamber or the poletips of the 6° bending magnet in the Cooler ring, producing a forward charged particle; the small-area scintillator (SUV in the figure) was intended to define the "beam spot" for a tagged proton beam used for diagnostics. A third upstream scintillator, called the beam-pipe veto (BPV) detector, was used to veto accidental coincidences between a real tagged neutron and a forward proton scattered at the tight restriction at the exit of the Cooler beam pipe from the 6° magnet vacuum chamber. Another veto scintillator (VETO2 in the figure), subtending approximately the same solid angle as the SUV at the GJT, was added immediately in front of the vertical elements of the rear hodoscope, to allow us to distinguish at trigger level between tagged protons that simply passed through the forward detector stack and those that rescattered by a substantial angle. Each MWPC contained three planes, measuring, respectively, x, y and u for the forward protons, with the latter coordinate oriented at 45° to the horizontal and vertical. One MWPC was positioned between the secondary target and the ΔE scintillator, to allow easy discrimination between np scattering events initiated in the target vs. in the ΔE scintillator material. The rear hodoscope, comprising 20 plastic scintillator bars of sufficient thickness to stop 200 MeV protons and give 15–20% detection efficiency for 100–200 MeV neutrons (at detection thresholds of several MeV electron equivalent), was used previously in an experiment to detect $\bar{p}p \to \bar{n}n$ charge exchange reactions at LEAR [9]. As can be seen in Table 1, the acceptance of the hodoscope and of the rear

Table 1
Parameters of elements in the forward detector array. The longitudinal distances (z) are specified for the center of each detector with respect to the center of the secondary scintillator target

Detector	Readout	Location	Transverse dimensions (cm)	# Elements	Element size/pitch (cm)	Function
Large Upstream Veto (LUV) scint.	Single PMT on large-angle end	Along vacuum box exit flange	55.9× 30.5	1	0.64 thick	Veto n conv. upstream of sec. target
Small Upstream Veto (SUV)	Single PMT on bottom	$z = -10.2$ cm	15.2× 15.2	1	0.64 thick	Define size of sec. p beam
Beam Pipe Veto (BPV)	Single PMT on top	Cooler pipe @ 6° vac. chmbr.	10.2× 10.2	1	0.64 thick	Veto accid. p coinc.
MWPC # 1	PCOS III	$z = +13.9$ cm	57.6× 57.6	288x 288y 260u	0.20x 0.20y 0.30u	Track + distinguish ps from sec. tgt.
ΔE scint.	4 PMTs: 2 bot. + 2 top	$z = +19.8$ cm	75.0× 75.0	1	0.64 thick	ΔE + time for fwd. p
MWPC # 2	PCOS III	$z = +26.0$ cm	57.6× 57.6	288x 288y 260u	0.20x 0.20y 0.30u	Tracking
MWPC # 3	PCOS III	$z = +59.3$ cm	91.2(x)× 129.6(y)	304x 432y 384u	0.30x 0.30y 0.41u	Tracking
Veto scint. # 2	Single PMT at large-angle end	$z = +72.9$ cm	30.5(x)× 38.7(y)	1	0.64 thick	Trigger on scat. vs. unscat. sec. ps
Hodoscope horiz. bars	2 PMTs/bar: left/right ends	$z = +75.6$ cm $y = \pm 64.5$ cm	130.0(x)× 32.0(y)	4	130.0× 8.0 × 20.0	E_{proton}+ n detection
Hodoscope vertical bars	2 PMTs/bar: top/bot. ends	$z = +95.6$ cm	128.0(x)× 130.0(y)	16	130.0× 8.0 × 20.0	E_{proton}+ n detection

MWPC are considerably larger vertically than horizontally. The forward array provides nearly complete azimuthal coverage for np scattering with $\theta_{\text{cm}} \gtrsim 120°$, plus substantial additional coverage down to $\theta_{\text{cm}} \approx 90°$, despite stringent space constraints imposed on the detector array by the Cooler beam pipe and mechanical support system.

3. Commissioning runs

The tagged neutron facility, including both the tagger and forward detectors described above, was commissioned in two runs taken in December 1999 and May 2000. Both utilized 200 MeV unpolarized proton beams stored in the IUCF Cooler. The primary luminosity for proton interactions in the D_2 gas jet varied from about 1×10^{30} to 1×10^{31} cm^{-2} s^{-1}. The typical beam cycle consisted of a 45-s acquisition period, followed by about 30 s of overhead to turn off the beam and the GJT, ramp down Cooler magnets and the DSSD and MWPC bias voltages, reinject beam for the next cycle and then reverse the ramping procedures. The Cooler RF power supplies were turned off before and during the 45-s data acquisition period, in order to remove microstructure from the beam time distribution, and thereby to minimize the ratio of accidental to real coincidences within the tagger.

3.1. Event trigger logic

The trigger logic for the commissioning runs was used to define five different event streams, three involving tagged neutrons and two involving tagged secondary protons. The detector hit requirements for these event streams are defined in

Table 2. Event stream number 1 is used to determine the number of tagged neutrons incident on the desired fiducial area of the secondary target. For events in this stream, a tagger hit pattern characteristic of forward neutron production is unaccompanied by signals from either the LUV or SUV veto counters, as well as by hits in the ΔE or hodoscope scintillators that would suggest neutron conversion somewhere within the forward arm. The np scattering events of ultimate interest are included in event stream 2, by requiring that a tagged neutron candidate be registered in coincidence with signals from both the ΔE and hodoscope scintillators, but in anticoincidence with the upstream veto scintillators. This pattern restricts the neutron to convert somewhere downstream of the SUV, but upstream of the exit face of the ΔE scintillator. (Signals from the target

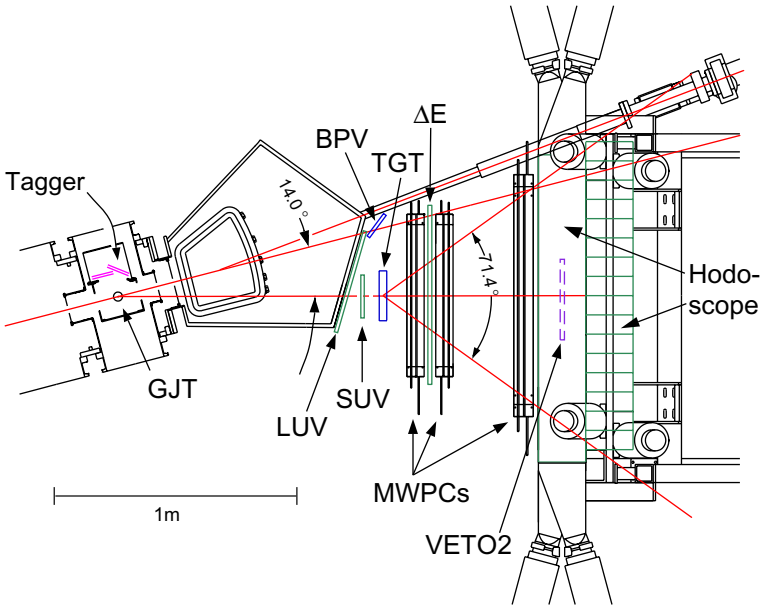

Fig. 6. A top view of the experimental setup for the np scattering experiment, including the tagger, the 6° Cooler magnet, and the forward detector array.

Table 2
Detector hit requirements defining the trigger logic for the five event streams acquired simultaneously during the commissioning run

Event Stream	Purpose	Tagger req'ment	LUV	SUV	BPV	Target scint.	ΔE (⩾3 PMTs)	Veto2	Hodoscope (2 PMT coinc.)	Other conditions	Pre-scale?
1	Count n tags	2 particles ("tagged n")	Veto	Veto	Veto	Unused	Unused	Unused	Unused	Veto by events 2,3	By 20
2	np Back-scatter	2 particles ("tagged n")	Veto	Veto	Veto	Unused	Coinc.	Unused	Coinc.	None in hardware	No
3	n Detect efficiency	2 particles ("tagged n")	Veto	Veto	Veto	Unused	Veto	Unused	Coinc.	None in hardware	No
4	p Tag lum-inosity monitor	1 particle ("tagged p")	Coinc.	Coinc.	Unused	Unused	Coinc.	Coinc.	Unused	None in hardware	By 10
5	pp Scat-tering	1 particle ("tagged p")	Coinc.	Coinc.	Unused	Unused	Coinc.	Veto	Coinc.	None in hardware	By 2

scintillator used during commissioning could have been added to the trigger logic to define the neutron conversion point more narrowly, but this would have eliminated the possibility of developing analysis procedures adaptable to the subsequent use of passive secondary targets.) Event stream 3 was defined to determine the detection efficiency for neutrons in the rear hodoscope, by using the ΔE scintillator signal as a veto for coincidences between a neutron tag and a hodoscope signal. The efficiencies determined from this event stream can then be compared to those measured previously [9] for the same detector, and to the results of conventional neutron detection efficiency simulations, such as that based on the Monte Carlo code developed by Stanton [16] and subsequently modified by McNaughton et al. [17] and Cecil et al. [18].

The simultaneous acquisition of events associated with tagged secondary *protons*, as well as neutrons, was invaluable for set up of all the detectors and electronics, as it permitted monitoring the simple two-body kinematic correlations for pd elastic scattering from the GJT. Furthermore, it provides for diagnostic purposes an abundant sample of tagged pp elastic scattering events acquired with precisely the same secondary target, forward detectors and beam conditions as the tagged np sample. The number of tagged protons incident on the secondary target could be deduced from event stream 4, where a single hit in the tagger arrived in coincidence with signals from the LUV, SUV, ΔE and VETO2 scintillators. Event stream 5 differed in using VETO2 in anticoincidence, and requiring instead a coincidence with a signal from the rear hodoscope. This stream thereby included events where a tagged proton had rescattered in the secondary target (or other material) out of the acceptance of the VETO2 scintillator. It also included a restricted sample of protons that did not rescatter, but originated from pd scattering in the upstream and downstream wings of the gas jet target density profile, which could produce forward protons that traversed the outermost edges of the SUV but missed VETO2. Analysis of event stream 5 data will not be further described in the present paper, as it does not directly affect our assessment of neutron tagging performance at the precision levels of interest here.

In order to limit the dead time introduced by data acquisition, it was desirable to prescale the event rates for event streams 1, 4 and 5 defined above, as the raw rates in these cases were significant. The prescale factors used during the commissioning runs were 20, 10 and 2, respectively, for these event streams. Events in all streams were vetoed in the trigger logic by a busy signal resulting from prior arrival of any event. This vetoing approach ensured that the different event streams had similar dead times (typically, $\sim 10\%$). However, small ($<1\%$) differences among the dead times for different streams were introduced by the prescaling, which gave different degrees of derandomization of arrival times for the various event types.

One of the characteristic raw tagger distributions that were checked online for the neutron event streams is shown in Fig. 7. The two frames of this figure show the correlations between the x' positions on the DSSDs for the two detected hits, for event streams 1 and 2. The real tagged neutrons correspond to the intense bands seen in the upper right corners of both plots. The narrower definition of this band in event stream 2 reflects a narrower selection of neutron angles, consistent with the domination of the secondary target in the np scattering yield. (In extracting cross-sections, the same cut will be placed on both event streams, selecting a well-defined region in predicted position of the tagged neutron at the plane of the secondary target, thus selecting the same bands in these x_1–x_2 plots.)

Fig. 7 also reveals the main source of beam-induced background among the 2-hit events in the tagger. The abundant events near the very center of these plots arise not from two separate particles in the tagger, but rather from a single energetic proton from a source considerably upstream of the GJT, which passes through both the forward edge of a rear DSSD quadrant and the backward edge of a forward quadrant. Different striations in this background band for event stream 1 (see Fig. 7) correspond to different upstream sources, and their relative intensity was very sensitive to the tune of the Cooler. The background band is

strongly suppressed in event stream 2 by the coincidence requirement with a forward-going particle. Since this background band is well separated from the region of true tagged neutrons for all neutron event streams, it does not complicate any of the ensuing analysis. Other, weaker, backgrounds arising from a single recoil particle mocking up a tagged neutron, by impinging on a DSSD at the boundary between two adjacent TA chips, are easily removed by requiring that two distinct energy clusters be recorded in the DSSD ADCs.

Examples of the pd scattering kinematic correlations for event stream 4 data, used during the setup of the tagging facility, are shown in Fig. 8. The two frames show the correlation of the energy deposition by the recoil particle detected in the tagger with the position of the coincident forward particle (in the left-hand frame) and the position of the recoil particle (on the right). In the left frame, increasing scattering angles for the forward-going proton correspond to decreasing wire chamber addresses, while on the right, smaller deuteron scattering angles occur for larger strip numbers.

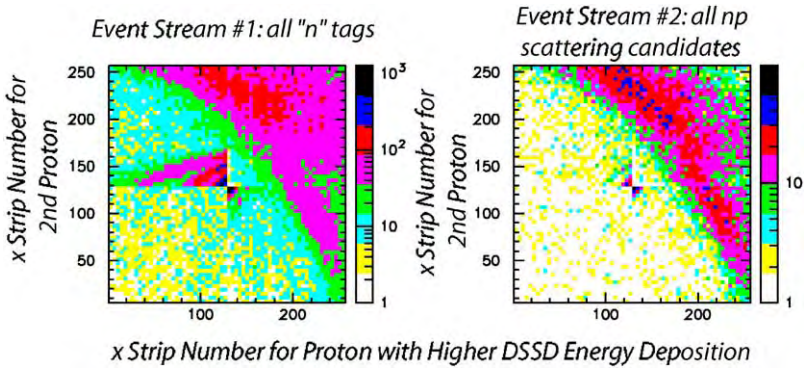

Fig. 7. The correlation of x-strip numbers for the two particles detected in the DSSDs for tagged neutron events in event streams 1 (left) and 2 (right). The coordinate of the particle depositing the higher energy in the DSSDs is plotted on the horizontal axis in each case. Real tagged neutron events fall within the intense bands seen near the upper right corner of each plot, while single proton background from upstream sources in the Cooler accounts for the structures near the center of each plot.

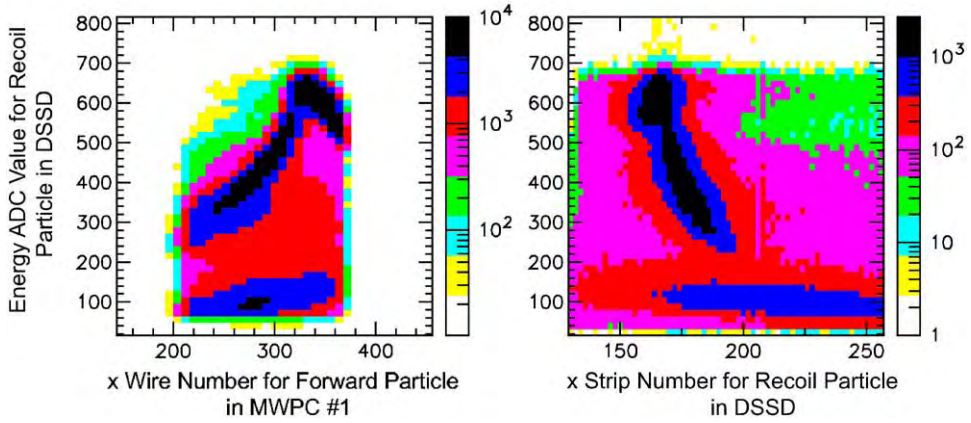

Fig. 8. The correlation of the single recoil particle pulse height (ADC channels) recorded in the DSSDs for event stream 4 with the x-positions of the coincident forward particle in the first wire chamber (left frame) and of the recoil particle in the DSSDs (right). In both plots, the upper intense locus arises from pd elastic scattering in the GJT, with the recoil deuteron just barely stopping in the DSSD at ADC channels near 700. The lower intense band arises from (p,2p) knockout events in the GJT.

The limited x-region in the DSSDs covered by the recoil deuterons in the right frame is restricted by pd elastic kinematics and the acceptance of SUV and VETO2 for the forward proton. The foldover in the upper locus in both plots occurs where the deuterons in the tagger possess enough energy that they are no longer stopped in a DSSD. Beyond this "punchthrough" point, increasing deuteron energies result in decreasing energy deposition in a DSSD. The band at lower pulse height in the plots in Fig. 8 comes from the $(p, 2p)$ reaction on deuterium, which gives a relatively high-energy recoil proton (hence low pulse height) in the tagger.

3.2. Calibration procedures

A number of auxiliary runs with and without beam were taken during commissioning, to aid in calibrating the positions, gains and timing of the various detectors. A ^{228}Th radioactive source placed at the nominal center of the beam-gas jet interaction region illuminated most of the tagger DSSD channels with α-particles of well known energy for gain calibration purposes. A second thorium source, placed behind the backing detectors inside the tagger enclosure, served a similar purpose for backing detector gain calibration. The ADC pedestals for every DSSD strip were determined occasionally during the run by activating the sequencer for VA-chip readout without the use of external triggering. Linearity of the VA-chip plus ADC systems was checked with a calibration pulser capable of injecting an adjustable amount of charge at the input of the VA chips. In combining the above information for DSSD gain calibration, special care was exercised in making corrections for α-particle energy loss and incidence angle through DSSD dead layers. This energy loss and straggling limited the α-particle energy resolution attained to typically FWHM ≈ 140 keV, considerably worse than the noise contribution (~ 50 keV FWHM) inferred from the pedestal width in each channel. For strips not well illuminated by the α-source, the calibration was extended by use of various features of the data acquired in event streams 4 and 5: the maximum energy deposition in the DSSDs for protons and for deuterons, and the energy of recoil deuterons from pd scattering events originating from the wings of the GJT profile.

Forward detector calibrations were done with cosmic rays. Two samples of cosmic ray events were collected. Those that fired at least one hodoscope bar in coincidence with the ΔE scintillator allowed ray-tracing analysis of straight tracks for relative position calibrations of the forward MWPCs and the hodoscope. (Calibrations of the forward detector positions *with respect to the tagger* were done using the main data from event stream 3, see Section 4.5.) Cosmic rays that fired at least eight adjacent hodoscope bars in time coincidence provided a sample useful for determining the gains and timing offsets of the hodoscope photomultipliers.

Finally, another set of runs with beam was taken to evaluate the neutron tagging efficiency, i.e., the fraction of neutrons, within the energy region of interest, headed toward the secondary target that actually get tagged. For this evaluation, it was important to collect events where an apparent np scattering event in the secondary target was *not* accompanied by two recoil particles detected in the DSSDs. These auxiliary runs involved a "pseudo-neutron" trigger, defined to require only a single hit (1 x-side TA chip firing in coincidence with 1 y-side TA chip on the same DSSD) in the tagger, in coincidence with signals from the active target scintillator, as well as the ΔE and hodoscope scintillators, but still in anticoincidence with the LUV and SUV scintillators. Tagging efficiencies determined from these auxiliary data will be presented in Section 4.6.

4. Performance of the tagged neutron facility

In addition to attaining proper operation of all detectors and software, the goals of the commissioning runs were to quantify the performance of the tagging facility with regard to a number of properties: timing resolution and ability to discriminate real vs. accidental tagger coincidences; precision of the vertex determinations for the primary neutron production and for the secondary neutron scattering; accuracy of the neutron flux determination; neutron tagging efficiency; and the

absolute tagged neutron flux, energy distribution and spatial profile at the secondary target location. In the ensuing subsections, we describe the analyses and results relevant to each of these features, in turn.

4.1. Tagger timing resolution

Timing information from the DSSDs is used only in distinguishing real from accidental coincidences, both within the tagger and with the forward detectors. The most important concern in this regard is the minimization (and subsequent subtraction) of accidental background contributions to the yield of tagged neutrons determined from event stream 1, where no detectors other than the tagger are required to fire. The timing information provided for the DSSDs by the TA front-end readout chips is based on leading-edge discrimination of the signals. In order to optimize the time resolution, it is therefore essential to apply software corrections to compensate for the significant (up to 60 ns) observed time walk with pulse height amplitude for each of the TA chips.

The walk correction is performed using data from the hodoscope efficiency event stream (number 3). The arrival time of the hodoscope signal can be taken as fixed because the time of flight difference from the GJT to a given hodoscope bar between a 200 MeV neutron and a 185 MeV neutron is less than 0.4 ns. A correction for the recoil proton's time of flight from GJT to the tagger is made using the reconstructed production vertex for the event (see Section 4.3) and the (x, y) coordinates of the hit along with its energy deposition in the tagger. The time difference between this kinematically corrected TA time and the hodoscope arrival time is then plotted versus the DSSD energy deposition. In the case of clusters of more than one strip, the energy used in the plot is that of the single strip with the highest pulse height, since this is the strip that most likely determines the timing of the TA output pulse. An exponential curve is then fitted to the centroids of the event loci in these walk plots, and the optimal parameters are stored separately for each of the 32 TA chips to provide the software walk correction [14].

A measure of the resulting time resolution can be made by comparing the walk-corrected time determinations obtained from the two sides (p-side and n-side) of a detector. Fig. 9 shows the difference between the two time determinations for the higher energy particle in tagged neutron events where both protons stop in a DSSD. The distribution shown incorporates all readout chip combinations and has a full-width at half-maximum (FWHM) of 3.7 ns. The tails in the distribution come primarily from events where the signal is distributed across more than one strip on at least one detector side. The resulting difference in individual-strip charges between the two sides for such an event leads to quite different walk corrections, with significant ambiguity regarding the proper correction for the side with substantial charge sharing. The tails observed in Fig. 9 point out the sensitivity to the walk correction.

The difference in times between the two recoil protons in tagged neutron events, as determined by the p-side measurements, is shown in Fig. 10. The time measurements are corrected for both walk and expected flight time differences deduced from the measured energies and positions for the

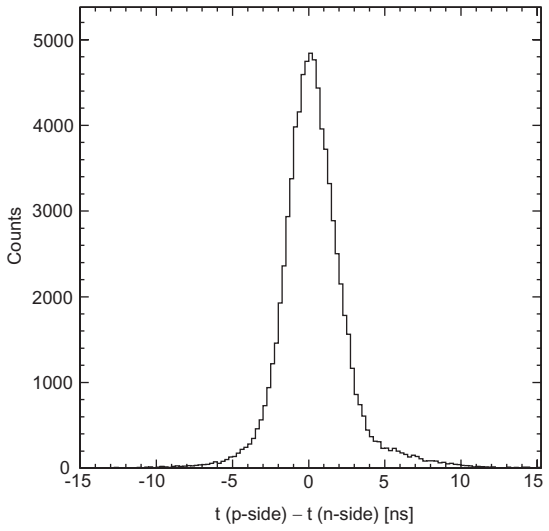

Fig. 9. The distribution of differences in arrival time between the hits recorded on the two sides of a DSSD, after correction of each for time walk in the leading-edge TA-chip discriminators.

two protons, so the distribution is expected to be centered about zero. As shown, the resolution in this time difference deteriorates when one or both particles give pulse heights near threshold, again reflecting imperfect walk correction, but also increased noise effects, at low pulse height.

The results in Figs. 9 and 10 indicate that the DSSD time resolution attained for a single particle and detector side is typically characterized by $\sigma \approx 1$–2 ns. This performance is adequate for discriminating against accidental coincidences at the level required for an eventual 1% cross-section determination, at the anticipated primary beam luminosities of ~ 1–2×10^{31} cm^{-2} s^{-1}.

4.2. Recoil particle identification

The large-area silicon backing detectors behind the DSSDs were not used in the trigger logic, but their pulse heights were recorded for each triggered event. The correlation of DSSD and backing detector energies can then be used both for particle identification (PID) of the recoils, and to expand the energy range of recoil protons usable for neutron tagging. Examples of raw PID spectra for both tagged proton and tagged neutron event streams are shown for one DSSD-backing detector combination in Fig. 11. The two-dimensional window drawn in both frames of Fig. 11 represents the gate used in tagged neutron analysis to select recoil protons that enter and stop inside the backing detector. The proton locus for each event stream bends backward and includes an intense band arising from D(p,2p) and D(p,pn) reactions on the GJT, which produce protons that punch through the backing detector. In addition, the expected intense band of recoil deuterons, with its own foldover arising from energetic punchthrough particles, is seen as the upper locus for the tagged proton event stream. The absence of a discernible deuteron band for event stream 1 indicates that neutron tags arising from accidental coincidences between two uncorrelated particles in the tagger were not a significant problem at the luminosities used in the commissioning runs. In the right-hand frame of Fig. 11, one does see appreciable background associated with backing detector noise, which was induced by the initiation of the DSSD readout sequence. This noise was, in general, easy to discern and remove, because it was strongly correlated among all four backing detector quadrants.

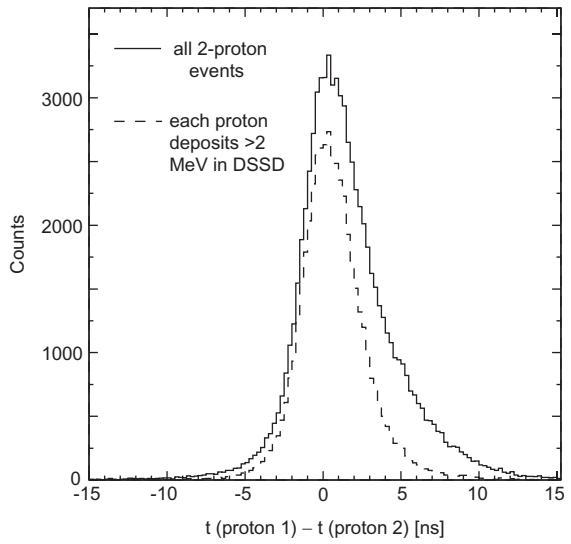

Fig. 10. The distribution of walk-corrected DSSD arrival time differences between the two recoil protons in tagged neutron events, where t(proton 1) is the time for the particle depositing the higher energy in one of the DSSDs and t(proton 2) is for the lower energy one. The dashed spectrum is restricted to events where the lower measured energy is larger than 2 MeV.

The potential tagged neutron events with (at least) two hits reconstructed in the tagger are subdivided into two classes: those unaccompanied by, and those accompanied by, correlated backing detector signals. A backing detector signal is judged to be correlated only if the following criteria are met: (1) the raw ADC value is above a threshold in a quadrant where the corresponding DSSD contains one of the two recoil protons, (2) the backing detector signal falls outside a two-dimensional noise correlation gate in comparison to signals in other backing detector quadrants, and (3) the DSSD and backing detector energies for the quadrant in question fall within the PID gate shown in Fig. 11. This PID gate rejects deuterons (which could conceivably contribute only via accidental coincidences in the tagger), noise that may have evaded other tests, and protons with sufficient energy to exit the backing detector, the latter in order to avoid the resulting uncertainty in

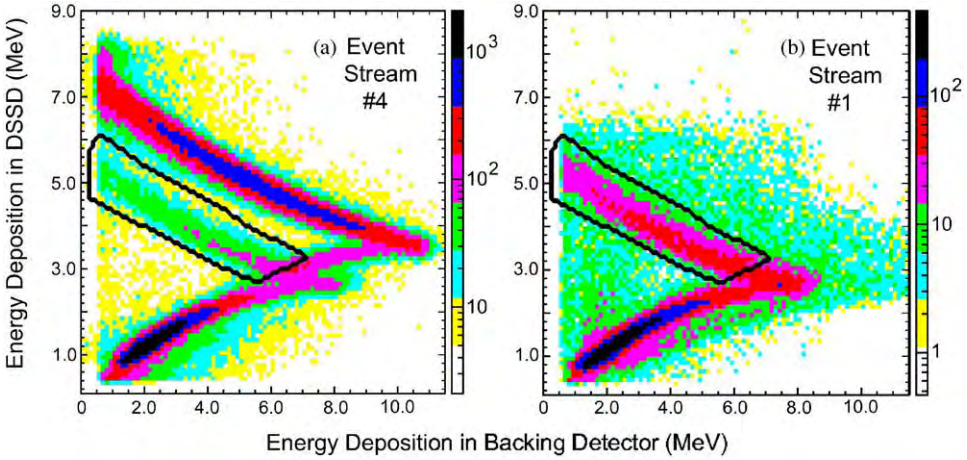

Fig. 11. Particle identification plots for one DSSD-backing detector combination for (a) event stream 4 (tagged protons) and (b) event stream 1 (tagged neutrons). A recoil deuteron locus is clearly visible in (a) but is absent in (b). The dark boundary in each frame encloses the gate area used to identify protons that stop in the backing detector.

that particle's full energy. In the analysis reported here, we have ignored events where *both* protons have correlated hits in their respective backing detectors, and where a backing detector is correlated with a DSSD quadrant on which both recoil protons were incident. These two categories of events can, in principle, be successfully reconstructed, but their neglect to date avoids some potential complications.

4.3. Primary vertex reconstruction

In reconstructing the tagged neutron's path, it is important to calculate the energies and angles of both recoil protons carefully. These two issues are intertwined because the correction for energy loss in detector dead layers depends on angle of incidence, while the angles depend on the primary vertex reconstruction, which uses the proton energies in Eq. (1). The vertex reconstruction is thus done iteratively. On the first pass, the event origin is taken as the center of the GJT, and this is combined with the measured DSSD hit positions to deduce the angle of incidence for each recoil proton. Using this incidence angle, the energy loss ($E_{\mathrm{loss}} \sim 100$ keV) through the entrance dead layer in the DSSD is then estimated for each proton. (Energy loss in the GJT itself is negligible.) For protons that stop in the DSSD, the energy used in Eq. (1) to find the next iteration on vertex location is then $E_{\mathrm{DSSD}} + E_{\mathrm{loss}}$. After a new vertex is found, the process is repeated, and iterations continue until the difference in longitudinal vertex position for successive passes is less than 0.1 mm.

For events involving a proton that made it into a backing detector, further energy corrections are needed during each step of this iterative vertex search. It was discovered after the commissioning runs that the noise induced on the backing detectors by the initiation of DSSD readout tended to reduce the peak pulse height measured by the backing detector ADCs by the equivalent of 600 keV. (This effect was not present for the thorium-source backing detector calibration runs, where DSSD readout was not performed.) This effective negative pedestal was determined by insisting that pd elastic scattering events where the deuteron stopped in a backing detector fall on the same smooth kinematic locus of deuteron energy vs. forward proton angle as the events where the deuteron stopped in a DSSD. The energy measured in a backing detector, after correction for this effective pedestal, is then used to make the incidence-angle-dependent correction for energy loss in the dead layers between the DSSD and the backing detector. A second

correction to the total proton kinetic energy is then made for the DSSD entrance dead layers, based on the sum of the recorded DSSD energy and the corrected backing detector energy.

The reconstructed primary vertex is furthermore sensitive to the assumed perpendicular distance of the closed proton orbit in the Cooler from the DSSDs. Since this distance can vary by several millimeters, depending on the detailed machine tune, it was treated as an adjustable parameter in the analysis, and was varied to optimize the resolution in the z-coordinate of the reconstructed vertex. An example of the resulting vertex distribution is shown in Fig. 12. The width of the peak is several mm (FWHM), in good agreement with expectations based on the density distribution of the GJT, and also with the gas jet profile extracted from tagged proton events (also shown in Fig. 12). This spectrum thus suggests that the primary vertex reconstruction resolution is $\sigma(z) \lesssim 2$ mm. The wings in the vertex distribution in Fig. 12 reflect the real tails in the target density distribution that result from the differential pumping in the target chamber. The asymmetry in the wings is due to the falloff in tagger coincidence acceptance for events originating downstream of the GJT nozzle.

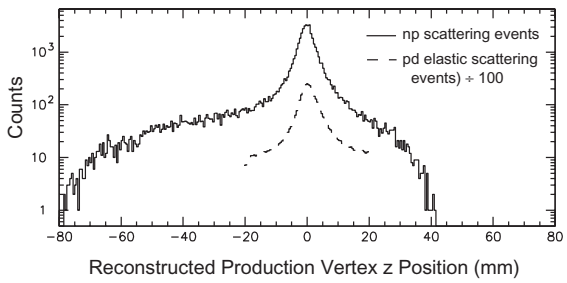

Fig. 12. Distribution of reconstructed production event vertices for the tagged neutrons that initiate secondary np scattering events (solid) and for the tagged protons reconstructed from pd elastic scattering events (dashed). The peak in each case reflects the core of the gas jet target, while the wings reflect differential pumping tails in the gas density, convoluted with tagger and forward detector arm acceptance. The two peaks are very similar in shape, because the vertex resolution attained for both the neutron production events and the pd elastic scattering events is significantly smaller than the intrinsic width of the gas jet.

4.4. Secondary vertex reconstruction

Important information concerning the quality of tagged neutron trajectory reconstruction can be obtained from the np scattering events in event stream 2, by comparing the transverse position determination at the nominal center of the secondary target from the wire chamber tracking of the scattered proton (x_{track}, y_{track}) to that from the reconstruction of the tagged neutron (x_{tag}, y_{tag}). For example, Fig. 13 shows the two-dimensional distribution of those scattering events where no signal is present in any of the backing detectors, with respect to the higher of the two energies deposited in the DSSDs and with respect to the difference $\delta x \equiv x_{\mathrm{track}} - x_{\mathrm{tag}}$. While most of the events are centered about $\delta x = 0$, a wing can be seen to extend from the central distribution toward negative δx at energy depositions above 5 MeV. This feature arises from the energy underestimate for events where the higher energy proton in the tagger does not stop in a DSSD, yet does not have sufficient energy to cause a signal above threshold in a backing detector. The effect

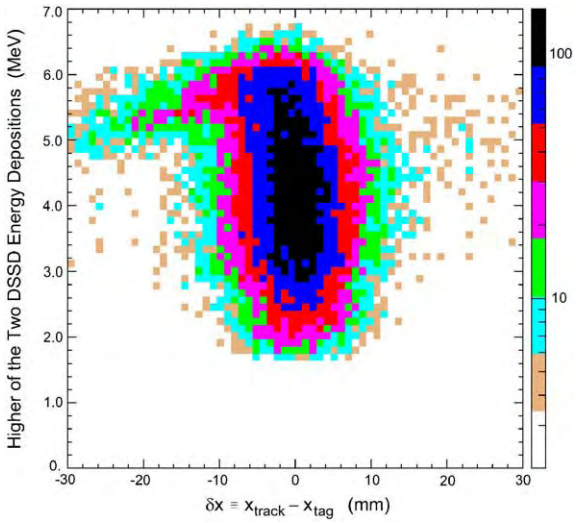

Fig. 13. The higher of the energies deposited by a recoil proton in a DSSD plotted against the difference in x-positions at the center of the secondary target found from wire chamber tracking and from neutron tagging. The observed correlation reveals the errors in neutron reconstruction from protons that do not quite stop in the DSSD but possess too little energy to be detected in a backing detector.

was exacerbated in the commissioning runs by the effective negative backing detector energy pedestal discussed earlier. When the energies used in the neutron reconstruction represent less than the full energy of the two recoil protons, the predicted neutron path is systematically shifted to artificially smaller angles (higher x_{tag}). The size of this reconstruction error grows with the missing energy.

To avoid the punchthrough ambiguity revealed by Fig. 13, the remaining analysis presented in this paper has been carried out by ignoring those tagging events where one or both recoil protons deposits > 5 MeV in a DSSD but gives no backing detector signal (i.e., ignoring all the events above 5 MeV in Fig. 13). The fraction of events thus ignored can be substantially reduced in future runs by eliminating the negative energy offset on the backing detectors and by substituting 500 μm thick DSSDs for the 300 μm thick ones used in the commissioning.

Since np scattering events can originate not only in the target scintillator, but also in surrounding material, we found that the most reliable method for testing the position resolution involves calculation of the distance of closest approach (DCA) between the predicted neutron and ray-traced proton straight-line trajectories. (We ignore the very small bending of the proton in the fringe field from the 6° magnet.) The DCA is calculated analytically based on the position and angles in x and y determined for both the neutron and proton at the center of the target scintillator. Denoting the calculated transverse position of the neutron at the target center ($z = 0$) as $(x_0^{\mathrm{n}}, y_0^{\mathrm{n}})$ and the corresponding slopes in the x–z and y–z planes as m_x^{n} and m_y^{n}, respectively, and similarly $(x_0^{\mathrm{p}}, y_0^{\mathrm{p}})$ and m_x^{p}, m_y^{p} for the quantities determined from the scattered proton ray-tracing, then the transverse distance between the two tracks at a given z is

$$r_{\mathrm{sep}}(z) = \sqrt{(x_0^{\mathrm{p}} + m_x^{\mathrm{p}} z - x_0^{\mathrm{n}} - m_x^{\mathrm{n}} z)^2 + (y_0^{\mathrm{p}} + m_y^{\mathrm{p}} z - y_0^{\mathrm{n}} - m_y^{\mathrm{n}} z)^2}. \quad (4)$$

Setting $\partial r_{\mathrm{sep}}/\partial z = 0$, we find the z-location at which the tagged neutron and scattered proton tracks have their minimum transverse separation to be

$$z_{\mathrm{min}} = \frac{(m_x^{\mathrm{p}} - m_x^{\mathrm{n}})(x_0^{\mathrm{n}} - x_0^{\mathrm{p}}) + (m_y^{\mathrm{p}} - m_y^{\mathrm{n}})(y_0^{\mathrm{n}} - y_0^{\mathrm{p}})}{(m_x^{\mathrm{p}} - m_x^{\mathrm{n}})^2 + (m_y^{\mathrm{p}} - m_y^{\mathrm{n}})^2}. \quad (5)$$

This DCA method automatically accounts for the depth of interaction in the target. One limitation is that the z_{min}-resolution deteriorates with decreasing proton scattering angle. This deterioration is illustrated in Fig. 14 by comparing the z_{min} spectra for all events and for events with $\theta_{\mathrm{p}}^{\mathrm{scat}} > 15°$. Note that the actual target scintillator thickness is 18.8 mm.

The central z_{min} peak found for $\theta_{\mathrm{p}}^{\mathrm{scat}} > 15°$ events is consistent with a uniform 18.8 mm wide distribution folded with a Gaussian-resolution function characterized by $\sigma_z = 7$ mm, as is shown in Fig. 14. The bump that appears in Fig. 14 at $z \approx -100$ mm corresponds to the location of the small upstream veto scintillator, SUV. The origin of these events is revealed in the lower left frame of Fig. 14, where we plot the transverse coordinates predicted for the neutron in this z_{min} range. The events in this frame spanning the full area of the SUV correspond to neutron scattering from its downstream face, with too little energy deposited in the SUV to pass its discriminator threshold and thus generate an event veto. However, we also see a more intense concentration of events 8–10 cm below the center of the SUV, corresponding to neutron scattering from its lucite lightguide, where no signal is generated to cause a veto. The physical boundary between scintillator and lightguide for the SUV was sharp and horizontal; its sharp localization in the neutron path reconstruction suggests that the transverse neutron coordinate resolution in the vicinity of the secondary target has a σ no worse than a few mm. This precise identification of background sources lends credibility to the DCA analysis, and illustrates one of the great advantages of a tagged neutron beam for making precise cross-section measurements.

Fig. 15 shows the difference in x and y determinations at the DCA between the ray-traced scattered proton path and the reconstructed tagged neutron path for events where both recoil protons stop in the DSSDs and deposit less than

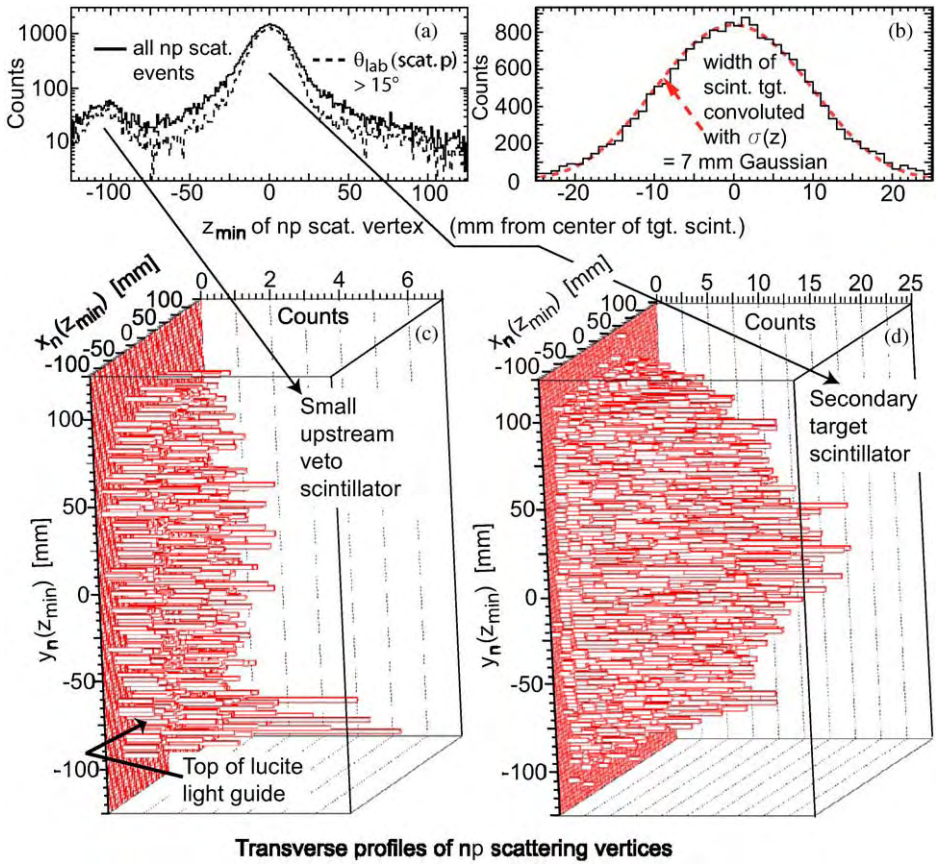

Fig. 14. Distributions of the secondary event vertex coordinates reconstructed by finding the distance of closest approach (DCA) of the tagged neutron and ray-traced proton paths. (a) Distribution of longitudinal coordinates at the DCA, where the center of the secondary target is at $z = 0$. The dashed histogram, with somewhat improved resolution, is restricted to events where the neutron and proton directions differ by at least 15°. (b) Closeup view of the dashed histogram from (a), compared to the convolution (dashed curve) of a rectangular distribution with the target width and a resolution Gaussian with $\sigma_z = 7$ mm. (c) The transverse coordinates at the DCA reconstructed from neutron tagging for events originating at the SUV scintillator ($-120 < z_{\min} < -85$ mm). (d) Same as (c), but for the secondary target scintillator ($-20 < z_{\min} < 20$ mm), showing the roughly symmetric beam profile centered on this target for the np scattering events of interest.

5 MeV apiece. The distributions each exhibit a narrow central peak with long tails. To quantify the resolution, we fitted each spectrum with the sum of a narrow and a broader Gaussian. The central Gaussians have widths $\sigma_x^c = 0.75$ mm and $\sigma_y^c = 0.65$ mm, while the tails of the distributions are characterized by Gaussian widths of $\sigma_x^t = 3.28$ mm and $\sigma_y^t = 2.74$ mm. These widths represent a convolution of comparable resolution contributions from the neutron tagging and the proton ray-tracing. Over 97% of all tagged neutron events fall within ± 10 mm in both the x and y difference plots. Thus, by defining a fiducial area that is at least 10 mm in from the physical edges of the secondary target, one can tag neutrons that hit the target with a certainty exceeding 99%.

The spatial resolutions deduced from Fig. 15 have contributions from many sources, including the intrinsic spatial resolutions of the tagger DSSDs and forward MWPCs, the energy resolution of the tagger and degree of gain matching among different strips, the size and divergence of the cooled proton beam, multiple scattering of the

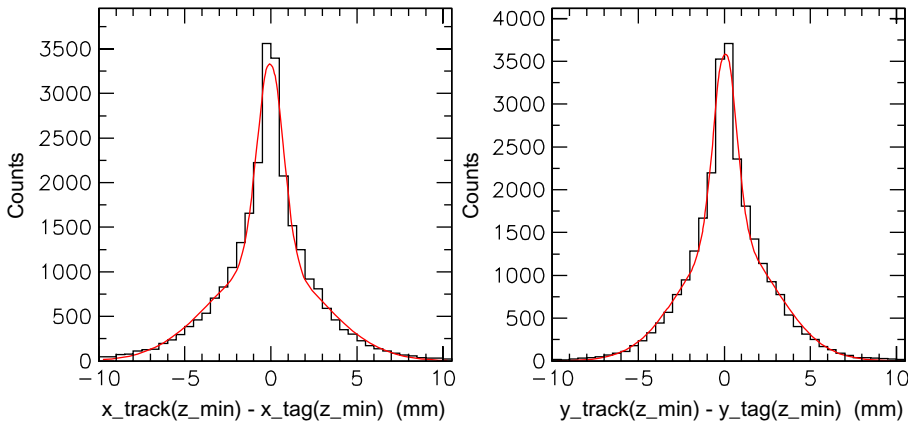

Fig. 15. The difference in x (left) and y (right) positions determined from tracking of the scattered proton and reconstruction of the tagged neutron at the distance of closest approach, for events where both protons stopped in the DSSDs. The smooth curves are the result of fitting a double Gaussian to the distributions.

forward protons, and the degree of optimization of the several parameters specifying the three-dimensional locations of tagger, forward detectors and primary beam. Improvements in any of these parameters can lead to improved reconstruction resolution. It is important to note that the resolutions already achieved would not have been attainable without the small beam size and divergence of a cooled primary beam [14].

4.5. Accuracy of absolute neutron flux determination

The major motivation for constructing the tagged neutron facility is to establish accurate absolute neutron scattering cross-section standards at intermediate energies. The paucity of good existing standards makes it a challenge to prove that the tagged neutron flux is, in fact, determined with the accuracy we seek. The best existing measured standards come from accurate measurements of total neutron cross-sections by target attenuation techniques [1], which do not rely on, and hence cannot be used to verify, accuracy of absolute flux determinations. While total cross-sections sensitive to flux determination can, in principle, be measured with the tagged beam by integrating measured differential cross-sections over all scattering angles, this is complicated by the need for two substantially different experimental setups to cover the backward and forward c.m. angle regions. Proponents of the Nijmegen partial wave analysis of np elastic scattering cross-sections and spin observables claim that their analysis *predicts* absolute np differential cross-sections with an accuracy better than $\pm 1\%$ [4]. But, as the data selection criteria for this analysis are controversial (a major fraction of intermediate-energy cross-section measurements are rejected), this is a prediction that we want to test.

We are thus forced to a staged approach. In the present paper, we establish that the tagged neutron flux is, indeed, accurate to the 5–10% level. We do this in two different ways: (1) via a preliminary comparison of np differential cross-section measurements made during the facility commissioning runs with the Nijmegen predictions, over a limited angular range, (2) by using the tagged beam to determine the neutron detection efficiency of individual hodoscope scintillator bars, and comparing the results to previous measurements for the same detectors [9] and to calculations based on standard neutron detection efficiency simulations [16]. When we report our final np cross-section measurements in a future paper, we will then include a number of internal consistency checks on the measurement, intended to make the ultimate $\pm 1\%$ accuracy plausible. A number of these internal consistency checks are described conceptually in Section 5 of the present paper.

Data obtained during the commissioning runs from event streams 1, 2 and 3 are used to carry out the np elastic cross-section and neutron detection efficiency determinations. The same cuts and conditions on tagger information (including cuts on the predicted tagged neutron transverse coordinates on the forward arm, as detailed below) are applied to all three event streams, but the conditions on forward arm detectors differ. For event stream 1, we require that no prompt signals be seen on any of the forward scintillators (including the target scintillator) and that no valid hits be recorded in the third wire chamber. Event stream 3 has the same forward detector requirements with the exception that at least one hodoscope bar register a prompt hit, in order to select events where a neutron converts inside the hodoscope. For event stream 2, the analysis requires prompt hits recorded in the ΔE and hodoscope scintillators in coincidence with the tagger hits, no hits in the LUV and SUV scintillators, and at least one hit on all three planes of the first MWPC (plus suitable hits on subsequent planes to allow proton ray-tracing). The requirement on MWPC #1 is important to eliminate np scattering events initiated in the ΔE scintillator, rather than in the target scintillator; for protons originating in the target scintillator this condition is satisfied with efficiency well in excess of 99%. The yield of relevant tagged neutrons appropriate to the analyses described below is determined from the summed number of events in the mutually exclusive event streams 1 (corrected for prescaling) and 3 that satisfy the common tagger cuts (with the small contribution from event stream 2 added when precision better than 1% is desired).

The scattering angle for np events in stream 2 is determined event-by-event by comparing the ray-traced proton path to that of the tagged neutron. The philosophy used for np scattering cross-section determination is to avoid kinematic cuts on these events as much as possible, and to rely instead on accurate subtraction of backgrounds measured with a secondary carbon target replacing the scintillator target. For example, cuts on the forward proton energy deposition in the hodoscope (where it stops) are avoided because they would introduce sensitivity to the proton "reaction tail" in the scintillator material. No cut has been imposed on the $z_{\min}$ distribution in Fig. 14, since the angle-dependence of the resolution could distort the extracted angular distribution slightly. The only kinematic cuts imposed here involve coarse gates on the proton energy loss in the ΔE scintillator as a function of scattering angle, and on the mean time difference between the recorded hodoscope hit and the tagger signal. These are intended to reduce background contributions from quasifree scattering and from accidental coincidences, respectively. A further cut restricts the predicted neutron position at the secondary target to the ranges $|x_{\mathrm{tag}}|<100$ mm, $|y_{\mathrm{tag}}|<100$ mm with respect to the target center, to include the entire secondary target but reduce background from other sources. The remainder of the quasifree scattering background, together with backgrounds originating from other sources than the secondary target, account for about 40% of the yield that survives the cuts, and are then subtracted via the carbon target data. The relative normalization of the scintillator and carbon runs is measured by the yield from each in event stream 4 (pd scattering events). The thicknesses of the two targets were closely matched, and were determined precisely by weighing.

In Fig. 16, we show preliminary absolute differential cross-sections for np scattering over the restricted angle range $20^\circ<\theta_{\mathrm{p}}^{\mathrm{scat,\ lab}}<30^\circ$, where the scattering angle is well measured and the forward detectors provide complete azimuthal coverage for events originating over the entire scintillator target area. The completeness of azimuthal coverage is confirmed for each angle bin included in Fig. 16 by the observed uniformity of the measured yields as a function of reconstructed azimuthal angle. The scattering cross-sections are then obtained straightforwardly from the ratio of the background-subtracted yield in event stream 2 to the incident tagged neutron yield from event streams 1, 2, and 3, and from the known hydrogen thickness of the scintillator target. Anticipated small corrections for the scattering of tagged neutrons out of the beam before they reach the scintillator target ($\lesssim 2\%$), for wire chamber inefficiencies ($<1\%$) and for dead

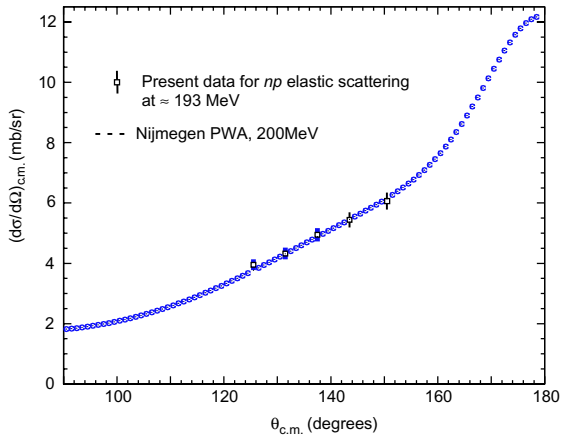

Fig. 16. Absolute np elastic scattering cross-sections deduced over a limited angle range from data collected during the commissioning run. The absolute normalization of the measurements is determined from the tagging. The differential cross-section expected from the Nijmegen partial wave analysis [4] is shown for comparison. In the experiment planned with the tagged neutron facility, absolute cross-sections will be obtained over the entire angular range in the plot, and with much better statistical precision than that shown here.

time differences between event streams 1 and 2 (<0.5%) have not yet been applied. Nonetheless, the excellent agreement seen in the figure between the absolute cross-sections extracted from the tagged neutron beam and those predicted by the Nijmegen partial wave analysis suggest that the tagged yields are well understood to at least 5–10% absolute accuracy.

For the hodoscope neutron efficiency event stream (#3), a reconstruction of the outgoing neutron is performed in exactly the same way as for the np scattering events, except here the neutron paths are projected to the location (midpoint in depth) of the scintillator hodoscope. The quality of neutron reconstruction in this case is illustrated in Fig. 17 by the histograms of predicted x_{tag}-position of the neutron at the hodoscope when a particular hodoscope bar, or two adjacent bars, fired. The firing of adjacent bars is expected when the neutron is incident near the interface of the two bars, yielding a significant probability that a charged particle recoiling from the neutron conversion will cross the boundary between the bars. The tagged neutron beam, now subjected to a transverse coordinate cut requiring only that the neutron fall within ± 15 cm of the vertical center of the hodoscope, illuminates 6 of the 16 vertically oriented hodoscope bars. The events in Fig. 17 involve single hits in each of these six bars, as well as the five possible pairs of adjacent bar hits. The single-bar spectra exhibit clear efficiency falloffs near the interfaces between the bars, while the efficiency for firing two adjacent bars peaks at these interfaces. The x_{tag} locations of these interfaces via the peaks and valleys in neutron detection efficiency reproduce the known spacings between adjacent hodoscope bars very well, with a transverse position resolution $\sigma(x_{tag})$ of a few mm over a flight path of about 2.0 m. The x_{tag} value at the interface between bars 8 and 9 determines the overall horizontal position offset of the forward detectors (calibrated relative to one another via cosmic rays) with respect to the tagger.

Each hodoscope bar's detection efficiency is evaluated for tagged neutrons predicted to fall within ± 2 cm horizontally and ± 15 cm vertically of the center of that bar. The efficiency is taken to be the observed fraction of such incident neutrons

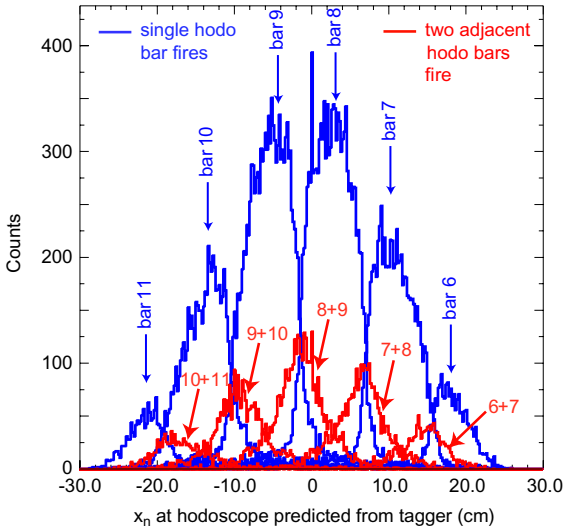

Fig. 17. Distributions of the neutron x-coordinate within a plane parallel to the hodoscope face but halfway through its depth, as predicted from neutron tagging for event stream 3. The larger peaks are for events where one hodoscope bar fires alone, as indicated by the labels and arrows, while the smaller peaks correspond to two adjacent bars firing in coincidence.

(summed over event streams 1 and 3) that actually fire the predicted bar either alone or in coincidence with one of its two nearest neighbors. Small corrections to this fraction are applied [14] to account for a number of potential complications: (1) accidental tags in which the two particles detected in the tagger do not actually come from the same reaction, (2) events where a particle is detected in the hodoscope in accidental coincidence with a real tag or where a disjoint second bar fires in accidental coincidence, and (3) events where the tagged neutron undergoes a scattering through an appreciable angle prior to arrival at the hodoscope, without generating a recoil charged particle of sufficient energy to veto the event. Candidate processes for the latter pre-scattering include $C(n,n)$, $C(n,n')$, and $C(n,2n)$ reactions induced within the forward scintillators, and more general neutron-induced reactions on heavier nuclei in the exit flange from the Cooler vacuum. The latter flange provides approximately 3% total interaction probability for neutrons near 200 MeV, where the majority of these interactions will not be vetoed. If such pre-scattering occurs upstream of the hodoscope, it can lead to significant errors in the predicted impact position of the neutron at the hodoscope. (This problem is considerably more severe for the hodoscope than for evaluation of np scattering cross-sections from the scintillator target, because in the case of the hodoscope there is significantly more relevant upstream material and longer flight paths over which an appreciable displacement can build up. However, the ± 15 cm restriction on y_{tag} at the hodoscope is imposed specifically to eliminate thick potential upstream sources associated with forward detector mounting frames and soft iron shields for phototubes.)

The above complications contribute to the $\sim 10\%$ background in Fig. 18, which plots the distribution of hodoscope bars actually hit when the tagger reconstruction predicts a tagged neutron passing through bar #8. Presumably, the single-bar hits in bars near #8 arise in significant part from neutron pre-scattering effects (including sub-threshold neutron pre-scattering within the impact bar of the hodoscope itself), while the more uniform yields in more distant bars reflect accidental coincidences. The time distribution of wrong-bar fires can be inferred by comparing the solid and dashed histograms in Fig. 19. In this figure, the low flat background represents accidental coincidences, while the excess events near zero time difference in the tail of the solid histogram peak presumably arise from neutron energy reductions and flight path increases caused by upstream pre-scattering.

The efficiency corrections associated with accidental coincidences and with neutron pre-scattering are estimated [14] on the basis of spectra such as those shown in Figs. 18 and 19. These estimates include an attempt to distinguish upstream pre-scattering, which alters our efficiency determination, from sub-threshold pre-scattering within the hodoscope, which represents a true inefficiency.

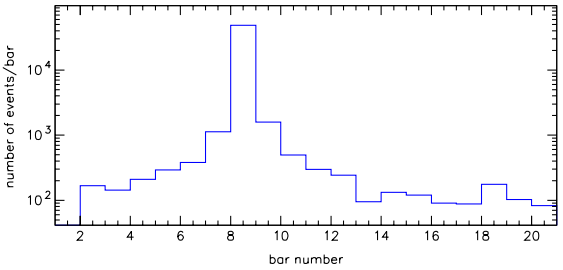

Fig. 18. Distribution of single-bar hits when the neutron was predicted to pass through hodoscope bar 8. The vertical bars are numbered 1–16 starting from the Cooler beam pipe, with bars 17–20 mounted horizontally at the top and bottom of the hodoscope area. Bar 1 is omitted from the analysis due to its high singles and accidental coincidence rates.

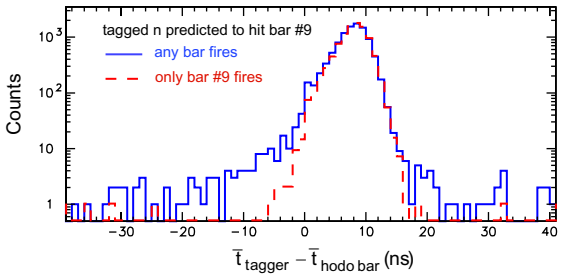

Fig. 19. Distribution for event stream 3 of the difference between the mean arrival time of the two particles in the tagger and the mean time extracted from the two phototubes on a single-fired hodoscope bar. The dashed histogram is restricted to events where the predicted bar fires, while the solid histogram shows the time difference regardless of which bar fired.

Both sources contribute to the near-bar hits in Fig. 18. Their relative contributions have been constrained by investigation of selected pre-scattering subsamples of the collected data: scattering events in the target scintillator (not used as a veto in the trigger logic), where a large-angle recoil proton led to recorded pulse height in that scintillator but no other detectors; in-hodoscope pre-scattering where at least one of the two phototubes on the expected impact bar showed an appreciable recorded pulse height when only a nearest neighbor of that bar recorded a hit. By far the largest correction we have made to the efficiency evaluation is to compensate for the estimated $(5\pm2.5)\%$ of incident tagged neutrons that scatter upstream through a sufficient angle to alter the bar of incidence at the hodoscope. The systematic uncertainty assigned to this correction dominates the error bars on the extracted efficiencies summarized in Table 3. The efficiencies in the table were determined for events where the two recoil protons stopped in two different DSSD quadrants, but consistent results were found also for events where both protons stop in the same DSSD, and where one of them punches through into a backing detector.

The experimental thresholds on each bar indicated in Table 3 are determined, in "electron-equivalent" MeV with a $\pm10\%$ uncertainty, from evaluation of cosmic ray calibration data for the hodoscope. The predicted efficiencies included in the table result from a Monte Carlo simulation [16] that assumes uniform illumination of each hodoscope bar with monoenergetic neutrons. The simulated efficiency varies slowly with both incident neutron energy and detector energy threshold, as can be seen by comparing the predictions for different bars with different thresholds.

The measured efficiencies are systematically lower than the predictions, by an average of about 8% of the efficiency value. Within the estimated systematic uncertainties, the four bars analyzed give consistent ratios of measured to predicted efficiency, despite a variation by more than a factor of four in the tagged neutron yield among the four bars. This consistency is encouraging, although a full simulation of the pre-scattering expected in the facility is needed to judge the degree to which the presently assigned systematic errors are truly uncorrelated among the different bars. The overall shortfall is perhaps not too surprising, since the efficiency simulation itself is probably not trustworthy to better than 10%. Over the years, the neutron cross-sections used in the code [16], particularly for the poorly known carbon inelastic channels, have been adjusted to improve agreement with experimental data [17,18]. However, both the cross-sections used in the code and the experimental efficiency determinations to which its results have been compared suffer from the very uncertainty in neutron flux normalization that has prompted the development of the tagged neutron facility. A previous measurement of the neutron detection efficiencies for this same hodoscope was also made with a tagged neutron beam of sorts, tagging by detection of an $\bar{n}$ from the $\bar{p}p\to\bar{n}n$ reaction studied at the LEAR antiproton ring [9]. The somewhat larger error bars on that measurement make the results of Ref. [9] inconclusive in the present context, consistent both with a similar Monte Carlo efficiency calculation and with a shortfall of magnitude comparable to what we find here.

Table 3
Comparison of measured and simulated neutron detection efficiencies for several different hodoscope bars. The error bars on the measured efficiencies are dominated by systematic uncertainties described in the text

Bar number	E_n range (MeV)	Threshold (MeV_{ee})	Measured efficiency	Simulated efficiency	Meas./sim. ratio
6	194–197	8.1 ± 0.8	0.156 ± 0.004	0.174	0.895 ± 0.025
7	192–196	4.7 ± 0.5	0.174 ± 0.005	0.185	0.941 ± 0.025
8	189–194	3.9 ± 0.4	0.173 ± 0.004	0.190	0.911 ± 0.023
9	187–192	4.3 ± 0.4	0.177 ± 0.005	0.187	0.947 ± 0.028

From the preliminary results reported here for np scattering differential cross-sections and from the measured neutron detection efficiencies, we conclude that: (1) the neutron tagging permits absolute flux determination to at least the 10% level, (2) careful simulations of neutron pre-scattering from sources upstream of a target of interest will be essential for reaching $\sim 1\%$ absolute accuracy, (3) we will have to rely on various types of internal consistency checks on data acquired with this facility to demonstrate the achievement of our ultimate accuracy goals, since the only existing, uncontroversial absolute standards for neutron cross-sections at intermediate energies involve total cross-sections to which it will be very difficult to make a meaningful comparison.

4.6. Tagging efficiency

The efficiency with which neutrons impinging on the secondary target are successfully tagged does not enter into neutron cross-section measurements with this facility, but it does directly affect the flux of tagged neutrons attainable. This tagging efficiency was determined from the auxiliary runs made with a "pseudo-neutron" trigger (see Section 3.2), where only a single recoil proton may have been recorded in the tagger. Events that appear to have a forward neutron interacting in the target scintillator were selected from event stream 2 in this mode, by requiring that scintillator to give a signal in prompt time coincidence with the tagger, while the LUV and SUV scintillators were still used in anticoincidence. The charged particle or particles detected in the tagger for such events were subjected to the usual requirements for a tagging proton. In particular, it was required that even a single recoil particle either stop in a DSSD (depositing less than 5 MeV) or fall within the particle ID gate shown in Fig. 11. The latter requirement eliminated from the sample the abundant events in which a recoil proton punched through a backing detector, in association with a ^{2}H(p, pn)p knockout neutron of energy much lower than the charge-exchange neutrons of interest.

Of the remaining pseudo-neutron sample, 13.3% of the events were found to be accompanied by two acceptable recoil protons in the tagger, and the rest by only a single proton in the tagger. This tagging efficiency was slightly reduced during the commissioning run by problems encountered with a single VA chip on one of the DSSDs. In the absence of this problem, the expected tagging efficiency would have been approximately 14.3%.

The tagging efficiency depends not only on the geometry of the tagged neutron facility and the properties of the tagger, but also critically on the energy and angular distributions of the neutrons and recoil diprotons produced in the ^{2}H(p, n) reaction. We have carried out a simulation of the facility based on a simplified reaction model, utilizing a code previously developed to account for ^{2}H(p, n) spectra measured as a function of neutron energy and angle at a proton bombarding energy of 135 MeV [19]. The model incorporates separate single-step calculations in the plane-wave impulse approximation for both the final-state interaction (FSI, proton charge-exchange followed by $^1S_0$ resonant pp interaction) and quasifree scattering (QFS, pn scattering with a spectator proton) production processes. The relative strengths of the FSI and QFS contributions were adjusted to optimize the agreement with the 135 MeV data, and were assumed to remain the same at 200 MeV. This ratio strongly influences the simulated excitation energy spectrum in the recoiling diproton system, and thereby the predicted tagging efficiency. In the simulations, the resulting diproton was assumed to decay isotropically in its rest frame, a valid assumption for the $^1S_0$ FSI, but not necessarily for the QFS contribution. Because of the questionable assumptions in this reaction model, we do not look to the simulations for quantitative reproduction of the measured properties of the neutron beam, but rather for illumination of qualitative trends, as described further below. We emphasize that a quantitative understanding of the neutron production reaction is not at all essential to the extraction of accurate absolute secondary reaction cross-sections with the tagged beam.

Detected particle information for the events simulated within the above model was generated using full knowledge of the tagger and forward detector geometry and other properties, including

tagger dead layers and detector resolutions. Simulated events with a produced neutron headed toward the secondary target were recorded and analyzed in a manner equivalent to that for pseudo-neutron events taken during the commissioning run, with equivalent cuts imposed on tagger information. The simulation thereby yields a simulated tagging efficiency that can be compared directly to the measured value.

The simulation indicates a strong dependence of the tagging efficiency on the energy threshold in the tagger, as can be seen in Table 4. Here the tagging efficiency is defined the same way as for the pseudo-neutron data: the fraction of neutrons on target for which both recoil protons are detected in the tagger, out of those where at least one proton is detected. The result for 1.5 MeV threshold (18.3%) is closest to the measured result and, as will be discussed in the following subsection, also yields neutron distributions most similar to the real data. However, the energy threshold observed in the tagged neutron data is closer to 1.0 MeV (there are some channel-to-channel variations). The discrepancy between simulation and measurement is presumably due, at least in part, to inadequacies in the model used to describe the ^{2}H(p, n) reaction.

The simulation suggests that, for a DSSD threshold of 1.0 MeV, slightly fewer than half of all neutrons passing through the secondary target are accompanied by even one recoil proton detected in the tagger. Combining this simulation result with the measured ratio of two-proton to one-proton events, we estimate that $\approx 6\%$ of *all* neutrons crossing the target in the vicinity of the maximum energy are successfully tagged. The clearest way to improve this efficiency in future runs, for the same tagger geometric acceptance, is to reduce DSSD noise so that the TA-chip energy thresholds can be significantly lowered.

Table 4
Simulated tagging efficiency results for three different DSSD energy thresholds

DSSD energy threshold (MeV)	Tagging efficiency (%)
0.5	27.8
1.0	25.0
1.5	18.3

4.7. Tagged neutron flux, spatial profiles and energy distribution

Analysis of the neutron flux event stream (Event 1) shows that, of the events satisfying all conditions for the tagger, typically 80% have predicted positions at the secondary target location that fall within the target's $20\ \text{cm} \times 20\ \text{cm}$ area. The measured tagged neutron flux profile within that area is shown in the upper frames of Fig. 20, with the contribution from events where one of the recoil protons stops in a backing detector clearly delineated. For comparison, the lower frames of the figure show analogous spatial distributions from the simulations performed for an assumed DSSD threshold of 1.5 MeV. With a DSSD threshold $\leqslant 1.0$ MeV, the simulation yields a forward-peaked (i.e., at $x_n = 10$ cm) neutron profile, in sharp contrast to that observed, even allowing for variations in the assumed FSI/QFS ratio. Fig. 21 allows a similar comparison of the measured to the simulated energy spectra for the tagged neutrons predicted to pass through the secondary target.

It is clear that the simulations provide only a qualitative understanding of the observed neutron distributions. The quantitative discrepancies may reflect shortcomings of the reaction model used in the simulations and/or unexpected instrumental problems with the tagger. For example, in comparison with the simulations we seem to observe too few tagged neutrons especially at the highest energies, most forward angles and above and below mid-plane. The highest-energy neutrons headed toward the top or bottom of the secondary target are kinematically correlated with recoil proton pairs where both protons tend to hit the same quadrant of the tagger. Thus, one possible origin for the discrepancy between the predicted and observed distributions could be an inefficiency for detection of two protons in a single DSSD, over and above the inability (included in the simulations) to distinguish two particles if they impinge on the same TA-chip $x - y$ pixel. Such an

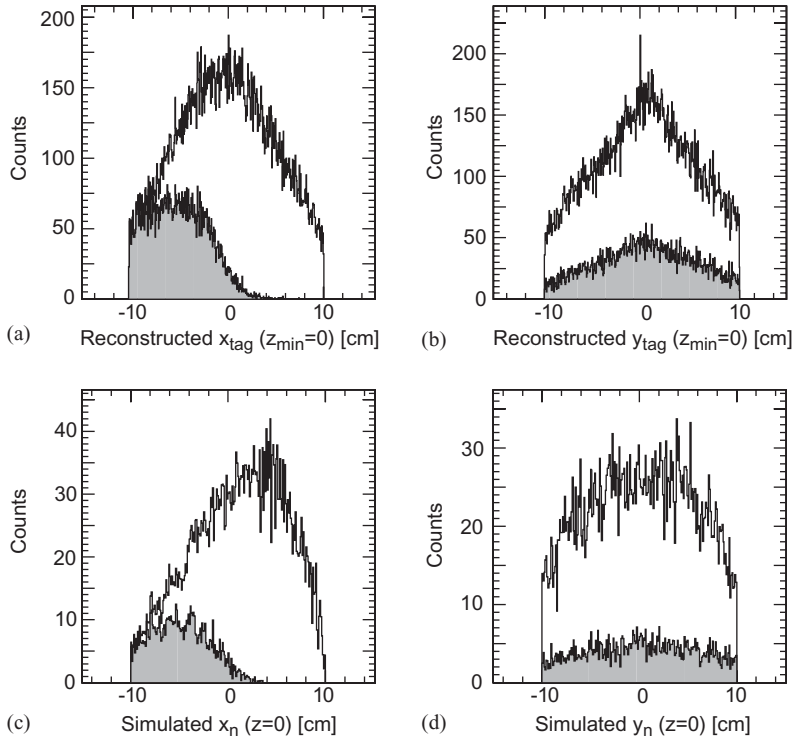

Fig. 20. The x and y distributions of neutrons at the center of the secondary target, as given by the tagging reconstruction (upper frames) and by the simulations described in the text (lower frames). The shaded regions in each frame indicate the contribution from events with one recoil proton depositing energy in a backing detector. Note that the positive x-direction is towards the Cooler beam pipe (i.e., towards smaller neutron production angles).

inefficiency might also account for the need for an artificially high DSSD threshold in the simulation. However, there is no other indication in the data for any unexpected problems in identifying or triggering on neutrons with both recoil protons in the same DSSD.

An alternative possible cause of some of the discrepancies is inadequacy of the assumption of isotropic diproton decay, used in the simulations. This could be (but has not yet been) checked by incorporating p-wave components with unequal magnetic substate populations into the outgoing two-proton system in the simulation. These p-waves must be present to a large degree at the higher excitation energies of the quasifree scattering region, although it is not known if the reaction mechanism leads to substantial vector or tensor polarization of these p-wave diprotons. If such polarization effects are strong in reality, they could certainly influence both the tagging efficiency and the neutron beam profiles.

The maximum neutron tagging rate on the secondary target attained during the commissioning runs, averaged over the data-taking portion of the Cooler cycle, was about 120 Hz. While precise luminosity determinations for the primary beam and GJT are not yet available, the time-averaged neutron tagging rate per unit of Cooler luminosity appears to be roughly 60 Hz/(10^{31} cm^{-2} s^{-1}). The rate per unit luminosity could be improved by as much as a factor of 2 by reducing DSSD noise and lowering the proton detection thresholds. Furthermore, the stability of the measured ratio of tagged neutron rate to Cooler luminosity, over the range of luminosities explored in the commissioning runs, implies that the facility could operate

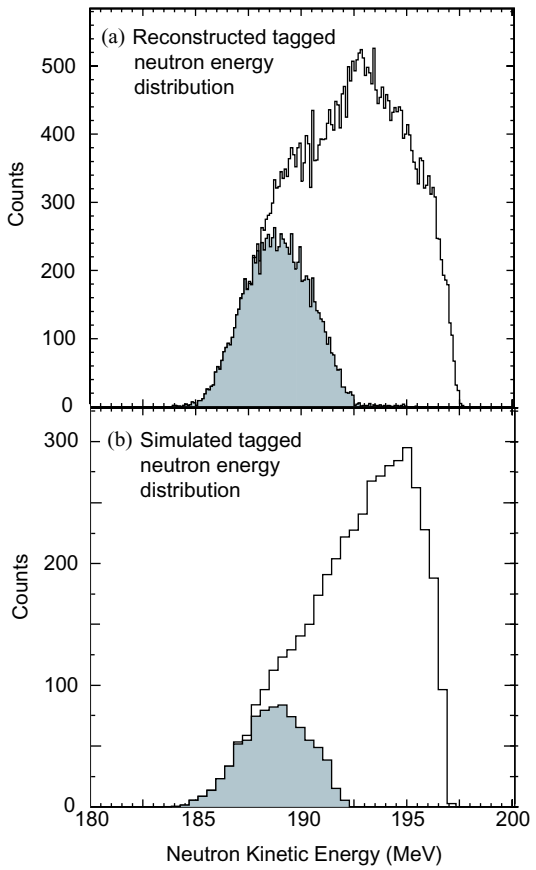

Fig. 21. The reconstructed (top) and simulated (bottom) distributions of tagged neutron energies for neutrons predicted to pass through the secondary target. The shaded region in each frame indicates the contribution from events with one recoil proton depositing energy in a backing detector.

successfully at substantially higher primary beam luminosities. In a subsequent run we have now achieved modest improvements in primary beam luminosity and secondary hydrogen target thickness (by replacing the scintillator by CH_2), reaching a detected, time-averaged, n–p free scattering rate of 1 Hz. Under these conditions, a 2-week run, with one-third of the data-taking time devoted to background measurements with a carbon target, was sufficient to permit attainment of typically $\pm 1\%$ statistical precision in the background-subtracted differential cross-section measurement, within c.m. angle bins of 5° width between 90° and 180°. Data from this subsequent run are currently being analyzed, and will be reported elsewhere.

5. Internal consistency crosschecks for absolute cross-section measurements with the tagged beam

The goal of the tagged neutron facility is to allow the establishment of absolute cross-section standards at $\pm 1\%$ accuracy level for intermediate-energy neutron-induced reactions. The paucity of reliable existing standards in the database leads one to a bootstrapping approach to demonstrate that the design goal accuracy has indeed been achieved. Follow-up measurements with the facility have included appropriate internal consistency checks to permit such a demonstration.

As in the commissioning runs, data were taken simultaneously for n–p scattering induced by the tagged neutron beam and for p–p scattering induced in the same secondary target by the tagged proton beam defined by detection of recoil deuterons in the tagger. (The latter events fall in event stream 5, which has been ignored in the present paper.) An absolute accuracy of $\pm 1\%$ has already been achieved for p–p cross-sections [20], so we can use our p–p measurements to provide an independent crosscheck of the target thickness and detector solid angle determinations as a function of impact position on the secondary target.

The precision of the tagging in determining the *relative* flux of neutrons as a function of position within the tagged beam can be checked by subdividing the acquired n–p scattering data into numerous bins in neutron transverse position on the secondary target. There are large angular overlap regions among the n–p cross-sections measured for the various target position bins. The different bins must give consistent cross-section results, after applying small corrections for known variations across the target in neutron energy, neutron polarization, and forward detector solid angles. (Polarization effects average out to better than 10^{-3} when averaging over the entire target, because the forward detectors are left-right symmetric with respect to this scattering. However, residual asymmetries of up to 1% can remain in cross-sections determined from off-center target

bins.) For a meaningful crosscheck, the statistical uncertainties obtained for the background-subtracted n–p scattering sample within *each* such target bin, over the overlap angle region, should be smaller than $\pm 1\%$.

An ultimate overall check of the absolute accuracy of tagged neutron flux determination would require comparison of a *full* measured angular distribution for np scattering with the *total* cross-section, which has been determined from attenuation measurements near 200 MeV to an absolute precision of $\pm 1\%$ [1]. Such a comparison would require a second, substantially different, experiment to cover the forward c.m. angles, since the present forward arm is optimized for n–p backscattering by detection of the energetic forward protons.

6. Conclusions

We have described the instrumentation and early performance characteristics of a tagged neutron facility established in the IUCF Cooler ring. The tagging is done by detection of a pair of low-energy recoiling protons produced in the reaction ^{2}H(p, n)2p with a cooled, stored proton beam of kinetic energy 200 MeV bombarding an ultrathin deuterium gas jet target. Energy, timing and two-dimensional position measurements are made for both recoil protons in a set of double-sided silicon strip detectors, outfitted with fast front-end readout electronics to permit operation of these detectors in a novel self-triggering mode. The recoil proton measurements provide a determination of the four-momentum of each tagged neutron, and of the event vertex for its production. Subsequent scattering of the tagged neutrons in a hydrogenic secondary target is signaled by detection of forward-going protons in wire chambers and scintillation detectors following the secondary target. The same equipment allows simultaneous production of a tagged secondary proton beam via detection of the recoil deuteron from p–d elastic scattering in the gas jet target, and study of the tagged proton's subsequent scattering.

The measured performance of the facility demonstrates that the tagging allows determination of the three-dimensional positions of the neutron's points of origin and of its subsequent scattering with, typically, several millimeter resolutions over flight paths of 1–2 m. This feature permits a clear identification of scattering from the desired secondary target and separation of backgrounds originating at other sources. The tagging also determines the neutron's energy, on an event-by-event basis, with a resolution of about 150 keV, or better than 0.1%. Thus, despite the fact that the tagged "beam" is large in size and broad in energy distribution, the energy and angle for each secondary scattering event are determined with high resolution.

The checks of n–p scattering cross-section and neutron detection efficiencies made during the facility commissioning runs demonstrate that the neutron flux is indeed determined by the tagging to within the absolute accuracy of existing standards, certainly to at least the 10% level. In principle, the flux accuracy should be better than 1%, after correcting for neutron outscattering at the few % level from material upstream of the desired secondary target. The flux accuracy, combined with the precision of neutron energy and angle determinations, make the tagged beam suitable for absolute n–p elastic scattering cross-section measurements to $\pm 1\%$ precision. Such measurements are needed to resolve discrepancies in the existing database, to check the validity of data selection procedures in conventional partial wave analyses of that database, and to establish reliable absolute standards for neutron reaction cross-sections at intermediate energies. Since the tagged neutron production rate is several orders of magnitude smaller than is typical of untagged neutron beams, the facility is best adapted for the study of neutron-induced secondary reactions with sizable ($\sim$mb/sr) cross-section.

Acknowledgements

We are grateful to Hal Spinka and Argonne National Laboratory for the long-term loan of multi-wire chamber readout electronics used in the forward detector array, and to Catherine Lechanoine-LeLuc and her group at the University of

Geneva for the long-term loan of the scintillator hodoscope used at the rear of the forward arm. We benefited enormously throughout the development of this facility from the untiring work of Dennis Friesel, Terry Sloan and the rest of the operations crew in producing IUCF Cooler beams that met our stringent demands on intensity and cleanliness. We thank Bill Lozowski for his efforts in preparing the secondary targets used. We are also grateful to Bryon Anderson for providing his reaction code for use in simulating the tagged beam properties. The work described herein has been performed with financial support from the US National Science Foundation under grant numbers PHY9314783 and PHY0100348.

References

[1] P.W. Lisowski, et al., Phys. Rev. Lett. 49 (1982) 255; V. Grundies, et al., Phys. Lett. 158B (1985) 15; W.P. Abfalterer, et al., Phys. Rev. C 63 (2001) 044608.
[2] J. Rahm, et al., Phys. Rev. C 57 (1998) 1077 and references therein.
[3] B.E. Bonner, et al., Phys. Rev. Lett. 41 (1978) 1200; M.C.M. Rentmeester, R.G.E. Timmermans, J.J. deSwart, Phys. Rev. C 64 (2001) 034004.
[4] V.G.J. Stoks, R.A.M. Klomp, M.C.M. Rentmeester, J.J. de Swart, Phys. Rev. C 48 (1993) 792.
[5] R.A. Arndt, I.I. Strakovsky, R.L. Workman, Phys. Rev. C 52 (1995) 2246.
[6] J. Blomgren (Ed.), Proceedings of Workshop on Critical Issues in the Determination of the Pion–Nucleon Coupling Constant, Uppsala, Sweden, 1999; J. Blomgren (Ed.), Phys. Scr. T 87 (2000).
[7] T.E.O. Ericson, et al., Phys. Rev. Lett. 75 (1995) 1046; T.E.O. Ericson, et al., Phys. Rev. Lett. 81 (1998) 5254; M.C.M. Rentmeester, R.A.M. Klomp, J.J. de Swart, Phys. Rev. Lett. 81 (1998) 5253; D.V. Bugg, R. Machleidt, Phys. Rev. C 52 (1995) 1203.
[8] R.E. Pollock, Ann. Rev. Nucl. Part. Sci. 41 (1991) 357.
[9] A. Ahmidouch, et al., Nucl. Instr. and Meth. A 326 (1993) 538.
[10] J. Thun, et al., Nucl. Instr. and Meth. A 478 (2002) 559.
[11] J.E. Doskow, F. Sperisen, Nucl. Instr. and Meth. A 362 (1995) 20.
[12] S.E. Vigdor, et al., Phys. Rev. C 46 (1992) 410.
[13] D.R. Tilley, H.R. Weller, Nucl. Phys. A 474 (1987) 1.
[14] T.E. Peterson, Development of a tagged neutron facility for absolute neutron scattering cross section measurements, Ph.D. Thesis Dissertation, Indiana University, 2000, unpublished.
[15] O. Toker, et al., Nucl. Instr. and Meth. A 340 (1994) 572.
[16] N.R. Stanton, A Monte Carlo program for calculating neutron detection efficiencies in plastic scintillator, Ohio State University, February 1971, preprint COO-1545-92.
[17] M.W. McNaughton, et al., Nucl. Instr. and Meth. 116 (1974) 25.
[18] R.A. Cecil, B.D. Anderson, R. Madey, Nucl. Instr. and Meth. 161 (1979) 439.
[19] B.D. Anderson, et al., Phys. Rev. C 54 (1996) 1531.
[20] A.J. Simon, et al., Phys. Rev. C 48 (1993) 662.

Appendix III

PHYSICAL REVIEW C **70**, 014607 (2004)

Nucleon-induced reactions at intermediate energies: New data at 96 MeV and theoretical status

V. Blideanu,[1,*] F. R. Lecolley,[1] J. F. Lecolley,[1] T. Lefort,[1] N. Marie,[1] A. Ataç,[2] G. Ban,[1] B. Bergenwall,[2] J. Blomgren,[2] S. Dangtip,[2,3] K. Elmgren,[4] Ph. Eudes,[5] Y. Foucher,[6] A. Guertin,[5] F. Haddad,[5] A. Hildebrand,[2] C. Johansson,[2] O. Jonsson,[7] M. Kerveno,[8] T. Kirchner,[5] J. Klug,[2] Ch. Le Brun,[9] C. Lebrun,[5] M. Louvel,[1] P. Nadel-Turonski,[10] L. Nilsson,[2,7] N. Olsson,[2,4] S. Pomp,[2] A. V. Prokofiev,[7] P.-U. Renberg,[7] G. Rivière,[5] I. Slypen,[11] L. Stuttgé,[8] U. Tippawan,[2,3] and M. Österlund[2]

[1]*LPC, ENSICAEN, Université de Caen, CNRS/IN2P3, Caen, France*
[2]*Department of Neutron Research, Uppsala University, Sweden*
[3]*Fast Neutron Research Facility, Chiang Mai University, Thailand*
[4]*Swedish Defence Research Agency, Stockholm, Sweden*
[5]*SUBATECH, Université de Nantes, CNRS/IN2P3, France*
[6]*DSM/DAPNIA/SPhN, CEA Saclay, Gif-sur-Yvette, France*
[7]*The Svedberg Laboratory, Uppsala University, Sweden*
[8]*IReS, Strasbourg, France*
[9]*Laboratoire de Physique Subatomique et de Cosmologie, Grenoble, France*
[10]*Department of Radiation Sciences, Uppsala University, Sweden*
[11]*Institut de Physique Nucléaire, Université Catholique de Louvain, Louvain-la-Neuve, Belgium*

(Received 31 March 2004; published 15 July 2004)

Double-differential cross sections for light charged particle production (up to $A=4$) were measured in 96 MeV neutron-induced reactions, at the TSL Laboratory Cyclotron in Uppsala (Sweden). Measurements for three targets, Fe, Pb, and U, were performed using two independent devices, SCANDAL and MEDLEY. The data were recorded with low-energy thresholds and for a wide angular range ($20°-160°$). The normalization procedure used to extract the cross sections is based on the *np* elastic scattering reaction that we measured and for which we present experimental results. A good control of the systematic uncertainties affecting the results is achieved. Calculations using the exciton model are reported. Two different theoretical approaches proposed to improve its predictive power regarding the complex particle emission are tested. The capabilities of each approach is illustrated by comparison with the 96 MeV data that we measured, and with other experimental results available in the literature.

DOI: 10.1103/PhysRevC.70.014607 PACS number(s): 25.40.−h, 24.10.−i, 28.20.−v

I. INTRODUCTION

The deep understanding of nucleon-induced reactions is a crucial step for the further development of nuclear reactions theory in general. In addition, complete information in this field is strongly needed for a large amount of applications, such as the incineration of nuclear waste with accelerator-driven systems (ADS), cancer therapy, or the control of radiation effects induced by terrestrial cosmic rays in microelectronics. For this reason, the problem of nucleon-induced reactions has gained renewed interest in the last few years. This interest has been expressed in part by extensive experimental campaigns, such as those carried out by several laboratories in Europe in the framework of the HINDAS program [1].

Particularly, nucleon-induced reactions in the 20–200 MeV energy range have for a long time been the subject of intensive theoretical studies. For this range, the first major step for the improvement of nuclear reaction models consisted of the introduction of the so-called "pre equilibrium process." This process has been proposed in order to explain the smooth dependence of the particle emission probability versus angle and energy, which has been observed experimentally. This preequilibrium process is supposed to occur at an intermediate stage and to consist of multiple nucleon-nucleon interactions that take place inside the target nucleus. During that process, particle emission occurs after completion of the one-step interaction phase, i.e., the direct process phase, but a long time before the statistical equilibrium of the compound nucleus has been reached.

During the last 40 years, several approaches attempted to give a theoretical description of this preequilibrium process. Some of them have shown all along a good predictive power for a wide set of experimental energy distributions of nucleons emitted in nucleon-nucleus reactions. However, those models were unable to reproduce the experimental distributions of complex particles, for which they systematically underestimate the production rates. Among them, the exciton model of Griffin [2] is a very good example. Originally introduced in 1966, this model has been quickly adopted by the community because of its adaptability and simplicity. In an attempt to increase its capability in reproducing the complex particle rates, two main approaches have been developed. The first one, proposed in 1973 [3], introduces a cluster formation probability during the nucleon-nucleon interactions inside the nucleus. The second one formulated by Kalbach in 1977 [4] is a completely different approach that takes into

*Electronic address: blideanu@lpccaen.in2p3.fr

account the possible contributions of direct pick-up and knock-out mechanisms.

Nowadays, the exciton model modified according to these theories is the only one available to calculate energy spectra of both nucleons and complex particles emitted in nucleon-induced reactions at intermediate energies. In the past, both approaches have been tested against data, and they both show satisfactory agreement with experimental distributions [4,5]. The comparisons were made using the data available at that moment and that concern a limited number of reaction configurations and incident energies, lower than 63 MeV. Despite this success, several questions are still open to discussion. An extended study of the influence of the entrance channel parameters is necessary, i.e, the dependence on the incident particle type and on the incident energy has to be investigated.

The measurements presented in this work are part of the HINDAS program and they concern double-differential distributions of light charged particles, up to $A=4$, emitted in 96 MeV neutron-induced reactions on three targets: iron, lead and uranium. Calculations for those reactions are performed with the basic exciton model implemented in the GNASH code [6], and with both independent approaches proposed respectively by Ribanský and Obložinský [3] and by Kalbach [4]. The robustness of those approaches are also tested for other reactions with incident protons at lower energies and with other targets for which experimental results are available in the literature. This study allows a global view of the predictive power of each model.

The experimental setup used for data taking is briefly presented in Sec. II. In Sec. III, details concerning the procedures used to obtain the energy spectra and the cross section normalization are given. The results are presented in Sec. IV. Section V is dedicated to the description of the theoretical calculations related to the particle emission in nucleon-induced reactions at intermediate energies, and the predictions of the models are compared to experimental data. The conclusions of this work are given in Sec. VI.

II. EXPERIMENTAL PROCEDURE

The experiments were performed using the neutron beam available at the TSL Laboratory in Uppsala (Sweden), whose facility is presented in Fig. 1. Neutrons were produced by $^{7}\mathrm{Li}(p,n)^{7}\mathrm{Be}$ reactions using a 100 MeV proton beam impinging on a lithium target. The beam monitoring was provided by a Faraday cup where the proton beam was dumped and by a fission detector composed of thin-film breakdown counters [7] placed in the experimental hall. The stability of the beam was checked regularly during the data taking. The deviations found between the indications of both monitors did not exceed 2%.

Difficulties encountered when working with neutron beams are related to their characteristics. The neutrons of the beam are not strictly mono energetic. This is illustrated in Fig. 2 where a typical neutron spectrum is shown. It presents two components: one is a peak centered at an energy slighty lower than the incident proton beam energy ($Q=-1.6$ MeV), diminished of the energy loss inside the production target, and the other is a low-energy tail that contains about 50% of the total number of produced neutrons, and which originates from highly excited states of ^{7}Be. For the data analysis, events associated with low-energy neutrons must be rejected. The method employed for this rejection will be described in the forthcoming sections. After selection, the intensity of the resulting 96 MeV neutron beam is of the order of $10^{4}\ n/\mathrm{cm}^{2}$ sec. The neutron beam is collimated to a solid angle of 60 μsr and the beam spot at about 10 m from the lithium target has a diameter of 8 cm (Fig. 2). These characteristics impose the use of an adequate detection setup in order to obtain a satisfactory counting rate, keeping, at the same time, the energy and angular resolutions within reasonable limits. Two independent detection systems, MEDLEY and SCANDAL, were used in our experiments. They were placed one after the other on the beam line as shown in Fig. 1.

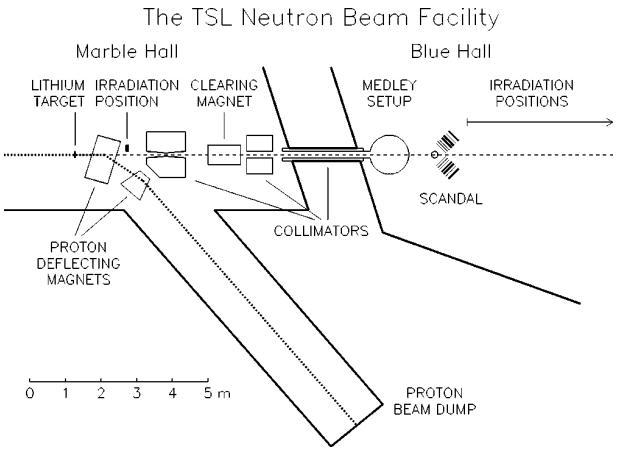

FIG. 1. TSL neutron beam facility and the location of the detection systems used in the experiment.

A. MEDLEY setup

The first setup downstream the beam was the MEDLEY detection array, described in detail in Ref. [8]. Composed of eight Si-Si-CsI telescopes, this system is used to detect light charged particles up to $A=4$, with a low-energy threshold and over an angular domain ranging from 20° to 160°, in steps of 20°. The telescopes were placed inside a vacuum reaction chamber of 100 cm diameter. The arrangement of the eight telescopes inside the chamber is given in Fig. 3. For the MEDLEY setup, the reaction target was placed at the center of the chamber and was tilted 45° with respect to the beam direction, in order to minimize the energy loss of the produced particles inside the target. Typically, 50 μm thick targets were used for all experiments. This allows small corrections for the energy loss of the emitted particles inside the target, but it also results in a low particle production rate. Due to the thin targets used and to the small solid angles of the telescopes, the statistics accumulated using the MEDLEY setup is relatively poor. The angular resolution was defined by the target active area and by the opening angle subtended by each telescope. It has been estimated

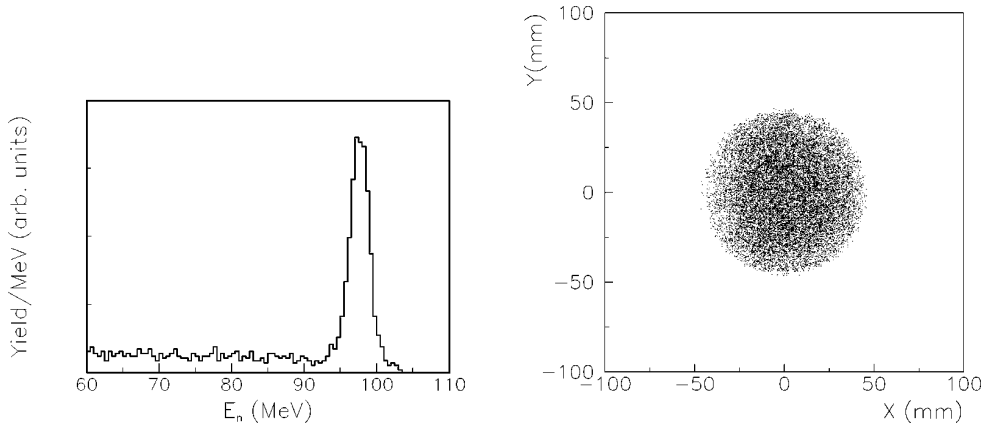

FIG. 2. Neutron energy spectra resulting from a 100 MeV proton beam on a 4 mm thick lithium target (left). Scatter plot showing the profile of the neutron beam at about 10 m from the lithium target (right).

using Monte Carlo simulations and typical values derived are of the order of 5°.

B. SCANDAL setup

A detailed description of SCANDAL is given in Ref. [9]. It consists of two identical systems located on each side of the neutron beam and which covered a detection angular range of $10° - 140°$ (Fig. 4). Since particles travel in air before entering the setup, only protons with energies larger than 30 MeV and a small number of deuterons could be detected. Each arm was composed of two 2 mm thick plastic scintillators used as triggers, two drift chambers used for the particle tracking, and an array of 12 CsI detectors enabling us to measure particle residual energies. The emission angle of each particle was determined from its trajectory through the drift chambers. With this method, the angular resolution was estimated to be of the order of 1°, which was a significant improvement compared to that obtained with the MEDLEY setup. An example of an angular distribution obtained with particles detected in one of the CsI detectors is shown, together with simulation results, in Fig. 5. The very good agreement observed is a necessary condition to demonstrate the validity of the tracking method used and the quality of the drift chambers. Using the trajectories, the coordinates of the nuclear reactions on the target plane could be determined with a backtracking procedure. Since the SCANDAL targets were larger than the neutron beam, it was crucial to determine the active target area with good precision.

The SCANDAL setup had the particularity to operate with a multitarget system (MTGT) [10], which allows an increase of the counting rate without impairing the energy resolution. An expanded view of the system is given in Fig. 6. Up to seven targets, inserted between multiwire proportional counters (MWPC's), can be mounted simultaneously. The information given by MWPC's allows us to determine the target from which the particle has been emitted, and to apply corrections to the particle energy by taking into account the energy losses inside the subsequent targets. In addition, by mounting simultaneously targets of different elements, several nuclear reactions can be studied at the same time. During our experiments, we operated with seven targets: five targets were made of the same material and dedicated to the reactions under study (iron, lead, or uranium), another one was a pure carbon target, and the last one was a CH_2 target. By these means, events associated with the reactions under study and events corresponding to the $H(n,p)$ elastic scattering were recorded at the same time. As will be explained in

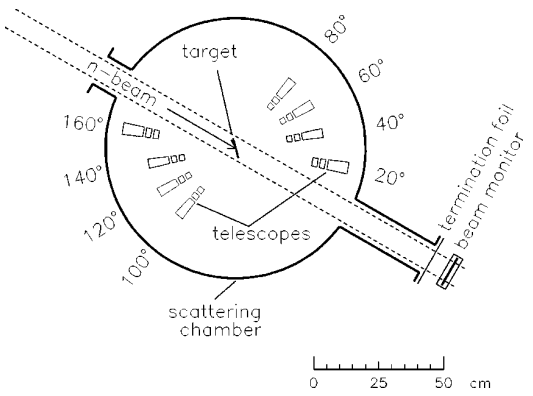

FIG. 3. MEDLEY detection array.

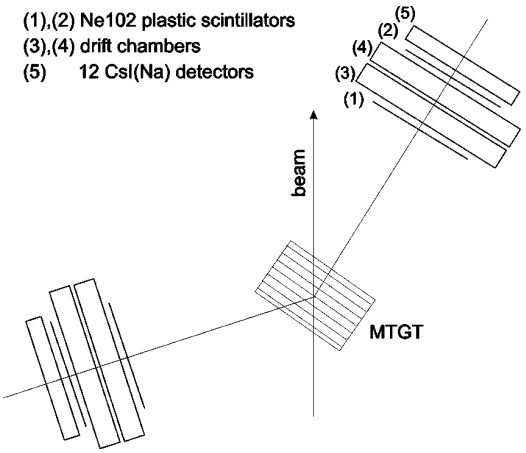

FIG. 4. Schematic view of SCANDAL setup.

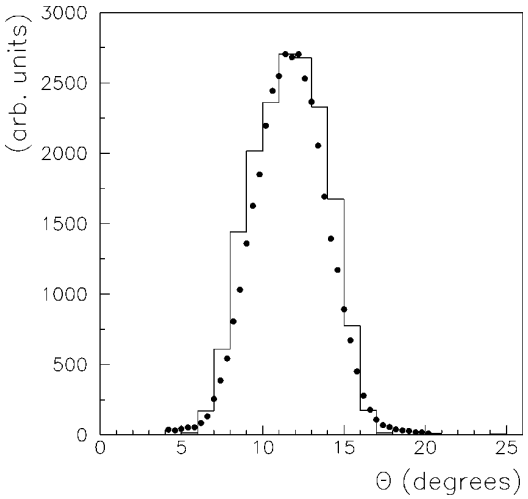

FIG. 5. Experimental distribution for emission angles of particles detected in a CsI detector (dots) compared with the simulation results (histogram).

Sec. III C, those events enabled us to apply an unambiguous normalization procedure for the extraction of the experimental cross sections, without requiring corrections for detection efficiencies, acquisition dead time, or beam intensity.

III. DATA REDUCTION

The data recorded using both detection systems were analyzed on a event-by-event basis in order to extract the energy spectra of the emitted particles. The procedures used for each setup are described in the next two subsections. The last subsection is dedicated to the cross section normalization method.

A. Event sorting for SCANDAL setup

The first step in the data analysis was to identify the target where the emission occurred inside the MTGT system. It was derived from the signals given by the multiwire proportional counters located between the targets. Then the trajectories calculated with the drift chambers enable us to determine the emission angle of each particle. In this way, both a target and an emission angle are associated with each recorded event.

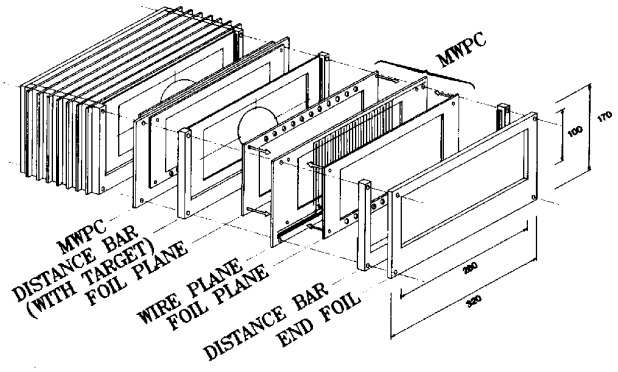

FIG. 6. Exploded view of the multitarget box.

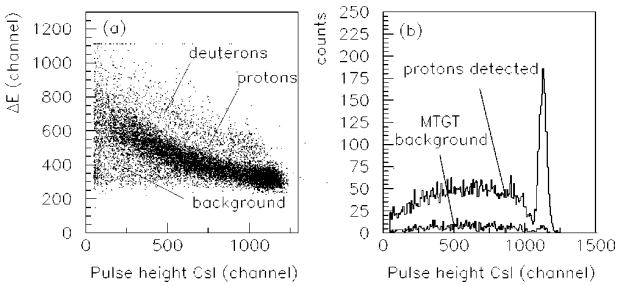

FIG. 7. (a) Two-dimensional scatter plot containing events recorded in the $10°-11°$ angular range using a CH_2 target. (b) Contamination in the recorded proton spectra due to reactions in the multitarget box.

The particle identification was made by the well known ΔE-E technique, using signals from the plastic scintillators and the CsI detectors. An example of such an indentification matrix is given in Fig. 7(a). It was obtained for the $10°-11°$ angular range, with a CH_2 target. The small contribution of the deuterons that reached the CsI detectors, and a part of the background, were rejected by applying two-dimensional contours around the proton band. Another source of background that is present in the proton band was due to protons from nuclear reactions that occurred inside other multitarget box elements, different from the targets of interest. Mainly, they were protons arising from *np* scattering reactions in the cathode foils. That additional pollution had to be rejected with another technique that consisted of recording "blank-target" events with the MTGT emptied of targets. Subtraction of the corresponding spectra to those recorded during "physics" runs was performed after normalization to the same neutron fluency and to the same data acquisition dead time. Examples of proton spectra associated to blank-target runs and physics runs are shown in Fig. 7(b).

With the CH_2 target, the energy calibration of the CsI detectors was done using protons produced in $H(n,p)$ reactions, for which the emission energies could be accurately calculated. In order to reject the contibution from $^{12}C(n,p)$ reactions, a pure carbon target was mounted together with the CH_2 target inside the MTGT. Data on both targets were recorded simultaneously, so that, after normalization to the same number of carbon nuclei as in the CH_2 target, events associated with $^{12}C(n,p)$ reactions could be subtracted from the spectrum obtained with the CH_2 target. Examples of spectra obtained with both targets are shown in Fig. 8, together with the proton spectrum resulting from the subtraction. The latter presents a peak and a tail, reflecting the incident neutron spectrum presented in Fig. 2. Both features correspond to $H(n,p)$ events induced, respectively, by 96 MeV projectiles and by neutrons of lower energies contained in the beam tail. The proton energy spectra were obtained after calibration of the CsI detectors and corrections for energy losses inside the setup. These corrections were determined by Monte Carlo simulations for which attention has been paid to reproduce accurately the experimental conditions. The proton energy threshold equals 30 MeV. This large value is related to the long flight (about 84 cm) through of air and detector materials of the system.

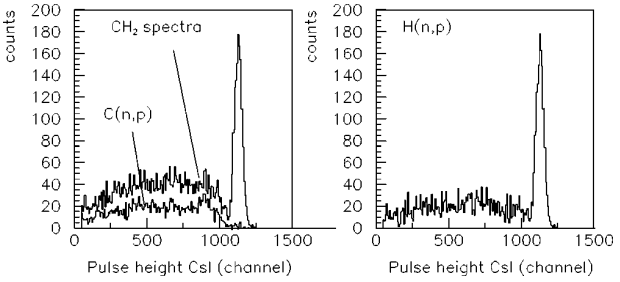

FIG. 8. Contribution of protons from the $^{12}C(n,p)$ reaction in the CH_2 spectra (left part). On the right, the spectra of protons from the $H(n,p)$ elastic scattering obtained after subtraction are shown.

B. Low-energy neutron rejection

In order to select only events induced by 96 MeV neutrons, the contribution of low energy neutrons had to be rejected. This has been done using a technique based on time-of-flight (TOF). The TOF values measured were the sum of the neutron TOF and the produced proton TOF. From the proton energy, the corresponding TOF can be calculated and subtracted from the total TOF measured. The result is the TOF of the neutrons that induced the reaction. In Fig. 9 are presented total time of flight, proton TOF, and neutron TOF spectra. The events associated with 96 MeV projectiles populate the peak centered at 78 nsec in the neutron TOF spectrum. This time corresponds to the experimental path of 1062.8 cm. A selection of that peak could then be easily applied.

In this way, spectra of protons from reactions induced by 96 MeV neutrons were constructed. In Fig. 10 two examples of such spectra obtained for $Pb(n,Xp)$ and $H(n,p)$ reactions recorded simultaneously with the MTGT system are presented. As it can be seen, for $H(n,p)$ elastic scattering reactions, after selection, only the peak at high energy remains in the spectrum, compared to that of Fig. 8, while the contribution originating from low-energy neutrons has been completely removed. This is a confidence check of the time-of-flight method used for the event selection. The statistics accumulated in both spectra presented in Fig. 10 corresponds to about 2 h of acquisition time.

C. Event sorting for MEDLEY setup

For the MEDLEY setup, the particle identification has been done using the well known ΔE-ΔE and ΔE-E techniques. Examples of two-dimensional plots obtained after energy calibration of each detector, for each particle type, are presented in Fig. 11. The top figure represents particles stopped inside the second silicon detector, while the lower one shows particles which reached the CsI scintillator.

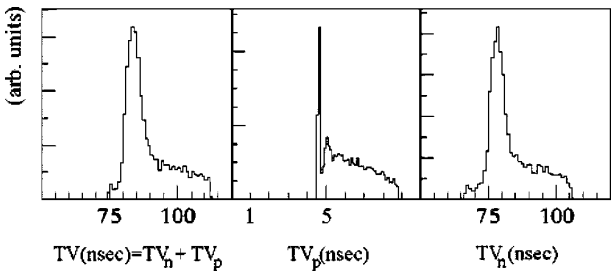

FIG. 9. Experimental determination of incident neutron time of flight.

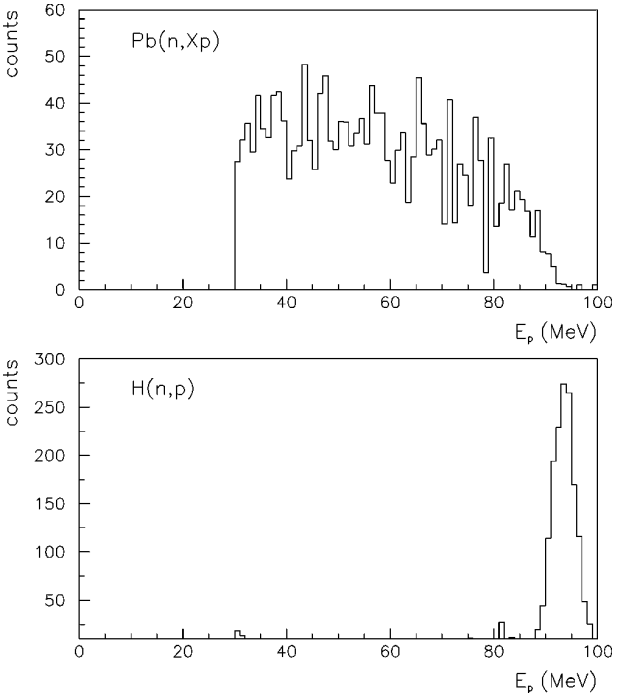

FIG. 10. Energy spectra of protons emitted in the angular range $10°-11°$ from neutron-induced reactions on a lead target (top) and from the elastic scattering reaction (bottom) at 96 MeV incident energy.

For calibration purposes, the points where each particle type start to punch through the silicon detectors were used. The corresponding energies were calculated with the detector thickness given by the manufacturer and the stopping power data from Ref. [11]. In addition, for the thin silicon detectors, the calibration was checked using 5.48 MeV α particles that stopped inside these detectors and that were emitted by a ^{241}Am source. The energy deposited in the CsI(Tl) detectors has been further calculated for each particle type using the energy losses inside the silicon detectors. Supplementary calibration points in the case of protons were provided by the $H(n,p)$ reactions on a CH_2 target. These points provide a cross-check of the corectness of the assumed silicon detector thicknesses. Even a very small error in the thickness would make the two sources of information, i.e., the energies calculated from the peaks and from the energy loss in the ΔE_1 and ΔE_2 detectors incompatible. The method and the different parameterizations used are presented in detail in Ref. [8].

Finally, the total energy of each emitted particle is deduced by adding the different energies deposited inside the three individual detectors of each telescope. Figure 12 shows energy spectra of p, d, t and α particles obtained from a lead target with the telescope placed at 40°. The arrows show the overlapping region between the second silicon and the CsI detector contributions.

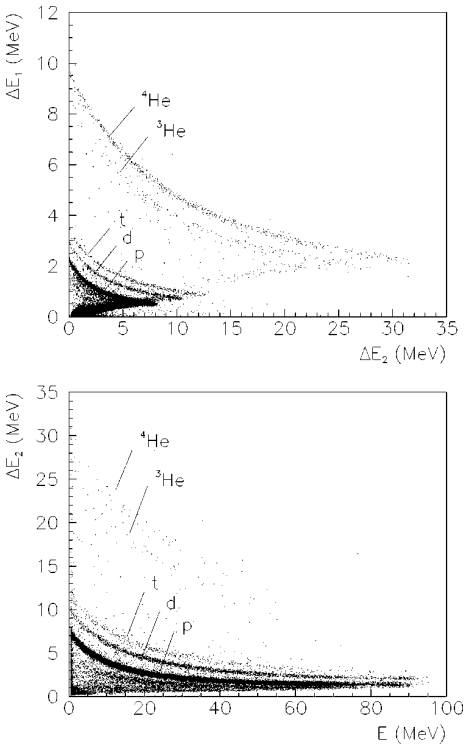

FIG. 11. Two-dimensional plots showing particles stopping in the second silicon detector (top) and in the CsI detector (bottom) of the telescope placed at 40° using a CH_2 target.

The detection thresholds are given by the thickness of the first silicon detector. It is about 2–3 MeV for the hydrogen isotopes and about 9 MeV for the helium isotopes, as it can be seen in Fig. 11. The spectra had to be further corrected for the particle energy loss inside the emission target. Those corrections were calculated using Monte Carlo simulations, with targets of about 50 μm thickness. The maximum correction value estimated is less than 4 MeV, for low-energy α particles. This shows that the corrections to be applied remain within reasonable limits.

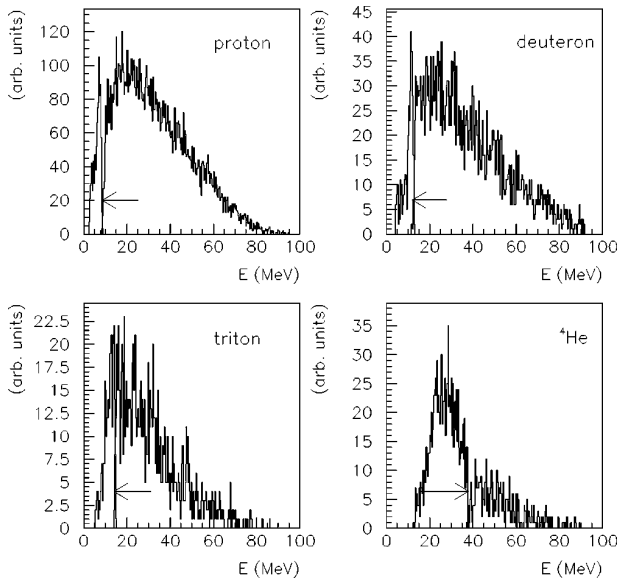

FIG. 12. Energy spectra for particles detected by the telescope placed at 40° with all neutrons from the beam incident on a lead target.

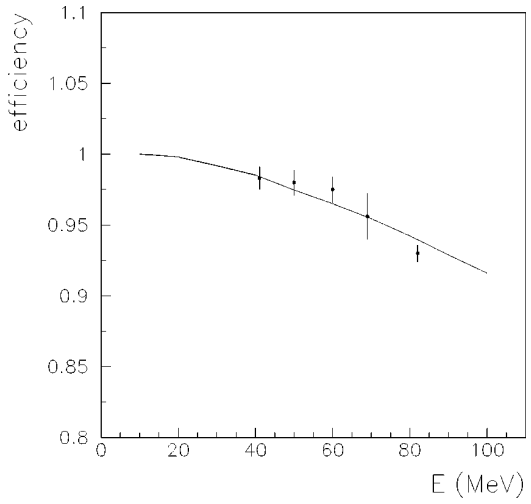

FIG. 13. Energy dependence of the CsI detection efficiency for protons. Simulation result (continuous line) is compared with the experimental values from Ref. [9].

The rejection of events associated with low-energy neutrons was done with the same procedure as for SCANDAL (Sec. III B). The background is dominated by protons arising from neutron-induced reactions inside the beam tube, at the entrance of the vacuum chamber. That contribution is subtracted by using the spectra accumulated during blank-target runs, applying a normalization to the same neutron fluency as for target-in runs, and taking into account corrections for the data acquisition dead time differences.

For the MEDLEY and SCANDAL setups, the CsI scintillator efficiency depends on the energy and type of the detected particle. Small corrections for the loss of light in the CsI detectors have then also to be applied. This effect is due to nuclear reactions that charged particles can undergo while slowing down inside the CsI. Corrections for this effect have been estimated for all charged particles, using reaction cross sections available in the GEANT library from CERNLIB [12]. Those estimations enable us to determine the CsI detector efficiency as presented in Fig. 13 for protons (continuous line). The loss of light inside the CsI detector is rather important for high energy protons and it is less pronounced for heavier particles. The detection efficiency at 100 MeV equals 91% for protons, 93% for deuterons, 95% for tritons, and 99% for α particles and it increases as the energy decreases. As shown in the figure, simulation results are in very good agreement with the experimental values from Ref. [9].

D. Cross section normalization

Due to the difficulty encountered when monitoring a neutron beam intensity, the absolute cross section normalization

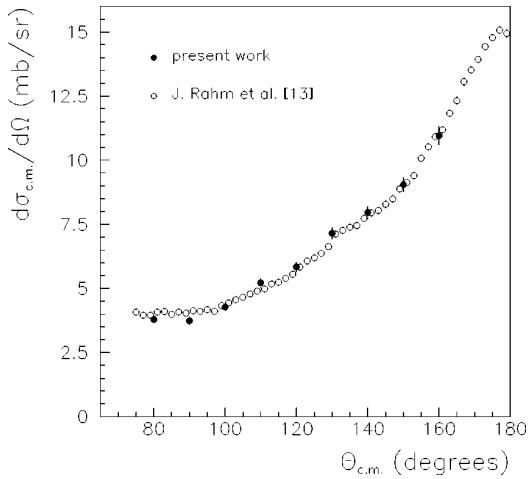

FIG. 14. Differential *np* scattering cross section at 96 MeV. The results obtained in the present work using the SCANDAL setup are compared to the data from Ref. [13].

in neutron-induced reactions is a notorious problem. In particular for our experiments, the uncertainty affecting the value given by the fission monitor equals 10%, which induces large uncertainties for the values of the measured cross sections. Therefore, the cross sections are measured relative to another one, considered as a reference. The reference cross section most often used is the $H(n,p)$ cross section, for which a recent measurement claims an absolute uncertainty of 2% [13]. We have used the values given in that reference to calculate the absolute cross sections. Nevertheless, in order to be able to apply the normalization procedure, we have to measure in the same experimental conditions the number of protons emitted in $H(n,p)$ reactions because that number intervenes in the normalization factor. When measuring that number, we took the opportunity to remeasure the angular distribution of the $H(n,p)$ cross section.

For that purpose, we used the SCANDAL setup. We determined the number of recoiling protons after subtraction of the $^{12}C(n,p)$ reaction component and the background contribution, following the procedure presented in Sec. III A. The angular range being limited in our measurements to $80°-160°$ for neutrons in the center of mass system, we extracted values for the other angles by fitting our data with a fourth-order Legendre polynomial. Then, considering other channels negligible at 96 MeV, we normalized the value of the deduced total *np* cross section to that given in Ref. [14]. Finally, we obtained the angular distribution, which is presented in Fig. 14 together with the experimental results of Ref. [13]. We observe a very good agreement between both. However, the uncertainties of the cross sections from Ref. [13] are significantly smaller than those in our experiment (2%). Indeed, for our data, the statistical errors are typically in the range 1.5–2.8 %, and the total uncertainty is estimated of the order of 4.1%, including the 1% contribution from the total *np* cross section [14]. The systematical errors affecting our results arise from the subtraction of reactions on carbon, from the integration over the *np* peak, and from the rejection of events induced by low-energy neutrons.

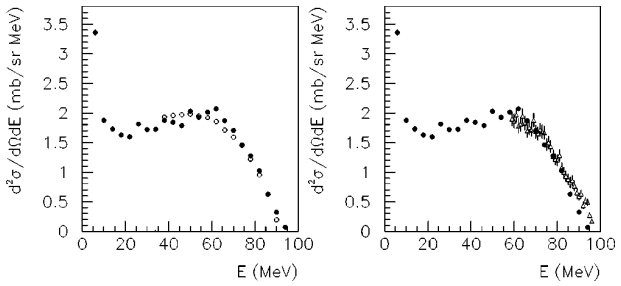

FIG. 15. Left panel: Fe(n,Xp) double-differential cross sections measured with MEDLEY setup at $\theta=20°$ (full circles), compared to the SCANDAL results (open circles). Right panel: same data compared to those from Ref. [15] (open triangles).

For the SCANDAL setup, the MTGT system was used to measure at the same time protons emitted from the target under study (iron, lead, or uranium) and in $H(n,p)$ reaction from the CH_2 target. The normalization procedure could then be applied without precise knowledge of the neutron flux. For the MEDLEY setup, all data have been normalized using the $H(n,p)$ scattering peak recorded by the telescope placed at 20° during separate runs with a CH_2 target.

For the proton emission, data recorded using the SCANDAL and MEDLEY setups were individually normalized, allowing two independent determinations of the cross sections for all targets studied. With this procedure, the estimated systematical uncertainties of the experimental cross sections are not greater than 5.1%. To calculate this value, we took into account the contributions from the number of target nuclei (2%), the solid angles calculated by simulations (0.75%), the beam monitor stability during the data taking (2%), the number of recoiling protons from the *np* reaction (3.7%), and the reference *np* cross sections (2%) according to Ref. [13].

IV. EXPERIMENTAL RESULTS

The double-differential cross sections of light charged particles were measured for three targets, Fe, Pb, U, with natural isotopic compositions, over an angular range of $20°-160°$. For the MEDLEY setup, the low energy threshold was 4 MeV for hydrogen isotopes, 12 MeV for ^{3}He, and 8 MeV for α particles. For the SCANDAL setup, it was 35 MeV for protons. Due to the detector energy resolution and the available accumulated statistics, a 4 MeV bin size has been choosen for the energy spectra.

In the left part of Fig. 15, proton double-differential cross sections measured independently with the MEDLEY setup (full circles) and with the SCANDAL setup (open circles) are compared. The spectra correspond to the Fe target and a 20° emission angle. Over the energy range covered by both detection devices, we observe a very good agreement. This shows that the systematical uncertainties induced by the cross section normalization are small. We obtained similar results for the other targets (Pb and U) and over the full angular range. In addition, it shows that the limited angular resolution of MEDLEY does not distort the distributions that

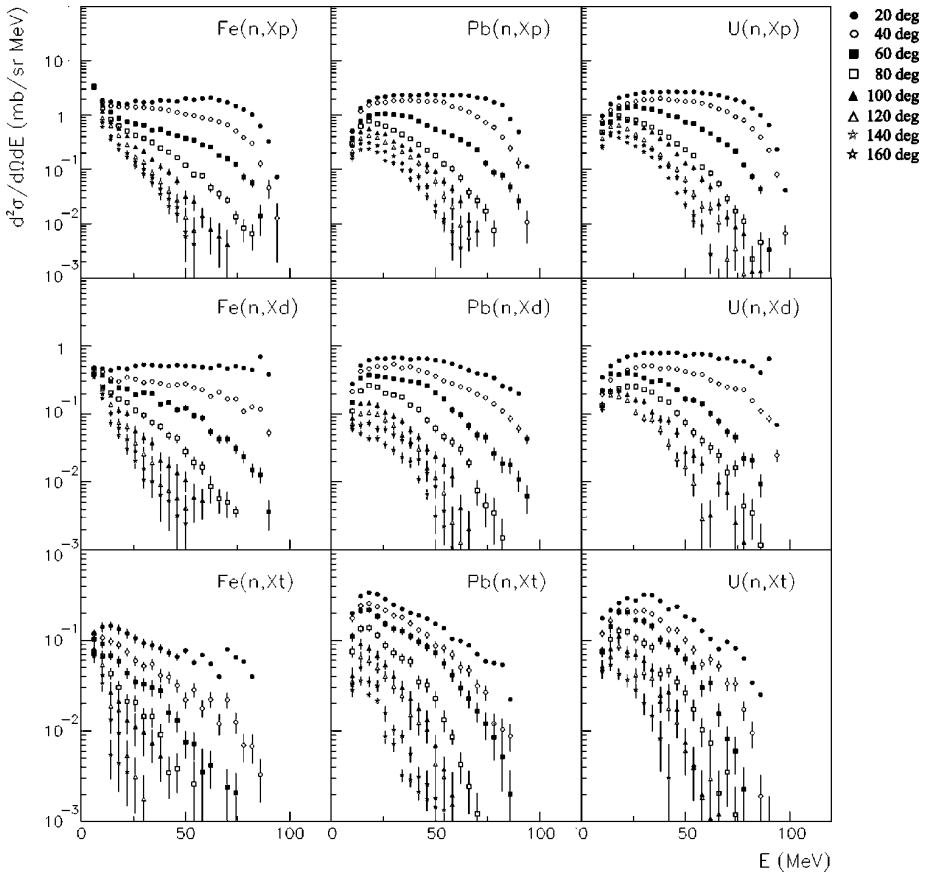

FIG. 16. Double-differential cross sections for p, d, and t (top, middle, bottom lines, respectively) produced in 96 MeV neutron-induced reactions on Fe, Pb, and U targets (left, middle, and right rows, respectively).

are comparable to that obtained with SCANDAL, for which the angular resolution is much better. The right part of Fig. 15 gives a comparison of the Fe(n,Xp) cross section measured at 20° with MEDLEY, with the data from Ref. [15] that were obtained using the magnetic spectrometer LISA. Very good agreement is found also between these two measurements. This shows the quality of our measurements and of the data analysis procedures employed. We observed a similar agreement for the Pb(n,Xp) cross sections.

In Fig. 16 are presented experimental double-differential cross sections for p, d, t (top, middle, bottom lines, respectively) produced in 96 MeV neutron-induced reactions on Fe, Pb, and U targets (left, middle, and right rows, respectively) and measured with the MEDLEY setup. In Fig. 17, for the same reactions, we report the complementary production cross sections of ^{3}He and α particles (top and bottom figures, respectively). The errors shown are purely statistical.

The general trend observed is a decreasing emission probability with increasing angle, over the full energy range. The angular distributions are slightly forward peaked at low energies, and at backward angles the emission probabilities are very low for energetic particles. In the case of the iron target, a quasi-isotropic component is observed at very low energy (0–10 MeV). This contribution is not present for heavier targets, for which Coulomb effects are much larger. For the rest of the energy range, the distributions obtained with the three targets are very similar in shape. For ^{3}He particles, distributions have been measured only for the iron target. Despite the long data acquisition time, no corresponding events were recorded for the other targets. This is related to the very low ^{3}He emission probability for heavy targets, which has been already observed in Ref. [16], where the ^{3}He production rate in 63 MeV proton-induced reactions on ^{208}Pb is about 10 times smaller than that for tritons.

For a more detailed analysis of the particle emission mechanisms, a separate inspection of angular and energy-differential distributions is needed. The angular distributions were obtained from double-differential cross sections by integration over the full energy range. For the energy distributions, we used the Kalbach systematics [17] in order to extrapolate the experimentally available angular range over the entire space. This can be done very accurately since the systematics described in Ref. [17] has been established using data measured in the same angular domain as in our experiments. Finally, the total production cross sections were derived for each particle type by integrating the corresponding energy-differential cross sections over the experimental energy range.

The energy-differential cross sections are presented in Fig. 18 for the iron and lead targets. The results obtained with the uranium target are very similar to those extracted for the lead one. By analyzing the spectra, we distinguish two regions. For energies greater than about 20 MeV, proton and deuteron spectra are very similar in shape, the emission probability decreasing slowly with energy for both targets. In the case of the iron target, the triton and ^{3}He spectra also show a similar behavior. For α particles, the spectra decrease very

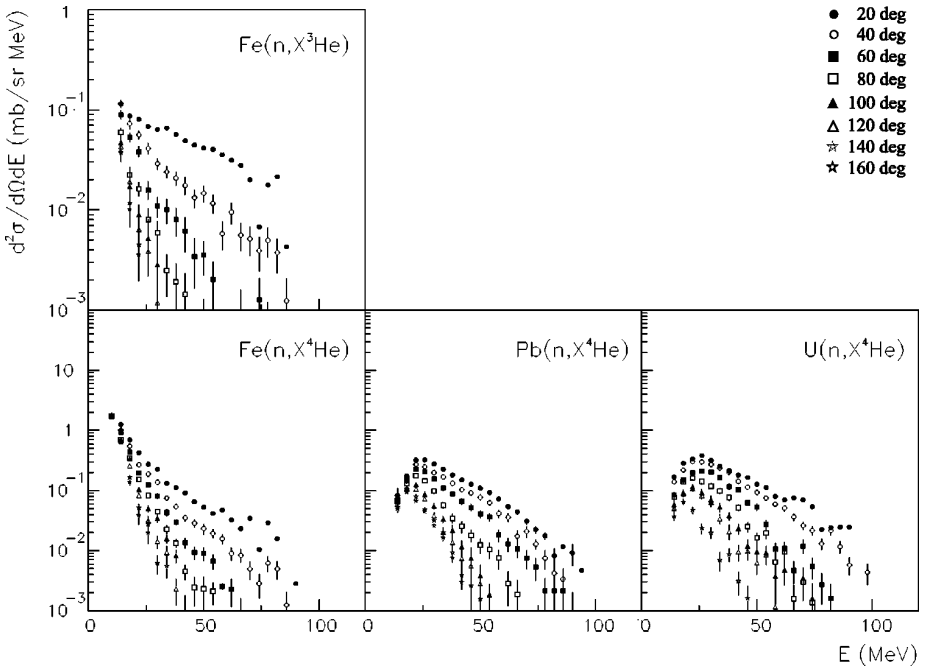

FIG. 17. Same as Fig. 16 for helium isotopes

rapidly with energy. For a given particle, the shapes of the iron and lead distributions are very similar. In this energy region, the emission probability distributions have steeper slopes for heavy particles than for light ones. Another important aspect to be noticed is the decreasing emission probability with the nucleon number of the emitted particle. However, an exception is observed for α particles for which the production cross sections in the low-energy part of the continuum region (20 MeV $< E <$ 35 MeV) are larger than those for tritons, suggesting a more complex mechanism for their emission. For low emission energies ($E <$ 20 MeV), a dominant contribution is observed for all particles in the case of the iron target. The shape of the distributions in Fig. 18, correlated to the slow variation of the amplitude with the emission angle observed in Figs. 16 and 17, suggests that these low energy particles are emitted mainly during the evaporation process of an excited nucleus. This component is not present in the spectra obtained with the lead and uranium targets because, for heavy targets, the emission of low-energy particles is strongly inhibited by Coulomb effects. This explains the low cross sections found in this energy range for both lead and uranium targets.

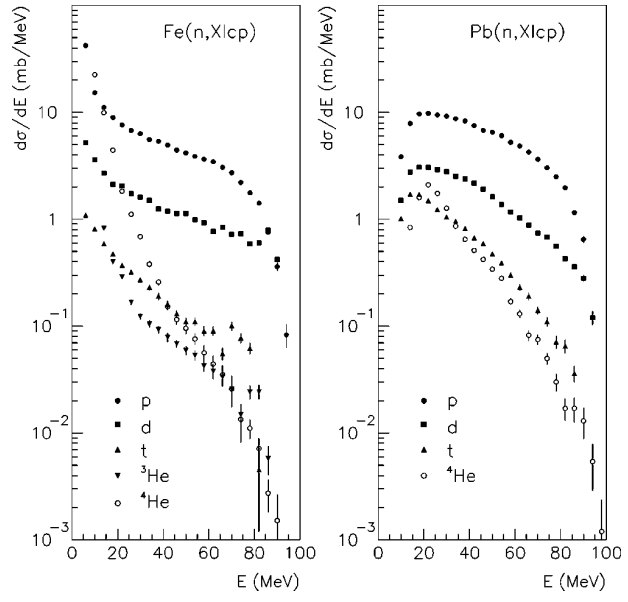

FIG. 18. Energy distributions for light charged particles produced in the 96 MeV neutron-induced reaction on iron and lead targets (left and right panels, respectively).

Figure 19 shows the angular distributions obtained by integrating double-differential distributions. Due to the detection thresholds, the integration domains range over 4–96 MeV for hydrogen isotopes, 12–96 MeV for ^{3}He, and 8–96 MeV for α particles. For all particles, the distributions are strongly forward peaked, suggesting that nonequilibrium processes are dominant for the reactions under study. An exception can be noticed for α particles in Fe(n,X) reactions, where the distribution is almost flat for angles larger than 50°. This suggests that the emission of α particles in the backward hemisphere could result mainly from evaporation processes. For a given particle, the angular distributions are more forward peaked for the heavier nuclei, suggesting that the nonequilibrium component increases with the nucleon number of the target.

This can also be observed from Table I, where integrated total cross sections (second column) and integrated nonequilibrium cross sections (third column) are presented as a function of the target mass, for all particles. Depending on the system considered, the nonequilibrium cross sections were extracted with different methods. For the Fe(n,Xlcp) reactions (lcp refers to light charged particles), the low-energy contribution in the energy-differential cross sections (Fig.

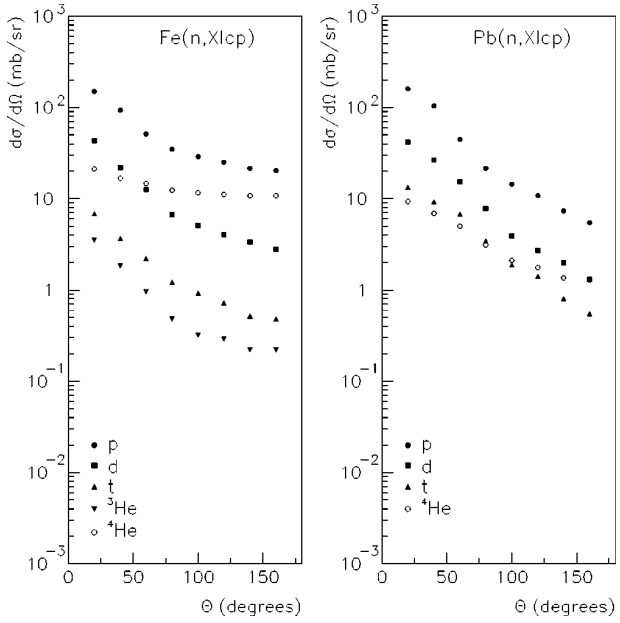

FIG. 19. Angular distributions for light charged particles produced in the 96 MeV neutron-induced reaction on iron and lead targets (left and right panels, respectively).

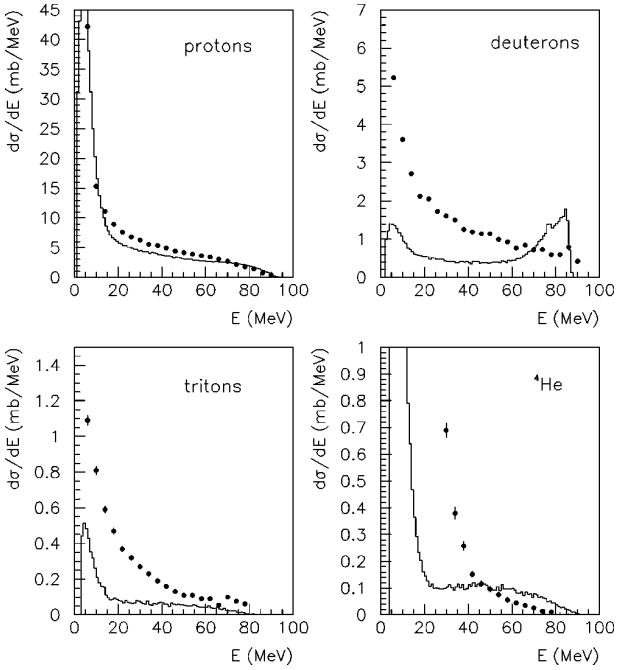

FIG. 20. Energy-differential cross sections calculated using the GNASH code for the ^{56}Fe(n,Xlcp) reaction at 96 MeV (histograms) compared with the present experimental results (points).

18) was fitted with an exponential function and its integral was then subtracted from the total cross section for each particle. For lead and uranium targets, we made the assumption that all particles were emitted during nonequilibrium processes, i.e., in a first approximation, the rather small contribution of evaporated particles expected at low energy is neglected.

The values from Table I show that for all targets studied, more than 30% of the total light-charged-particle production are particles heavier than protons. This is an important aspect to be pointed out, because, with such a production rate, the contribution of these particles should not be neglected.

TABLE I. Total light-charged-particle integral cross sections and estimated contributions from the nonequilibrium emission in neutron-induced reactions at 96 MeV.

Reaction	Total cross section (mb)	Non-equilibrium cross section (mb)
Fe(n,Xp)	584±29.2	326
Pb(n,Xp)	485±24.3	485
U(n,Xp)	589±29.5	589
Fe(n,Xd)	131±6.5	96
Pb(n,Xd)	137±6.9	137
U(n,Xd)	170±8.5	170
Fe(n,Xt)	21±1.1	15
Pb(n,Xt)	53±2.7	53
U(n,Xt)	54±2.8	54
Fe(n,X^3He)	10±0.5	7
Fe(n,X^4He)	167±8.3	31
Pb(n,X^4He)	45±2.2	45
U(n,X^4He)	52±2.6	52

V. THEORETICAL CALCULATIONS

At this moment, the exciton model [2] is the most commonly used to calculate the preequilibrium emission in nucleon-induced reactions at intermediate energies. This model assumes that the excitation process takes place by successive nucleon-nucleon interactions inside the nucleus. Each interaction produces another exciton, leading the system to the final state of statistical equilibrium through more complex states. Occasionally a particle can receive enough energy to leave the system and subsequently be emitted. The resulting preequilibrium spectrum is the sum of the contribution from each state. Particles emitted in the early stages have more energy than those emitted in the later ones. In the framework of this model, only energy distributions of emitted particles can be calculated.

The GNASH code [6] is one example that uses the exciton model to calculate the preequilibrium component. It is able to calculate spectra for nucleons and complex particles. In this code, the equilibrium contribution is calculated using the Hauser-Feshbach formalism [18]. Cross sections that were evaluated with GNASH are at present implemented in MCNPX, a code widely used for specific applications such as medical or engineering studies. In Figs. 20 and 21, we compare, respectively, the ^{56}Fe(n,Xlcp) and ^{208}Pb(n,Xlcp) energy-differential cross sections of the present work (points) to the GNASH predictions (histograms) obtained with MCNPX. The maximum value in the α-particle spectrum for the iron target

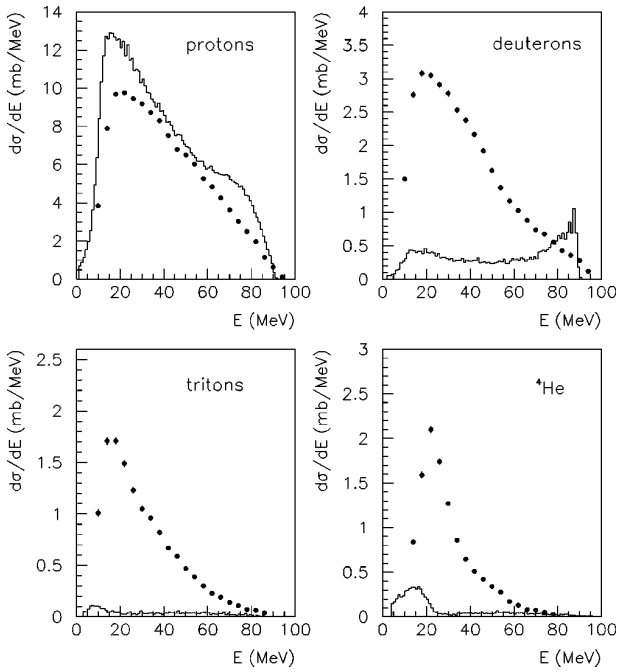

FIG. 21. Same as in Fig. 20 for the ^{208}Pb(n,Xlcp) reaction.

has been set to 1 mb/MeV for better visualization. While the proton emission is relatively well described, we observe that the production of complex particles is strongly underestimated.

This comparison suggests that significant improvements are needed in the original exciton model in order to increase its prediction level concerning the cluster emission. To modify it according to this request, a first approach was proposed in 1973 by Ribanský and Obložinský [3]. It introduces the probability of a cluster formation during the nucleon-nucleon interactions inside the target. In 1977, Kalbach formulated a second approach [4], which includes contributions from direct pick-up and knock-out mechanisms. Both approaches have been tested in the past against data and they lead to a satisfactory agreement with the experimental results [4,5], despite their completely different basic assumptions. Nevertheless, conclusions about their global predictive power were limited, mainly because a restricted number of experimental results were available at that moment. In order to get a wider view on their predictive capabilities, we performed calculations with both approaches for the ^{56}Fe(n,Xlcp), ^{208}Pb(n,Xlcp), ^{238}U(n,Xlcp) reactions at 96 MeV, but also for other projectiles, at different incident energies and for other targets, for which experimental data are available in the literature. In the following, we will give a basic description of both approaches and discuss the comparisons of the calculations with a set of data that cover a wide domain of reaction entrance-channel parameters.

A. Cluster formation probability in nucleon-nucleus reactions

Difficulties were encountered in the original exciton model proposed by Griffin to reproduce the experimental distributions of complex particles, which was then modified first by Ribanský and Obložinský [3]. The modification consists of the introduction in the particle production rate expression of a multiplicative term containing the cluster formation probability γ_β where β is the type of the emitted particle. The physical meaning of this parameter has been given in Ref. [19] in the framework of the coalescence model. This approach assumes that complex particles are formed during the preequilibrium stage from excited nucleons that share the same volume in the momentum space. In this way, for example, an excited proton and an excited neutron can coalesce into a deuteron if the transverse momentum between both is small. The drawback of this approach is its limited predictive power since the parameter γ_β has to be adjusted in order to reproduce as well as possible the amplitude of the experimental energy-differential distribution under study. Nevertheless, it is always interesting to compare the tuned results of a model with experimental data.

The formation probability γ_β of a complex particle β is given as a function of the radius of the coalescence sphere P_0 in the momentum space by the formula:

$$\gamma_\beta = \left|\tfrac{4}{3}\pi(P_0/mc)^3\right|^{p_\beta - 1}, \tag{1}$$

where p_β is the number of nucleons of the emitted particle. Of course, $\gamma_\beta = 1$ in the case of the emission of a nucleon. According to Eq. (1), γ_β and thus, P_0 are the free parameters of the model.

The following expression for the cluster formation probability has been proposed in Ref. [20]:

$$\gamma_\beta = (p_\beta)^3 (p_\beta/A)^{p_\beta - 1}, \tag{2}$$

where A is the mass of the target nucleus. This approach is implemented in the latest version of the code GEANT [21], which is intensively used for simulations among the physics community. However, calculations from Ref. [20] strongly overestimates deuteron, triton and ^{3}He distributions, while the production rates for α particles are underestimated. This shows that the calculation of the cluster formation probability according to Eq. (2) is not very appropriate. For this reason, calculations in this work have been done with the PREEQ program [22], keeping the cluster formation probability as a free parameter. A complete explanation about the different parameters of the model and the method we applied to calculate them can be found in Ref. [5]. In the forthcoming discussion, we will focus onto the cluster formation probability γ_β because of its particular importance for the model predictions.

In the first step of our investigation, we performed calculations with PREEQ for the 96 MeV neutron-induced reactions presented in this work. We determined two sets of values for the γ_β parameter by normalizing individually the calculated energy distributions to the Fe(n,X) and Pb(n,X) experimental data. For those reactions, PREEQ results (histograms) and data (points) are presented in Fig. 22 for ^{56}Fe and ^{208}Pb targets. We have to remind readers that the model calculates only the preequilibrium component of the emission spectra, so that in our comparison, we should not consider either the low-energy region populated with particles evaporated by excited nuclei or the high-energy region where di-

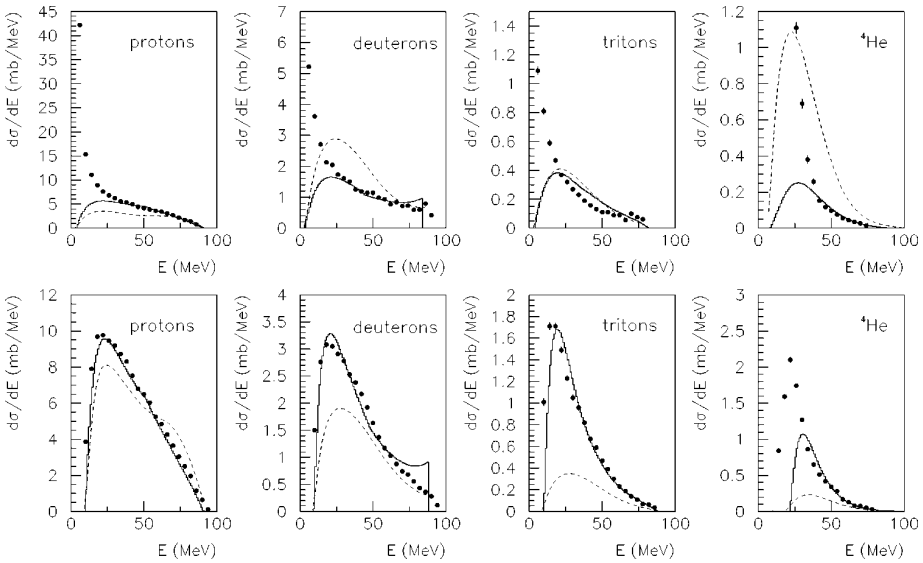

FIG. 22. Energy-differential cross sections calculated using PREEQ (histograms) and PRECO-2000 (dashed line) for ^{56}Fe(n,Xlcp) (top) and ^{208}Pb(n,Xlcp) (bottom) reaction at 96 MeV, compared with the experimental results of the present work (points). Maximum value in the plotting scale for the α particle in the case of the iron target has been set to 1.2 mb/MeV for a better visualization.

rect reactions are supposed to be dominant. Considering those restrictions, we observe that the shapes of the calculated distributions are in good agreement with the experimental results. As expected, the model fails in reproducing the very-low-energy component of the iron spectra. For all particles in the ^{208}Pb(n,X) reactions, except α particles, the calculated preequilibrium contribution accounts for almost the entire energy range, showing that almost all particles are emitted during the preequilibrium stage. For α particles, the preequilibrium processes are still underestimated by PREEQ in the low-energy region of the continuum. By comparison with the GNASH predictions presented in Figs. 20 and 21, we clearly see that this approach improves dramatically the original exciton model, for all particles.

For protons, for which the γ_β parameter equals 1 and does not need to be adjusted, the amplitudes of the distributions are very well described by the model in the energy range where it is applicable. It must be pointed out that only the primary preequilibrium contribution is calculated by this code. The good agreement found for protons suggests that the second-chance preequilibrium component is very small, in agreement with the calculations from Ref. [23]. For complex particles, no conclusion about the predictive capabilities of PREEQ can be drawn at the moment, the amplitude of the distributions being obtained by adjusting the γ_β parameter in order to get good agreement with the experimental data. Therefore, the next step in our analysis was to check the stability of this parameter while changing the entrance channel, i.e., the incident energy and the projectile, for a target nucleus in the mass region $A=208$. For that aim, using the values of the cluster formation probabilities previously obtained for the 96 MeV ^{208}Pb(n,X) reactions, we calculated the energy-differential cross sections for 39 MeV ^{209}Bi(p,X) and 63 MeV ^{208}Pb(p,X) reactions. In Fig. 23, the resulting PREEQ calculations (histograms) are compared with the experimental data (points) measured at 39 MeV with a ^{209}Bi

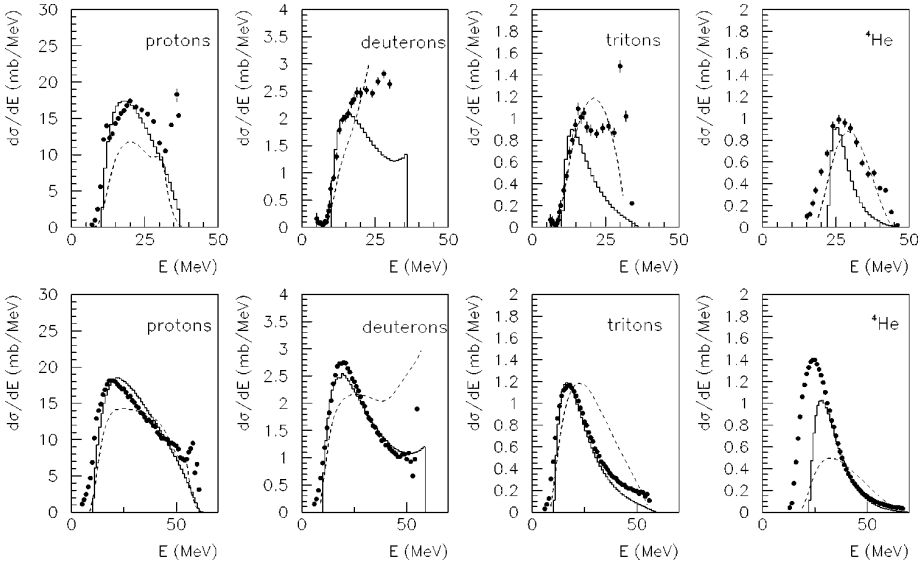

FIG. 23. Energy-differential cross sections calculated using PREEQ (histograms) and PRECO-2000 (dashed line) for ^{209}Bi(p,Xlcp) reactions at 39 MeV (top) and ^{208}Pb(p,Xlcp) reactions at 63 MeV (bottom), compared with the experimental results from Refs. [24,16] (points).

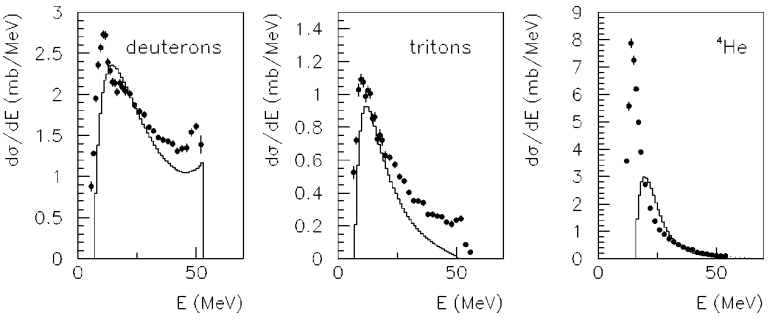

FIG. 24. Energy-differential cross sections calculated using the PREEQ code (histograms) for ^{120}Sn(p,Xlcp) reaction at 62 MeV compared with the experimental results from Ref. [24] (points).

target [24] (top panels) and to the data measured at 63 MeV with the ^{208}Pb target [16] (bottom panels). Over the energy domain where the model is applicable, we observe again a good agreement between the calculations and the experimental results. In addition and especially at 39 MeV, we see that the noncalculated direct process contribution is dominant.

From this study, we conclude that the free parameter γ_β depends neither on the projectile type (neutron or proton) nor on the incident energy and that, once the cluster formation probability has been adjusted to the reaction system, the model has a good predictive power for reactions with the same target. To go further, we have now to investigate its possible dependence with the target mass. Since we have just determined the formation probability γ_β for two target nuclei with masses $A=56$ and $A=208$, we choose an intermediate target with a mass $A=120$ for which experimental data were measured, i.e., the ^{120}Sn(p,Xlcp) reaction at 62 MeV incident energy [24]. With the same method described previously, we calculated the new set of γ_β values associated to the ^{120}Sn target. In Fig. 24, we compare the corresponding PREEQ calculations (histograms) to the data (points). As for the other targets, we observe the same global good reproduction of the data in the preequilibrium energy region.

In Table II, we gather the values of the cluster formation probabilities, as well as the related P_0 parameters, obtained for the three target nuclei $A=56$, $A=120$, and $A=208$ and for each complex particle type. The formation probability for each particle type is also represented as a function of the target mass in Fig. 25.

TABLE II. Cluster formation probability in nucleon-induced reactions on three targets and corresponding radii of the coalescence sphere in the momentum space.

Target	Emitted particle	Formation probability γ_β	P_0 (MeV/c)
^{56}Fe	d	0.0278	175
	t	0.0065	250
	^{3}He	0.0060	246
	^{4}He	0.0052	322
^{120}Sn	d	0.0230	164
	t	0.0050	238
	^{4}He	0.0035	304
^{208}Pb	d	0.0186	153
	t	0.0035	225
	^{4}He	0.0018	286

We observe that for a given particle, the formation probability and then the coalescence sphere radii are smaller for heavier nuclei. Under the assumption of phase space relations, a smaller P_0 value means a larger volume inside the nucleus from which the particle is emitted. This volume is then larger for heavier nuclei. In addition, for a given target nucleus, the figure shows that the formation probability decreases as the number of nucleons of the emitted particle increases. This could be explained by the fact that it is less probable, for example, for three nucleons to coalesce in order to form a triton, than for two nucleons to form a deuteron. The formation probability of deuterons is much larger than that for other complex particles, suggesting that the most probable mechanism is the pick-up of one nucleon by another.

The presently obtained values are in rather strong disagreement with those from Ref. [20]. Thus, for the ^{208}Pb(p,Xlcp) reaction, the γ_β probability calculated according to Eq. (2) is 0.077 for deuterons, 0.0056 for tritons, and 0.00046 for α particles. As it can be observed, the values for hydrogen isotopes are larger than those obtained in this work, leading to the overestimation found in Ref. [20] for the production of these particles. On the other hand, the values for α particles are smaller than ours and thus the distributions calculated in Ref. [20] are systematically below the experimental results.

Another interesting aspect to point out is that the presented P_0 values obtained for nucleon-nucleus reactions are

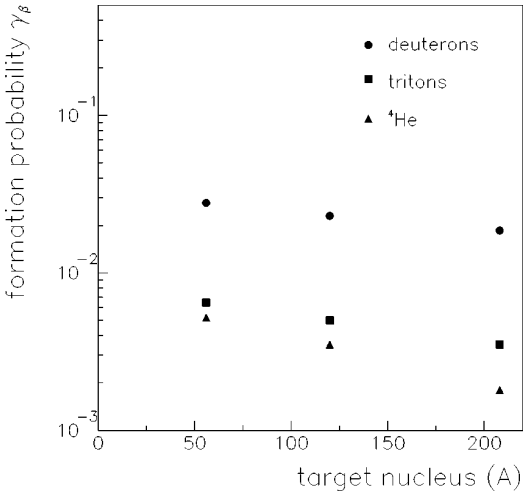

FIG. 25. Formation probability for each complex particle versus target mass.

in the same range as those extracted for reactions induced by complex projectiles (deuterons, ^{3}He, and α particles) at intermediate energies [25] and for reactions induced by heavy ions at high energies [26,27]. This suggests a weak dependence of this parameter with the projectile mass and energy.

To conclude, compared to the original exciton model existing in the GNASH code, the approach proposed by Ribanský and Obložinský and implemented in the PREEQ code improves greatly the predictions concerning complex particle production rates in preequilibrium processes, with the adjustement of one free parameter depending only on the target mass.

B. Exciton model and direct reactions

In order to modify the original exciton model concerning the complex particle emission in nucleon-induced reactions, a completely different approach has been proposed by Kalbach [4]. It is based on the fact that direct reactions such as the nucleon pick-up process and the cluster knock-out process are not included inside the exciton model. Therefore this approach calculates their associated contributions separately and adds them to the preequilibrium component calculated with the original exciton model. Contrarly to the PREEQ program, this approach does not use any multiplication factor in the particle production rate expression, and thus it has no adjustable parameter. In other words, this approach proposes to replace the cluster formation probability introduced in Ref. [3] by the contribution of direct reactions. This modification is taken into account in the code PRECO-2000 [28] that calculates nucleon and complex particle nonequilibrium spectra in nucleon-induced reactions using (i) the two-component version of the exciton model and (ii) phenomenological models for direct reaction processes. This code is open to the community via the Data Bank Computer Program Services of the NEA. The same approach has been recently implemented in the TALYS code [29], which is still under development and therefore not yet available to the community.

Calculations have been done with the PRECO-2000 code using the set of global parameters recommended by the author for the contribution of direct processes. Details can be found in Ref. [28]. For the exciton model contribution, the same values for specific parameter as for the PREEQ calculations have been used. In Fig. 26 an example of the PRECO-2000 results obtained for the α-particle emission in ^{56}Fe(n,X) reactions at 96 MeV is given. The three individual contributions in the nonequilibrium spectrum are displayed. We observe that the very low contribution of the preequilibrium processes predicted by the exciton model (dash-dotted line) is compensated by the other two direct processes now included, i.e, the pick-up of three nucleons (dashed line) and the knock-out of α particles (dotted line), which are assumed to be preformed inside the nucleus. The total nonequilibrium spectrum is obtained by summing all these contributions.

Following the same procedure as in the Sec. V A, calculations have been performed first for the data that we measured at 96 MeV. The results are presented in Fig. 22 for the ^{56}Fe(n,Xlcp) and ^{208}Pb(n,Xlcp) reactions (dashed lines). The

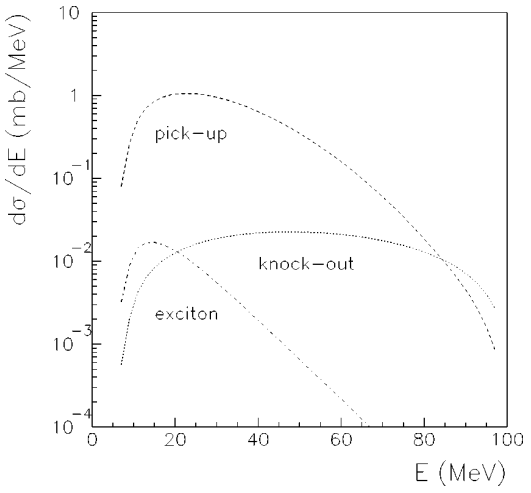

FIG. 26. Different mechanism contributions in the nonequilibrium α-particle spectrum calculated using the PRECO-2000 code for the ^{56}Fe(n,X) reaction at 96 MeV.

disagreement with the experimental distributions is rather strong for both systems. For the iron case, the nonequilibrium complex particle production is overestimated while the proton emission is underestimated. For the lead target, composite ejectile rates are underestimated, as well as the proton distribution. In addition, for a given target, the disagreement seems to become more important as the mass of the emitted particle increases. Even if the model in PRECO-2000 code predicts more particles in the preequilibrium region than GNASH does, experimental shapes and amplitudes are not as well reproduced as with the PREEQ code. In the case of nucleon ejectiles, the secondary preequilibrium emission can be considered in this code. However, this contribution was not included in the calculated spectra in order to get the same calculation conditions as in Sec. V A This can explain the underestimation found for energies around 20 MeV in the proton spectra.

Despite its bad data reproduction observed at 96 MeV, we tested PRECO-2000 again by changing the incident particle and energy of the entrance channel. Doing so, we found a better agreement as it can be seen in Fig. 23, where the predictions of the PRECO-2000 code (dashed lines) for the 39 MeV ^{209}Bi(p,Xlcp) (top panels) and the 63 MeV ^{208}Pb(p,Xlcp) (bottom panels) reactions are compared to the experimental results from the Refs. [24,16] (points). Even if a tremendous disagreement still exists at low incident energies, the model predictions are sensibly improved with proton projectiles compared to those related to incident neutrons at 96 MeV. This suggest that the PRECO-2000 predictions strongly depend on the incident energy and the projectile type. That latter aspect can be studied in more detail since data with both neutron and proton projectiles are available for ^{208}Pb at the same incident energy (63 MeV). In Fig. 27, are presented the experimental energy distributions of deuterons for both reaction types (top left panel): (i) (p,xd) [16] (open circles), and (ii) (n,xd) [30] (full circles). The experimental results are very similar in shape and in amplitude for both projectiles. The corresponding PRECO-2000 calculated distributions are

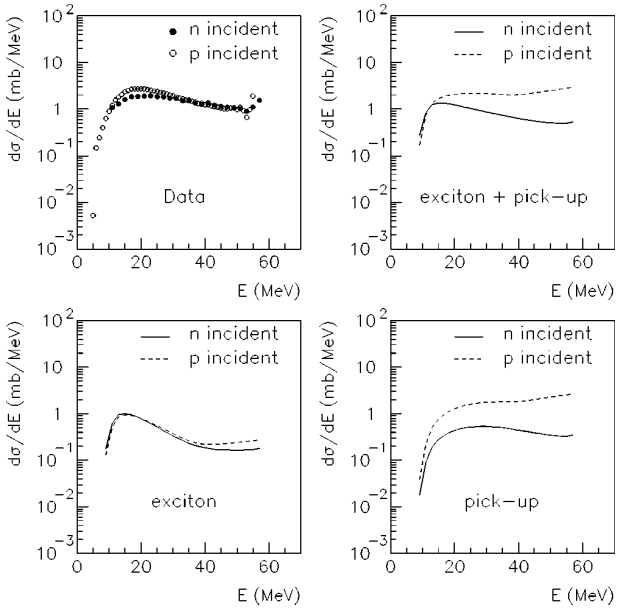

FIG. 27. Deuteron emission in proton- and neutron-induced reactions on ^{208}Pb at 63 MeV. Experimental results (top left panel) are compared to the distributions calculated using PRECO-2000 code (top right panel). Contributions from preequilibrium (exciton model) (left bottom panel) and nucleon pick-up reaction (bottom right panel) are presented.

shown in the top right panel. As it can be seen, the theoretical distributions are very different when changing the incident nucleon type (neutron or proton), in a strong contradiction with the data. This disagreement does not originate from the preequilibrium contributions calculated by the exciton model because we checked that the corresponding distributions are similar for neutron- and proton-induced reactions (bottom left panel). On the other hand, the calculated contributions for the nucleon pick-up process (right bottom panel) are very different from each other and, since this mechanism is dominant, this difference generates the disagreement observed with the data. To conclude, the contribution of direct reactions as calculated in PRECO-2000 strongly depends on the incident particle type, contrary to the experimental data. This effect constitutes, of course, a shortcoming of the model.

C. Particle emission at equilibrium

Compared to PRECO-2000 simulations, the calculations performed with the code PREEQ have shown that this last approach allows a better description of the particle emission in the preequilibrium stage. For that reason, the results obtained with this model will be used in the further discussion.

As already discussed previously, the results presented in Figs. 22 and 23 suggest that for heavy targets, almost all particles are emitted during the preequilibrium phase of the reaction. Except for low-energy α particles, the PREEQ calculated distributions allow a good description of the experimental results over the full energy range, showing that the contribution of the evaporation process should be small. On the other hand, for light target nuclei (Figs. 22 and 24), the low-energy component of the experimental distributions suggest that the particle emission at equilibrium is rather important.

In this section, we propose to determine the contribution of the evaporation process. This component can be calculated separately assuming that it results from two different sources. The first source is the so-called "pure evaporation" and concerns the evaporation from the compound nucleus that has reached a statistical equilibrium. In Ref. [31], its contribution is given by a fraction $f_{EQ}(E)=[1-f_{PE}(E)]$ of the total reaction cross section, where $f_{PE}(E)$ is the fraction of the preequilibrium emission, considering n, p, d, t, ^{3}He, and α particles, and E is the composite nucleus excitation energy. We determined this fraction using the preequilibrium spectra calculated with the PREEQ code for all ejectile types. The resulting value obtained for the 96 MeV ^{56}Fe(n,X) reactions is $f_{PE}(E)=0.993$, in agreement with that estimated for 62 MeV ^{54}Fe(p,X) reactions in Ref. [32]. That value very close to 1 shows that almost the entire reaction cross section is available for the preequilibrium emission, and that the evaporation process of a compound nucleus represents a very small component with an associated value of $f_{EQ}(E)=0.007$. The second source of the equilibrium component, which can be considered is the evaporation from a residual nucleus left in an excited state just after the preequilibrium emission has occurred. In order to estimate the excitation energy of such a nucleus and its formation probability after the preequilibrium emission of each outgoing particle type, again, we used the energy differential distributions previously calculated with PREEQ. The residual nucleus excitation energy is given by the formula $U=E-B_\beta-e\beta$, where B_β and e_β are the binding energy of the emitted particle β and its emission energy, respectively, and E is the excitation energy of the compound nucleus. Having determined that quantity, the evaporation spectra are further calculated using the Hauser-Feshbach formalism [18]. Particles are emitted until the evaporation process is no longer energetically possible and the nucleus remaining energy is released in the form of γ rays.

The results obtained for the 96 MeV ^{56}Fe$(n,X$lcp) reactions are given in Fig. 28 (dotted lines), together with the preequilibrium component calculated with PREEQ as described in Sec. V A (dashed lines). The total particle emission spectrum determined by summing both mechanism contributions (continuous line) is also presented and compared to the experimental data (points). The agreement found over the full energy range is relatively good, except for helium isotopes around 20 MeV, where the calculated distributions are below the experimental results. The same effect has been found for the ^{208}Pb$(n,X^4$He) reaction, showing that the preequilibrium contribution for helium isotopes is underestimated in this energy region for both light and heavy targets. For hydrogen isotopes the introduction of the evaporation contribution allows a good description of the particle emission over a wide energy range.

D. Angular distributions

To complete our analysis about the models, we would like to compare the experimental angular differential cross sec-

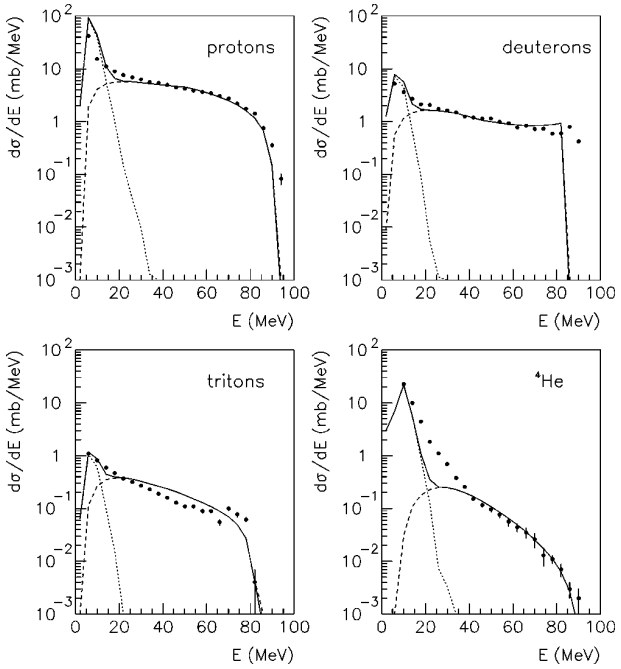

FIG. 28. Calculated preequilibrium and evaporation contributions (dashed and dotted lines, respectively) in the particle emission spectra for the 96 MeV ^{56}Fe(n,Xlcp) reaction, compared to the experimental results of the present work (full circles). The calculated total distributions (sum of preequilibrium and evaporation spectrum) are presented as continuous lines.

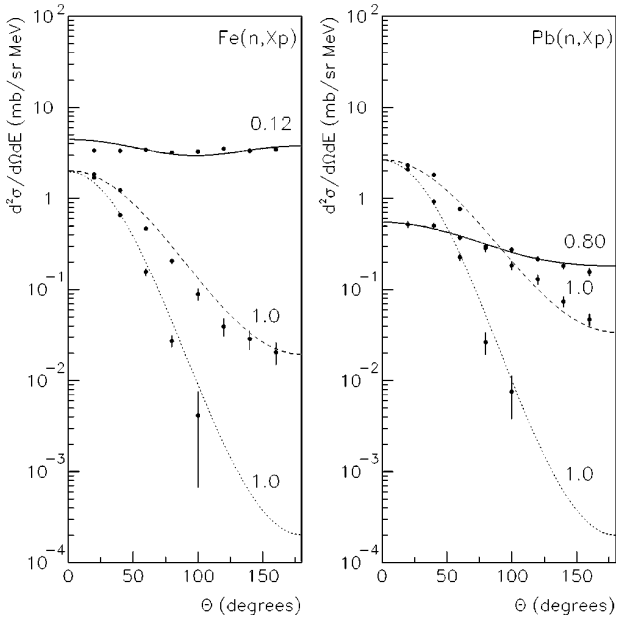

FIG. 29. Double-differential distributions calculated using the parameterization from Ref. [17] (lines) for proton emission in 96 MeV neutron-induced reactions on ^{56}Fe and ^{208}Pb compared with the experimental results (points). The continuous, dashed, and dotted lines correspond to the 8–12 MeV, 40–44 MeV, and 68–72 MeV emission energy ranges, respectively. The contribution of the preequilibrium emission in the total cross section (f_{PE} factor) for each domain is also given near the corresponding distribution.

tions to the theoretical ones. While the exciton model is largely used to calculate angle integrated energy spectra, the determination of angular distributions is out of its capabilities. In order to overcome this difficulty, several approaches involving modifications of the exciton model have been proposed, as in Ref. [33]. However, most of them contain serious approximations or induce computational complexities and they can be applied only for a limited set of reaction configurations. For this reason, a phenomenological approach proposed in Ref. [17] is often preferred to study the continuum angular distributions. It is based on a systematical study of a wide variety of experimental data. The parameterization established for the double-differential cross section as a function of the total energy-differential cross section is given by the equation:

$$\frac{d^2\sigma}{d\Omega de} = \frac{1}{4\pi}\frac{d\sigma}{de}\frac{a}{\sinh(a)}[\cosh(a\cos\theta) + f_{PE}\sinh(a\cos\theta)]. \tag{3}$$

In this expression, θ is the emission angle in the center of mass frame, and the term a is the slope parameter depending on the incident particle type and energy, the target nucleus and the exit channel. It can be calculated using the procedure described in Ref. [17]. The f_{PE} parameter is the fraction of particle emission apart from equilibrium. It will be called further the fraction of preequilibrium emission and it is calculated using the formula

$$f_{PE} = \frac{(d\sigma/de)_{PE}}{(d\sigma/de)} = \frac{(d\sigma/de)_{PE}}{(d\sigma/de)_{PE} + (d\sigma/de)_{EQ}}, \tag{4}$$

where the *PE* and *EQ* symbols refer respectively to preequilibrium and equilibrium emissions. Using the energy-differential cross sections for these two processes calculated in Secs. V A and V C, the double-differential cross sections are calculated according to Eq. (3). In Fig. 29 are presented the resulting angular distributions (lines) obtained for the proton emission in ^{56}Fe(n,X) and ^{208}Pb(n,X) reactions at 96 MeV (right and left figures, respectively), together with the experimental data (points). In order to have a better illustration of the different reaction mechanisms that contribute to the particle emission spectra (evaporation and preequilibrium emission), when we constructed the angular distributions, we chose three different energy domains: 8–12 MeV (continuous lines), 40–44 MeV (dashed lines), and 68–72 MeV (dotted lines). The contribution of the preequilibrium emission in the total cross section (f_{PE} factor) for each domain is also given near the corresponding distribution.

We observe in general satisfactory agreement between the theoretical results and the experimental distributions. At low energies (8–12 MeV), particles are emitted from both evaporation and preequilibrium processes whose respective contributions depend on the target nucleus mass. For the iron case, we found f_{PE}=0.12 and we observe a quasi-isotropic distribution, both signals indicating that the evaporation pro-

cess is dominant for light targets. For the lead target, $f_{PE}=0.80$ and the angular distribution is slightly forward peaked, showing that low-energy particles are mainly emitted during the preequilibrium stage. For more energetic particles, $f_{PE}=1$ for both targets, and we observe that they are mainly emitted at small angles, following the beam direction. From this, we deduce that those ejectiles are emitted before an equilibrium has been reached. We found a similar agreement when we built the complex particle distributions, showing that the Kalbach parameterization is able to give a proper description of the double differential cross sections, whatever the target or the emitted particle. In addition, a physical basis for this parameterization has been established in Ref. [34], allowing a more detailed theoretical understanding of the properties of the angular distributions in the continuum energy domain.

VI. SUMMARY

In this paper, we report a new set of experimental data concerning light-charged-particle production in 96 MeV neutron-induced reactions on natural iron, lead, and uranium targets. Double-differential cross sections of charged particles have been measured over a wide angular range ($20°-160°$). With the MEDLEY setup, data were measured for p, d, t, ^{3}He and α particles, with low-energy thresholds. The SCANDAL setup has been used to measure proton production cross sections in the same angular range, with good statistics and angular resolution, but with an energy threshold of about 30 MeV. For proton emission, very good agreement found between both sets of measurements obtained with both independent detection systems shows that we had a good control of the systematical uncertainties involved. This is due, in part, to the unambiguous cross section normalization that has been applied using very accurate data on the np scattering cross section [13]. In our experiment, we also measured this cross section and we obtained a good agreement with data from Ref. [13]. The estimated systematical uncertainties affecting the double-differential cross sections reported in this work are of the order of 5%.

Data presented in this paper allow the extension to higher energies (up to 96 MeV) of the available experimental results on nucleon-induced reactions in the 20–200 MeV energy range, which were up to now limited to about 60 MeV incident energy. This new data set, together with the data already existing in the literature, allows us to study in detail both main theoretical approaches [3,4] available nowadays for the description of nucleon and complex particle emission in nucleon-induced reactions at intermediate energies. These approaches have been proposed mainly to improve the exciton model predictions concerning the production of clusters, which was originally strongly underestimated by the model, as shown with the calculations we have performed with the GNASH code [6]. Since the cross sections evaluated with GNASH are at present implemented in the MCNPX code, we would like to issue a warning that some important information needed in specific application as the power deposited in a spallation target of an ADS could be underestimated.

In order to test both approaches, we performed calculations with the PREEQ [20] and PRECO-2000 [28] codes. The PREEQ results have shown that by taking into account the cluster formation probability in the preequilibrium stage of the reaction, one can obtain a global agreement over a wide set of configurations. The formation probability is a free parameter in the PREEQ code and we have adjusted it for each target nucleus. The evolution of the resulting values shows that, for a given outgoing particle, the probability decreases with the target mass. In addition, for a given target, the formation probability is larger for lighter particles. This parameter depends very little on the incident particle type and energy. Proposed as an alternative to this approach, the method used in the PRECO-2000 code and implemented in the more recent code TALYS [29] to calculate complex particle production cross sections considers contributions of direct reactions in the outgoing spectra. In many cases, however, this approach does not lead to a good reproduction of the experimental distributions. Despite the acceptable agreement found in some particular situations, it cannot be used for the moment in a global description of nucleon-induced reactions. This deficiency is due in part to the strong dependence of its predictions on the projectile type. It is our hope that the work performed at present in the development of the TALYS code will soon provide an improved version of this approach.

We have completed the description of the particle emission over the full energy range by adding the contribution of the evaporation process to the preequilibrium emission calculated using the PREEQ code. That calculation scheme has shown that for heavy targets, almost all particles are emitted during the preequilibrium stage of the reaction, while for light targets, a strong component from the evaporation process is present at low emission energy. In addition, the most important contribution in the equilibrium component originates from the decay of residual nuclei left in an excited state after the preequilibrium particle emission. Finally, we have shown that a correct description of the energy-differential distributions and of the different mechanisms contributing to the total cross section allows us to calculate double-differential cross sections by including also the parameterization from Ref. [17] for the angular distribution determination. The good reproduction of the shapes of the double-differential distributions that we obtained with this method suggests that theoretical models must provide at least a good description of the energy-differential cross sections. The parameterization established in Ref. [17] allows a more detailed study of the reaction with a rather satisfactory accuracy by allowing the prediction of the double-differential distributions.

The results presented in this work show that the understanding of nucleon-induced reactions at these energies is far from complete. Two approaches are available in the framework of the exciton model for the description of cluster emission in these specific reactions and among them, only that based on the coalescence model seems to have a satisfactory predictive power. It is, however, based on a scale factor associated with the formation probability of complex particles, which has to be adjusted to experimental data. Therefore, further theoretical progress must be done in this field in order to improve the existing theoretical approaches of the exciton model and to provide new models based on

different considerations. An alternative has been recently proposed in this direction, which uses the wavelet technique to simulate the nuclear dynamics and whose results are very encouraging. They will constitute the subject of a future publication [35].

ACKNOWLEDGMENTS

This work was supported by the European Community under the HINDAS project (Contract No. FIKW-CT-2000-0031), the GDR GEDEON (Research Group CEA-CNRS-EDF-FRAMATOME), Vattenfall AB, the Swedish Nuclear Fuel and Waste Management Company, the Swedish Nuclear Power Inspectorate, Barsebäck Power AB, Ringhals AB, the Swedish Defence Research Agency, and the Swedish Research Council. We would like to thank the TSL staff for assistance and quality of the neutron beam. We are also grateful to Dr. E. Betak for very useful discussions concerning calculations with the PREEQ code. Special thanks to Dr. C. Kalbach for her significant contributions to the progress of theory in nucleon-induced reactions.

[1] HINDAS: High and Intermediate Energy Nuclear Data for Accelerator-Driven Systems, European Community, Contract No. FIKW-CT-2000-0031.
[2] J. J. Griffin, Phys. Lett. **17**, 478 (1966).
[3] I. Ribanský and P. Obložinský, Phys. Lett. **45B**, 318 (1973).
[4] C. Kalbach, Z. Phys. A **283**, 401 (1977).
[5] J. R. Wu and C. C. Chang, Phys. Rev. C **17**, 1540 (1978).
[6] P. G. Young, E. D. Arthur, and M. B. Chadwick, "Comprehensive Nuclear Model Calculations: Introduction to the Theory and Use of the GNASH Code," Report No. LA-12343-MS, 1992.
[7] A. N. Smirnov, V. P. Eismont, and A. V. Prokofiev, Radiat. Meas. **25**, 151 (1995).
[8] S. Dangtip, A. Ataç, B. Bergenwall, J. Blomgren, K. Elmgren, C. Johansson, J. Klug, N. Olsson, G. Alm Carlsson, J. Söderberg, O. Jonsson, L. Nilsson, P.-U. Renberg, P. Nadel-Turonski, C. Le Brun, F.-R. Lecolley, J.-F. Lecolley, C. Varignon, Ph. Eudes, F. Haddad, M. Kerveno, T. Kirchner, and C. Lebrun, Nucl. Instrum. Methods Phys. Res. A **452**, 484 (2000).
[9] J. Klug, J. Blomgren, A. Ataç, B. Bergenwall, S. Dangtip, K. Elmgren, C. Johansson, N. Olsson, S. Pomp, A. V. Prokofiev, J. Rahm, U. Tippawan, O. Jonsson, L. Nilsson, P.-U. Renberg, P. Nadel-Turonski, A. Ringbom, A. Oberstedt, F. Tovesson, V. Blideanu, C. Le Brun, F.-R. Lecolley, J.-F. Lecolley, M. Louvel, N. Marie, C. Schweitzer, C. Varignon, Ph. Eudes, F. Haddad, M. Kerveno, T. Kirchner, C. Lebrun, L. Stuttgé, I. Slypen, A. N. Smirnov, R. Michel, S. Neumann, and U. Herpers, Nucl. Instrum. Methods Phys. Res. A **489**, 282 (2002).
[10] H. Condé, S. Hultqvist, N. Olsson, T. Rönnqvist, R. Zorro, J. Blomgren, G. Tibell, A. Häkansson, O. Jonsson, A. Lindholm, L. Nilsson, P.-U. Renberg, A. Brockstedt, P. Ekström, M. Österlund, F. P. Brady, and Z. Szeflinski, Nucl. Instrum. Methods Phys. Res. A **292**, 121 (1990).
[11] J. F. Ziegler, *The Stopping and Range of Ions in Solids* (Pergamon, Elmsford, NY, 1985).
[12] GEANT Detector Description and Simulation Tool, CERN Program Library Long Write-up W5013.
[13] J. Rahm, J. Blomgren, H. Condé, S. Dangtip, K. Elmgren, N. Olsson, T. Rönnqvist, R. Zorro, O. Jonsson, L. Nilsson, P.-U. Renberg, A. Ringbom, G. Tibell, S. Y. van der Werf, T. E. O. Ericson, and B. Loiseau, Phys. Rev. C **63**, 044001 (2001).
[14] P. W. Lisowski, R. E. Shamu, G. F. Auchampaugh, N. S. P. King, M. S. Moore, G. L. Morgan, and T. S. Singleton, Phys. Rev. Lett. **49**, 255 (1982).
[15] T. Rönnqvist, H. Condé, E. Ramström, R. Zorro, J. Blomgren, A. Häkansson, A. Ringbom, G. Tibell, O. Jonsson, L. Nilsson, P.-U. Renberg, S. Y. van der Werf, W. Unkelbach, and F. P. Brady, Nucl. Phys. **A563**, 225 (1993).
[16] A. Guertin, N. Marie, S. Auduc, V. Blideanu, Th. Delbar, Ph. Eudes, Y. Foucher, F. Haddad, T. Kirchner, Ch. Le Brun, C. Lebrun, F.-R. Lecolley, J.-F. Lecolley, X. Ledoux, F. Lefèbvres, M. Louvel, A. Ninane, Y. Patin, Ph. Pras, G. Rivière, and C. Varignon (to be published).
[17] C. Kalbach, Phys. Rev. C **37**, 2350 (1988).
[18] W. Hauser and H. Feshbach, Phys. Rev. **87**, 366 (1952).
[19] H. Machner, Phys. Lett. **86B**, 129 (1979).
[20] K. K. Gudima, S. G. Mashnik, and V. D. Toneev, Nucl. Phys. **A401**, 329 (1983).
[21] GEANT4 Physics Reference Manual, http://wwwasd.web.cern.ch/wwwasd/geant4/geant4.html.
[22] E. Betak, Comput. Phys. Commun. **9**, 92 (1975).
[23] M. Blann, R. R. Doering, A. Galonski, D. M. Patterson, and F. E. Serr, Nucl. Phys. **A257**, 15 (1976).
[24] F. E. Bertrand and R. W. Peele, Phys. Rev. C **8**, 1045 (1973).
[25] H. Machner, Phys. Rev. C **21**, 2695 (1980).
[26] T. C. Awes, G. Poggi, C. K. Gelbke, B. B. Back, B. G. Glagola, H. Breuer, and V. E. Viola, Jr., Phys. Rev. C **24**, 89 (1981).
[27] H. H. Gutbrod, A. Sandoval, P. J. Johansen, A. M. Poskanzer, J. Gosset, W. G. Meyer, G. D. Westfall, and R. Stock, Phys. Rev. Lett. **37**, 667 (1976).
[28] C. Kalbach-Walker, users manual for PRECO-2000, 2001.
[29] A. Koning (unpublished).
[30] M. Kerveno, F. Haddad, Ph. Eudes, T. Kirchner, C. Lebrun, I. Slypen, J. P. Meulders, C. Le Brun, F. R. Lecolley, J. F. Lecolley, M. Louvel, F. Lefbvres, S. Hilaire, and A. J. Koning, Phys. Rev. C **66**, 014601 (2002).
[31] J. R. Wu and C. C. Chang, Phys. Rev. C **16**, 1812 (1977).
[32] J. R. Wu and C. C. Chang, Phys. Lett. **60B**, 423 (1976).
[33] G. Mantzouranis, D. Agassi, and H. A. Weidenmüller, Phys. Lett. **57B**, 220 (1975).
[34] M. B. Chadwick and P. Obložinský, Phys. Rev. C **50**, 2490 (1994).
[35] F. Sébille, C. Bonilla, V. Blideanu, and J.-F. Lecolley (to be published).

Search for three-body force effects in neutron-deuteron scattering at 95 MeV

P. Mermod [a], J. Blomgren [a,*], B. Bergenwall [a], A. Hildebrand [a], C. Johansson [a], J. Klug [a], L. Nilsson [a,b], N. Olsson [a,c], M. Österlund [a], S. Pomp [a], U. Tippawan [a], O. Jonsson [b], A. Prokofiev [b], P.-U. Renberg [b], P. Nadel-Turonski [d], Y. Maeda [e], H. Sakai [e], A. Tamii [e]

[a] *Department of Neutron Research, Uppsala University, Box 525, S-75120 Uppsala, Sweden*

[b] *The Svedberg Laboratory, Uppsala University, Sweden*

[c] *Swedish Defence Research Agency (FOI), Stockholm, Sweden*

[d] *Department of Radiation Sciences, Uppsala University, Sweden*

[e] *Department of Physics, University of Tokyo, Japan*

Abstract

The neutron-deuteron (*nd*) elastic scattering differential cross section has been measured at 95 MeV incident neutron energy. The neutron-proton (*np*) differential cross section has also been measured for normalization purposes. An inclusion of three-nucleon forces gives a considerable improvement in the theoretical description of the *nd* data in the angular region of the cross-section minimum.

Key words:
three-nucleon forces, neutron-deuteron scattering, angular distribution
PACS: 21.45.+v, 25.10.+s, 25.40.Dn

1 Introduction

High-precision nucleon-nucleon (*NN*) potentials [1–4] have been developed recently with parameters adjusted by means of a large data base. Still, *NN*

* Corresponding author. Tel. +46 18 471 3788.
Email address: jan.blomgren@tsl.uu.se (J. Blomgren).

phenomenology alone cannot reproduce the binding energies of nuclei containing three nucleons or more. This indicates that three-nucleon ($3N$) forces may play some significant role and should be included in the description. However, $3N$ forces are difficult to investigate because they are expected to be weak in comparison with NN forces.

Recent developments in computational techniques allow exact solution of $3N$ bound and nd scattering states through the Faddeev equations [5], with an NN potential as input for the calculations. It is also possible to include $3N$ forces in the Faddeev equations. Such computations of the nd differential cross section have been performed by Witała *et al.* [6], using for the $3N$ force a 2π-exchange model with parameters adjusted to the triton binding energy. For an incident neutron energy of 95 MeV, the estimates show that $3N$ forces should account for about 30% of the cross section in the angular region of the cross-section minimum.

A basic way to understand $3N$ forces is that a 95 MeV neutron has a de Broglie wave length of 2.9 fm and is at the limit of resolving nucleons as extended objects. A fundamentally correct attitude would be to consider the process as interactions between quarks, the constituents of nucleons. However, quantum chromodynamics (QCD) is of limited use at these scales, where the coupling constant is too strong to allow perturbative calculations. Hybrid theories must be developed in between perturbative QCD and NN phenomenology. Effective field theories provide a systematic expansion with a rigourous connection to QCD, allowing in some cases to perform approximations in a very efficient way and to keep the error estimates under reasonable control [7]. An approach based on chiral perturbation theory (CHPT) has been developed recently by Epelbaum *et al.* [8]. The original idea of applying CHPT to few-nucleon systems was formulated by Weinberg [9,10]. The theory allows the description of interactions between pions, and between pions and nucleons (or other matter fields) and relies on a most general effective Lagrangian consistent with (approximate) chiral symmetry of QCD. Three-body forces appear naturally at next-to-next-to-leading order in the CHPT expansion. The nd differential cross section predicted by CHPT is close to the Faddeev calculations of NN interactions, except in the region of the minimum where three-body force effects raise the cross section, although not as much as predicted by Faddeev calculations including $3N$ forces.

There exist high-quality proton-deuteron (pd) scattering data at 65—250 MeV incident proton energy covering the full angular distribution and tending to follow the predictions including $3N$ forces [11–19]. However, Coulomb force effects are not included in the theoretical descriptions, and even if they are not expected to contribute strongly to the cross section in the minimum region, they must be investigated carefully before far-reaching conclusions can be drawn about the role of $3N$ forces in pd scattering. For this reason, nd data

sets are of great value, but unfortunately very few are available. Besides one set of *nd* data covering the full angular distribution at 65 MeV [20] with limited statistical precision in the minimum region, there exists data in the $80-170°$ range at 152 MeV [21] and recent data covering the full angular distribution at 250 MeV [22]. The *nd* data at 250 MeV can be directly compared with *pd* data at the same energy [19]. This comparison shows that, at this energy, Coulomb force effects are reasonably small. The *nd* and *pd* differential cross sections at 250 MeV are underestimated by the models in the minimum region, even when $3N$ forces are included. An important theoretical weakness is related to the fact that it is still unknown to what extent relativistic effects contribute to the cross section.

2 Experimental procedure

The data of the present experiment were obtained with the Medley experimental setup at The Svedberg Laboratory (TSL) in Uppsala. A 98 MeV proton beam of about 5 μA struck an 8 mm thick ^{7}Li target, producing full-energy peak neutrons of 95 MeV (2.7 MeV FWHM). The neutron beam intensity was about $5 \cdot 10^4$ n/(cm$^2\cdot$ s). More details about the TSL neutron beam facility are presented in Ref. [23]. The Medley setup consists of eight detector telescopes. Each of them can be equipped with one or two silicon detectors and one CsI detector, being capable of light ion detection and identification in the energy range 3–130 MeV. Medley is described in detail in Ref. [24]. For the present experiment, the telescopes were all placed in the forward hemisphere at various angles and at distances from the target that optimize the conditions in the region of the *nd* cross-section minimum.

Polyethylene CD_2 (280 μm thickness) and CH_2 (1 mm or 195 μm thickness) target foils were used for the *nd* and *np* measurements respectively, as well as a C (150 μm thickness) target for carbon background subtraction and an empty target frame for instrumental background subtraction. The relative neutron fluences were determined by two independent fission-based neutron monitors.

For each telescope, protons and deuterons were identified by a selection in a ΔE–E two-dimensional plot. Events due to low-energy neutrons were partly rejected by time-of-flight (TOF) techniques. The accepted events were projected as energy spectra. Instrumental background and carbon background were subtracted and the remaining peak was fitted with a Gaussian and integrated in the range mean $\pm 2.35\sigma$ to obtain the number of elastic events, as shown in Fig. 1.

A correction was needed to compensate for the unwanted inclusion of events due to low-energy neutrons. For a given neutron energy resolution, the fraction

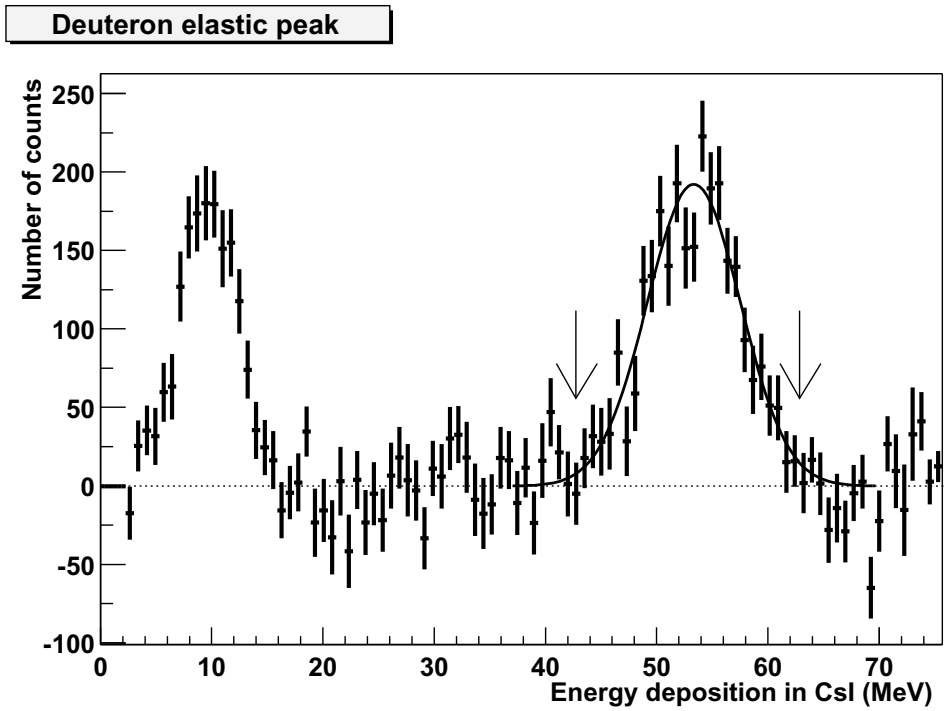

Fig. 1. Typical energy spectrum for a telescope placed at 35° obtained after deuteron selection, low-energy neutron rejection and background subtraction. The signal/background ratio before ^{12}C(n,d) subtraction is 1.3. The error bars are purely statistical. The *nd* elastic events are integrated between the two arrows. The line is a Gaussian fit to the *nd* elastic peak, used to define the integration limits. The peak at low energy is due to wrap-around effects, caused by low-energy neutrons from the preceding beam pulse.

of contaminating events could be determined from an analysis of the neutron spectrum obtained with a magnetic spectrometer [25,26]. In the present experiment, the energy resolution was 3 to 15 MeV (FWHM) varying from telescope to telescope, and the corresponding correction factor was between 0.99 and 0.74, with an uncertainty of up to 2% . The data were also corrected for the CsI detection efficiency, which was estimated to be between 0.92 and 1.00 with an uncertainty of up to 1%. A few experimental points were affected by large energy losses inside the target. The loss of events was estimated using an MC program. At the smallest neutron c.m. angle, i.e., where the deuteron energy is very low, the data were corrected by about a factor of two. The uncertainty in the correction is 10%, due to experimental uncertainties in the target orientation and thickness.

The uncertainty in the absolute neutron flux given by the neutron monitors was about 10%. However, high-quality *np* data at 96 MeV obtained with the LISA magnetic spectrometer [27] exist in the 74−180° angular range, with a claimed uncertainty of 1.9% in the absolute scale. A precise absolute normalization could be achieved by normalizing the present *np* data to the

LISA data. The same factor was used to renormalize the *nd* data. As a cross-check, a normalization using the Nijmegen partial-wave analysis PWA93 [28] as a reference *np* cross section was also considered. The data normalized to PWA93 are about 4% higher on the absolute scale than those normalized to the LISA data. We have chosen to take this difference as the normalization uncertainty in our measurement.

Data points taken on both sides of the beam and whose neutron c.m. angles are separated by 2° or less from each other were combined in order to reduce the statistical uncertainty per point and cancel out systematic errors due to possible asymmetry effects. For the combined data, the uncertainty in the c.m. angle is 0.5°. Counting statistics account for about 4% relative uncertainty in the region of the *nd* scattering minimum. The uncertainty in the absolute normalization does not affect all combined data points in the same way, because they are not always correlated to the same sets of data (that were normalized independently before the data were combined), and the normalization error is therefore included in the systematic uncertainty. The systematic uncertainty contains uncertainties in the setup geometry and detector response (typically about 2%), event identification (typically about 3%) and absolute normalization (4%), summing to about 5%.

3 Results and outlook

The results are presented in table 1 and in Fig. 2. The *np* data are shown in the upper panel of the figure. They agree with the LISA data [27] with a reduced χ^2 of 0.3, and are also in good agreement with PWA93 with a reduced χ^2 of 1.2. If using PWA93 as a reference, the reduced χ^2 is 0.6 with respect to both the LISA data and PWA93. Since the goal of the measurement is to investigate an effect in the shape of the *nd* angular distribution, it is quite comfortable that the *np* angular distribution has the expected shape.

The *nd* data are shown in the middle and lower panels of Fig. 2. They are compared with three different theoretical approaches: i) Faddeev calculations of *NN* interactions using the CD-Bonn potential without $3N$ forces, ii) the same with $3N$ forces from a 2π-exchange model [6], and iii) CHPT at next-to-next-to-leading order [8]. All calculations are able to give a good overall description of the data. In order to investigate $3N$ forces, it is appropriate to compute the reduced χ^2 in the angular region of the cross-section minimum, where the effects are expected to be significant. The reduced χ^2 for the three points between 107° and 140° neutron c.m. angle are 7.9 for i), 0.7 for ii) and 2.0 for iii). If the six points shown in the lower panel of Fig. 2 are included, the reduced χ^2 are 5.4, 1.1 and 1.7, respectively. Using PWA93 instead of the LISA data for the normalization raises slightly the cross section, and the re-

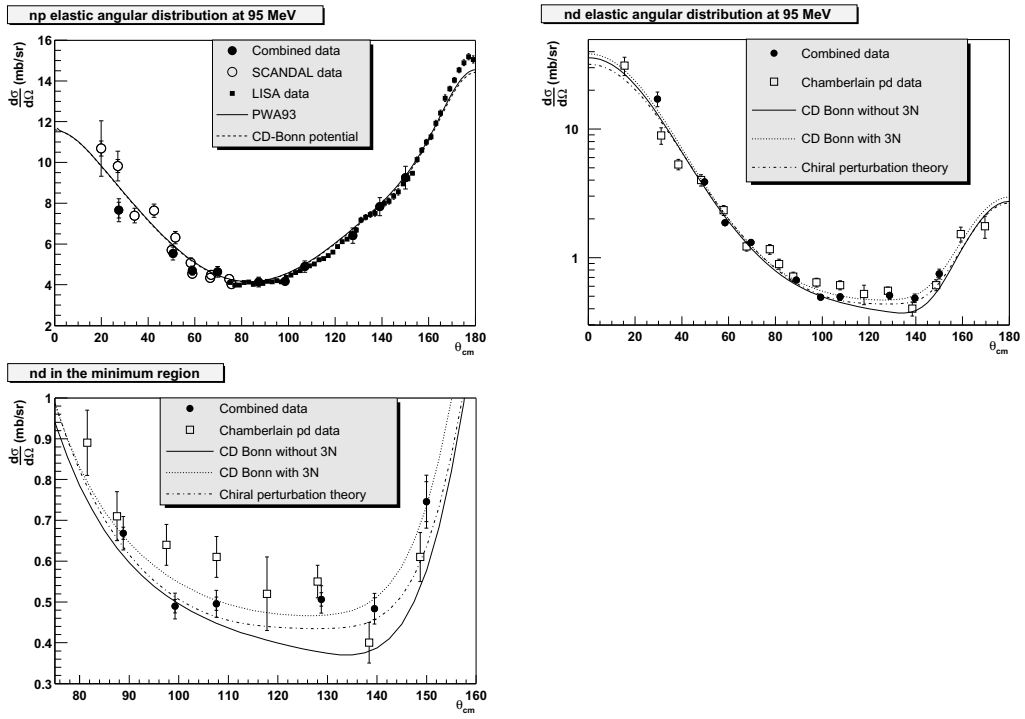

Fig. 2. The *np* and *nd* differential cross sections at 95 MeV neutron energy versus neutron c.m. angle. The filled points are the results of the present experiment normalized to the LISA *np* data [27]. The inner vertical error bars are due to statistics and the extended error bars represent the total uncertainty, including the systematic uncertainty contribution. In the upper panel the *np* results are compared to the LISA data, recent SCANDAL data [29], the prediction of the CD-Bonn potential [3], and the Nijmegen partial-wave analysis PWA93 [28]. The middle panel shows the *nd* results together with *pd* data at the same energy [12]. The theoretical curves are calculations using the CD-Bonn potential with and without $3N$ forces [6], and CHPT calculations [8]. The same is plotted in the lower panel in the region of the cross-section minimum and with a linear vertical scale.

duced χ^2 for the three points in the minimum are then 11.0, 1.0 and 3.8 for i), ii) and iii), respectively. Calculations with the CD-Bonn potential without three-body forces are unable to describe the data in the region of the minimum, while an inclusion of $3N$ forces in the Faddeev equations results in a remarkable agreement with the data. The approach based on CHPT gives also a considerable improvement, but still underestimates slightly the data.

Furthermore, the ratio of the *nd* cross section to the *np* cross section, which must be expressed as a function of the detected particle angle in the laboratory frame, allows normalization-free comparisons. This ratio is shown in Fig. 3. The conclusions are the same: a very good agreement with the theoretical curve based on calculations with the CD-Bonn potential with $3N$ forces, and large discrepancies in the minimum region when $3N$ forces are not included. The χ^2 are comparable with the ones given above.

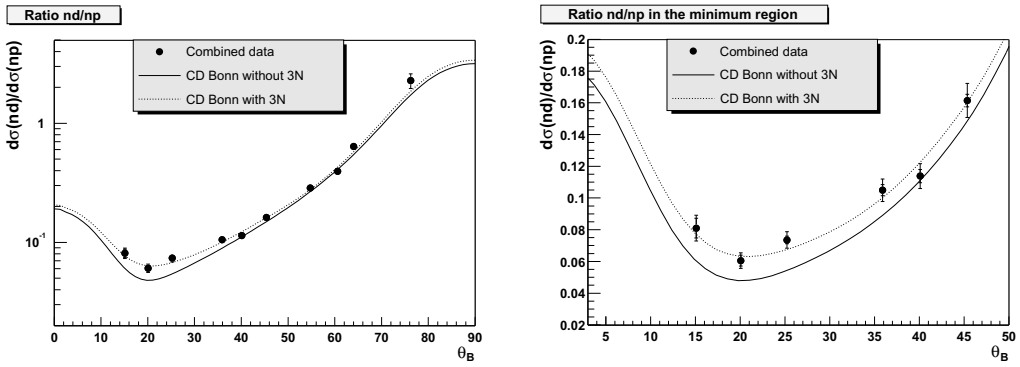

Fig. 3. Ratio of the nd cross section to the np cross section at 95 MeV, as a function of the detected particle lab angle θ_B. The inner vertical error bars are due to statistics and the extended error bars represent the total uncertainty. The uncertainty in θ_B is $\pm 0.25°$. The theoretical curves are calculations with the CD-Bonn potential, the nd cross section being obtained from Faddeev calculations with and without $3N$ forces [3,6]. The same is plotted in the lower panel in the region of the minimum and with a linear vertical scale.

At the same energy in the c.m. system, pd data measured in inverse kinematics [12] are shown together with the present nd data in Fig. 2. The reduced χ^2 between nd and pd is 2.6. The pd data are quite old (1954) and, although probably very good for their time, have larger uncertainties than the present nd data. This motivates a new pd experiment at this energy to study Coulomb effects in detail. Indeed, such an experiment has recently been performed at RCNP in Osaka, and the data are under analysis [30].

Acknowledgments

We wish to thank the technical staff of the The Svedberg Laboratory for enthusiastic and skillful assistance. We are very thankful to E. Epelbaum, W. Glöckle, H. Kamada and H. Witała for contributions concerning the theoretical part. We have appreciated the precious collaboration of K. Hatanaka and N. Kalantar-Nayestanaki. This work was supported by the Swedish Nuclear Fuel and Waste Management Company, the Swedish Nuclear Power Inspectorate, Ringhals AB, the Swedish Defence Research Agency and the Swedish Research Council.

References

[1] V.G.J. Stoks, R.A.M. Klomp, C.P.F. Terheggen, J.J. de Swart, Phys. Rev. C 49 (1994) 2950.

[2] R.B. Wiringa, V.G.J. Stoks, R. Schiavilla, Phys. Rev. C 51 (1995) 38.

[3] R. Machleidt, F. Sammarruca, Y. Song, Phys. Rev. C 53 (1996) R1483.

[4] R. Machleidt, Phys. Rev. C 63 (2001) 024001.

[5] W. Glöckle, H. Witała, D. Hüber, H. Kamada, J. Golak, Phys. Rep. 274 (1996) 107.

[6] H. Witała, W. Glöckle, D. Hüber, J. Golak, H. Kamada, Phys. Rev. Lett. 81 (1998) 1183.

[7] P.F. Bedaque, U. van Kolck, Ann. Rev. Nucl. Part. Sci. 52 (2002) 339.

[8] E. Epelbaum, A. Nogga, W. Glöckle, H. Kamada, Ulf-G. Meissner, H. Witała, Phys. Rev. C 66 (2002) 064001.

[9] S. Weinberg, Phys. Lett. B 251 (1990) 288.

[10] S. Weinberg, Nucl. Phys. B 363 (1991) 3.

[11] H. Shimizu, et al., Nucl. Phys. A 382 (1982) 242.

[12] O. Chamberlain, M.O. Stern, Phys. Rev. 94 (1954) 666.

[13] H. Sakai, et al., Phys. Rev. Lett. 84 (2000) 5288.

[14] G. Igo, et al., Nucl. Phys. A 195 (1972) 33.

[15] H. Postma, R. Wilson, Phys. Rev. 121 (1961) 1229.

[16] K. Kuroda, A. Michalowicz, M. Poulet, Nucl. Phys. 88 (1966) 33.

[17] K. Ermisch, et al., Phys. Rev. C 68 (2003) 051001.

[18] R.E. Adelberger, C.N. Brown, Phys. Rev. D 5 (1972) 2139.

[19] K. Hatanaka, et al., Phys. Rev. C 66 (2002) 044002.

[20] H. Rühl, et al., Nucl. Phys. A 524 (1991) 377.

[21] J.N. Palmieri, Nucl. Phys. A 188 (1972) 72.

[22] Y. Maeda, Ph.D. thesis, University of Tokyo (2004).

[23] J. Klug, et al., Nucl. Instr. Meth. A 489 (2002) 282.

[24] S. Dangtip, et al., Nucl. Instr. Meth. A 452 (2000) 484.

[25] J. Rahm, et al., Phys. Rev. C 57 (1998) 1077.

[26] R.C. Byrd, W.C. Sailor, Nucl. Instr. Meth. A 274 (1989) 494.

[27] J. Rahm, et al., Phys. Rev. C 63 (2001) 044001.

[28] V.G.J. Stoks, R.A.M. Klomp, M.C.M. Rentmeester, J.J. de Swart, Phys. Rev. C 48 (1993) 792.

[29] C. Johansson, et al., in manuscript.

[30] K. Hatanaka, private communication.

Table 1
Measured *np* and *nd* elastic scattering differential cross sections at 95 MeV incident neutron energy. The absolute scale is determined by *np* elastic scattering normalized to the LISA data [27]. The angular uncertainty is 0.5° (c.m.).

θ_{cm} (degrees)	$\frac{d\sigma}{d\Omega}\ \left(\frac{mb}{sr}\right)$	$\pm\delta_{stat}\ \left(\frac{mb}{sr}\right)$	$\pm\delta_{syst}\ \left(\frac{mb}{sr}\right)$
np data			
27.5	7.66	0.38	0.41
50.6	5.53	0.11	0.30
58.9	4.69	0.08	0.21
69.7	4.63	0.07	0.25
87.2	4.13	0.04	0.24
98.6	4.16	0.06	0.19
107.0	4.89	0.05	0.28
127.6	6.41	0.05	0.37
139.1	7.83	0.10	0.43
150.0	9.25	0.11	0.54
nd data			
29.5	17.1	0.2	2.2
49.6	3.87	0.06	0.20
58.3	1.86	0.03	0.10
69.5	1.31	0.03	0.07
88.8	0.668	0.015	0.038
99.2	0.490	0.016	0.027
107.6	0.495	0.017	0.029
128.7	0.506	0.016	0.029
139.5	0.483	0.027	0.026
150.0	0.746	0.049	0.043

Appendix V

Nuclear data for single-event effects

J. Blomgren

Department of Neutron Research, Uppsala university, Box 525, 751 20 Uppsala, SE

Abstract. The importance of cosmic radiation effects in electronics, on board aircrafts as well as at sea level, has been highlighted over the last decade. When, e.g., an electronic memory circuit is exposed to particle radiation, the latter can cause a flip of the memory content in a bit, which is called a single-event upset (SEU). This induces no hardware damage to the circuit, but unwanted re-programming of memories, CPUs, etc., can have consequences for the reliability, and ultimately also for the safety of the system. Since neutrons have no charge, they can only interact via violent, nuclear reactions, in which charged particles are created. In this paper, the SEU problem is presented from a nuclear physicist's perspective. Experimental efforts to improve the nuclear reaction database for silicon are described, as well as the conclusions about the nuclear physics origin of the effect that can be drawn from device testing activities.

1 Introduction

The importance of cosmic radiation effects in electronics, on board aircrafts as well as at sea level, has been highlighted over the last decade. When, e.g., an electronic memory circuit is exposed to particle radiation, the latter can cause a flip of the memory content in a bit, which is called a single-event upset (SEU). This induces no hardware damage to the circuit, but unwanted re-programming of memories, CPUs, etc., can have consequences for the reliability, and ultimately also for the safety of the system. Such software errors were in fact discovered by accident in a portable PC used at an airplane a few years ago, and later the effect has been verified under controlled conditions, both in flight measurements[1,2], as well as in the laboratory[3-5].

The reason that the errors are referred to as single-event upsets is that they are induced by a single particle hitting the device (see Figure 1). This is in contrast to radiation damage of electronics, a phenomenon caused by the integrated dose, which is normally delivered by a large quantity of particles.

The cosmic ray particles in space are mainly protons and alpha-particles, and a small fraction of heavier atomic nuclei. When passing the atmosphere, most of these particles are absorbed, and some of them create cascades of secondary particles. At flight altitudes, as well as at sea level, the cosmic ray flux is dominated by neutrons and muons. The latter do not interact strongly with nuclei, and therefore neutrons are most important for SEU[6-8].

Since neutrons have no charge, they can only interact via violent, nuclear reactions, in which charged particles are created. If this happens in the silicon substrate of an electronic device, the free charge created by the ionization of the particle can be large enough to induce an SEU. Thus, to obtain a full understanding of the SEU problem, knowledge is needed about both the nuclear interaction of neutrons with silicon and the electrical and dynamical properties of pn junctions.

In this paper, the SEU problem will be discussed from a nuclear physicist's perspective. Some experimental efforts to improve the nuclear reaction database for silicon, as well as device testing activities, will be described, followed by an outlook.

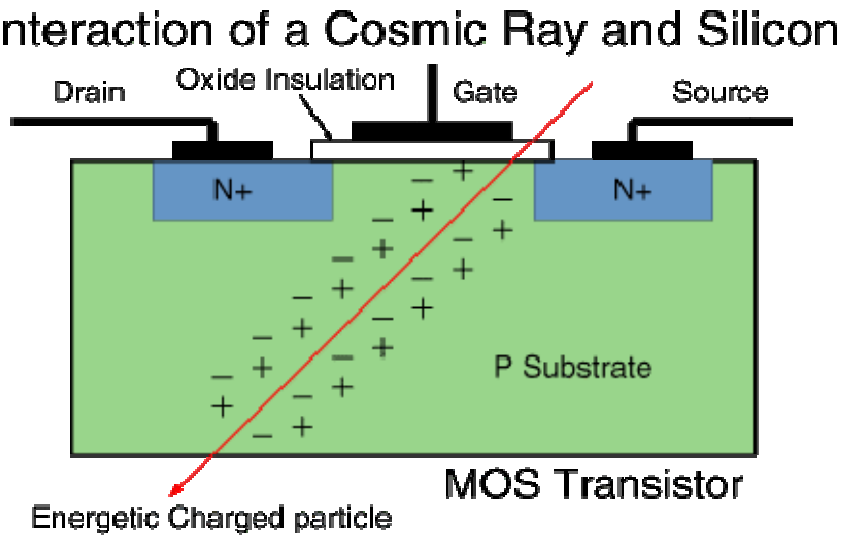

Figure 1. Illustration of a single event in a memory device.

2 The single-event problem

It is known that the cosmic-ray flux in space consists to 92% of protons and to 6% of alpha-particles; the remainder being heavier atomic nuclei. The total particle flux is very large, of the order of 100,000 $m^{-2} \cdot s^{-1}$. Most of these particles are absorbed in the atmosphere by atomic and nuclear interactions with nitrogen and oxygen nuclei of the air, some of which create cascades of secondary particles, mainly neutrons and protons, which are created to approximately the same amount. At typical aircraft flight altitudes (≈10 km) most of the secondary protons have, because of their positive charge, been stopped by atomic interactions with the atmosphere. Thereby, the atmospheric radiation environment is dominated by neutrons[6-8], having a total flux of the order of 10,000 $m^{-2} \cdot s^{-1}$, and showing a 1/E spectrum extending to several GeV of energy. There is also a substantial amount of muons, which have a peak energy of about 1 GeV. Since the latter cannot couple to nuclei via the strong interaction, the neutrons are the most important for creation of SEUs. At sea level, the neutron spectrum looks similar, although the intensity is about a factor of 100 lower.

Since neutrons have no charge, they cannot deposit their energy in, e.g., silicon by interaction with the atomic electrons. The only way of interaction is by violent nuclear reactions, in which charged particles, such as protons, alpha-particles or heavier nuclei are created. It is these secondary ionizing particles that occasionally induce SEU in semi-conducting devices, by generating electron-hole pairs, and thus free charge, during their path in the sensitive volume. Thus, knowledge of the nuclear interaction of neutrons with silicon is needed as a first step to obtain a full understanding of the SEU problem. This includes the probability (cross section) of creating different kinds of particles, as well as their energy and angular distributions. Firm experimental information about neutron-induced cross sections is very scarce, and one has had to rely heavily on calculations based on nuclear models[9]. Typically, nuclear spallation reaction models, built on intranuclear-cascade processes and compound nuclear reactions have been used. Unfortunately, there are very few data to test these models, especially with respect to production of particles heavier than alpha-particles, and therefore the precision in the results is essentially unknown. More data exist on proton-induced reactions, but since the two particles differ both in charge and isospin, the corresponding cross sections can be quite different, especially in the range of 10 to a few hundred MeV. At higher energies, these cross sections are expected to be more similar.

What nuclear processes are responsible for inducing SEUs? It is not very well known, but a few simple arguments can serve as guidance. For this exercise, we use the parameters of an old device, for which this information is now accessible. Although the parameters of modern devices differ significantly, the order of magnitude of relevant ratios are the same, and the general conclusions about the origin of the effect is not dramatically different. Typically, about 100 fC of free charge was needed a few years ago to flip a bit. The average energy needed to create an electron-hole pair in silicon is 3.6 eV, which results in a minimum deposition of about 2 MeV for a SEU to occur. The thickness of the active volume in a memory is typically 2 μm, and hence an ionization of around 1 MeV/μm is required. This is with most standards a very high ionization, which is found only at the lowest energies for a certain particle. Therefore, it does not seem likely that SEUs are caused by energy loss of penetrating particles. Low-energy nuclear fragments released in nuclear reactions within the chip itself appears to be a more probable source. When using sensitivity parameters of a previously common memory (SRAM IMS 1601), it is evident that protons have no effect; they simply ionize too sparsely. Lithium and heavier ions can play a role, while alpha-particles are on the margin. With increasing device densities, smaller geometries and decreasing critical charges, the sensitivity to radiation increases, and it is possible that also the full alpha-particle spectrum can contribute to SEUs. Thus, detailed knowledge of basic nuclear data might allow prediction of new sensitivity effects before they actually appear in commercial technology.

The atmospheric neutron spectrum has a 1/E intensity distribution, which is typical for cascades and spallation reactions. Experimental studies of the cross section for SEU induction have revealed that it has a threshold at about 10 MeV, rises almost linearly up to about 100 MeV and then it saturates, or increases less rapidly[10]. When multiplying these effects, the SEU rate in a real circuit as a function of neutron energy is obtained, resulting in a distribution that peaks around 100 MeV.

Once the production rates of various charged particles are known, the liberated charge and charge density from the stopping of the ion by the atomic electrons can be calculated using well-known physics. The second problem area of SEU is the interplay between the released charge and the pn-junctions of the circuit. The circuit contains a large number of pn-junctions, often in complex geometry, in a scale comparable with the stopping length of the particles. It is therefore a complex task to evaluate the electrical effect of the deposited charge. One way to cope with this problem is to perform a simulation of the semiconductor, by simulating voltages and currents close to the pn-junctions, and their time dependencies, resulting from the charge deposition. An important aspect of such simulations is to find if a single particle affects several pn-junctions, as multiple correlated events may give rise to more severe system errors than single events.

The last step in the understanding is how the full circuit, or the system, is affected by the disturbance at one or several pn-junctions. Here, multiple correlated events may give rise to multiple errors, which are much harder to handle by error-correction codes than single errors. Because of the strong relation between particle track geometry, pn-structure geometry, and circuit topology, all of the same scale, the full problem may not be easy to separate, leading to a very high complexity. One goal of the research should be to see to what extent the various problems can be separated.

3 Artificial neutron fields

It is very time-consuming to use the natural flux of cosmic neutrons for testing of SEU effects in devices. Thus, it is of interest to perform accelerated testing, i.e., using a neutron flux far larger than the natural one. This can be provided by neutron

production using particle accelerators, where two major types of neutron beams are produced; white or monoenergetic. Such facilities are also needed to determine various neutron-induced nuclear cross sections for silicon, as was discussed above, in an efficient and well controlled way.

White neutron beams refer to beams with a broad range of neutron energies produced simultaneously. Typically, they are produced by letting a high-energy proton beam hit a thick (most often stopping) target and large amounts of neutrons of all energies are produced, with typically a 1/E spectrum. This results in an intense neutron flux, which strongly resembles the atmospheric neutron spectrum, so if only the overall sensitivity of a specific device is required to be investigated, this would be the preferred technique.

If, however, detailed studies of the origin of SEU effects are of interest, white beams have a clear disadvantage; they do not allow investigations of the SEU rate versus neutron energy. As has been demonstrated recently[10,11], energy-resolved measurements can provide essential information, but these studies require another type of neutron beams; mono-energetic ones.

The concept mono-energetic is a truth with qualification that might need some explanation. Truly mono-energetic neutron sources are unavailable above about 20 MeV, because neutrons have to be produced via nuclear reactions, and therefore multiple neutron emission is always possible above a certain energy that is sufficient to break the binding of two neutrons from the same nucleus. The ^{7}Li(p,n) reaction is the most common production reaction for mono-energetic neutron beams above 50 MeV energy. At 100 MeV, about 50% of the neutrons fall within 1 MeV at maximum energy, while the remaining half are distributed about equally from maximum energy down to zero. Hence, such beams are not strictly mono-energetic, but this is the closest to mono-energetic conditions nature provides.

Albeit white neutron beams have much a larger total number of neutrons than monoenergetic ones, the difference is not as profound for SEU studies. The reason is that the intensity of white beams falls dramatically with energy, while it is fairly constant for monoenergetic beams, and SEU effects are to a large extent produced by rather high neutron energies.

As was discussed above, if the focus is on detailed investigations on the mechanisms behind the SEU effect, monoenergetic neutron sources have an advantage. An example of such a facility is the neutron beam at The Svedberg Laboratory, Uppsala, Sweden, at which the examples presented in this article were obtained. For a detailed description of the entire facility, see Refs.[12,13].

4 Device testing activities

Groups from universities, as well as from industry, have performed device testing of several different devices at various neutron sources over the years. The device manufacturers are becoming more aware of the SEU problem, as are the companies within the airplane business. Up to now, extensive series of SRAMs and DRAMs have been tested in-beam, as well as FIFOs and a few processors. These tests have shown that memory devices, computer caches included, are especially susceptible to neutron radiation.

Typical results of energy-resolved measurements[10] at TSL are shown in Figure 2. The data presented are for the following memories: Cypress (cy7c199), MHS (HM3-65756), Micron (MT5C2568), NEC (D431000) and Toshiba (TC551001), all manufactured with 4-transistor CMOS technology. As can be seen, the data for different devices show similar energy dependencies, although the absolute magnitude differs. Furthermore, the cross section curves seem to saturate, or even decrease slightly, at energies beyond 100 MeV. A similar behavior has also been observed in proton measurements[14].

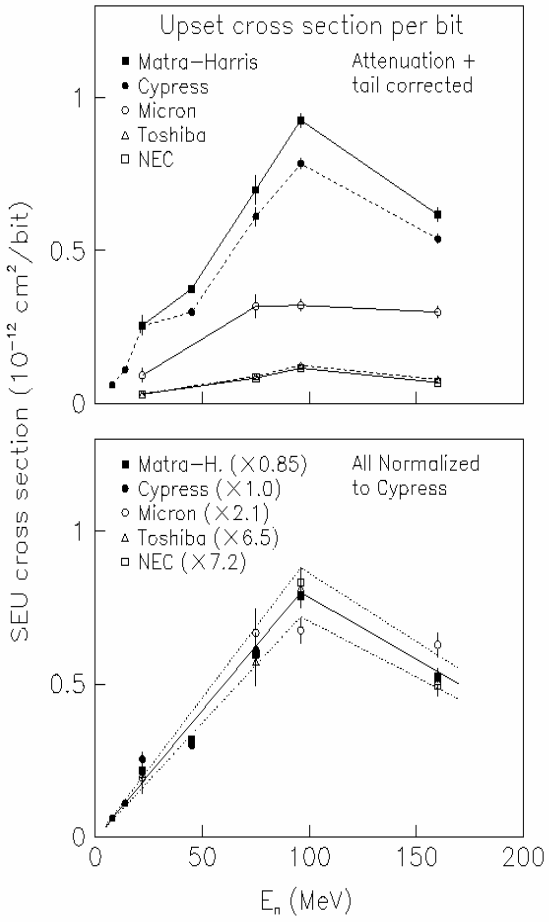

Figure 2. The SEU sensitivity versus incident neutron energy for some memory devices. The upper panel shows the absolute SEU cross sections. In the lower panel, all devices are normalized to Cypress, showing that the energy dependence is similar for all devices, but the absolute magnitude differs. The solid line is an eye-guide showing an average, and the dotted lines indicate 10 % deviation from the average. See the text for details.

These findings are compatible with the discussion in section 2, where the critical charge seemed to suggest release of relatively heavy ions as the major source of the SEU effect. The energy dependence of neutron-induced heavy ion production reactions strongly resembles the SEU data; there is a threshold at about 10 MeV, the cross section rises slowly with energy, and a maximum is reached in the 50-200 MeV range (the maximum differs for different ions produced).

The data on SEU effects induced by protons and neutrons look fairly similar at relatively high energies (200 MeV and above) while serious discrepancies are present at lower energies. Part of these discrepancies has, however, a trivial explanation. The charge of the proton results in a lower cross section, simply because of Coulomb repulsion. After having corrected for this effect, the discrepancies are small enough (up to a factor 3) to be compatible with differences in nuclear parameters like isospin. Thus, proton and neutron data are so similar that it makes sense to assume the origin of the SEU effect to be the same for the two, i.e.,

production of ions heavier than alpha particles, but the differences are large enough that proton-induced data cannot be used to predict the sensitivity to neutrons if a precision better than a factor two is required. Moreover, the atmospheric neutron spectra has its largest intensity at low energies (<100MeV) and therefore discrepancies between neutron and proton generated cross sections in this range could have a large effect on the SEU rate.

What did appear surprising for a while was that the anticipated increased sensitivity (see section 2) for SRAMs and DRAMs, when going from 5 V generations to 3.3 and down to 1.8 V devices, was not seen. On the contrary, the devices seemed to get more robust. One explanation can be that the sensitive volumes were smaller for later generations, thus compensating for the increased sensitivity caused by the decreased supply voltage. More recent devices, however, do indeed display this expected increase in error rate, not only in total error rate, but even per bit of the memory[15]. It is indeed hard to predict the future for coming generations of memories, where lighter particles, like alpha-particles, might come into play. To make this forecast one needs to understand the physics and the mechanisms involved in the creation of an SEU, involving both nuclear data and device behavior.

To study the SEU phenomenon in some detail, one needs to perform both measurements and simulations. The measurements needed are energy-resolved neutron measurements, covering a wide energy range, and possibly supported by some proton measurements. For flight altitudes, as well as at sea level, neutron measurements are most needed, while for space applications, proton-silicon interactions are more interesting to study. For SEUs caused by the atmospheric neutron environment, the energy range from 10 to a few hundred MeV is especially interesting. Measurements at mono-energetic facilities obtain more information than at white beams, and are therefore preferred for detailed studies of the mechanisms behind the SEU phenomenon. Measurements at white neutron sources can then be very valuable for an integral check, and to calibrate the absolute SEU rate in a realistic spectrum. Moreover, when the SEU mechanism is well known, the higher intensity at a white beam makes screening of large series of components feasible.

Such a cross-check has in fact been carried out. By folding energy-resolved data from the 20-180 MeV monoenergetic neutron beam at TSL with a white neutron spectrum, the SEU rates measured at TSL have been compared with corresponding data measured at the white source of the Weapons Neutron Research Facility (WNR) in Los Alamos. For devices that have been studied with both beams, the results are in agreement[16].

5 Measurements of neutron-induced cross sections in silicon

Relying completely on experimental information for assessment of the SEE problem is difficult, because of a number of reasons. First, the energy range to be covered is very large. Therefore, theory modelling is needed for interpolation in between energies where data are available. Second, many of the reactions causing the effect are not accessible to experimental determination. Especially, experimental data can be obtained for production of one particle type at the time (singles), but coincidence data are unavailable, and will probably remain so for a foreseeable future. Thus, the role of experimental data is to guide theory, which in turn will be used as input to device simulation codes.

This in turn means that the data to measure should provide important information for theory development. With these constraints, roughly three types of data are important; elastic scattering, light-ion production and heavy recoil production.

Elastic scattering plays a major role in the determination of the optical potentials involved, i.e., the effective interaction between a neutron and a nucleus.

This information is, in turn, used in virtually every cross section calculation with a neutron in the incident or exit channel. Until recently, the maximum energy where high-quality neutron elastic scattering data have been produced has been 65 MeV. Recently, data at 96 MeV on carbon and lead have been published[17], and a series of nuclei, including silicon, have been or are planned to be measured.

Light-ion production is at present motivated by theory development only, but it might be possible that such data can be of direct importance in a not so distant future, i.e., alpha-production reactions might cause SEEs in future technologies with lower critical charge needed for a bit flip. The data situation for light-ion production resembles the elastic scattering data situation, in that up to now high-quality data up to about 70 MeV have been available. The MEDLEY detector set-up[18] at TSL has been designed for production of p, d, t, ^{3}He, and α data (and possibly also ^{6}Li and ^{7}Li) in the 50-130 MeV range. Recently, silicon data at 96 MeV have been obtained that will be provided for improvement of the data bases, and finally for use within the SEU community[19]. Additional experiments at 180 MeV are planned, which requires a moderate upgrade of MEDLEY.

As has been discussed above, the most important nuclear reactions ultimately causing the SEE effects in present technologies are probably neutron-induced production of heavy, low-energy recoils. Direct measurement of such cross sections with a neutron beam on a silicon target is in reality impossible with present technology, because these recoils have such low energies that an extremely thin target is needed if they should escape it to be able to hit a detector, but then the luminosity is so small that reasonable statistics cannot be obtained in a reasonable time. This problem can be circumvented if using inverse kinematics. Such an experiment is under development at TSL, which is presented by Yuri Murin et al. elsewhere in these proceedings, and this is therefore not further elaborated upon here.

6 Simulations

As was mentioned, device manufacturers have become more aware of the SEU problem. Many, if not all, of the big manufacturers have taken the problem so seriously that they have developed their own computer programs to simulate SEU effects in their devices already at the design stage. Their complete knowledge of the process parameters make their input data to the simulations more accurate. An excellent example is the IBM model SEMM, with a complete 3D geometry of the device as input[20], a code which is completely parameter free. A common model used by non-device manufacturers is the BGR method[21]. There are many different types of BGR programs available today, and they have improved over the years due to better data bases and computer programs.

Here, we will present some very preliminary simulation results from a BGR type of program under development at AerotechTelub/Saab[22]. The program uses stopping power and range data from SRIM calculations[23], and neutron-silicon cross-section data calculated using the GNASH code by Chadwick and Young at LANL[24]. These cross-section data, which can be considered as state-of-the-art today, covers the neutron energy range from 20 to 150 MeV, and include all ejectiles from hydrogen up to silicon, including all possible isotopes of each element.

The input to the calculations are the line-width and the sensitive thickness of the device. Typical values for 0.8 μm CMOS technology are 2.5 μm for the sensitive thickness, yielding a sensitive volume of about 80 μm^3, and a threshold for upsets of about 2 MeV. In this calculation only particles heavier than boron give contributions to the SEU cross-section. The result of the calculation, scaled by a factor of 0.63 to give a charge collection efficiency (C) and volume (V) product of CV=50 μm^3, is

shown in Figure 3, together with the memories studied experimentally at TSL[10]. As can be seen, good agreement is obtained with these rather rough estimates of the input parameters. The simulation does neither include funneling nor diffusion calculations of free charges. Though, funneling and diffusion are probably effectively taken care of through the charge collection efficiency factor and the choice of the size for the sensitive volume.

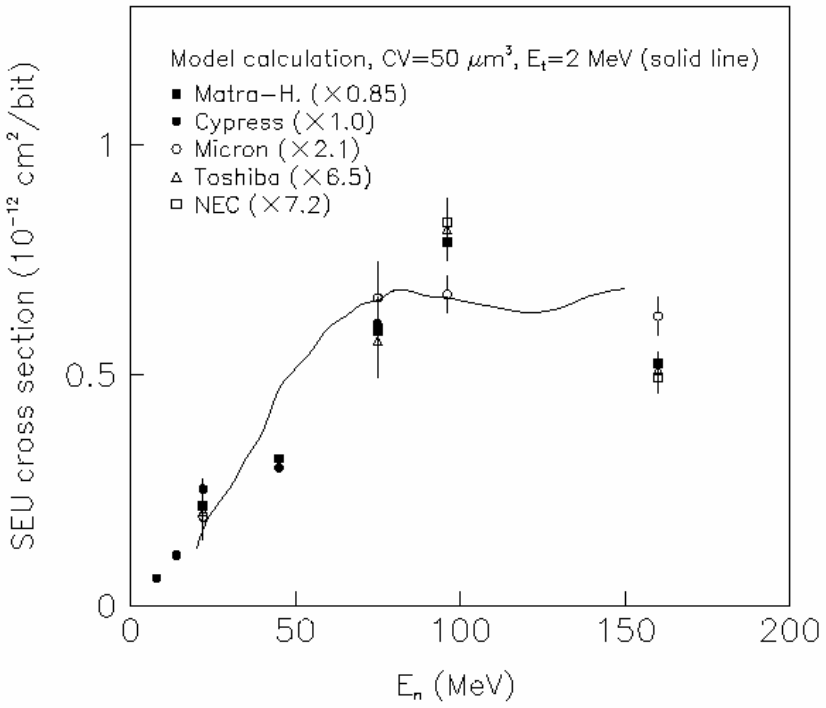

Figure 3. The SEU cross section for a few memory devices versus neutron energy. The line refers to a model calculation of the SEU cross section. See the text for details.

It is striking that this simple calculation translates, more or less directly, the nuclear cross sections into cross sections for SEU with a surprisingly good agreement. This illustrates the importance of fundamental nuclear data for a deep understanding of the SEU problem.

7 Outlook

As has been stated above, a better knowledge of the neutron-induced production cross sections for a wide range of fragments in silicon is of utmost importance for a better understanding of the SEU problem, and for the possibilities to perform reliable simulations of the SEU sensitivity of new circuits and for optimization of the architecture of such devices.

One important reason for development of precise and reliable simulation tools is the limited availability of facilities for device tests. At present, less than ten neutron beam facilities with relevant performance are available worldwide. Testing is so time-consuming that even if all facilities in the world were dedicated to SEU testing, only a small fraction of all devices introduced on the market could be investigated. Therefore, it can be anticipated that simulations will become the method of choice for the large bulk of devices, and in-beam testing will be performed for validation of the simulations. This scenario strongly suggests a dedicated campaign for cross-section measurements, because this represents the presently largest uncertainties in the simulation input.

References

1. J. Olsen, P.E. Becher, P.B. Fynbo, P. Raaby, and J. Schultz, *IEEE Trans. Nucl. Sci*. **40** (1993) 74.

2. A. Taber and E. Normand, *IEEE Trans. Nucl. Sci*. **40** (1993) 120.

3. E. Normand, D.L. Oberg, J.L. Wert, J.D. Ness, P.P. Majewski, S.A. Wender, and A. Gavron, *IEEE Trans. Nucl. Sci*. **41** (1994) 2203.

4. C.A. Gossett, B.W. Hughlock, M. Katoozi, G.S. LaRue, and S.A. Wender, *IEEE Trans. Nucl. Sci*. **40** (1993) 1845.

5. E. Normand, D.L. Oberg, J.L. Wert, P.P. Majewski, G.A. Woffinden, S. Satoh, K. Sasaki, M.G. Tverskoy, V.V. Miroshkin, N. Goleminov, S.A. Wender, and A. Gavron, *IEEE Trans. Nucl. Sci*. **42** (1995) 1815.

6. A.J. Sims, C.S. Dyer, C.L. Peerless, K. Johansson, H. Pettersson, and J.E. Farren, *IEEE Trans. Nucl. Sci*. **41** (1994) 2361.

7. J.F. Ziegler, *IBM J. Res. Develop*. **40** (1996) 19.

8. E. Normand and T.J. Baker, *IEEE Trans. Nucl. Sci*. **40** (1993) 1484.

9. H.H.K. Tang, *IBM J. Res. Develop*. **40** (1996) 91.

10. K. Johansson, P. Dyreklev, B. Granbom, N. Olsson, J. Blomgren, and P.-U. Renberg, *IEEE Trans. Nucl. Sci*. **45** (1998) 2519.

11. K. Johansson, M. Ohlsson, N. Olsson, J. Blomgren and P.-U. Renberg, *IEEE Trans. Nucl. Sci*. **46** (1999) 1427.

12. H. Condé, S. Hultqvist, N. Olsson, T. Rönnqvist, R. Zorro, J. Blomgren, G. Tibell, A. Håkansson, O. Jonsson, A. Lindholm, L. Nilsson, P.-U. Renberg, A. Brockstedt, P. Ekström, M. Österlund, F.P. Brady, and Z. Szeflinski, *Nucl. Instr. Meth*. **A292** (1990) 121.

13. J. Klug, J. Blomgren, A. Atac, B. Bergenwall, S. Dangtip, K. Elmgren, C. Johansson, N. Olsson, A. Prokofiev, J. Rahm, O. Jonsson, L. Nilsson, P.-U. Renberg, P. Nadel-Turonski, A. Ringbom, A. Oberstedt, F. Tovesson, V. Blideanu, C. Le Brun, J.-F. Lecolley, F.-R. Lecolley, M. Louvel, N. Marie, C. Schweitzer, C. Varignon, Ph. Eudes, F. Haddad, M. Kerveno, T. Kirchner, C. Lebrun, L. Stuttgé, I. Slypen, A. Smirnov, R. Michel, S. Neumann, and U. Herpers, *Nucl. Instr. Meth*. **A489** (2002) 282.

14. C. Sanderson and C. Dyer, (private communication).

15. T. Granlund, B. Granbom and N. Olsson, Soft error rate Increase for New Generations of SRAMs, *40th Annual International Nuclear & Space Radiation Effects Conference, Monterey, California, USA, July 2003*.

16. T. Granlund and N. Olsson, A Comparative study Between Two Neutron Facilities Regarding SEU, *7th European Conference on Radiation and its Effects on Components and Systems, Noordwijk, the Netherlands, September 2003*.

17. J. Klug, J. Blomgren, A. Atac, B. Bergenwall, A. Hildebrand, C. Johansson, P. Mermod, L. Nilsson, S. Pomp, U. Tippawan, K. Elmgren, N. Olsson, O. Jonsson, A.V. Prokofiev, P.-U. Renberg, P. Nadel-Turonski, S. Dangtip, P. Phansike, M. Österlund, C. Le Brun, J.F. Lecolley, F.R. Lecolley, M. Louvel, N. Marie-Noury, C. Schweitzer, Ph. Eudes, F. Haddad, C. Lebrun, A.J. Koning and X. Ledoux, accepted for publication in Phys. Rev. C.

18. S. Dangtip, A. Atac, B. Bergenwall, J. Blomgren, K. Elmgren, C. Johansson, J. Klug, N. Olsson, G. Alm Carlsson, J. Söderberg, O. Jonsson, L. Nilsson, P.-U. Renberg, P. Nadel-Turonski, C. Le Brun, F.-R. Lecolley, J.-F. Lecolley, C. Varignon, Ph. Eudes, F. Haddad, M. Kerveno, T. Kirchner, and C. Lebrun, *Nucl. Instr. Meth*. **A452** (2000) 484.

19. U. Tippawan, private communication (2003).

20. G. R. Srinivasan, H. K. Tang, and P. C. Murley, *IEEE Trans. Nucl. Sci*. **41** (1994) 2063.

21. J. F. Ziegler and W. A. Lanford, *Science* **206** (1979) 776.

22. T. Granlund, private communication (2003).

23. J. F. Ziegler, J. P. Biersack, and U. Littmark, *The Stopping and Range of Ions in Solids* (Pergamon Press, New York, 1985).

24. M.B. Chadwick, H.H. Barschall, R.S. Caswell, P.M. DeLuca, Jr., G.M. Hale, D.T.L. Jones, R.E. MacFarlane, J.P. Meulders, H. Schuhmacher, U.J. Schrewe, A. Wambersie, and P.G. Young, *Med. Phys*. **26** (1999) 974; and *ICRU Report* **63** (International Commission on Radiation Units and Measurements, Bethseda, MD, 2000)

Appendix VI

Inverse kinematics studies of intermediate energy reactions relevant for single event effects in microelectronics and medical applications

J.Aichelin[5], J.Blomgren[2], A.Budzanowski [9], M.Chubarov[1], C.Ekström[3], B.Jakobsson[4], A.Kolozhvari[3], O.Lozhkin[1], Yu.Murin[1], P.Nomokonov[8], N.Olsson[2], V.Pljuschev[1], I.Skwirczynska[9], H.H.K.Tang [6], P.-E.Tegner[7], Y. Watanabe[10], L.Westerberg[3], M.Zubkov[1]

1) V.G. Khlopin Radium Institute, 2nd Murinsky 28, 194021, St. Petersburg, Russia
2) Department of Neutron Research, Angström Laboratory, Uppsala University, Box 525, S-75120, Uppsala, Sweden
3) The Svedberg Laboratory, Box 553, S-75121, Uppsala, Sweden
4) Department of Physics, University of Lund, Box 118, S-22100, Lund, Sweden
5) SUBATEX, University of Nantes, F-44307, Nantes, France
6) IBM T.J.Watson Research Center, Yorktown Heights, NY 10598, USA
7) Stockholm University, Box 6730, S-11385, Stockholm, Sweden
8) High Energy Laboratory, JINR, 141980, Moscow Region, Dubna, Russia
9) Institute of Nuclear Physics, 31-342 Krakow, Poland
10) Kyushu University, Kasuga 86-8580, Japan

Abstract. A new experiment is scheduled to run in April 2004 at The Svedberg Laboratory (TSL) in Uppsala, Sweden. The basic objective is to measure both light and heavy secondary fragments produced from intermediate energy nucleon-nucleus reactions, by applying inverse kinematics techniques and exploiting the unique features of the CELSIUS storage ring at TSL. This project has been largely motivated by two important areas of applications: single event effects (SEEs) in microelectronics and proton beam cancer therapy. High-quality data of secondary fragments and recoils provide stringent constraints for nuclear reaction models that generate critical inputs for realistic SEE simulation models and accurate dosage distribution calculations. The scarcity of such essential recoil data has rendered our research proposal timely. Here we report the results that demonstrate the feasibility of our experimental setups.

1. Motivation of Present Work: SEE in Microelectronics

The importance of single event effects in electronics caused by cosmic ray particles is well known in space programs. Their technology impacts in commercial electronics in terrestrial applications and in aircrafts, however, has only been recognized in the past 15 years or so [1-3].

SEEs include a variety of radiation effects. Among them, single event upsets (SEUs), or soft errors, are presently considered the most important effects for the electronics. SEUs provide the best illustration of the nuclear physics origin of SEE phenomena [4,5]. In an SEU event the memory state is flipped when a circuit is exposed to a single particle such as proton or neutron. This occurs because the radiation particle interacts with the circuit materials via nuclear spallation reactions. This nuclear interaction produces secondary fragments such as He ions and heavy recoils. These nuclear fragments are injected into a sensitive device region and cause a transient pulse which ends up being collected by a node. Unlike radiation with large dosage, an SEU event usually does not cause a permanent damage in the circuit. But it may cause serious reliability and performance problems that must be addressed in advanced technologies.

Figure 1, taken from Ref. 6, shows the trend of single-bit soft error rate (SER) observed for typical advanced static random access memory (SRAM) cells. Due to the miniaturization of device/circuit elements and decrease of voltage supply – all

constrained by well-prescribed scaling rules - SER is seen to increase (on a failure per chip basis) in the last three generations of SRAMs (0.18 um, 0.13 um, and 0.09 um). Atmospheric neutrons are a major particle source of SERs.

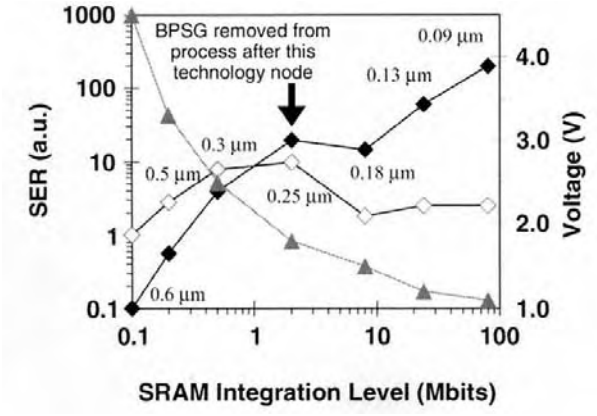

Figure 1. Upsets of advanced SRAMs: open squares – single-bit SER; full squares – system SER; triangles – voltage vs integration (courtesy of R. Baumann)

It is easy to underestimate SEE problems because SEE events may seem unlikely. In the electronics industry, the reliability of a device is measured in units of FITs; one FIT stands for one failure in 10^9 operating hours of a device. The SER of advanced processors with a few Mbit SRAMs may have a typical value of 50,000 FITs [6]. A SER of 50,000 FITs is equivalent to about *one failure in two years* for all-around-the clock operation of the device. This, of course, does not impose problems for the cellular phone users. However, for a system such as the mainframe for a communication server, in which hundreds of CPUs may be invoked, here system reliability is critical. Indeed, failures of such system caused by intermediate energy atmospheric neutrons are expected to appear *once in two weeks.* It has been experimentally measured [7] that from sea level to the altitude of commercial flights (10 km) the intensity of the atmospheric neutron flux increases approximately 200-300 times. This means that the same system when taken aboard an aircraft will generate soft errors *once in an hour!*

2. Motivation of Present Work: Proton Beam Therapy and Radiobiology

In Ref. 8 the authors point out that energy deposition in micro-volumes is a key problem common to SEU simulation work and dosimetry in proton beam cancer therapy. Conventional treatment of proton beam dosimetry is based on the Bragg curve derived from standard electronic energy loss calculations. The authors of Ref. 8 simulate thick water targets irradiated by medium energy protons. By including nuclear spallation reactions, they are able to make quantitative estimates of the secondary radiation energy due to the spallation fragments (protons, light ions and heavy recoils). They observe that these contributions are not as small as usually believed. Clearly these theoretical findings, which may have fundamental implications on dosimetry, must be checked by experiments.

There are essentially two ways to damage a cancer cell by radiation [9]. Ionising radiation create free radicals which are very chemically active and can affect the cell chemistry. Standard low-LET[1] cancer therapy, using photons and electrons,

[1] LET is Linear Energy Transfer proportional to dE/dx

is based on these processes. Unfortunately, such conventional therapy is not very effective for some tumors with low oxygen content. For such tumors, high-LET ionizing radiation can break two strands of the DNA of the cancer cell beyond repair. In this respect, there are similar features in medical and SEE applications.

3. Recoil Spectra Measurements

Heavy recoils are large-LET fragments and they are a major source of secondary radiation. However, compared with the lighter secondary fragments like protons and He ions, their ranges are much shorter. Their detection is very difficult in conventional experiments using proton or neutron beams on stationary targets. This is a major reason why there are so few recoil measurements. The experiment of Ref. 10 – 180 MeV protons on aluminum – is an exception to this rule.

Inverse kinematics would be an ideal technique to measure heavy recoils. However, there are only a few facilities which are equipped to do these special measurements. Apart from TSL, the National Superconducting Cyclotron Laboratory at the Michigan State University (MSU) in USA is another place where recoil experiments can be done, but in a lower energy region. Ref. 11 reports an MSU recoil experiment of 80A MeV Si on H.

4. Nuclear Models

An important motivation of the present project is to generate new data from nucleon-nucleus spallation reactions in the intermediate energy region. They are essential for checking nuclear models which would be the ultimate tools to simulate theoretical data in situations in which there are no experiments. In the following we list the major reaction models or theoretical approaches which appear in the literature in recent years, and which are relevant for SEE and medical applications.

Since the mid-1980s, IBM researchers have developed SEU simulation tools for their technology developments [1,2,4,5]. A central component of the IBM SEU simulation system is a nuclear database generated by a reaction model NUSPA. This nuclear model is based on a simulation framework which combines intranuclear cascade processes and statistical decays of compound nuclei; the model has been applied over a wide energy range [12].

The GNASH code developed by the Los Alamos National Laboratory researchers [13,14] is constantly evaluated and has been popular in radiation physics communities in recent years. However the code is limited to reactions of below 150 MeV.

The Cascade Exciton Model (CEM) combines intranuclear cascade model and exciton model [15, 16]. In recent years, a Quantum Molecular Dynamics (JQMD) model has been developed for nuclear reactions [17]. Both CEM and JQMD may overcome some of the drawbacks of GNASH. But it remains to be seen how well these models can reproduce experiments in the future.

To classify the final channels of the reaction capable to create a SEU a simplified picture is often used which neglects charge collection efficiencies, time constants and other related effects to electronics or applied condensed state physics (funneling, for example). Here, one assumes that SEU occurrence depends only on two parameters of the device i.e. (i) Sensitive Volume (SV), within which it is taking place with subsequent charge collection on the nodes; (ii) Critical Energy (E_{crit}) which has to be exceeded by the ionizing energy (E_{dep}) deposited within the SV in order to trigger an upset.

The theory describing the energy loss of slow ions in solids is developed to a great accuracy and ionization losses of products of nuclear reactions in silicon slab of a device in close vicinity of the SV can be calculated. Electronic specialists often refer to the value E_{cr}=1 MeV μm^{-1} as a typical threshold value of energy deposit by the product of reaction generating SEU athough in reality this parameter can differ considerably from device to device. Then, calculations of ionization losses of heavy ions in thin layers of Si allow one to define an event when A>5 recoil nucleus acquires kinetic energy E within the range of 1÷20 MeV as "a SEU hazardous event". Investigation of reaction channels in which such recoils appear is our primary goal.

5. TSL Experimental Setups

The layout of such experiment is shown in Figure 2. The experimental setup situated at the CELSIUS nuclear accelerator and storage facility of The Svedberg Laboratory (Uppsala, Sweden) consists of four systems for registration of reaction products emitted in collisions of 100÷470A MeV Si ions with atoms of the internal hydrogen cryogenic cluster-jet target of CELSIUS. Secondary particles are registered simultaneously by the Small Angle Detector (SAD), the Forward Wall Detector (FWD), the Zero Angle Detector (ZAD), and the Spectator Tagging Detector (STD). All detectors, but SAD, are used in experiments at CELSIUS and described elsewhere [18-23]. SAD plays the key role in our project since it detects the very products, recoils of Si and its fragments, which in real life are inducing SEE in silicon devices.

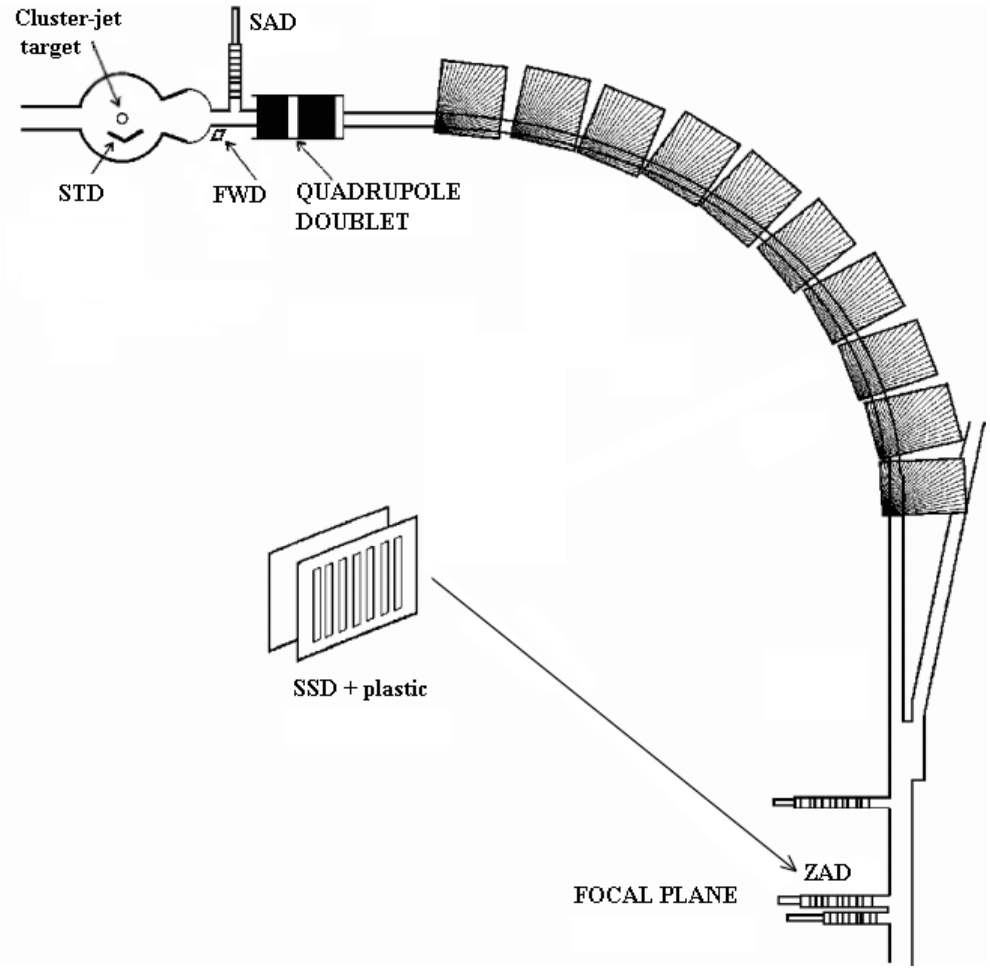

Figure 2. A layout of the experiment scheduled for April 2004 at TSL

Small Angle Detector (SAD) detects fragments of the Si ions emitted at angles $0.6^{o} \div 1.1^{o}$ from the intersection point of stored ion beam with the cluster-jet target of CELSIUS. Thus, the unique properties of CELSIUS cooled beam are fully exploited. During the injection-acceleration cycle the beam occupies the whole volume of CELSIUS vacuum chamber and only by its end after the beam is cooled it shrinks to 2 mm. To prevent SAD detectors from radiation damage they are moved out during the beam injection and moved back to the working position only when the beam is finally formed.

SAD constitutes a telescope of two 300 μm Silicon Strip Detectors (SSDs) followed by a 8 mm thick plastic scintillator. The first SDD has circular and the second radial strips total 32 of each type. Plastic scintillators are used as triggers of the readout cycle and for timing. The position of the particle registered by both detectors simultaneously is derived from the circular and radial strip numbers. The charge of the fragment is identified by the corresponding SSD pulse amplitude.

The Zero Angle Detector (ZAD) is also a telescope of two SSDs and a plastic scintillator. Here we take the advantage of the technique developed at TSL [19] using the quadrant after the cluster-jet target of CELSIUS as a magnetic spectrometer. ZAD is positioned at 22757 mm from the target at the focal plane of the spectrometer [20]. As distinct to SAD, strips of ZAD make up the 32x32 rectangular net. Vertical and horizontal strips of ZAD SSDs are used to register projectile-fragments, identify their charge (Z) and determine the position of the hit point with respect to the nominal beam centerline. Electronic schemes of SAD and ZAD are identical.

The Forward Wall Detector (FWD) [21] is suggested for detection of light (A<5) secondaries emitted within the polar angle of 3.9^{o}-11.7^{o} in coincidence with the recoil registered by SAD. Beam-time estimations based on the results of our computer simulations and expected beam-target luminosity show that the requested time for accumulating 10K SEU-hazardous events (FWD–SAD coincidences) is about 30h for five energies of Si ions.

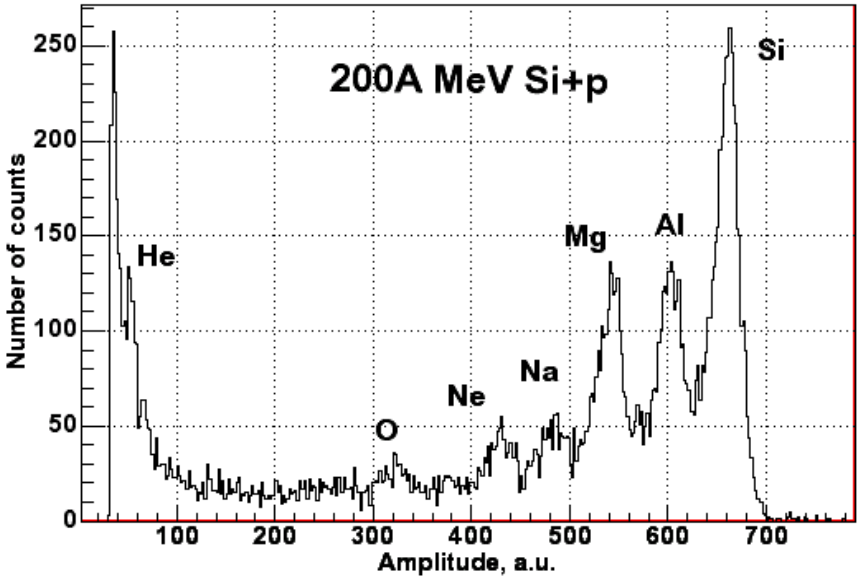

Figure 3. Amplitude distribution from scintillator detector in position of SAD

The Spectator Tagging Detector (STD) [22] or the CHICSi detector [23] could be used for tagging spectator-proton emitted within $60^{o} \div 120^{o}$. It would be interesting to perform selection of such events in Si+d reaction and confront the results to the

similar data for Si+p reaction and thus evaluate information on Si fragmentation on a quasi-free neutron of deuteron.

Figure 3 shows the results of the feasibility experiment conducted in October 2003 with a 8x10 mm^2 8mm-thick plastic scintillator situated at the planned position of SAD. Positions of the peak amplitudes are proportional to the charge of the products of 200 MeV Si+p reaction measured with the average current Si ion beam of 50 μA and a thickness of the hydrogen target around $2\cdot 10^{14}$ atoms $\cdot cm^{-2}$.

6. Summary

We have done feasibility studies for a new experimental program at TSL, measuring light and heavy fragments from intermediate energy nucleon-nucleus reactions. The initial stage of this program is for SEE applications. But in the near future we plan to use the experimental technique developed here for the medical application. The second stage of the program would be the study of reactions with 60÷250 A MeV carbon and oxygen ions on atoms of H, He and N.

This work is supported by the International Scientific Technological Center (Project #1956), Moscow, Russian Federation.

References

1. IBM J. Res. Dev. **40**, No.1, 1996. (Special issue on terrestrial soft errors in microelectronic systems).
2. MRS Bulletin. **28**, No.2, 2003. (Special issue on single event upsets in microelectronics).
3. J. Blomgren, Contribution to the Proceedings of this Workshop.
4. H.H.K. Tang, IBM J. Res. Dev. **40**, 91 (1996).
5. H.H.K. Tang and K.P. Rodbell, MRS Bulletin, **28**, 111(2003).
6. R. Baumann, MRS Bulletin, **28**, 117(2003).
7. P. Goldhagen, MRS Bulletin, **28**, 131(2003).
8. H.H.K. Tang and J.L. Romero, American Institute of Physics Conference Proceedings No. 392, 325(1997).
9. M. Tubiana, J. Dutreix, and A. Wambersie, Introduction to Radiobiology. Taylor & Francis, London, 282(1990).
10. K. Kwiatkowski et al., Phys. Rev. Lett. **50**, 1648(1983).
11. J.L. Romero et al., American Institute of Physics Conference Proceedings No. 392, 655(1997).
12. H.H.K. Tang et al., Phys. Rev. **C42**, 1598(1990).
13. P.G.Young, E.D.Arthur, M.B.Chadwick, **LANL Report LA-12343-MS**, 1992.
14. S. Weili, Y. Watanabe, et al., Evaluation of neutron and proton nuclear data of ^{12}C and ^{28}Si for energies up to 200 MeV, private communication.
15. K.K.Gudima, S.G.Mashnik, V.D.Toneev, Nucl.Phys. **A401**, 329(1983).
16. S.G.Mashnik, A.J.Sierk, O.Bersillon, T.A.Gabriel, **LANL Report LA-UR-97-2905**(1997).
17. K.Niita, S.Chiba, et al., Phys.Rev. **C52**, 2620(1995).
18. Yu.A. Murin et al., Proc. 4th ISTC Scientific Advisory Committee Seminar,Novosibirsk, April 23-27, 2001.
19. Chr. Bargholtz, K. Lindh et al., Nucl. Instr. Meth. **A390**, 160(1997).
20. Ringbom, G. Tibell et al., Nucl. Instr. Meth. **A373**, 57(1996).
21. A.Budzanowski, et al. Nucl.Instr.Meth. **A482**, 528(2002).
22. R. Bilger, W. Bodowski, H. Calen et al., Nucl. Instr. Meth. **A457**, 64(2001).
23. B.Jakobsson, Nucl.Phys.News, **9**, 22(1999).

Appendix VII

Measurements of Neutron-Induced Fission Cross-Sections for ^{209}Bi, ^{nat}Pb, ^{208}Pb, ^{197}Au, ^{nat}W, and ^{181}Ta in the Intermediate Energy Region

A.N. Smirnov,* V.P. Eismont, and N.P. Filatov
V.G. Khlopin Radium Institute, 2oi Murinskiy Prospect 28, Saint-Petersburg 194021, Russia

J. Blomgren† and H. Condé
Department of Neutron Research, Ångström Laboratory, Uppsala University, Box 525, S-751 20 Uppsala, Sweden

A.V. Prokofiev‡
The Svedberg Laboratory, Uppsala University, Box 533, S-751 21 Uppsala, Sweden; V.G. Khlopin Radium Institute, 2oi Murinskiy Prospect 28, Saint-Petersburg 194021, Russia

P.-U. Renberg
The Svedberg Laboratory, Uppsala University, Box 533, S-751 21 Uppsala, Sweden

N. Olsson
Department of Neutron Research, Ångström Laboratory, Uppsala University, Box 525, S-751 20 Uppsala, Sweden; Swedish Defense Research Agency (FOI), S-172 90 Stockholm, Sweden

(Dated: August 24, 2004)

Neutron-induced fission cross-section ratios ^{nat}Pb/^{209}Bi, ^{208}Pb/^{209}Bi, ^{197}Au/^{209}Bi, ^{nat}W/^{209}Bi, ^{181}Ta/^{209}Bi, and ^{209}Bi/^{238}U have been measured in the 30 - 180 MeV energy range using the neutron beam facility at The Svedberg Laboratory in Uppsala. The ^{7}Li(p,n) reaction was employed as a neutron source. The fission fragments were detected by thin-film breakdown counters. Cross-sections at specific energies were determined using unfolding techniques with respect to the excitation function and the neutron spectra, the latter obtained from recent measurements and an evaluation. The absolute fission cross-sections were obtained using the standard ^{238}U(n,f) cross-section. The ^{nat}W(n,f) and ^{181}Ta(n,f) cross-sections have been measured for the first time. The results for ^{209}Bi(n,f), ^{nat}Pb(n,f), ^{208}Pb(n,f), and ^{197}Au(n,f) cross-sections have been compared with available literature data. A universal easy-to-use parameterization has been suggested for all measured cross-sections. The common features of sub-actinide neutron-induced fission cross-sections are found to be similar to those of the proton-induced fission data.

PACS numbers: 25.85.Ec, 25.40.-h, 28.20.-v

I. INTRODUCTION

Concepts of accelerator-driven systems (ADS) for incineration of long-lived radioactive waste and energy production (see, e.g., [1]) suggest irradiation of a massive target made of heavy elements by a high-intensity charged particle beam. As a result of nuclear interactions in the target, caused by the primary beam and secondary particles, an intense spallation neutron source is created with an energy distribution extending up to the incident particle energy. This source is intended to feed a subcritical reactor that surrounds the neutron production target and contains the nuclides to be transmuted.

One of the prerequisites for computational modeling of ADS is the availability of evaluated nuclear data for the most important reactions involved. This motivates the choice of nuclides and reactions included in the high priority request list of intermediate-energy nuclear data, which is formulated and periodically updated by Koning *et al.* [2].

The recent high priority list includes requests for nucleon-induced fission cross-section data for a few nuclides considered as prospective spallation target materials. The fission channel contributes to the radioactivity produced in the spallation target, as well as to the chemical and radiological toxicity of the reaction products. For example, fission products in a lead target irradiated by 1.6-GeV protons will contribute 10-15% to the overall residual activity after one year of cooling [3]. On the other hand, the predictive power of available nuclear reaction models and codes (e.g., LAHET [4], CEM95 [5]) with respect to the description of the fission process is not sufficiently good at present (see, e.g., the studies of Prael [4], Prokofiev *et al.* [5], Duijvestijn *et al.* [6], and a re-

*Electronic address: Smirnov@atom.nw.ru
†Electronic address: jan.blomgren@tsl.uu.se
‡Electronic address: Alexander.Prokofiev@tsl.uu.se

cent comparison of codes for activation yield calculation [7]. For example, the ^{nat}W(p,f) cross-section predicted by the LAHET code was found to be about 20 times lower than the experimental result of Ref. [6]. Further progress in nuclear reaction modeling, especially with respect to fission, may therefore lead to significant improvements in ADS performance calculations.

Data on intermediate energy fission cross-sections are important also for nuclear theory, e.g., in connection with studies of the dynamic effects of the nuclear fission process, which reflect the connection between collective and single-particle degrees of freedom in nuclei (see, e.g., [8]).

Proton-induced fission cross-sections have been studied extensively (see, e.g., a recent review [9] and references therein). On the other hand, neutron-induced fission experiments above 20 MeV are sparse, mainly because of the lack of suitable neutron sources. In addition, a truly monoenergetic neutron source is not available in this energy domain. Neutron data measurement and processing techniques are therefore unavoidably more complicated than in the case of charged particle beams.

The (n,f) cross-section database is especially poor for sub-actinide nuclei. The early experiments of Kelly and Wiegand [10], Goldanskiy *et al.* [11], Reut *et al.* [12], and Dzhelepov *et al.* [13] are rather of a qualitative character. The studies of Vorotnikov and Larionov [14] and Vorotnikov [15] are of a high methodological quality, but cover only a narrow energy region near the fission barrier, where the cross-sections are extremely small, and therefore only upper limits for cross-sections could be obtained in many cases.

During the last decades, a new generation of intermediate energy neutron sources has become available. At a few of them, (n,f) cross-section measurements, in particular, for sub-actinide nuclei have been included in the experimental programs.

The measurements at the LANSCE neutron facility at Los Alamos National Laboratory were performed by Vonach *et al.* [16] and Staples *et al.* [17, 18] in the early 90ies using a parallel-plate ionization chamber. None of these studies has resulted in a final publication. The similar technique was employed in the work of Shcherbakov *et al.* [19] performed at the neutron facility GNEIS at Petersburg Nuclear Physics Institute in Gatchina, and in the work of Nolte *et al.* [20] performed at neutron facilities in Louvain-la-Neuve and Cape Town. A complication in interpreting data of this type is the need to separate sub-actinide fission events from a background of non-fission products, which contribute significantly to the pulse height spectra.

The (n,f) cross-section measurements at the neutron facility in The Svedberg Laboratory (TSL) in Uppsala are part of an experimental program performed in frame of collaboration between V.G. Khlopin Radium Institute, St. Petersburg, and Uppsala University. Measurements for sub-actinide nuclei have been performed using two different techniques for fission fragment detection, thin-film breakdown counters (TFBC) [21–26] and a Frisch-gridded ionization chamber [24, 27–29].

This paper presents final (n,f) cross-section data for ^{209}Bi, ^{nat}Pb, ^{208}Pb, ^{197}Au, ^{nat}W, and ^{181}Ta, obtained with the TFBC technique. The measurements for natural lead, tungsten and tantalum are important because these elements are either considered as candidates to the neutron production target material in concepts of future ADS or are already used in existing spallation neutron sources. The doubly magic nucleus ^{208}Pb is included because of its importance for improvements in the theoretical modeling of the fission process. In addition, the ^{197}Au(n,f) cross-section was studied in view of its recent application in neutron monitoring [30].

Earlier analyses and preliminary experimental data have been published elsewhere [21–26]. In the present study, the results of further measurements have been added, and the data from our earlier studies have been re-analyzed using new neutron spectrum data [31] and new calculations of energy-dependent detection efficiency corrections [32, 33].

II. EXPERIMENTAL APPARATUS AND PROCEDURE

The measurements were performed at the TSL neutron beam facility in Uppsala, using the Gustaf Werner cyclotron to produce neutrons through the ^{7}Li(p,n) reaction. The neutron beam facility and the positioning of the experimental chambers in the beam are described in Sect. II.A.

Because of the low beam intensity, inherent for secondary beams, the irradiation position for the most measurements of the present experiment was chosen to be at a short distance from the neutron production target. The incident neutron spectrum is not monoenergetic, but consists of a high-energy peak accompanied by a low-energy tail, which also contributes to the fission reaction rate. To determine the (n,f) cross-section at the energy of the peak, one needs to know the fraction of fission events due to that peak. This fraction can be determined using the time-of-flight (TOF) technique. However, in most cases it was not possible to implement the TOF techniques because of the short flight path in combination with the limited time resolution, dominated by duration of the proton beam pulse. Therefore, the fraction of peak fission events was obtained in an iterative unfolding procedure, taking into account relative fission reaction rates at as many incident neutron energies as possible, together with corresponding information on the neutron spectra. The determination of the latter is discussed in Sect. II.B.

A severe γ-radiation background was present at the irradiation position chosen for most of the studied reactions. This hampered the use of traditional fission fragment detection techniques and justified the choice of TFBCs, which are sensitive only to particles with specific ionization losses exceeding the detection threshold. The TFBCs and the experimental chambers are described in

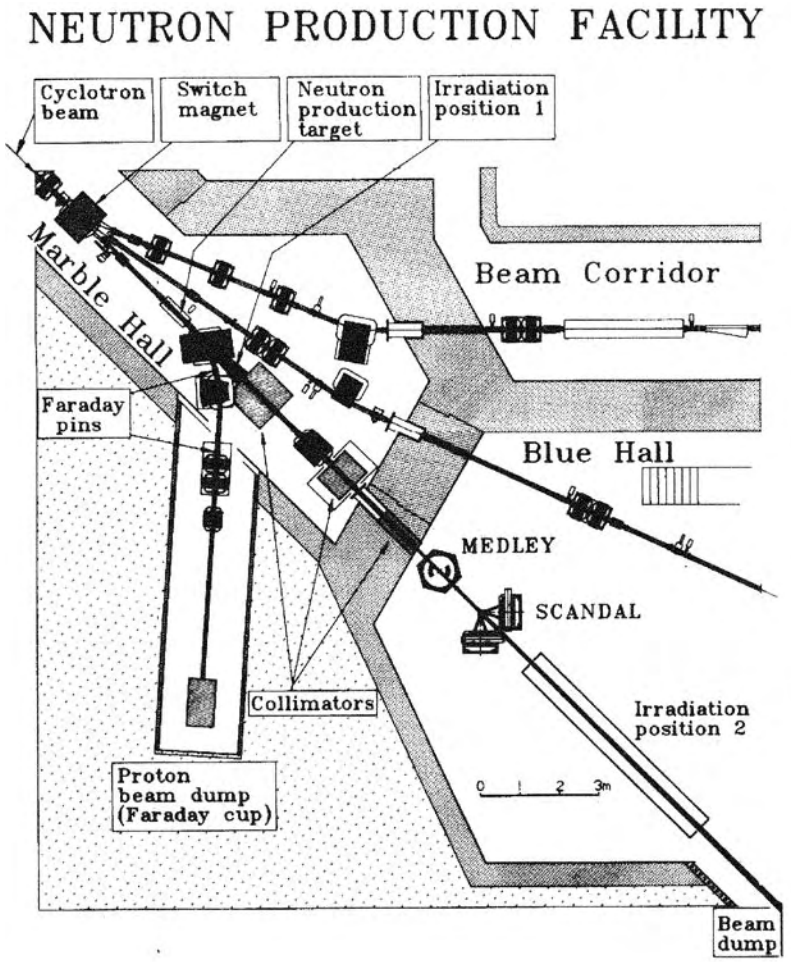

FIG. 1: An overview of the neutron beam facility.

Sect. II.C.

The preparation and characterization of the samples are discussed in Sect. II.D. Finally, an outline of the electronics and the data acquisition system is given in Sect. II.E.

The most of studied cross-sections were measured relative to the ^{209}Bi(n,f) one. The latter has already been studied in earlier experiments (see, e.g., [21, 22]) and has been adopted by IAEA/NDS as a secondary neutron standard [34]. However, further measurements of the ^{209}Bi(n,f) cross-section and a new analysis of the earlier results have led to some changes that are discussed in Sect. IV.B.

A. Neutron beam facility

An overview of the neutron beam facility is presented in Fig. 1. A comprehensive description of the facility can be found in [35, 36], and therefore only the features essential for the present experiment are discussed below.

The proton beam from the Gustaf Werner cyclotron impinged on a 4-15 mm thick target of lithium, enriched to 99.98% in ^{7}Li. Downstream the target, the proton

beam was deflected by two magnets into an 8 m long tunnel, where it was focused onto a water-cooled graphite beam dump. The neutrons produced within a 60-msr cone around 0^o passed through a collimating system before reaching the experimental hall at a distance of about 8 m from the production target. The respective area is marked as Irradiation position 2 in Fig. 1. This position was employed in our earlier studies [21, 22] and kept in the present work for the ^{209}Bi/^{238}U ratio measurements above 50 MeV, due to a rather large magnitude of the studied cross-sections. On the contrary, it was found impractical to measure cross-sections of nuclei lighter than Bi and the ^{209}Bi(n,f) cross-section below 50 MeV in Irradiation position 2 because of insufficient neutron flux density and small cross-section values. Therefore, in these cases the experimental setup had to be positioned closer to the production target. On the other hand, the neutron field in the irradiation position has to be clean from contamination by primary or scattered protons. In addition, locations close to the 0^o direction are preferable, because the production of high-energy neutrons is strongly forward-peaked. The given conditions were satisfied by placing the experimental setup between the proton bending magnet and the first neutron collimator, at a distance of about 2 m from the production target (Irradiation position 1, see Fig. 1). To facilitate simultaneous experiments at the neutron beam line, the setup was placed outside the vacuum tube at an angle of about 4^o to the beam axis.

Thus, the TFBC-based chambers with samples of ^{238}U, ^{209}Bi,^{nat}Pb, ^{208}Pb, ^{197}Au, ^{nat}W and ^{181}Ta were installed in Irradiation position 1, and the chambers with ^{238}U and ^{209}Bi were installed in Irradiation position 2. In addition to count-rate determination, the chamber with ^{238}U was employed as a neutron spectrum sensor (see Sect. II.B).

TABLE I: Thicknesses of the ^{7}Li targets and energy parameters of the primary proton and secondary neutron beams.

E_p primary	^{7}Li target thickness	E_p average in the target	E_{npeak} average
(MeV)	(mm)	(MeV)	(MeV)
37.96± 0.07	4	36.4	34.5
49.2± 0.1	4	48.2	46.3
69.1± 0.2	4	68.4	66.6
76.4± 0.2	4	75.8	73.9
92.1± 0.3	4	91.4	89.6
96.8± 0.3	4	96.3	94.5[a]
	8	95.6	93.8[a]
114.2± 2.0	8	113.1	111.3
136.7± 1.0	15	134.7	132.9
148.4± 0.6	15	146.4	144.6
177.3± 1.0	15	175.2	173.3

[a]The peak neutron energy averaged over the two production modes is 94.1 MeV

Table I shows thicknesses of the ^{7}Li targets and various energy parameters of the primary proton and secondary neutron beams employed in the different irradiations. In most of the runs, the energy of the protons irradiating the lithium target was measured by time-of-flight techniques with an uncertainty as given in Table I. From this information, the peak neutron energy was calculated using the reaction Q-value and the energy loss in the lithium target, estimated using the SRIM code [37].

The proton beam current at the production target was typically 4-6 μA in the 30-100 MeV energy range and 0.3-0.6 μA at the higher energies. The resulting flux density of high-energy peak neutrons at Irradiation position 1 amounted to 3x10^4- 3x10^5 s^{-1}cm^{-2}, which is a factor of 30-40 more than in Irradiation position 2. This gain was acquired at the price of a limited access to the setup in the course of the experiment and harder requirements on the stability of the detectors with respect to radiation.

The Irradiation position 1 was situated close to the facility for neutron activation studies [36, 38]. In Ref. [38], the relative proton (and/or H^0 atom) contamination in the neutron field was estimated to be as much as 4x10^{-3}. However, in that case most of the protons were produced inside the activation target stack itself. Since the thickness of the stack was much larger than the total amount of material between the neutron production target and any sample in the present experiment, the estimate given above can be considered as an upper limit for the proton or H^0 atom contamination of the neutron beam that encounters the fission samples.

B. Neutron spectrum

As was mentioned, an unfolding procedure is needed to obtain fission cross-sections from the measured reaction rates. Information on the neutron spectrum at the irradiation position for the various incident neutron energies is therefore required.

A complete set of characterization measurements is not available for the TSL neutron beam. Moreover, the intense background radiation around the production target would hamper the use of most instruments for neutron beam characterization. The present study therefore relies on the following assumptions about the neutron spectrum:

- The neutron spectrum at the Irradiation position 1 is a sum of two components. One of them originates directly from the ^{7}Li target. The other is a background arising from interactions of primary protons with the beam transport system, the beam dump, the walls, and other material in the surroundings, with subsequent propagation and slowing-down of secondary neutrons.

- The background component dominates in the low-energy end of the spectrum and vanishes at neutron energies of about 10 MeV [38]. This component could hamper cross-section measurements for reactions with a threshold at lower energy, e.g.,

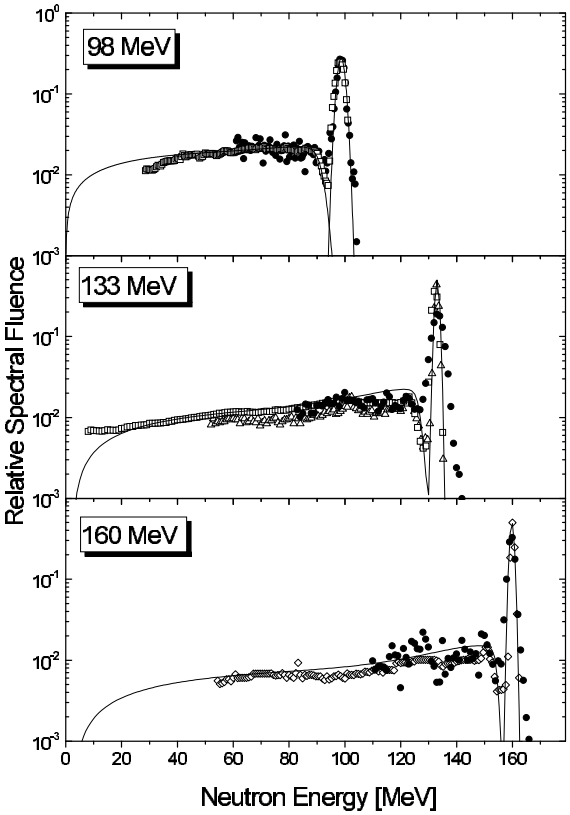

FIG. 2: Neutron spectra from the ^{7}Li(p,n) reaction at 0^{o} for the peak energy of 98, 133, and 160 MeV. The filled circles represent measurements at the TSL neutron facility [35, 39] in Irradiation position 2. The open symbols represent data from other facilities: the Indiana University Cyclotron Facility [40, 41] (shown as triangles and diamonds, respectively), and the RIKEN facility [42] (shown as squares). The lines represent the neutron spectrum calculations discussed in the text. All spectra are normalized so that the area under the high-energy peak is unity.

^{238}U(n,f) or ^{235}U(n,f). For sub-actinide nuclei, with the fission reaction threshold of about 20 MeV or more, the influence of the low-energy background is negligible.

- The energy and angular distribution of neutrons in the first component is defined only by the double-differential cross-section (DDX) of the ^{7}Li(p,n) reaction. The basis of this assumption is that no significant amounts of material were present between the neutron production target and the fission samples.

Support for the last assumption is given by the fact that the neutron spectra measured at TSL agree with data from other sources. Fig. 2 shows neutron spectra obtained in the course of earlier n-p scattering studies at TSL [35, 39] at 0^{o} for the peak neutron energies 98, 133, and 160 MeV (shown by filled circles). For comparison, neutron spectra from other facilities are shown as open symbols. The shown spectra were obtained by Byrd and Sailor [40] (triangles) and by Stamer *et al.* [41] (diamonds) at the Indiana University Cyclotron Facility, and by Nakao *et al.* [42] at the RIKEN facility (squares) at peak neutron energies close to the ones in the TSL data. For readability of Fig. 2, the spectra from Refs. [40–42] are shifted by a few MeV in order to match the position of the high-energy peaks. The solid curves represent the neutron spectrum calculations discussed further in the text.

As seen in Fig. 2, the neutron spectrum consists of a high-energy peak and a low-energy tail. The high-energy peak corresponds to the ^{7}Li(p,n) reactions that leave the ^{7}Be nucleus in the ground state or in the first excited state at 0.43 MeV. The low-energy tail is related to excitation of higher states in ^{7}Be and to break-up reactions.

The neutron spectrum calculations were performed in two different ways depending on the peak neutron energy. For peak energies below 45 MeV, interpolated and smoothed experimental data of Byrd and Sailor [40], Baba *et al.* [43], and Schuhmacher *et al.* [44] were used. In cases when the measured spectra do not cover sufficiently wide range of secondary neutron energies, we used a constant extrapolation to lower energies, which was found to be a reasonable approximation, according to Nolte *et al.* [45]. Above 45 MeV, the calculations employed semi-empirical systematics developed in [31], which is based on a phase-space distribution [46] corresponding to the three-body breakup process ^{7}Li(p,n ^{3}He)^{4}He for description of the continuum part of neutron spectra and an empirical correction factor taking into account experimentally observed peculiarities of the high-energy part of the continuum spectra.

As has been mentioned, the experimental setup in Irradiation position 1 was placed at an angle of 4^{o} with respect to the primary proton beam direction. As soon as the production of high-energy neutrons is strongly forward-peaked, the difference between the neutron spectra at 0^{o} and 4^{o} has to be taken into account.

A correction taking into account the decrease in high-energy peak neutron production at 4^{o} relative to 0^{o} was obtained by least-squares fitting to experimentally measured angular distributions from the literature [47–51], with subsequent fitting with respect to incident proton energy. The correction increases from 4% at 38 MeV to 24% at 177 MeV.

For continuum neutron production, a similar corrections were calculated, which depend on the incident proton energy and the secondary neutron energy. The calculations employed angular distribution data for continuum neutrons from the ^{7}Li(p,n) reaction included in the LA150 library [52]. The latter were obtained with the GNASH code [53], which, in turn, employs Kalbach representation of the angular distribution [54]. At 150-175 MeV region, where the LA150 data are not available, an extrapolation was made on the basis of the correction obtained at lower energies.

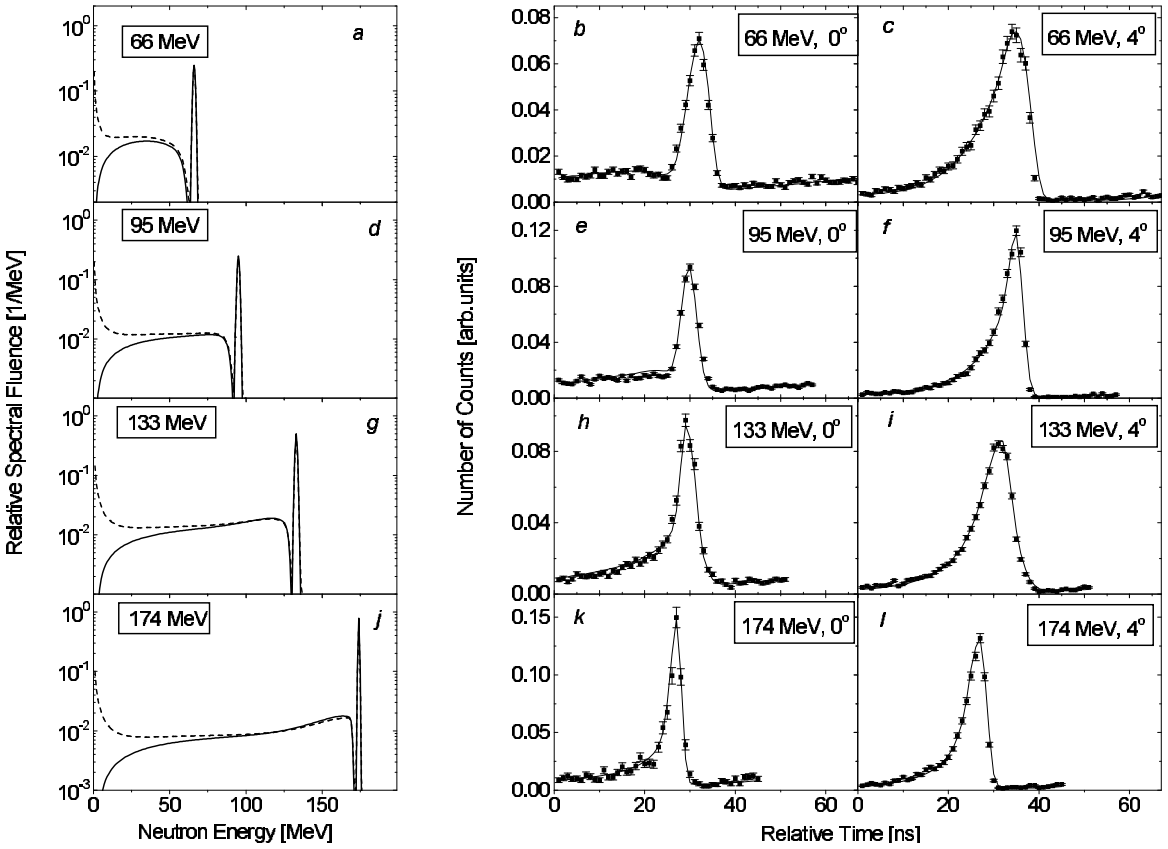

FIG. 3: Calculations of neutron spectra (left panel) for the incident proton energies of 69.1 (a), 96.8 (d), 136.7 (g), and 177.3 MeV (j) used in the present experiment for 0^o (solid lines) and 4^o (dashed lines). The middle panel (b, e, h, k) represents experimental (symbols) and calculated (lines) distributions of ^{238}U fission events induced by neutrons at a flight path of about 10 m at 0^o (in Irradiation position 2). The right panel column (c, f, i, l) represents experimental (symbols) and calculated (lines) distributions of ^{238}U fission events induced by neutrons at a flight path of about 2 m at 4^o (in Irradiation position 1).

Validation of the calculations was carried out by means of folding of the calculated spectra with the standard ^{238}U neutron fission cross-section [34], followed by conversion to the TOF scale and folding with a function that takes into account the time resolution of the measurement system. Modeled in this way time distributions of ^{238}U neutron-induced fission events were compared with experimental data obtained both at 0^o at Irradiation position 2 and at 4^o at Irradiation position 1 simultaneously in the same neutron beam.

In Fig. 3, we show the calculated relative neutron spectral fluence at 0^o and 4^o for several incident proton energies used in the present experiment, and corresponding calculated and experimental time distributions of fission events in ^{238}U. The spectra at 4^o are the sum of the two components mentioned above. The background component is described by an $1/E_n$ distribution. The relative intensity of the background component was fitted to reproduce the experimental distributions of the ^{238}U(n,f) events obtained at Irradiation position 1.

As seen in Fig. 3, the experimental time distributions of the ^{238}U(n,f) events can be successfully reproduced by the model. This ensures adequacy of the chosen representation of the neutron spectra.

C. Fission fragment detectors and experimental chambers

The fission fragments were detected by thin-film breakdown counters (TFBC). A detailed description of the TFBC technique can be found in [55] and references therein; only a brief description is given here. The operation principle of the TFBC is based on the phenomenon of electric breakdown in a MOS structure caused by an ion passing through a thin silicone dioxide layer. The breakdowns are non-shorting, since they lead to vaporization of a small part of the electrode area and leave no conducting path between the electrodes. The features of the TFBCs are threshold behaviour, i.e., the insensitivity to light charged particles, neutrons and γ-radiation, real-time operation and good timing properties, easy oper-

ation (no high voltage required, no gases, large output signals, which makes preamplifiers unnecessary), compact design, and long-term stability under heavy radiation conditions. The last feature was of primary importance for the present experiment, because of the severe γ-radiation background in the Irradiation position 1.

The choice of detection system design is governed first by the low beam intensity, which necessitates the use of sandwich geometry, i.e., the detector has to be situated as close as possible to the fission sample. The sample-detector sandwich and its mechanical housing constitute an experimental chamber, which is placed in the neutron beam. The amount of material in a chamber along the beam direction is dominated by the thickness of the TFBC (0.3 mm Si). Consequently, the probability of interaction of an incident neutron with the chamber is small, and it is possible to stack several chambers after each other in the neutron beam without any significant influence on the beam characteristics. In this way, relative fission cross-sections can be measured using detectors sandwiched with samples of different nuclides and being irradiated by the same neutron beam.

The detection system design is further governed by a trade-off between count rate and time resolution. The latter can be as good as several hundreds of picoseconds for a single TFBC of 1 cm^2 sensitive area. However, to get sufficient statistics, a larger area is required. This can only be achieved at the price of a worsening of the time resolution, because of the unavoidable spread in propagation time of signals originating from different parts of the sensitive area. To achieve both good timing and sufficient count rate, mosaic TFBC arrangements were employed.

The design of a single experimental chamber is shown in Fig. 4. The chamber consists of a mosaic arrangement of detectors, a similar arrangement of samples, and a thin mechanical housing. Each chamber contains six TFBCs with a diameter of about 1 cm, placed symmetrically in the plane perpendicular to the neutron beam direction. Six samples of the same nuclide were placed face-to-face to the detectors so that the sensitive area of each detector received fission fragments emitted by the corresponding sample in the forward hemisphere. The distance between the sample and the detector sensitive area (not more than 0.5 mm) could be passed by fission fragments in air without any significant energy loss. Therefore, evacuation of the chamber was not necessary. Upstream and downstream the sample-detector sandwiches, the incident neutron beam passed through the entrance and exit windows, respectively, which were made of 0.2-mm thick aluminum foils.

The entire experimental setup consisted of 6 to 9 chambers described above, depending on the specific irradiation. The chambers were stacked along the neutron beam direction, so that each set of sample-detector sandwiches was exposed to virtually the same neutron fluence. Each chamber was equipped either with samples of one of the studied nuclides (^{209}Bi, ^{nat}Pb, ^{208}Pb, ^{197}Au, ^{nat}W, and ^{181}Ta) or with the monitor samples (^{238}U or ^{209}Bi).

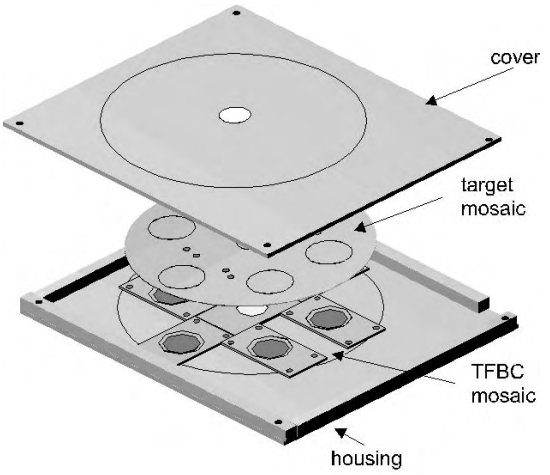

FIG. 4: The design of an experimental chamber.

All detectors have common bias voltage and a common signal output. Typically, the mosaic arrangement provides an output pulse height of about 1 - 2 V and a time resolution of about 2 ns (FWHM).

D. Fission samples

The samples were prepared by deposition on circular 0.1-mm thick aluminum backings of 1 cm^2 area. In all cases, the area of the sample exceeded the sensitive area of the respective TFBC. Therefore, the latter defined the effective area of the sandwich.

The employed deposition techniques, the chemical composition, and the thickness of the samples are listed in Table II. The samples of ^{208}Pb and ^{238}U had an isotopic purity of 98.7% and 99.999%, correspondingly, while the other samples contained either monoisotopic elements (^{209}Bi, ^{197}Au, ^{181}Ta) or natural isotopic compositions (^{nat}Pb, ^{nat}W).

The thickness of the samples was determined by Rutherford backscattering spectroscopy (in case of the sub-actinide targets), by direct α-spectroscopy (in case of ^{238}U), and/or by direct weighing of the sample backing before and after deposition of the material.

Since the expected fission cross-sections of the studied sub-actinide nuclei were a few orders of magnitude smaller than those of actinide nuclei are, the actinide contamination of the samples was checked using the following techniques:

- direct α-spectroscopy measurements using semiconductor detectors,
- α-activity measurements using low-background nu-

TABLE II: Characteristics of the fission samples.

Target	Chemical composition	Deposition technique	Average sample thickness (mg/cm^2)
^{238}U	$^{238}U_3O_8$	multiple smearing	0.1 - 1.1
^{209}Bi	^{209}Bi	vacuum evaporation	1.1 - 3.1
^{nat}Pb	^{nat}Pb	vacuum evaporation	1.1 - 2.4
^{208}Pb	^{208}Pb	vacuum evaporation	1.3 - 2.4
^{197}Au	^{197}Au	vacuum evaporation	2.8
^{nat}W	$^{nat}WO_3$	vacuum evaporation	2
^{181}Ta	^{181}Ta	magnetron evaporation	0.5 - 1.2

clear track detectors [56],

- irradiation by a 21-MeV neutron beam. Because of the very low fission cross-sections of the studied nuclei at this energy, virtually all detected fission events could be attributed to actinide contaminants.

In addition, an upper limit of the contamination could be deduced from the TOF spectra of fission events accumulated during the irradiations. The results obtained with the listed techniques were mutually compatible. The obtained upper limit for the relative abundance of actinide nuclei in the sub-actinide samples amounted to 10^{-5} - 10^{-6} depending on the studied nuclide.

E. Electronics and data acquisition system

A schematic view of the electronics and the data acquisition system is shown in Fig. 5. Since the signals from the TFBCs are large (see Sect. II.C), they could be fed into a fast multichannel leading-edge discriminator without any preceding amplification. The discrimination level could always be set so that virtually all detector pulses were accepted. The logical signals from the discriminator were summed and fed into the start input of a TDC. A pulse, phase-locked to the cyclotron RF, served as the stop signal for the TDC. In addition, the discriminated signal from each fission chamber was recorded by a scaler, and this information was used in the analysis to separate the TOF spectra of fission events from the different chambers. The TOF spectra and the count-rate data were stored in a computer on an event-by-event basis and could be inspected on-line.

As discussed above, in most cases it was not possible to fully separate the high-energy peak fissions from those of the low-energy tail using TOF techniques. Nevertheless,

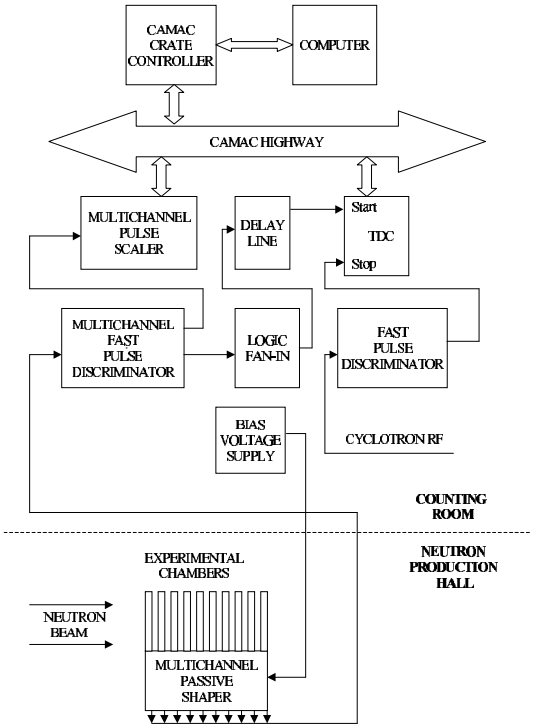

FIG. 5: A schematic view of the electronics and the data acquisition system.

TOF techniques were useful for rejection of intrinsic detector background events, as well as of those from spontaneous fission of contaminating nuclides. In addition, inspection of the low-energy part in the TOF spectra allowed us to check that no significant actinide contamination was present in the sub-actinide fission samples.

III. DATA ANALYSIS

A. Fission cross-section ratio

The number of detected fission events per unit incident energy, induced by neutrons with an arbitrary spectrum, is

$$n_f(E) = \rho S_{sample} \varphi_n(E) \sigma_f(E) \varepsilon(E), \qquad (1)$$

where E is the incident neutron energy, ρ is the number of nuclei in the sample per unit area, S_{sample} is the sample area (1 cm^2 in our case), $\varphi_n(E)$ is the spectral density of the neutron fluence, $\sigma_f(E)$ is the fission cross-section, and $\varepsilon(E)$ is the detection efficiency, defined as the ratio of the number of detected fragments to the number of fissions in the sample.

The efficiency, as defined above, accounts for the anisotropy of the fragment angular distribution in the laboratory frame, as well as for loss of fragments due to a possible mismatch between the area of the sample and the sensitive area of the TFBC, S_{TFBC}. Since each TFBC was exposed to a calibration sample of 1 cm^2 area containing ^{252}Cf, the difference between S_{sample} and individual S_{TFBC} was automatically taken into account, and the detection efficiency for fragments of neutron-induced fission can be expressed as

$$\varepsilon(E) = k_\varepsilon(E)\varepsilon^{Cf}, \quad (2)$$

$$\varepsilon^{Cf} = n_{sf}/a_{sf}, \quad (3)$$

where n_{sf} is the count rate of fragments from spontaneous fission, a_{sf} is the spontaneous fission activity of the ^{252}Cf sample, and

$$k_\varepsilon^X(E) = \frac{\varepsilon_{ac}^X(E)}{\varepsilon_{ac}^{Cf}}, \quad (4)$$

where ε_{ac}^{Cf} and ε_{ac}^X are the calculated absolute detection efficiencies of the TFBC and a sample of unit area for the fragments of ^{252}Cf spontaneous fission and induced fission of nuclide X, respectively.

Combining Eqs. (1) and (2) gives

$$n_f(E) = \langle\rho\varepsilon^{Cf}\rangle k_\varepsilon^X(E)\varphi_n(E)\sigma_f(E), \quad (5)$$

where $\langle\rho\varepsilon^{Cf}\rangle$ is the product of the values ρ and ε^{Cf} averaged over all sandwiches for the corresponding fission chamber. Integration over the entire incident neutron spectrum gives the total number of detected fissions,

$$N_f = \langle\rho\varepsilon^{Cf}\rangle \int_0^{E_{max}} k_\varepsilon^X(E)\varphi_n(E)\sigma_f(E)dE. \quad (6)$$

The number of fissions induced by the high-energy peak neutrons in the quasi-monoenergetic spectrum can be obtained by integration over the peak only. Since the relative efficiency and the fission cross-section vary slowly with energy, they can be replaced by the values corresponding to the peak energy E_0, i.e., $k_{\varepsilon 0} = k_\varepsilon^X(E_0)$ and $\sigma_{f0} = \sigma_f(E_0)$. Thus,

$$N_{fpeak} = \langle\rho\varepsilon^{Cf}\rangle k_{\varepsilon 0}\sigma_{f0}\Phi_{n0}, \quad (7)$$

where Φ_{n0} is the fluence of the high-energy peak neutrons. The fraction of detected fissions due to the peak, $k_{peak} = N_{fpeak}/N_f$, can be deduced from Eqs. (6) and (7):

$$k_{peak} = \frac{\sigma_{f0}k_{\varepsilon 0}\Phi_{n0}}{\int_0^{E_{max}} k_\varepsilon(E)\varphi_n(E)\sigma_f(E)dE}. \quad (8)$$

Combining Eqs. (6) and (8) gives the peak fission cross-section

$$\sigma_{f0} = \frac{N_f k_{peak}}{\langle\rho\varepsilon^{Cf}\rangle k_{\varepsilon 0}\Phi_{n0}}. \quad (9)$$

Finally, the fission cross-section ratio measured with a pair of sandwich arrangements X and Y, stacked one after the other in the neutron beam, is

$$\frac{\sigma_{f0(X)}}{\sigma_{f0(Y)}} = \frac{N_{f(X)}\langle\rho\varepsilon^{Cf}\rangle_{(Y)}k_{peak(X)}\varepsilon_{ac}^X(E_0)R_{(X)}^2}{N_{f(Y)}\langle\rho\varepsilon^{Cf}\rangle_{(X)}k_{peak(Y)}\varepsilon_{ac}^Y(E_0)R_{(Y)}^2}, \quad (10)$$

where R is the distance between the production target and the chamber. The quantities $\langle\rho\varepsilon^{Cf}\rangle$, R, and N_f were obtained in direct measurements for the respective chambers. The latter quantity was corrected for intrinsic detector background on the basis of the obtained TOF spectra of fission events. The determination of the remaining parameters in Eq. (10), $\varepsilon_{ac}^X(E)$ and k_{peak}, is discussed in Sect. III.B and C, respectively.

B. Determination of the detection efficiency

The detection efficiency of a TFBC in sandwich geometry cannot be directly measured for a particle source with unknown intensity and arbitrary angular-energy distribution, since the counting characteristics (efficiency versus bias voltage) does not have a plateau corresponding to detection of all fragments that reach the sensitive area. Instead, a model calculation has to be employed, and the parameters of the model have to be determined in dedicated measurements for each specific detector (or for a group of detectors with similar properties), operated at a given bias voltage.

A model and a computer code for calculation of the TFBC detection efficiency have been described in our earlier report [32]. A thorough description is going to be published elsewhere [33]. A brief outlook of the model and the code is given below.

The model and the code are based on semi-empirical dependences of the detection threshold voltage on specific energy losses of fission fragments in SiO_2 and on the incident angle of fission fragments to the sensitive surface of the detector [57]. The code makes use of Monte Carlo techniques to model the process of detection for fission fragments from either spontaneous or nucleon-induced fission. The model takes into account angular anisotropy of fission and transferred longitudinal momentum that define angular distributions of fission fragments. A change in fission fragment kinetic energy due to the transferred momentum is taken into account, as well as the energy losses of fission fragments in the sample material and their dependence on the fragment angular distribution.

The input data of the code include:

- Charge, mass and kinetic energy distributions of fission fragments, taking into account the emission of pre-fission neutrons. In case of the ^{238}U(n,f) reaction, experimental data of Zoller [58] were employed. At present, data of this type for neutron-induced fission of sub-actinide nuclei re-

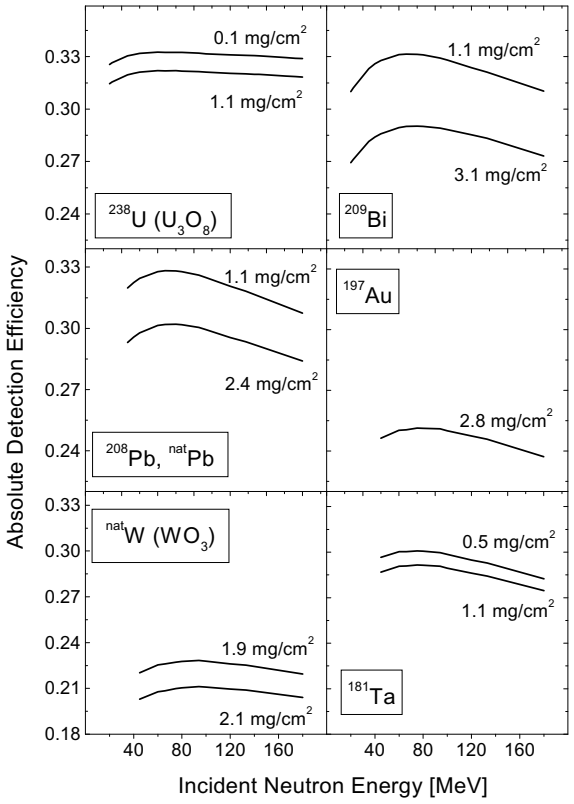

FIG. 6: The calculated fission fragment detection efficiency for the TFBC and a sample of the unit area, versus incident neutron energy.

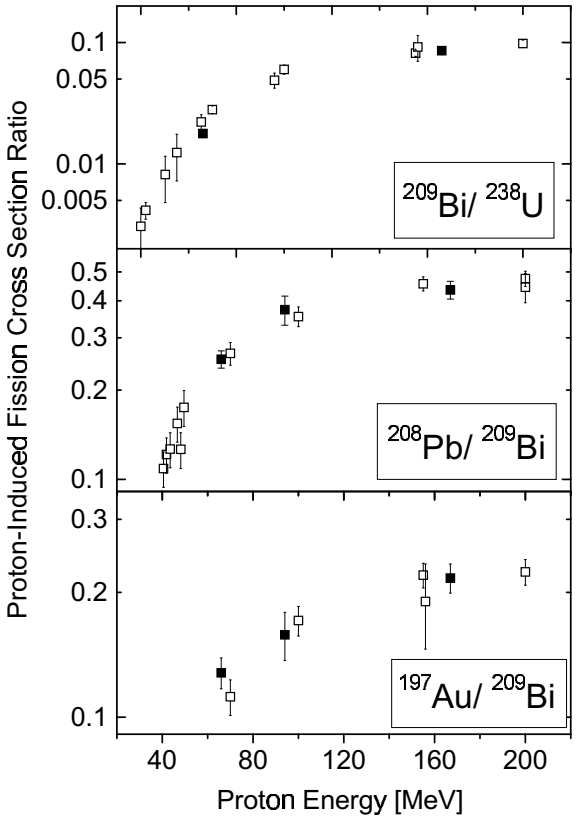

FIG. 7: Energy dependences of the ^{209}Bi/^{238}U, ^{208}Pb/^{209}Bi and ^{197}Au/^{209}Bi proton-induced fission cross-section ratios. The filled symbols represent the results of the present work. The open symbols represent results extracted from a compilation of literature experimental data [9].

main unmeasured. Therefore, we used symmetric Gaussian-shaped charge and mass distributions that are typical for similar fissioning systems formed in reactions of charged particles with subactinide nuclei [59, 60].

- The total kinetic energy of fission fragments from the systematics of Viola *et al.* [61].
- Energy-range data [62] for fission fragments in sample materials and SiO_2.
- Energy-dependent data on fission anisotropy and longitudinal linear momentum transferred to fissioning nuclei, from systematics developed in [26].

The code was verified using experimental results for TFBC detection efficiency for spontaneous fission of ^{252}Cf as well as for proton- and neutron-induced fission of different nuclides [32, 33]. The estimated error of the calculated efficiency is not more than 5% for the whole range of the projectile energies.

The calculated absolute efficiency is plotted in Fig. 6 versus incident neutron energy for the samples of $^{238}U_3O_8$, ^{209}Bi, ^{nat}Pb, ^{208}Pb, ^{197}Au, $^{nat}WO_3$, and ^{181}Ta samples employed in the present study. The values given in the graphs represent the sample thickness, averaged over the corresponding mosaic arrangement. As can be seen, the efficiency for a given sample material and neutron energy decreases with the sample thickness, which reflects the increase in the fraction of fragments escaping detection due to the energy loss in the sample. The results for different sample materials show a decrease in efficiency from the heaviest considered nuclides, ^{238}U and ^{209}Bi, to the lightest, ^{181}Ta, which is mainly governed by a decrease in the average fragment kinetic energy. A special case is the samples of tungsten trioxide. The presence of oxygen atoms in the sample material increases its stopping power and, therefore, diminishes the detection efficiency. This effect is not so pronounced for the $^{238}U_3O_8$ samples because of their relatively small thickness.

The same model and code were employed in processing of experimental data on proton-induced fission cross-sections [32], obtained at the broad proton beam facility at TSL [63] with the same detector arrangement as in the present study. The relative (p,f) cross-section results are presented in Fig. 7 together with data of other authors

from a review [9]. As seen in Fig. 7, the data of our work [32] agree with the literature data within the uncertainty limits. This provides an additional check of the developed model and code for detection efficiency calculations.

C. Determination of the fraction of peak fission events

To determine the fraction of peak fission events, k_{peak}, defined in Eq. (8), two different methods were employed.

- For the ^{238}U(n,f) reaction, we used TOF techniques supplemented by model calculations (see Sect. III.C.1).
- For the other studied reactions, an iterative unfolding procedure was used (see Sect. III.C.2).

Uncertainties in determination of the factor k_{peak} are discussed in Sect. III.C.3.

1. *Determination of the factor k_{peak} using TOF techniques*

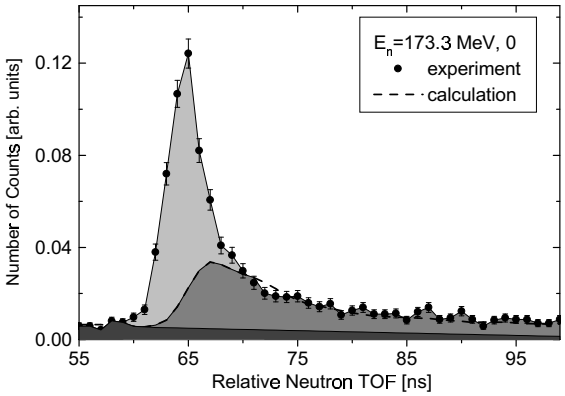

FIG. 8: The TOF spectrum of ^{238}U neutron-induced fission events induced by neutrons from the 7Li(p,n) reaction with the peak neutron energy of 173.3 MeV and its decomposition. The symbols represent experimental data of the present work. The dashed curve represents calculated TOF distribution of fission events induced by the continuum part of the neutron spectrum. The light-gray area represents fission events induced by high energy peak neutrons. The events in the dark-gray area originate from high energy continuum neutrons with energy above about 60 MeV. The black area corresponds to fission events induced by "wrap-around" neutrons with energy lower than 60 MeV, which are produced by previous proton beam micropulses.

Distributions of ^{238}U fission events on the relative neutron TOF were measured using an experimental chamber placed at a flight path of about 10 m at 0^o. An exemplary distribution, shown in Fig. 8, was obtained in irradiation by neutrons with the peak energy of 173.3 MeV. The light-gray area in the spectrum corresponds to fission events induced by the high-energy peak neutrons. Thus, the sought factor is a ratio between the light-gray area and the total area under the spectrum.

Fission events in the dark-gray area in Fig. 8 originate from high-energy continuum neutrons with energy above about 60 MeV. The black area corresponds to fission events induced by "wrap-around" neutrons with energy lower than 60 MeV, which are produced by previous proton beam micropulses. In order to estimate and subtract the last two components, the studied TOF distribution was modeled. Input data for the model calculations included the standard ^{238}U(n,f) cross-section [34] and the incident neutron spectra. The latter were either calculated according to the systematics [31] or inter- or extrapolated from the experimentally measured spectra [35, 39–44]. The resulted values of the factor k_{peak} are given in Table III.

Similar TOF spectra were obtained for ^{209}Bi fission events at the same flight path of about 10 m. However, the statistics was not sufficient for the spectrum decomposition procedure. The decomposition was not possible either for the nuclides lighter than Bi, because those measurements were performed only at a short flight path. Therefore, for all sub-actinide nuclei, we had to skip the TOF information and to employ an iterative unfolding procedure discussed in the subsequent subsection.

2. *Determination of the factor k_{peak} using the iterative unfolding procedure*

The unfolding procedure in the present work is similar to the one that was implemented in an analysis of neutron-induced single-event upsets performed by Johansson *et al.* [64]. However, the present study makes use of a more advanced description of the incident neutron spectrum (see Sect. II.B). The procedure is described below for the ^{209}Bi(n,f) reaction.

To get a first estimate of the factor k_{peak}, we constructed a trial input cross section $\sigma_f(^{209}Bi) = \sigma_f(^{238}U)N_f(^{209}Bi)/N_f(^{238}U)$, where $\sigma_f(^{238}U)$ is the standard ^{238}U(n,f) cross-section [34], and N_f denotes the fission count rate for a given nuclide, integrated over the whole corresponding TOF spectrum. The trial cross-section, fitted by a smooth curve, together with the experimental [35, 39–44] or calculated [31] neutron spectra at 0^o and the relative detection efficiency, were used to calculate the factor k_{peak} for each beam energy employed in the study. Then, the ^{209}Bi/^{238}U fission cross-section ratios were calculated according to Eq. (10), using the factors $k_{peak}(^{209}Bi)$ obtained as described above and the factors $k_{peak}(^{238}U)$ obtained with TOF techniques as described in Sect. III.C.1. Finally, multiplication of the obtained ^{209}Bi/^{238}U ratios and the standard ^{238}U(n,f) cross-section [34], with subsequent smoothing of the energy dependence, resulted in the new trial ^{209}Bi(n,f) cross-section. The procedure was repeated until convergence

TABLE III: Correction factor k_{peak} for the ^{238}U(n,f) and ^{209}Bi(n,f) reactions for neutron spectra at 0^o.

E_{npeak} (MeV)	$k_{peak}(^{238}U)$	$k_{peak}(^{209}Bi)$
34.5	0.55± 0.02	0.98± 0.02
34.5	0.43± 0.02[a]	0.97± 0.02[a]
34.5	0.35± 0.02[b]	0.96± 0.02[b]
46.3	0.44± 0.01	0.95± 0.03
66.6	0.37± 0.01	0.82± 0.01
73.9	0.36± 0.01	0.81± 0.01
89.6	0.37± 0.01	0.73± 0.02
94.1	0.37± 0.01	0.71± 0.02
111.3	0.37± 0.01	0.67± 0.02
132.9	0.39± 0.01	0.64± 0.01
144.6	0.35± 0.01	0.61± 0.01
173.3	0.42± 0.01	0.63± 0.01

[a]Correction factor at the position of the facility for activation studies [36, 38] at about 1^o.
[b]Correction factor at the Irradiation position 1 at about 4^o.

was reached. Usually, two iterations were sufficient. The correction in the last iteration did not exceed 0.5%. The resulted values of $k_{peak}(^{209}Bi)$ are presented in Table III.

The similar procedure was employed for the studied reactions with the nuclei lighter than Bi. In this case, the calculated neutron spectra at 4^o were used only. The factor k_{peak} for the monitor ^{209}Bi(n,f) reaction was calculated using the parameterization of the experimental cross-section obtained in the present work (see Sect. IV.D). In all cases, the result was found to be independent of the initially assumed cross-section.

3. *Uncertainties in the factor k_{peak}*

The uncertainties in the factor k_{peak} amounted to 2-3 % depending on the neutron energy and the studied reaction. In case of the ^{238}U(n,f) reaction, the uncertainties reflect statistical errors in the TOF spectra, as well as uncertainties in the input data of the model calculations and ambiguities in the spectrum decomposition procedure. For the other reactions, the uncertainties reflect the ones in the neutron spectrum data, which served as input in the unfolding procedure.

The studied excitation functions of the sub-actinide fission reactions have rather similar shapes, and therefore it is possible to further suppress the contribution that comes from the determination of the factor to the total uncertainty in the relative cross-section measurement. For this purpose, we studied sensitivity of the ratio $k_{peak}(X)/k_{peak}(^{209}Bi)$ (where X denotes the studied target nuclide) to the neutron spectrum data used as input in the unfolding procedure. Using different experimental [42, 43] and calculated [31] neutron spectra, we estimated that the variation in the ratio $k_{peak}(X)/k_{peak}(^{209}Bi)$ did not exceed 1 % for any studied nuclide.

IV. EXPERIMENTAL RESULTS

A. The ^{209}Bi(n,f) cross-section

The ^{209}Bi/^{238}U ratios measured in the present work were converted into absolute values using the standard ^{238}U(n,f) cross-section taken from the work of Carlson *et al.* [34]. The ^{209}Bi(n,f) cross-sections obtained in our earlier studies [21, 22] have been revised using the new approach to the fission fragment detection efficiency and the factor k_{peak}, and have been taken into account in processing of the results of the present work. The results are presented in Table IV.

TABLE IV: Neutron-induced fission cross-section of ^{209}Bi

E_{npeak} (MeV)	^{209}Bi(n,f)/^{238}U(n,f) cross-section ratio	^{209}Bi(n,f) cross-section (mb)
34.5	$(1.90\pm 0.20)\times10^{-4}$	0.311± 0.034
46.3	$(1.05\pm 0.10)\times10^{-3}$	1.71± 0.17
66.6	0.0054± 0.0005	8.42± 0.81
73.9	0.0082± 0.0007	12.6± 1.2
89.6	0.0133± 0.0012	19.2± 1.9
94.1	0.0157± 0.0014	22.4± 2.2
111.3	0.0247± 0.0027	33.5± 3.9
132.9	0.0307± 0.0027	40.5± 4.1
144.6	0.0335± 0.0031	44.2± 4.7
160.0	0.0415± 0.0038	54.6± 5.7
173.3	0.0417± 0.0040	54.9± 5.9

The uncertainties in the absolute fission cross sections given in Table IV include the uncertainty in the standard ^{238}U(n,f) cross-section [34], which amounts to 2-5% depending on the neutron energy. The uncertainties in the relative measurements are discussed in Sect. IV.B for all studied reactions together.

Our data on the ^{209}Bi(n,f) cross-sections are shown in Fig. 9 together with earlier data of Vorotnikov *et al.* [14], as well as with recent data of Nolte *et al.* [20] and Shcherbakov *et al.* [19]. In order to avoid complicating the figure, we do not show data of Staples *et al.* [17, 18], because they are very close to the results of Shcherbakov *et al.* [19].

As seen in Fig. 9, our data agree within the uncertainties with the data of Shcherbakov *et al.* [19] in the neutron energy range above about 95 MeV. However, there is a systematic deviation at lower energies. The latter data systematically exceed our data in the energy range from 30 to about 95 MeV. The deviation is most clearly seen in the energy region below about 50 MeV. This could possibly be explained by a well-known problem of non-fission background in ionization chambers discussed frequently in the literature (see, e.g., [29]). The data of Nolte *et al.* [20] are in good agreement with our data in the entire neutron-energy range of their measurements.

The ^{209}Bi(n,f) cross-section has been adopted as standard in 1996 [34], and the corresponding parameteriza-

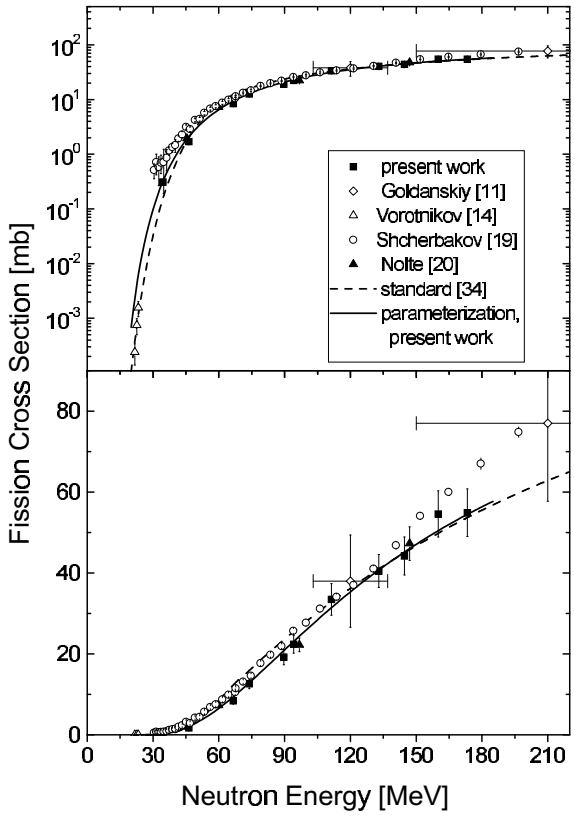

FIG. 9: Absolute neutron-induced fission cross-sections of ^{209}Bi. The scale of the vertical axis is logarithmic and linear in the upper and lower panels, respectively, in order to show the behavior of the cross-section in the different energy regions.

tion is shown in Fig. 9 as a dashed line. However, in the recommendations of the IAEA [34], it was noted that the available experimental database was not sufficient, and new experimental results were needed in order to make a more accurate parameterization. Such new parameterization is suggested in the present work (see Sect. IV.D) and shown in Fig. 9 as a solid line. A comparison of the recent parameterization with the standard one [34] shows considerable differences. The standard fit lies about 40 % lower than the new one in the 20-45 MeV energy range, and about 20 % higher between 50 and 90 MeV. For energies above 90 MeV, the standard fit lies not more than 10 % higher than the new one. The mentioned differences, however, are within the declared uncertainties for the standard parameterization [34].

B. Relative cross-sections for the nuclei lighter than Bi

The fission cross-section ratios obtained in this work for the nuclei lighter than Bi are given in Table V and

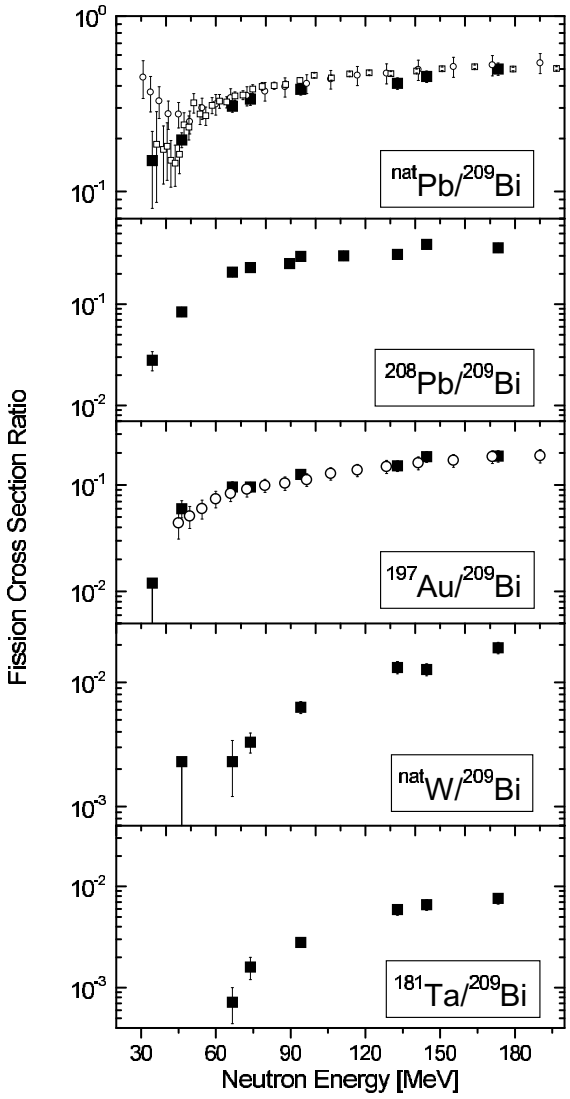

FIG. 10: Neutron-induced fission cross-section ratios ^{nat}Pb/^{209}Bi, ^{208}Pb/^{209}Bi, ^{197}Au/^{209}Bi, ^{nat}W/^{209}Bi, and ^{181}Ta/^{209}Bi versus incident energy. The results of the present study are shown as filled squares. The open squares and circles show data deduced from the results of Shcherbakov *et al.* [19] and Staples *et al.* [17, 18], respectively.

are shown in Fig. 10 together with data deduced from the previously reported results of Staples *et al.* [17, 18] for ^{209}Bi/^{235}U, ^{nat}Pb/^{235}U, and ^{197}Au/^{235}U fission cross-section ratios and Shcherbakov *et al.* [19] for ^{209}Bi/^{235}U and ^{nat}Pb/^{235}U.

The following uncertainties for the relative fission cross-sections were considered:

- sample thickness determination (2-7 % depending on specific sample arrangement),
- counting statistics in the ^{252}Cf calibration (1-2 % depending on specific detector arrangement),

- calculation of relative detection efficiency (5 %),
- variations of neutron beam intensity, sample thickness, and detection efficiency from one sandwich to another in a mosaic arrangement ($\leq$ 0.3 % in most cases, 0.6 % in the worst case),
- in-beam counting statistics and subtraction of background (0.5-50 % depending on neutron energy and specific detector-sample arrangement),
- determination of the fraction of peak fission events k_{peak} ($\leq$ 4% for the ^{209}Bi/^{238}U ratio and $\leq$ 1% for the other ratios, see Sect. III.C.3).

The total uncertainties of the obtained cross-section ratios given in Tables IV and V amount typically to 10-15 %, depending on the studied reaction and neutron energy. At the lowest energy points, the total uncertainties are dominated by statistical errors and amount to 20-50 % depending on the studied reaction.

A number of other possible error sources were considered. The direct measurements of the irradiation geometry gave uncertainty contributions of not more than 0.1%. The influence on the results caused by proton (and/or H^0 atom) contamination in the neutron field was estimated using the (p,f) systematics [9] and was found to be negligible. The attenuation of the neutron beam along the stack of the experimental chambers in Irradiation position 1 was measured directly with a pair of chambers with ^{209}Bi samples placed upstream and downstream the other chambers in the stack, and no significant effect was found. No correction was necessary for neutron-induced and spontaneous fission of contaminating heavier nuclides in the sub-actinide samples. The calibrations with a ^{252}Cf sample were performed before and after each experimental period, in order to reveal possible changes in the detector efficiency and sensitive area. In addition, possible drifts of the detector parameters during the beam exposure were checked by monitoring the respective count-rate ratios. In all cases, no effect was found outside the statistical uncertainties.

In many cases, the presented data were determined with samples of different thicknesses and obtained during different experimental periods. In all cases, the results agreed within the uncertainties, and therefore the respective weighted average values were adopted as final.

The presented upper limits of the cross-sections were obtained using the prescriptions of Schmidt *et al.* [65] for analysis of data with small counting statistics.

C. Absolute cross-sections for the nuclei lighter than Bi

The relative fission cross-sections for the nuclei lighter than Bi were converted into absolute ones using the revised set of the experimental ^{209}Bi(n,f) cross-section data given in Table IV. The resulted absolute cross-sections are given in Table VI and shown in Fig. 11 together with our earlier data for ^{208}Pb [21, 22], as well as with earlier data of Reut *et al.* for ^{197}Au and ^{nat}Pb [12], Dzhelepov *et al.* for ^{nat}W [13], Vorotnikov *et al.* [14], Shcherbakov *et al.* [19], and Nolte *et al.* [20] for ^{nat}Pb, Vorotnikov [15], and Staples *et al.* [17, 18] for ^{197}Au. The given uncertainties of our results include those of the new data set for the ^{209}Bi(n,f) cross-section (see Table IV). The

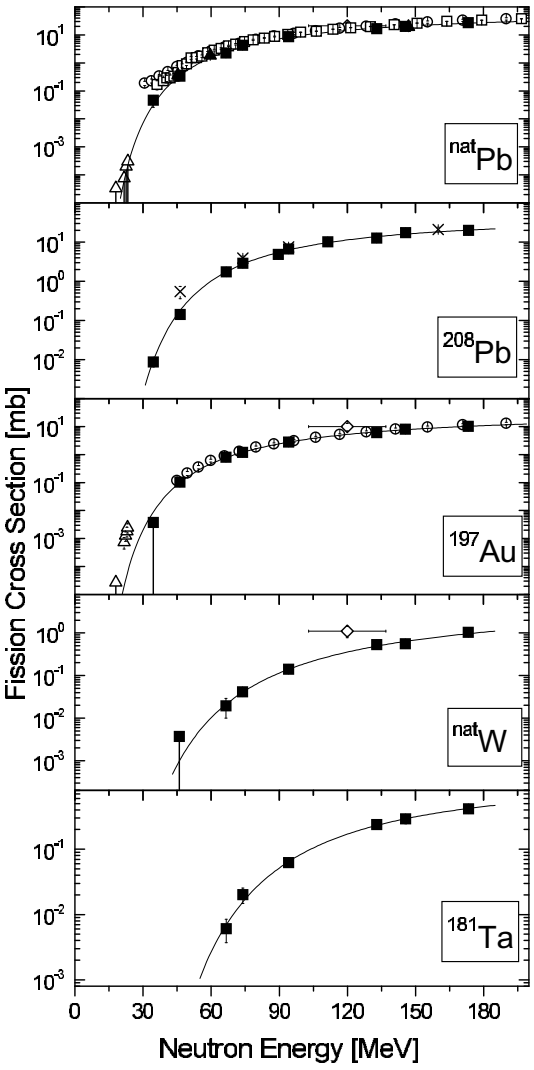

FIG. 11: Absolute neutron-induced fission cross-sections of ^{nat}Pb, ^{208}Pb, ^{197}Au, ^{nat}W, and ^{181}Ta. The results of the present study are shown as filled squares. Crosses represent our earlier data for ^{208}Pb [21, 22]. Filled triangles represent recent data of Nolte *et al.* for ^{nat}Pb [20]. Open squares, circles and triangles represent data of Shcherbakov *et al.* [19], Staples *et al.* [17, 18] and Vorotnikov *et al.* [14, 15], respectively. Results of Reut *et al.* [12] and Dzhelepov *et al.* [13] are shown as diamonds, with horizontal error bars that represent the energy spread of the neutron beam. The lines represent parameterizations of the present work (see the text).

TABLE V: Relative neutron-induced fission cross-sections for the nuclei lighter than Bi.

	Fission cross-section ratios				
E_{npeak}	^{nat}Pb/^{209}Bi	^{208}Pb/^{209}Bi	^{197}Au/^{209}Bi	^{nat}W/^{209}Bi	^{181}Ta/^{209}Bi
(MeV)					
34.5	0.15± 0.07	0.028± 0.006	< 0.012		
46.3	0.197± 0.019	0.084± 0.007	0.060± 0.011	< 0.0023	
66.6	0.306± 0.023	0.208± 0.016	0.096± 0.011	0.0023± 0.0011	(7.2± 2.8)10¯4
73.9	0.336± 0.026	0.230± 0.018	0.096± 0.010	0.0033± 0.0006	0.0016± 0.0004
89.6		0.252± 0.020			
94.1	0.383± 0.028	0.297± 0.023	0.126± 0.013	0.0063± 0.0007	0.0028± 0.0003
111.3		0.301± 0.026			
132.9	0.414± 0.031	0.310± 0.024	0.151± 0.017	0.0132± 0.0015	0.0059± 0.0007
144.6	0.452± 0.034	0.39± 0.03	0.184± 0.021	0.0127± 0.0014	0.0066± 0.0008
173.3	0.50± 0.04	0.36± 0.03	0.187± 0.023	0.019± 0.002	0.0076± 0.0009

TABLE VI: Absolute neutron-induced fission cross-sections.

	Fission cross-section				
E_{npeak}	^{nat}Pb	^{208}Pb	^{197}Au	^{nat}W	^{181}Ta
(MeV)	(mb)	(mb)	(mb)	(mb)	(mb)
34.5	0.047±0.021	0.0087±0.0021	< 0.0038		
46.3	0.336±0.044	0.143±0.018	0.103±0.019	< 0.004	
66.6	2.58±0.30	1.75±0.21	0.81±0.12	0.020±0.010	0.0061±0.0024
73.9	4.24±0.47	2.90±0.33	1.20±0.17	0.041±0.008	0.020±0.005
89.6		4.8±0.5			
94.1	8.6±1.0	6.6±0.8	2.81±0.39	0.141±0.020	0.063±0.009
111.3		10.1±1.3			
132.9	16.8±1.7	12.6±1.3	6.1±0.9	0.53±0.08	0.24±0.04
144.6	20.0±2.3	17.3±2.0	8.1±1.2	0.56±0.08	0.29±0.05
173.3	27.5±3.7	19.9±2.7	10.3±1.6	1.04±0.15	0.42±0.07

absolute data of Staples *et al.* shown in Fig. 11 were deduced by multiplying the ^{197}Au/^{235}U ratios [17, 18] with the standard ^{235}U(n,f) cross-section [34].

D. Cross-section parameterizations

Parameterizations of the absolute (n,f) cross-sections of sub-actinide nuclei suggested in the present work are based on our data presented in Tables IV and VI, together with the data of Nolte *et al.* [20] for ^{209}Bi and ^{nat}Pb. The following universal parameterization of the cross section σ_f versus neutron energy E_n is suggested:

$$\sigma_f(E_n) = P_1 exp(-(P_2/E_n)^{P_3}), \qquad (11)$$

where P_1, P_2, and P_3 are fitting parameters that depend on the target nuclide. The values of the parameters, obtained by the least-squares method, are given in Table VII. The parameterizations are shown as solid lines in Figs. 9 and 11.

V. DISCUSSION

The first published measurement results are presented for the ^{nat}Pb, ^{197}Au, ^{nat}W, and ^{181}Ta(n,f) cross-sections. The ^{208}Pb(n,f) reaction has been studied by our group earlier [21, 22], and those results, shown as crosses in Fig. 11, are in reasonable agreement with the present ones. The only exclusion is the datum at 45 MeV, which is believed to be erroneous in our early study, due to a poor signal-to-background ratio in that particular measurement. The present results are obtained with better counting statistics and more sophisticated data processing techniques.

Earlier measurements for ^{197}Au and ^{nat}Pb in the energy region 18-23 MeV were performed by Vorotnikov [15] and Vorotnikov and Larionov [14], respectively, using a d-T neutron source and solid-state nuclear track detectors. Their results for ^{nat}Pb are compatible with the present data, while the results for ^{197}Au seem to be too high.

A measurement for ^{nat}Pb and ^{197}Au was performed by Staples *et al.* [17, 18] using a parallel-plate ionization chamber irradiated by neutrons from the LANSCE facility with "white" spectrum. Only preliminary data are available. The data for ^{197}Au are in reasonable agreement with the present ones, while the data for ^{nat}Pb lie systematically higher. In the energy range below about

TABLE VII: Parameters of the (n,f) cross-section parameterizations in Eq. (11) .

Target nuclide	P_1	P_2	P_3	χ^2/ν	Energy region of applicability
	(mb)	(MeV)			(MeV)
^{209}Bi	109.2	131.5	1.32	1.33	30-180
^{nat}Pb	70.4	171.9	1.27	0.53	30-180
^{208}Pb	45.4	150.3	1.47	0.64	30-180
^{197}Au	35.0	207.2	1.18	0.09	45-180
^{nat}W	6.1	292.5	1.17	0.47	60-180
^{181}Ta	1.29	186.0	1.61	0.32	60-180

50 MeV, the data of Staples *et al.* for ^{nat}Pb are distinctly larger. The disagreement increases with decreasing incident energy and amounts to about one order of magnitude at 35 MeV. Furthermore, the ^{nat}Pb/^{209}Bi ratios deduced from the data of Staples *et al.* (see Fig. 10) show an unexpected energy dependence. As the neutron energy decreases to below 50 MeV, the smooth decrease of the ratio turns into a sharp rise, which is difficult to understand, having in mind that the fission barrier for lead isotopes is higher than that for bismuth [66]. This leads to the suggestion that some background contribution may not have been fully taken into account in the LANSCE measurements. A similar feature is seen in the dataset of Shcherbakov *et al.* for ^{nat}Pb [19] obtained at the "white" neutron source at the GNEIS facility in Gatchina. Their data are similar to the data of Staples *et al.* at neutron energies above about 45 MeV, although at lower energies they are somewhat closer to our results. The disagreement with our data amounts to a factor of about three at about 35 MeV.

Early measurements by Reut *et al.* [12] for ^{nat}Pb and ^{197}Au and by Dzhelepov *et al.* [13] for ^{nat}W were made using neutrons from the Cu(d,n) reaction with a broad spectrum, as indicated by the horizontal error bars in Fig. 11. The results agree qualitatively with the more recent and precise data.

The data presented in Fig. 11 allow some conclusions on common features of sub-actinide neutron fission cross-sections. The cross-section increases with neutron energy and with the atomic number of the target nucleus. The slope of the cross-section versus energy is steepest in the near-barrier region (20-25 MeV), and becomes flatter with increasing energy. The slope at a specific incident energy is steeper for lighter nuclei. The properties summarized above (see also [24]) are similar to those of the (p,f) data (see, e.g., [9]).

VI. CONCLUSIONS

Experimental (n,f) cross-sections for sub-actinide nuclei in the intermediate energy region have been measured. Most of the data are obtained for the first time. Progress in data processing has been achieved due to good control of the incident neutron spectrum and the detection efficiency corrections. In most cases, the results are compatible with scarcely available earlier data, but a large discrepancy is observed with respect to the recent data of Staples *et al.* [17, 18] and Shcherbakov *et al.* [19] for the ^{209}Bi(n,f) and ^{nat}Pb(n,f) cross-sections at energies below 50 MeV.

Acknowledgments

The authors are thankful to the staff of The Svedberg Laboratory where the experimental part of the study was performed. The samples were partly provided and/or characterized by Drs. S.M. Soloviev, Yu.G. Pokrovskiy, and A.V. Gromov at V.G. Khlopin Radium Institute. The present work was supported in part by ISTC.

[1] H. Nifenecker, S. David, J. M. Loiseaux and O. Meplan, Nucl. Instr. and Meth. in Phys. Res. A463, 428 (2001).
[2] A.J. Koning, J.-P. Delaroche, and O. Bersillon, Nucl. Instr. and Meth. in Phys. Res. A414, 49 (1998).
[3] Yu.N. Shubin, A.V. Ignatyuk, A.Yu. Konobeev, V.P. Lunev, and E.V. Kulikov, Proc 2nd Conf. on ADTT, Kalmar, Sweden, June 3-7, 1996, ed. H. Condé: Uppsala University, 1997, vol. 2, p. 953.
[4] R.E. Prael, Trans. Am. Nucl. Soc. 73, 349 (1995).
[5] A.V. Prokofiev, S.G. Mashnik, and A.J. Sierk, Nucl. Sci. Eng. 131, 78 (1999).
[6] M.C. Duijvestijn, A.J. Koning, J.P.M. Beijers, A. Ferrari, M. Gastal, J. van Klinken, and R.W. Ostendorf, Phys. Rev. C59, 776 (1999).
[7] R. Michel and P. Nagel, NEA Report NSC/DOC(97)-1, January 1997.
[8] W.U. Schröder and J.R. Huizenga, Nucl. Phys. A502, 473 (1989).
[9] A.V. Prokofiev, Nucl. Instr. and Meth. in Phys. Res. A463, 557 (2001).
[10] E.L. Kelly and C. Wiegand, Phys. Rev. 73, 1135 (1948).
[11] V.I. Goldanskiy, V.S. Penkina, and E.Z. Tarumov, Sov.

Phys. - JETP 29, 778 (1955) (in Russian).
[12] A.A. Reut, G.I. Selivanov, and V.V. Yuriev, Institute of Nuclear Problems report, Moscow, 1950 (in Russian, unpublished).
[13] V.P. Dzhelepov, B.M. Golovin, and Yu.M. Kazarinov, Institute of Nuclear Problems report, Moscow, 1950 (in Russian, unpublished).
[14] P.E. Vorotnikov and L.S. Larionov, Sov. J. Nucl. Phys. 40, 552 (1984).
[15] P.E. Vorotnikov, Sov. J. Nucl. Phys. 47, 1147 (1988).
[16] H. Vonach, A. Pavlik, R. Nelson and S. Wender, unpublished; R.E. Prael, Report LA-UR-94-1817, Los Alamos National Laboratory, 1994 (unpublished); H. Vonach, private communication.
[17] P. Staples, P.W. Lisowski, and N.W. Hill, presented in APS/AAPT Conference, Washington, April 18-21, 1995; Bull. Am. Phys. Soc. 40, 962 (1995).
[18] P. Staples, private communication (1996) with an update of the data from Ref. [17].
[19] O. Shcherbakov, A. Donets, A. Evdokimov, A. Fomichev, T. Fukahori, A. Hasegawa, A. Laptev, V. Maslov, G. Petrov, S. Soloviev, Y. Tuboltsev and A. Vorobyev, Journal of Nuclear Science and Technology, Supplement 2, 230 (2002).
[20] R. Nolte, M.S. Allie, P.J. Binns, F.D. Brooks, A. Buffler,V. Dangendorf, K. Langen, J.-P. Meulders, W.D. Newhauser, F. Ross, and H. Schuhmacher, Journal of Nuclear Science and Technology, Supplement 2, 311 (2002).
[21] V.P. Eismont, A.V. Prokofiev, A.N. Smirnov, K. Elmgren, J. Blomgren, H. Condé, J. Nilsson, N. Olsson, T. Rönnqvist, and E. Tranéus, Phys. Rev. C53, 2911 (1996).
[22] V.P. Eismont, A.V. Prokofiev, A.N. Smirnov, J. Blomgren, H. Condé, K. Elmgren, J. Nilsson, N. Olsson, and E. Ramström, Proc. 2nd Int. Conf. on Accelerator Driven Transmutation Technologies and Applications, Kalmar, Sweden, June 3-7, 1996, ed. H. Condé: Uppsala University, 1997, vol. 2, p. 606.
[23] V.P. Eismont, A.V. Prokofiev, A.N. Smirnov, S.M. Soloviev, H. Condé, K. Elmgren, and N. Olsson, Proc. 3rd International Conference on Accelerator Driven Transmutation Technologies and Applications, Praha (Pruhonice), Czech Republic, June 7 - 11, 1999 (available as CD-ROM, paper Mo-O-C8).
[24] V.P. Eismont (Project Manager), "Measurements of Neutron-Induced Fission Cross Sections in Energy Region $15 < En < 160$ MeV for Basic and Applied Researches", Final Project Technical Report of ISTC 540-97, V.G.Khlopin Radium Institute, St.-Petersburg, 1999.
[25] V.P. Eismont, I.V. Ryzhov, A.N. Smirnov, G.A. Tutin, H. Condé, N. Olsson, and A.V. Prokofiev, Proc. 6th OECD/NEA Information Exchange Meeting on Actinide and Fission Product Partitioning and Transmutation, Madrid, December 11-13, 2000 (available as CD-ROM, paper 36).
[26] A. Prokofiev, PhD Thesis, Uppsala University (2001).
[27] V.P. Eismont, A.V. Kireev, I.V. Ryzhov, G.A. Tutin, H. Condé, K. Elmgren, and S. Hultqvist, Proc. 2nd Int. Conf. on Accelerator Driven Transmutation Technologies and Applications, June 3-7, 1996, Kalmar, Sweden, ed. H. Condé: Uppsala University, 1997, vol. 2, p. 618.
[28] V.P. Eismont, A.V. Kireev, I.V. Ryzhov, S.M. Soloviev, G.A. Tutin, H. Condé, K. Elmgren, N. Olsson, and P.-U. Renberg, Proc. 3rd Int. Conf. on Accelerator Driven Transmutation Technologies and Applications, Praha, Czech Republic, 1999 (available as CD-ROM, paper Mo-O-C7).
[29] I.V. Ryzhov, G.A. Tutin, V.P. Eismont, A.G. Mitryukhin, V.S. Oplavin, S.M. Soloviev, H. Condé, N. Olsson and P.-U. Renberg. Journal of Nuclear Science and Technology, Supplement 2, 1410 (2002).
[30] R.K. Jain, A.V. Prokofiev, A.N. Smirnov, and L. Tommasino, Radiat. Meas. 34, 129 (2001).
[31] A.V. Prokofiev, S.G. Mashnik, M.B. Chadwick, N. Olsson, and L.S. Waters, Journal of Nuclear Science and Technology, Supplement 2, 112 (2002).
[32] V.P. Eismont (Project Manager), "Measurements and Comparison of Proton- and Neutron-Induced Fission Cross Sections of Lead and Neighboring Nuclei in the 20-200 MeV Energy Region." Final Project Technical Report of ISTC 1309-99, V.G. Khlopin Radium Institute, St.-Petersburg, 2002.
[33] A.N. Smirnov, N.P. Filatov, A.V. Prokofiev, and P.-U. Renberg, Nucl. Instr. and Meth. in Phys. Res. A (to be submitted).
[34] A.D. Carlson, S. Chiba, F.-J. Hambsch, N. Olsson, and A.N. Smirnov, IAEA Report INDC(NDS)-368, Vienna, 1997; Proc. Int. Conf. on Nuclear Data for Science and Technology, Trieste, Italy, May 19-24, 1997, Part II, p. 1223.
[35] H. Condé, S. Hultqvist, N. Olsson, T. Rönnqvist, R. Zorro, J. Blomgren, G. Tibell, A. Hakånsson, O. Jonsson, A. Lindholm, L. Nilsson, P.-U. Renberg, A. Brockstedt, P. Ekström, M. Österlund, F. P. Brady, and Z. Szeflinski, Nucl. Instr. and Meth. in Phys. Res. A292, 121 (1990).
[36] J. Klug, J. Blomgren, A. Atac, B. Bergenwall, S. Dangtip, K. Elmgren, C. Johansson, N. Olsson, A.V. Prokofiev, J. Rahm, O. Jonsson, L. Nilsson, P.-U. Renberg, P. Nadel-Turonski, A. Ringbom, A. Oberstedt, F. Tovesson, C. Le Brun, J.F. Lecolley, F.R. Lecolley, M. Louvel, N. Marie, C. Schweitzer, C. Varignon, Ph. Eudes, F. Haddad, M. Kerveno, T. Kirchner, C. Lebrun, L. Stuttge, I. Slypen, A.N. Smirnov, R. Michel, S. Neumann, and U. Herpers, Nucl. Instr. and Meth. in Phys. Res. A489, 282 (2002).
[37] J.F. Ziegler, J.P. Biersack, and U. Littmark, The Stopping and Range of Ions in Solids, Pergamon Press, New York, 1985.
[38] S. Neumann, Ph.D. thesis, University of Hannover (1999); R. Michel, W. Glasser, S. Neumann, A.N. Smirnov, A.V. Prokofiev, P. Malmborg, and O. Jonsson, The Svedberg Laboratory Progress Report 1998-1999, Uppsala, 2000, p. 20 (unpublished).
[39] T. Rönnqvist, private communication.
[40] R.C. Byrd and W.C. Sailor, Nucl. Instr. and Meth. in Phys. Res. A274, 494 (1989).
[41] S. Stamer, W. Scobel, and R.C. Byrd. Proc. of a Specialists' Meeting on Neutron Cross-Section Standards for the Energy Region above 20 MeV, Uppsala, Sweden, May 21-23, 1991, NEANDC-305/U, p. 154.
[42] N. Nakao, Y. Uwamino, T. Nakamura, T. Shibata, N. Nakanishi, M. Takada, E. Kim, and T. Kurosawa, Nucl. Instr. and Meth. in Phys. Res. A420, 218 (1999).
[43] M. Baba, Y. Nauchi, T. Iwasaki, T. Kiyosumi, M. Yoshioka, S. Matsuyama, N. Hirakawa, T. Nakamura, Su. Tanaka, S. Meigo, H. Nakashima, Sh. Tanaka and N. Nakao, Nucl. Instr. and Meth. in Phys. Res. A428, 454 (1999).
[44] H. Schuhmacher, H.J. Brede, V. Dangendorf, M. Kuhfuss, J.P. Meulders, W.D. Newhauser, and R. Nolte, Nucl. Instrum. Methods in Phys. Res. A421, 284 (1999).

[45] R. Nolte, M.S. Allie, P.J. Binns, F. Brooks, A. Buffler, V. Dangendorf, J.P. Meulders, F. Roos, H. Schuhmacher, and B. Wiegel, Nucl. Instr. and Meth. in Phys. Res. A476, 369 (2002).
[46] G.G. Ohlsen, Nucl. Instr. Meth. 37, 240 (1965).
[47] S.D. Schery, L.E. Young, R.R. Doering, S.M. Austin, and R.K. Bhowmik, Nucl. Instr. and Meth. 147, 399 (1977).
[48] H. Orihara, S. Nishihara, K. Furukawa, M. Kabasawa, T. Kawamura, Y. Takahashi, T. Nakagawa, and K. Maeda, Nucl. Instr. and Meth. in Phys. Res. 257, 189 (1987).
[49] C.J. Batty, B.E. Bonner, E. Friedman, C. Tschalar, L.E. Williams, A.S. Clough, and J.B. Hunt, Nucl. Phys. A120, 297 (1968).
[50] J.W. Watson, B.D. Anderson, A.R. Baldwin, C. Lebo, B. Flanders, W. Pairsuwan, R. Madey, and C.C. Foster, Nucl. Instr. and Meth. in Phys. Res. 215, 413 (1983).
[51] X. Yang, L. Wang, J. Rapaport, C.D. Goodman, C.C. Foster, Y. Wang, E. Sugarbaker, D. Marchlenski, S. de Lucia, B. Luther, L. Rybarcyk, T.N. Taddeucci, and B.K. Park, Phys. Rev. C52, 2535 (1995).
[52] S.G. Mashnik, M.B. Chadwick, P.G. Young, R.E. MacFarlane, and L.S. Waters, LANL Report LA-UR-00-1067, Los Alamos (2000) (unpublished); presented at 2000 ANS/ENS International Meeting, Nuclear Applications of Accelerator Technology (AccApp00), November 12-16, Washington, DC, USA; e-print: http://xxx.lanl.gov/e-print/nucl-th/0011066.
[53] M.B. Chadwick, P.G. Young, S. Chiba, S.C. Frankle, G.M. Hale, H.G. Hughes, A.J. Koning, R.C. Little, R.E. MacFarlane, R.E. Prael, and L.S. Waters, Nucl. Sci. Eng. 131, 293 (1999).
[54] C. Kalbach, Phys. Rev. C37, 2350 (1988).
[55] V.P. Eismont, A.V. Prokofiev, and A.N. Smirnov, Radiat. Meas. 25, 151 (1995).
[56] V.A. Nikolaev, Radiat. Meas. 25, 337 (1995).
[57] V.P. Eismont and A.N. Smirnov, Pribory i tehnika experimenta (Sov. Journal of Experimental Techniques and Devices) No. 6, pp. 5-9 (1983) (in Russian).
[58] C.M. Zoller, Ph.D. thesis, Darmstadt (1995) (in German).
[59] Yu. P. Gangrskiy, B. Dalhsuren and B.N. Markov. Nuclear Fission Fragments. Moscow, Energoatomizdat, 1986 (in Russian).
[60] M.C. Duijvestijn, A.J. Koning, and F.-J. Hambsch, Phys. Rev. C64, 014607 (2001).
[61] V.E. Viola, K. Kwiatkowski, and M. Walker, Phys. Rev. C31, 1550 (1985).
[62] L.C. Northcliffe and R.F. Schilling, Nucl. Data Tables A7, 233 (1970).
[63] O. Jonsson, P.-U. Renberg, A. Prokofiev, and A. Smirnov, TSL Progress Report 1998-1999, Ed. A. Ingemarsson, Uppsala University (2000), p. 43 (unpublished).
[64] K. Johansson, P. Dyreklev, B. Granbom, N. Olsson, J. Blomgren, and P.-U. Renberg, IEEE Trans. Nucl. Sci. 45, 2519 (1998).
[65] K.-H. Schmidt, C.-C. Sahm, K. Pielenz, and H.-G. Clerc, Z. Phys. A316, 29 (1984)
[66] A.V. Ignatyuk, G.N. Smirenkin, M.G. Itkis, S.I. Mulgin, and V.N. Okolovich, Sov. J. Part. Nucl. 16, 307 (1985).

Appendix VIII

Measurement of the Absolute Differential Cross Section for np Elastic Scattering Near 200 MeV

M. Sarsour[a], T. Peterson[a], M. Planinic[a], S.E. Vigdor[a], C. Allgower[a], B. Bergenwall[b], J. Blomgren[b], T. Hossbach[a], W.W. Jacobs[a], C. Johansson[b], J. Klug[b], A.V. Klyachko[a], P. Nadel-Turonski[b], L. Nilsson[b], N. Olsson[b], S. Pomp[b], J. Rapaport[c], T. Rinckel[a], E.J. Stephenson[a], U. Tippawan[b], S.W. Wissink[a] and Y. Zhou[a]

[a]Indiana University Cyclotron Facility, Indiana University, Bloomington, IN, USA

[b]Uppsala University, Uppsala, Sweden

[c]Ohio University, Athens, OH, USA

We report preliminary results of a double-scattering experiment applying the technique of neutron tagging to measure the absolute differential cross section for np scattering in an energy and angle region where earlier experiments have shown serious discrepancies among themselves and with energy-dependent partial wave analyses.

The np scattering database at intermediate energies is marred by significant shape inconsistencies and absolute normalization errors in differential cross section measurements [1,2]. These problems have led to controversy [2,3] over the selection criteria for data in partial wave analyses [4] and over extracted values of the charged πNN coupling constant. We report preliminary results of an np scattering experiment designed to give better control over systematic errors, and thus to resolve discrepancies in the database. The tagged neutron technique we apply differs extensively from previous methods, and can provide absolute cross section precision approaching $\pm 1\%$.

The experimental setup is illustrated in Fig. 1. The neutron production reaction p+d $\rightarrow$ n+2p is induced by a 203 MeV electron-cooled, stored proton beam on a D_2 gas jet target (GJT) in the IUCF Cooler [5]. Energy, time, and two-dimensional position measurements for both recoil protons in the tagger determine the 4-momentum of each produced neutron on an event-by-event basis. The tagger comprised an array of four 6.4×6.4 cm^2 silicon double-sided strip detectors (DSSD) with 480 μm readout pitch, each followed by a silicon pad (backing) detector of the same area. Fast front-end electronics for the DSSD's permitted a tagger-based event trigger on neutron candidates, regardless of whether they interacted in the forward target and/or detectors. The forward setup included a solid secondary scattering target of CH_2 or C, a forward array of plastic scintillators for triggering and energy information, and a set of (x, y, u) multi-wire proportional chambers (MWPCs) to track forward protons from np scattering events.

Tagged neutron events were recorded in three mutually exclusive event streams, triggered by a two-particle hit pattern in the tagger in anti-coincidence with scintillators (LUV, SUV) used to veto charged particles produced upstream of the secondary target,

and coupled with (a) no forward coincidence (for neutron flux monitoring); (b) both ΔE scintillator and rear hodoscope in coincidence (for np scattering candidates); or (c) rear hodoscope but not ΔE in coincidence (for evaluating the neutron detection efficiency of the hodoscope). Neutron beam properties were defined by identical cuts for all three event streams, so that associated systematic uncertainties would cancel in the ratios from which the absolute np scattering cross section was extracted. Among the common cuts was one on particle identification in the tagger, requiring either that both recoil particles stop in the DSSD's ("2-stop" events) or that one of the two be consistent with a proton stopping in its backing detector ("1-punch" events). Other common cuts defined the area on the secondary target within which acceptable tagged neutrons had to impinge.

The analysis used additional cuts to define np free-scattering very sparingly, relying instead on accurate background subtraction via frequent switching between the precisely matched CH_2 and C targets. This removed not only p-C quasifree scattering events, but also background from other sources, such as scattering from the aluminum support frame for the secondary target, or protons produced in the GJT that passed above the top of the LUV and SUV scintillators. The success of the subtraction is illustrated in Fig. 2, which shows the vertical position (y_{tag}) of neutrons on the secondary target, as reconstructed from the tagger information. Background-subtracted spectra were used to evaluate efficiencies for the few non-common cuts imposed to select free-scattering events, including ones on ΔE *vs.* θ_p^{scat} and on the MWPC proton track quality. Cuts on $E_{hodoscope}$, and associated sensitivity to the reaction tail in this thick scintillator, were avoided.

Currently, the analysis of the absolute differential cross sections is done for the "2-stop" events to $\sim \pm 5\%$ systematic uncertainty, while the total flux of "1-punch" events is still being evaluated. The two event classes give completely consistent angular distribution shapes - an important crosscheck on the reliability of the experiment and analysis, because these events come from complementary regions of the tagged beam profile and energy distribution - but for now the 1-punch absolute cross section has simply been normalized to that for 2-stop events. The present results, averaged over the 2-stop and normalized 1-punch samples, are shown in Fig. 3 as filled circles and compared with the J. Rahm et al. [2] results at 162 MeV and the Nijmegen partial wave analysis (PWA93) at neutron energy TLAB = 194 MeV [6]. Our results are so far reasonably consistent with PWA93, within systematic uncertainties of $\sim \pm 5\%$. Both the statistical and systematic errors should improve significantly as the analysis is completed.

REFERENCES

1. B.E. Bonner *et al.*, Phys. Rev. Lett. **41**, 1200 (1978); W. H*ü*rster *et al.*, Phys. Lett. B**90**, 367 (1980).
2. J. Rahm *et al.*, Phys. Rev. C**57**, 1077 (1998).
3. D.V. Bugg and R. Machleidt,Phys. Rev. C**52**, 1203 (1995); M.C.M. Rentmeester, R.G.E. Timmermans and J.J. deSwart, Phys. Rev. C**64**, 034004 (2001).
4. V. Stoks *et al.*, Phys. Rev. C**48**, 792 (1993).
5. T. Peterson, Ph.D. Thesis Dissertation, Indiana University (2000) unpublished.
6. http://nn-online.sci.kun.nl/NN/

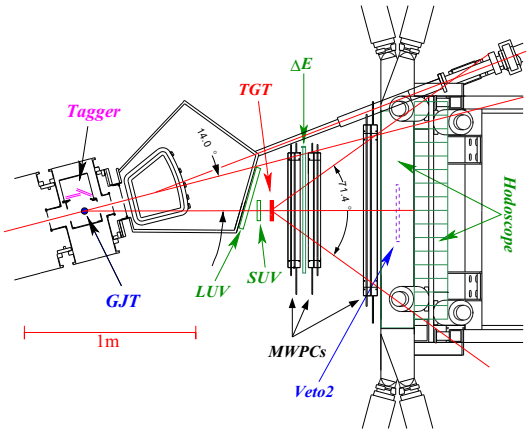

Figure 1. A top view of the experimental setup for the np scattering experiment.

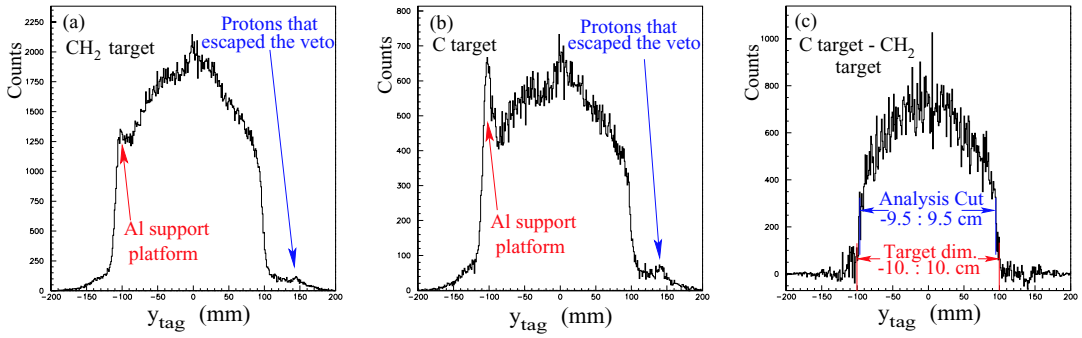

Figure 2. y_{tag} distributions for (a) CH_2, (b) C, and (c) the difference between them.

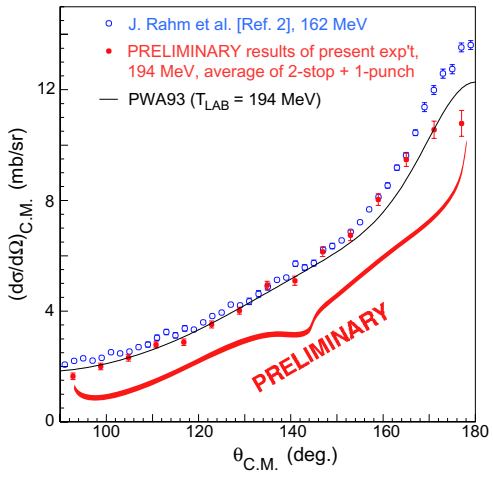

Figure 3. Preliminary cross section results (statistical errors only) from the present experiment.

Appendix IX

FAST-NEUTRON DIAGNOSTICS FOR ACCELERATOR-DRIVEN TRANSMUTATION

J. BLOMGREN
Department of Neutron Research, UppsalaUniversity, Sweden.
E-mail: jan.blomgren@tsl.uu.se

R. NOLTE
Physikalisch-Technische Bundesanstalt, Braunschweig, Germany.
E-mail:ralf.nolte@ptb.de

A. PLOMPEN
Insitute for Reference Materials and Measurements,Geel, Belgium.
E-mail:arjan.plompen@cec.eu.int

I. RYZHOV
Khlopin Radium Institute, St. Petersburg, Russia.
E-mail:igor.ryzhov@atom.nw.ru

In traditional critical reactors, the neutron energies extend up to a few MeV. The neutron diagnostics is commonly based on activation techniques and fission ionization chambers. In accelerator-driven systems, the neutron spectrum will extend all the way up to the incident beam energy, i.e., several hundred MeV or even up to GeV energies. The high energy allows diagnostics with a set of measurement techniques hitherto not used in reactor environments.

1. General aspects of neutron detection in reactors

1.1. *Neutron detection in critical reactors*

Neutrons cannot be detected directly, because they do not ionize; instead they have to interact with a nucleus, and the emitted secondary particles can be detected. Therefore, the neutron detection techniques for a given application depend strongly on the neutron energy, because the available nuclear reactions vary significantly with energy.

In critical reactors, neutrons of energies from essentially zero up to a few MeV are present. At these energies, only a few types of nuclear reaction channels are open. These are scattering and capture in essentially all materials, and fission in actinides. In addition, (n,p) and (n,α) reactions take place in some elements.

Since neutrons are needed to sustain the chain reaction, they are of obvious interest for reactor diagnostics, and the neutron energy spectrum contains indeed important information about the state of the core. At critical reactors, however, it is extremely difficult to measure the neutron energy spectrum precisely. The

reason is that for a general neutron-induced nuclear reaction, the energy of the ejectile is not directly linked to the incident neutron energy. Only a few reactions preserve the information about the incident energy, for instance neutron-proton scattering. If the direction of the incident neutron is known, measurement of the recoil proton energy can be used to determine the incident neutron energy. In reality, this is not useful inside the core of a reactor, because neutrons travel in all directions, and the energies are so low that recoil detection is very difficult.

An important practical prerequisite for detection of low-energy neutrons is that it employs a nuclear reaction with large positive Q-value, i.e., with significantly larger energy of the secondary particles than the incident neutron. This is necessary to get a signal sufficiently large to record, but it has the drawback that the sensitivity to the incident neutron energy is in reality lost. Thus, measurement of the energy of the secondary particles is in practice not a useful tool for neutron energy determination. What remains is then energy measurements based on threshold techniques. This means that many nuclear reactions, all with a significant energy release, are used, so that detection of a certain secondary product signals the presence of neutrons over a certain energy threshold.

As a consequence, measurements of low-energy neutron energy spectra have to be done with a limited set of methods. Measurements of fission using ionization chambers can give some energy information, if performed with chambers loaded with different actinides with different fission thresholds. Similarly, activation using a number of reactions with different thresholds can provide some energy spectrum information.

For introductions and reviews of neutron detection methods, see, e.g., refs. [1,2].

1.2. *Classification of neutron diagnostics techniques*

When discussing neutron diagnostics, it is useful to make a few distinctions. First, diagnostics can be either active or passive. Active means that some type of detector is used and read out in real time. Thus, information about the state of the core can be obtained immediately. Fission ionization chambers have these properties. Passive diagnostics refer to techniques where the time information is lost. Activation can serve as an example.

A second distinction is between inside-core and outside-core diagnostics. At critical reactors, the neutron penetration is rather limited. Therefore, most or all of the diagnostics devices have to be located inside the core. For ADS, this is not necessarily the case. The total cross sections for neutrons have a wide minimum in the 200-400 MeV range for most elements. This means that the penetration has a maximum. Therefore, neutrons in this energy range might be used to probe phenomena deep inside the reactor system even with detectors placed outside the active volume.

Whether the diagnostics is within the core or outside it can be of major importance. For high-energy neutrons, it might be possible to move diagnostics to outside the core, where the environment is very different. For instance, outside the core, essentially all types of background are dramatically lower, and there is

more space available. Hence, much more advanced techniques than for inside-core diagnostics can be used. A potentially important side-effect of putting diagnostics outside the core is that it becomes intrinsically direction-sensitive, since only the outgoing flux is determined. Which parts of the system to investigate now becomes a matter of the technical design of the entire system. The location of channels and viewports for neutrons to escape from the core determines which information can be accessed.

A third aspect is directional sensitivity. In critical reactors, the diagnostics used is in general insensitive to the neutron direction. In the central regions of such a core, the flux is essentially uniform. For accelerator-driven systems, however, the high-energy neutrons are created in a localized region, the target, while no such fast neutrons are created in the blanket. Low-energy neutrons, on the other hand, are created all over the volume, i.e., both in the target and the blanket, but they might be created un-evenly, resulting in a net flux direction.

Finally, the energy sensitivity is an important aspect. In general, information on the incident neutron energy is lost when a neutron induces a nuclear reaction, i.e., the energies of the secondary particles have no direct relation with the incident neutron energy. An example is neutron capture, which results in a cascade of gamma rays emitted from the daughter nucleus. The energies of these gamma rays do not carry information on the incident neutron energy.

The other extreme are nuclear reactions that do preserve this information fully. A pre-requisite for such a reaction is that the secondary particle has no excited states. Otherwise, energy can be lost due to ejectile excitation followed by an undetected decay. This limits the possibilities to light nuclei, i.e., the hydrogen and helium isotopes. These have no excited states, and consequently detection of the recoil of these can give information on the incident neutron energy, if the direction of the neutron is known.

There is also an intermediate category, where the neutron energy cannot be determined event-by-event, but can be inferred on a statistical basis. For instance, when a neutron induces nuclear reactions inside a plastic scintillation detector, a whole range of reactions can take place, which results in a pulse height spectrum for a large number of neutrons of a given incident energy. If the shape of this spectrum depends on the neutron energy, which is in general the case, a statistical unfolding analysis can be performed to provide information about the neutron energy distribution.

1.3. *The role of neutron diagnostics*

In critical power reactors, the main role of neutron diagnostics is to monitor the energy release through fission measurements, and to verify a reasonably uniform power profile. This instrumentation is often fairly simple. In research reactors, more advanced diagnostics are often used, however still often primarily with an emphasis on power release measurements.

In accelerator-driven systems, with the presence of neutrons with very high energies, other aspects also become important. For instance, high-energy neutrons, albeit being a relatively modest fraction (which is not the same as saying that the absolute number is small), might play a significant role in causing materials damage. Effects like cracking, swelling and embrittlement, which are well-known phenomena in critical reactors, are induced by, e.g., (n,p) and (n,α) reactions. The cross sections for these reactions are dramatically larger at high

energies (if including all reaction channels involved). An example of a critical point in an ADS where such materials damage needs to be known is the beam entrance window.

The neutron total cross sections have minima in the 200-400 MeV range for most elements. This means that the penetrability is very large, which has some profound consequences. First, it means that the leakage can be severe, with radiation protection concerns as a consequence. Second, this large penetration might be turned into a possibility. These high-energy neutrons might be able to probe phenomena deep inside the system with a minimum intrusion, thereby supporting system simulation validation.

In this paper, we concentrate the discussion to diagnostics for monitoring of technical aspects of the system. Thus, the monitoring needed for radiation protection in a future ADS will not be dealt with.

2. Neutron diagnostics in accelerator-driven systems

The presence of very fast neutrons in accelerator-driven systems (ADS) allows a wide range of measurement techniques that are inaccessible at traditional critical reactors. The most important aspects are that with high incident neutron energy, nuclear reactions that preserve the energy information can be employed, and outside-core diagnostics becomes much more viable.

2.1. *Inside-core diagnostics*

In general, the inside-core diagnostics techniques do not differ very much for low and high energy neutrons. The choice of techniques is to a large degree dictated by the environment, with very intense neutron fluxes, high temperatures and lack of space.

The techniques used at low energies, activation [1] and fission ionization chambers [3], can be employed irrespective of energy. In the case of activation, there is a very wide range of reactions to utilize, and concerning the detection of the activation products, the techniques are not different from those for low-energy neutron diagnostics. The main problem at high energy is to find well-known activation cross sections.

In the case of fission detection, threshold-based energy determination contains some interesting features. The actinides have thresholds ranging from zero neutron energy up to a few MeV. For high-energy neutrons, also significantly lighter elements, like lead, can fission. The threshold energies are in general smooth functions of the nuclear mass, with decreasing thresholds as a function of nuclear mass. The thresholds are not very sharp, so using a neighbouring element makes a relatively modest difference, in contrast to the actinides where the variation from one element to the next can be dramatic. In nature, bismuth is the heaviest non-actinide with a reasonable abundance. Its fission threshold is around 20 MeV. Thereby, threshold-based methods can be used for neutrons up to 2-3 MeV, and above 20 MeV. In between, there is a gap due to the lack of suitable elements.

2.2. *Outside-core diagnostics*

All inside-core techniques can in principle be used also outside the core. They might, however, need some modifications, because of the significantly lower flux.

As has been described above, it is difficult to obtain energy information using fission ionization chambers in the 2-20 MeV range. Plastic scintillator spectrum unfolding would probably be the preferred choice in this energy range, and it could possibly also be used over an even wider range [4]. A major reason why spectrum unfolding has not been used in reactor applications up to now is that it cannot be used inside the core. This technique has the advantage of using relatively inexpensive and small equipment. It does, however, require a quite advanced data treatment. The count rate capability is fairly high, but not superior.

The technique that probably has the largest potential to provide detailed, high-quality information is magnetic proton recoil (MPR) spectrometry. Neutrons impinging on a target containing hydrogen induces neutron-proton scattering, where recoil protons in the direction of the incident neutron has the same energy as the neutron. These protons are bent in a magnetic field and recorded by a detector system at a focal plane located outside the neutron beam. With a proper design of such a system, the position at the focal plane has a direct relation to the incident neutron energy. Thus, relatively simple particle counting can provide energy information event-by-event with very high resolution (1-2 MeV) all the way up to GeV energies. The detection arrangement also makes very high count rates feasible. In fusion applications, such a system has been routinely used with MHz count rates with essentially no dead time [5]. Thereby, this technique can be used to monitor very rapid changes in the neutron spectrum, since good statistics can be obtained in fractions of a second. This property in turn might make it possible to use the information for feedback to the control of the accelerator, the core, or the entire transmutation system.

If being simple in principle, the practical arrangements might be considerable to make the technique working in reality. First, directional sensitivity is mandatory. This means that the system must be located outside the core, and the neutron flux must be collimated to a small diameter beam (typically a few centimeters). Therefore this technique can provide detailed information only along a narrow line of sight through the system. The physical size of magnets with sufficient bending capability is large, typically 1-2 m in side length and 20-40 tons in weight. Needless to say with such parameters, only one or a few MPR systems can be installed, and they are used at places where detailed information is very valuable. Possible locations might be in the forward direction from the target, and in the backward direction using the incident proton beam line as neutron guide.

3. Summary and outlook

In accelerator-driven systems for transmutation, a significant number of very fast neutrons will be present. This allows for novel diagnostics techniques to be used. Primarily, these techniques will probably be useful for monitoring of the neutron production target, although it should not be excluded that these high-energy neutrons could also reveal information about properties of the surrounding blanket.

No single technique can be used all over the very wide neutron energy range of an ADS and in the very different environments at various locations in the system. Therefore, a combination of techniques can be foreseen.

We would like to suggest a working group of fast-neutron diagnostics for accelerator-driven transmutation to be part of the upcoming EUROTRANS project. This working group should encompass expertise on fast-neutron detection, low-energy diagnostics (to investigate possible combinations of information), system modeling (to couple neutron spectrum information at various locations to measurements), technical system design (to identify suitable places for diagnostics) and reactor physics (to exploit what can be learned).

References

1. G.F. Knoll, Radiation detection and measurement, John Wiley & Sons, New York (1979, 1989).
2. Proceedings of the NEUSPEC workshop, *Nucl. Instr. Meth.* **A476** (2002). See especially F.D. Brooks and H. Klein, *Nucl. Instr. Meth.* **A476**, 1 (2002).
3. S.A. Wender, S. Balestrini, A. Brown, R.C. Haight, C.M. Laymon, T.M. Lee, P.W. Lisowski, W. McCorkle, R.O. Nelson and W. Parker, *Nucl. Instr. Meth.* **A336**, 226 (1993).
4. M. Matzke, *Nucl. Instr. Meth.* **A476**, 230 (2002).
5. J. Källne, L. Ballabio, S. Conroy, G. Ericson, J. Frenje, G. Gorini, P. Prandoni, M. Tardocchi and E. Traneus, *Rev. Sci Instr.* **70**, 1181 (1999).

Appendix X

A New Facility for High-Energy Neutron-Induced Fission Studies

A.V. PROKOFIEV[1, 2,*], S. POMP[3], U. TIPPAWAN[3, 4], B. BERGENWALL[3], S. DANGTIP[4], L. EINARSSON[1], Yu.A. GAVRIKOV[5], T. GERMANN[6], A. HILDEBRAND[3], C. JOHANSSON[3], A.A. KOTOV[5], P. MERMOD[3], L.A. VAISHNENE[5], M. ÖSTERLUND[3], and J. BLOMGREN[3]

1 The Svedberg Laboratory, Uppsala University, Box 533, 751 21 Uppsala, Sweden
2 V.G. Khlopin Radium Institute, 2oi Murinskiy Prospect 28, St. Petersburg 194021, Russia
3 Department of Neutron Research, Uppsala University, Box 525, 751 20, Uppsala, Sweden
4 Fast Neutron Research Facility, PO Box 217, Chiang Mai University, Chiang Mai, 50202, Thailand
5 Petersburg Nuclear Physics Institute, Gatchina, Leningrad District 188350, Russia
6 University of Konstanz, 78457 Konstanz, Germany

A new facility is constructed for measurements of neutron-induced fission cross-sections in the 20-180 MeV energy region versus the *np* scattering cross-section, which is adopted as the primary neutron standard. The advantage of the experiment compared to earlier studies is that the fission-fragment detection and the neutron-flux measurement via *np* scattering are performed simultaneously and at the same position in the beam, and, therefore, many sources of systematic errors cancel out. Further reduction of systematic errors is achieved due to "embedded" determination of effective solid angle of particle detectors using α-particles from the radioactive decay of the target nuclei. The performance of the facility is illustrated by first data obtained for angular distributions of fission fragments in the ^{238}U(n,f) reaction.

INTRODUCTION

Fission is one of the important processes that occur in the spallation target and in the reactor core of an accelerator-driven system (ADS). The fission channel contributes to the neutron production, to the radioactivity produced in the target, as well as to the chemical and radiological toxicity of the reaction products.

Furthermore, neutron-induced fission reactions of ^{235}U, ^{238}U, and ^{209}Bi are internationally recommended as standards for monitoring of high-energy neutron beams[1)]. The ^{238}U(n,f) reaction is most widely used due to the compromise between the magnitude of the cross-section, the insensitivity to low-energy neutrons, and the availability of the target material. Monitors based on the ^{238}U(n,f) reaction are employed at many high-energy neutron facilities, *e.g.*, at LANL (USA)[2)], UCL (Belgium)[3)], NAC (South Africa)[4)], JAERI (Japan)[5)], and at TSL (Sweden)[6)]. Schuhmacher *et al.*[3)] have reported the use of the ^{238}U(n,f) reaction for neutron-spectrum measurements as well.

It is still a long way towards a theory for high-energy fission that would give consistent description even for the simplest fission observables (fission cross-section, angular distribution of fragments) and that would be able to *predict* these quantities for an arbitrary unmeasured fission reaction. The reason of the difficulties in the theoretical description of fission is the great complexity of the fission process, which is concerned with alterations of the nuclear shape, and with reiterated redistribution of nuclear excitation energy between its different forms. An additional complication for high-energy fission stems from the fact that, for sufficiently large excitation energy, fission becomes energetically possible even after emission of a light particle. Thus, the fissioning nucleus in a given reaction is not unique, but belongs to a distribution in mass, charge and excitation energy.

During the last decade, great interest has been paid to dynamic effects in the fission process, *i.e.*, effects that are not taken into account in the statistical description of the process. An appropriate way to account for fission dynamics is to consider fission as a diffusion process over the fission barrier. In the framework of such an approach, suggested long ago by Kramers[7)], the fission width, which serves as a

* Corresponding author. E-mail: Alexander.Prokofiev@tsl.uu.se

measure of the fission probability, depends on a dissipation coefficient, which characterizes the viscosity of nuclear matter. In addition, formation of such a large-amplitude collective motion as the fission process requires a finite time, and fission will be suppressed during that time, while competing decay channels are active. Calculations of Grange and Weidenmüller[8] show that these effects grow rapidly with increasing excitation energy of the fissioning nucleus. Considering such effects has been found necessary for the description of nucleon-induced fission at intermediate energies (see, *e.g.*, an evaluation of Ignatyuk *et al.*[9]).

The particle that induces fission may leave a part of its linear momentum to the fissioning nucleus, or transfer the momentum completely, which corresponds to fission of the true compound nucleus. Due to this effect of linear momentum transfer (LMT), the folding angle between two complementary fission fragments is no longer equal to 180° in the laboratory frame, and fragments are preferentially emitted in the forward hemisphere. Measurements of LMT data are of interest not only in fission physics, but also for fundamental theories of nuclear reactions and nuclear matter. Another closely related effect is the anisotropy of the fission-fragment angular distribution in the frame of the fissioning nucleus. The fact that more fragments are emitted at 0 and 180° than at 90° with respect to the incident beam direction is a consequence of the angular-momentum transfer. The theory of anisotropy, developed by Halpern and Strutinsky[10], links the experimental observables to fundamental nuclear quantities, *e.g.*, the nuclear moment of inertia.

Despite the importance of the high-energy (n,f) cross-section data for theory and applications, there have been few attempts[4, 11-14] to measure them in absolute scale, i.e. versus the *np* scattering cross-section, which is adopted as the primary neutron standard[1]. Only two studies[11, 13] have resulted in journal papers, and one of them[11] is in apparent disagreement with newer data above 20 MeV. The current standard ^{235}U(n,f) and ^{238}U(n,f) cross-sections recommended by IAEA[1] are based on the data sets of Lisowski *et al*.[12]. The latter data have undergone a few revisions, but a publication is still awaited that would include the results and the thorough description of the experimental technique. The data of Newhauser *et al*.[14] have been superseded by newer results of the same group[4], not finally published either. Even fewer data sets are available for angular distributions of fragments from neutron-induced fission above 20 MeV[15-17].

In the framework of the **FIRANDET** project (**Fi**ssion **R**esearch with **A**dva**n**ced **Det**ectors), a new facility is constructed for measurements of neutron-induced fission cross-sections in absolute scale. As a first step towards the cross-section measurements, we have obtained data on angular distributions of fission fragments from the ^{238}U(n,f) reaction.

EXPERIMENTAL SETUP AND METHODS

The neutron beam

The facility makes use of the Uppsala neutron beam produced via the ^{7}Li(p,n) reaction by protons in the 20-180 MeV energy range. A thorough description of the facility may be found in a recent paper of Klug *et al.*[6]

Fig. 1 shows an example of the incident neutron spectrum, measured using a CH_2 target via *np* scattering at 20° angle with time-of-flight (TOF) techniques. The lines in Fig. 1 represent predictions of semi-empirical systematics of Prokofiev *et al.*[18] Satisfactory agreement is observed between the data and the systematics. The systematics gives correct prediction of the share of the high-energy peak neutrons in the spectrum (39.0% versus 37.8% for the experimental spectrum extrapolated to zero energy). This agreement confirms that the neutron spectrum is sufficiently well known and controlled.

The MEDLEY setup

An extensive description of the MEDLEY setup may be found in the paper of Dangtip *et al.*[19], and only a brief description is given below, emphasizing features that are specific for studies of neutron-induced fission.

A photograph of the MEDLEY vacuum chamber is shown in Fig. 2. The chamber was situated at a distance of about 9.2 m from the neutron production target. It has circular shape with a target assembly in the center and eight detector telescopes mounted at the angles of 20 to 160° relative to the beam direction, in steps of 20°.

The target assembly consists of two layers of $^{238}UF_4$, each about 1 mg/cm^2 thick, deposited on polyethylene backings, about 90 μm thick, and mounted back-to-back so that the angle between the target surface and the beam direction is 45°. The target assembly is 65 mm in diameter, and is fully covered by the central homogeneous area of the neutron beam.

Each detector telescope consists of two fully depleted surface barrier Si detectors, about 50- and 400-μm thick, and a 5-cm long CsI(Tl) scintillator crystal. α-particles from the radioactive decay of ^{238}U and fission fragments are fully stopped and detected by the first Si detector. Recoil protons, coming from the H(n,p) reaction with the hydrogen nuclei in the target backing, pass through both Si detectors and are stopped in the CsI(Tl) scintillator. The protons are discriminated against other charged particles using ΔE-E techniques. Only information from the telescopes at 20 and 40° is useful for neutron beam monitoring, since the elastic peak becomes too wide at larger angles, and the relative contribution of background from the $^{12}C(n,p)$ reaction increases. TOF techniques are employed to distinct fission and recoil proton events due to the high-energy peak and the low-energy tail in the neutron spectrum.

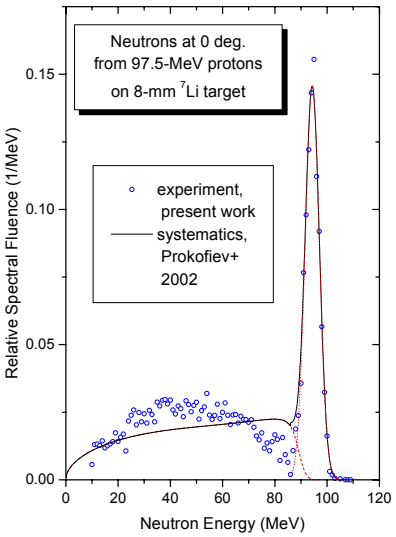

Fig. 1.
The neutron spectrum at 0º for 97.5-MeV protons incident on 8-mm thick ^{7}Li target. The symbols show data obtained in the present work. The lines represent the predictions of the systematics developed by Prokofiev et al[18]. The dotted, dashed and solid lines show the predictions for the high-energy peak, the low-energy tail and the sum of the two components, respectively. The width of the predicted high-energy peak component is adjusted to the experimental data. Both experimental and systematics data are normalized so that the area under the high-energy peak is unity.

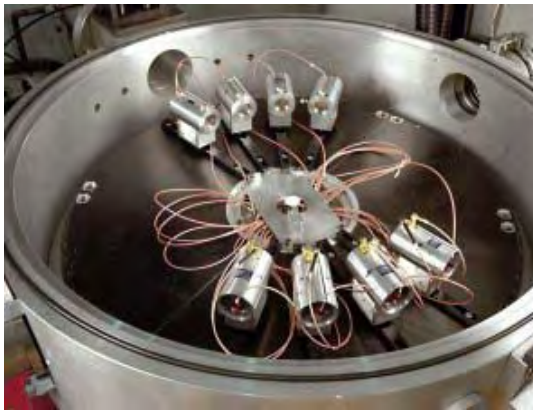

Fig. 2.
The view of the MEDLEY chamber. The neutron beam entrance is located at the right upper corner of the photograph. Eight telescope housings at different angles are seen. The target assembly is mounted under the chamber lock and is not seen on the photograph.

DATA ANALYSIS

An advantage of the experiment compared to earlier studies is that the fission-fragment detection and the neutron-flux measurement via *np* scattering are performed simultaneously and at the same position in the beam, and, therefore, many sources of systematic errors cancel out, as it is shown below.

The count rate of fission events induced by high-energy peak neutrons and registered by *i*-th detector is:

$$n_f(\vartheta_i) = \frac{\Omega_i}{2\pi} m \frac{N_A}{A} j_n \frac{d\sigma_f}{d\Omega}(\vartheta_i), \quad (1)$$

where Ω_i is the solid angle subtended by *i*-th detector, ϑ_i is its angular coordinate, m is the mass of the fissile nuclide in the target, N_A is the Avogadro number, A is the atomic mass of the fissile nuclide, j_n is the peak neutron flux on the target, and $\frac{d\sigma_f}{d\Omega}$ is the differential fission cross-section.

The count rate of α-particles from radioactive decay of target nuclei is:

$$n_\alpha(\vartheta_i) = m a_{spec} \frac{\Omega_i}{4\pi}, \quad (2)$$

where a_{spec} is the specific α-activity of the fissile nuclide in the target. Combining Eqs. (1) and (2) gives:

$$\frac{d\sigma_f}{d\Omega}(\vartheta_i) = W(\vartheta) \frac{a_{spec} A}{2 N_A} \frac{1}{j_n}, \quad (3)$$

where

$$W(\vartheta) = \frac{n_f(\vartheta_i)}{n_\alpha(\vartheta_i)} \quad (4)$$

is the relative angular distribution of fission fragments. Thus, the described procedure allows us to reduce the angular-distribution measurement to the simple counting of fragments and α-particles, the latter being done either during the beamtime or in additional runs without the beam.

The second term in Eq. (3) includes only well-known physical constants, and the third one is the inverse neutron flux. Neither the amount of the fissile nuclide in the target nor the solid angle subtended by the detector are present in Eq. (3). Thus, counting α-particles from radioactive decay of target nuclei provides an "embedded" determination of the effective solid angle of the detectors and allows one to reduce further the systematic errors. In particular, the described procedure is insensitive to a possible inhomogeneity of the target.

It is known from past studies (see, *e.g.*, the works of Tutin *et al.*[15] and Ryzhov *et al.*[16]) that the fragment angular distribution from fission induced by high-energy neutrons may be expressed as:

$$W(\vartheta) = \frac{k_{norm}}{2\pi}(1 + B\cos^2\vartheta), \quad (5)$$

where B is the angular anisotropy factor and k_{norm} is a normalization constant. Combining Eqs. (3) and (5) and integrating over angle ϑ gives the final expression for the fission cross-section:

$$\sigma_f = \frac{a_{spec} A k_{norm}}{N_A j_n}\left(1 + \frac{B}{3}\right). \quad (6)$$

EXPERIMENTAL RESULTS

A few neutron-beam runs have been performed at different energies, and the data are being analyzed with the goal to deduce fission cross-sections and angular distributions of fission fragments. In order to

illustrate the performance of the facility, we report angular distributions of fission fragments in the ^{238}U(n,f) reaction at quasi-monoenergetic neutrons with the peak energy of 21 MeV.

Sufficiently good separation between fission fragments and products of non-fission reactions is observed in the energy spectra for all detectors, and, therefore, the uncertainty in the fission count rate is virtually purely statistical. In Fig. 3, the fragment angular distribution is shown, obtained according to Eq. (4). Since the TOF information has not been used yet, the shown angular distribution is a superposition of contributions from reactions induced by neutrons of different energies in the incident spectrum. The line in Fig. 3 represents the least squares fit to the data according to Eq. (5). It is seen that the distribution is successfully approximated by the fit. The deduced angular anisotropy factor *B*, related to the entire incident neutron spectrum, is 0.55±0.11.

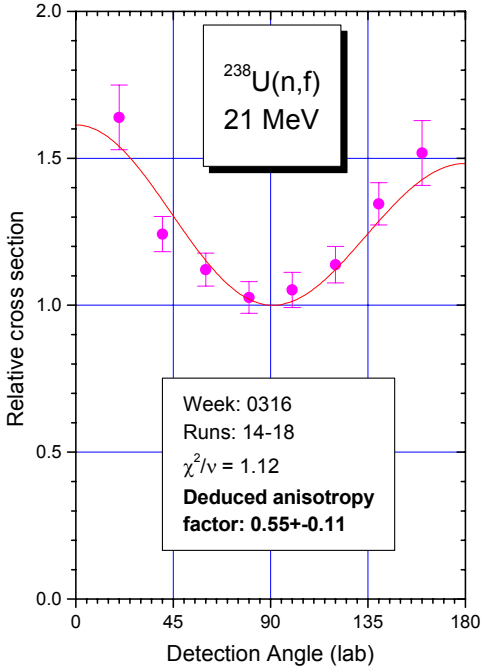

Fig. 3.
Angular distribution of fragments from fission of ^{238}U induced by quasi-monoenergetic neutrons with the peak energy of 21 MeV. No TOF selection is performed, and, therefore, the data correspond to the entire neutron spectrum. The shown uncertainties are solely due to statistical errors.

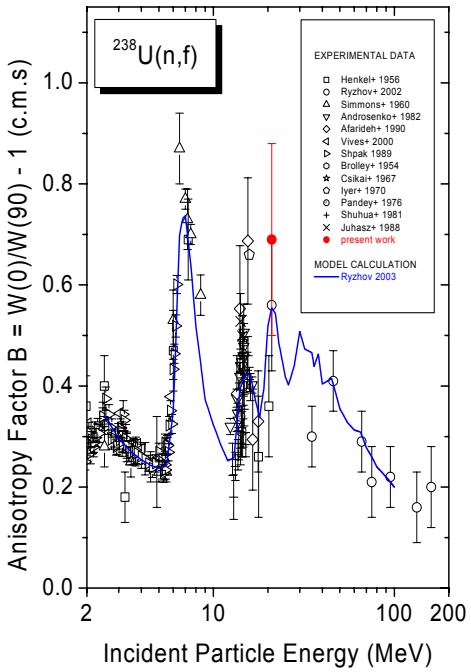

Fig. 4
Energy dependence of the anisotropy of neutron-induced fission of ^{238}U. The symbols represent experimental data of the present work and from earlier studies[22]. The line represents theoretical calculations[17, 21]. The experimental datum of the present work has been corrected for the contribution of reactions induced by low-energy neutrons, as described in the text.

In order to deduce the angular anisotropy for the peak neutron energy, one has to correct for the contribution of reactions induced by low-energy tail neutrons. Such a correction can be obtained either by application of a TOF cut to the experimental data or by a model calculation based on data on the incident neutron spectrum, the fission cross-section, and the angular anisotropy in the low-energy region. In the present work, only the second option has been applied. The neutron spectrum from the ^{7}Li(p,n) reaction at 0° is taken from the evaluation of Mashnik *et al.*[20] included in the LA150 library. The ^{238}U(n,f) cross-section data come from the ENDF-VI library (below 20 MeV) and from the evaluation of Carlson *et al.*[1] (above 20 MeV). By folding the neutron spectrum and the fission cross-section, we obtain the distribution of fission events on incident neutron energy. The resulted distribution is folded with fission anisotropy calculated using the STAPRE-H code[17, 21] for the neutron energies below 20

MeV. The result is the contribution to the anisotropy due to the low-energy tail neutrons. Comparing it with the measured integral anisotropy factor given above, we arrive at the anisotropy factor related to fission induced by high-energy peak neutrons:

$$B\ (E_n = 21\ \text{MeV}) = 0.69 \pm 0.19. \qquad (7)$$

The obtained result is shown in Fig. 4 together with other experimental data[22] and the model calculation [17, 21]. As can be seen, the result of the present work is in agreement with the data of Ryzhov *et al.*[16, 17], as well as with the STAPRE-H calculation[17, 21].

CONCLUSIONS AND OUTLOOK

First experimental data from the FIRANDET project are reported. The obtained angular distributions of fragments from the ^{238}U(n,f) reaction are in agreement with earlier experimental results and theoretical calculations. This ensures adequacy of the performance of the experimental setup and the data analysis techniques.

Measurements and processing of the obtained experimental data will be continued. It is planned to analyze the data including the TOF information, to improve the statistics, and to perform measurements of angular distributions and cross-sections for the most important fission reactions in the 20-180 MeV energy region.

ACKNOWLEDGEMENTS

The authors are grateful to R. Nolte and I. V. Ryzhov for valuable discussions and for sending us their results prior to publication. We are thankful to the staff of The Svedberg Laboratory for providing us with the beam and for other various help. The study was supported in part by The Swedish Foundation for International Cooperation in Research and Higher Education (STINT).

REFERENCES

1) A.D. Carlson, *et al.*, Proc. Int. Conf. on Nuclear Data for Science and Technology, Trieste, Italy, May 19-24, 1997, Part II, 1223-1229.
2) S. A. Wender, *et al.*, NIM A336, 226-231 (1993).
3) H. Schuhmacher, *et al.*, NIM A421, 284-295 (1999).
4) R. Nolte, *et al.*, J. Nucl. Sci. Techn., Suppl. 2, 311-314 (2002).
5) M. Baba, *et al.*, NIM A428, 454-465 (1999).
6) J. Klug, *et al.*, NIM A489, 282-303 (2002).
7) H.A. Kramers, Physica 7, 284 (1940).
8) D. Grange and H.A. Weidenmüller, Phys. Lett. B96, 26 (1980).
9) A.V. Ignatyuk *et al.,* Nucl. Sci. Eng. 136, 340-356 (2000).
10) I. Halpern and V.M. Strutinsky, Proc. 2nd Conf. on the Peaceful Uses of Atomic Energy. Geneva, 1958, v. 15, p. 408.
11) V.M. Pankratov, Atomnaja Energiya 14, 177 (1963) (in Russian).
12) P.W. Lisowski, *et al.*, Proc. of a Specialists' Meeting on Neutron Cross Section Standards for the Energy Region above 20 MeV, Uppsala, Sweden, May 21-23, 1991, OECD/NEA Report NEANDC-305 'U', 177-186.
13) V.P. Eismont, et *al.*, Phys. Rev. C53, 2911-2918 (1996).
14) W.D. Newhauser, *et al.*, Proc. Intern Conf. on Nuclear Data for Science and Technology, May 19-24, 1997, Trieste, Italy, 1236-1238.
15) G. A. Tutin, *et al.*, NIM A457, 646-652 (2001).
16) I. V. Ryzhov *et al*., J. Nucl. Sci. Techn., Suppl. 2, 295-298 (2002).
17) I. V. Ryzhov, Ph. D. thesis, V.G. Khlopin Radium Institute, St. Petersburg (2003) (in Russian).
18) A.V. Prokofiev, *et al.*, J. Nucl. Sci. Techn., Suppl. 2, 112-115 (2002).
19) S. Dangtip, *et al.*, NIM A452, 484-504 (2000).
20) S. G. Mashnik, *et al.*, LANL Report LA-UR-00-1067 (2000).
21) M. Avrigeanu, M. Ivascu, V. Avrigeanu, Report NP-63 (1987).
22) The CSISRS data base, http://www.nndc.bnl.gov/nndc/exfor.html

Appendix XI

How Strong is the Strong Interaction?

J. Blomgren[a], B. Bergenwall[a], A. Hildebrand[a], C. Johansson[a], J. Klug[a], P. Mermod[a], L. Nilsson[a], S. Pomp[a], U. Tippawan[a,e], M. Österlund[a], O. Jonsson[b], A.V. Prokofiev[b], P. Nadel-Turonski[c], N. Olsson[a,d], S. Dangtip[e]

a) Department of Neutron Research, Uppsala University, Box 525, S – 751 20 Uppsala, Sweden
b) The Svedberg Laboratory, Uppsala University, Box 533, S – 751 21 Uppsala, Sweden
c) Department of Radiation Sciences, Uppsala University, Box 535, S – 751 21 Uppsala, Sweden
d) Swedish Defence Research Agency, S – 172 90 Stockholm, Sweden
e) Fast Neutron Research Facility, Department of Physics, Chiang Mai University, 50200 Thailand

Elastic neutron scattering plays a key role in establishing the neutron-nucleus potential, i.e., the interaction strength between a neutron and a nucleus. In ADS applications, this information is useful in many different ways. Elastic scattering data are needed when determining the neutron intensity profile in and ADS system. In addition, the optical potentials derived from elastic neutron scattering data are used as input in every model calculation with a neutron in the incident or exit channel.

Recently, there has been intense international debate on the neutron-proton scattering cross section. In the global data base, the backward cross section differs by 10 % or even more at energies above 100 MeV. It is difficult to overemphasize the importance of this issue. The np scattering cross section is used as cross section reference in essentially all measurements of neutron-induced cross sections. Thus, for many applied cross sections the absolute scale is uncertain by the same amount. Moreover, the np scattering cross section has been used to derive the pion-nucleon coupling constant, i.e., the absolute strength of the strong interaction. It is annoying to have such a large uncertainty for such a fundamental parameter.

We are presenting new data on elastic neutron scattering at 96 MeV from ^{12}C and ^{208}Pb, where the latter is part of the HINDAS project. In addition, new data on np scattering at 190 MeV will be presented. The impact on ADS and fundamental physics will be discussed.

Why elastic scattering for ADS?

It is beyond reasonable efforts to measure every nuclear reaction taking place in an accelerator-driven system (ADS). Therefore, the main role of nuclear data is to provide guidance for theory development, which in turn will be used in design, safety assessment, etc. The optical model, which is the prime tool in nuclear models for these kinds of systems, relies essentially on two types of experimental information; elastic scattering, and total (or reaction) cross sections. Since total cross sections are relatively well known in the relevant energy range, the elastic scattering cross section is the most important missing piece of information when determining the optical model. The optical model, which is the standard representation of the force between a nucleon (proton or neutron) and a nucleus, is used as input in virtually every cross section calculation where a nucleon is present either in the incident or exit channel, and is therefore of major importance for theory development. This makes, e.g., neutron elastic scattering measurements much more important than they would be if they were only useful for direct use in calculations of the spatial distribution of neutrons in a core.

The total cross section is the sum of all possible interactions, i.e., the probability that anything happens at all. The reaction cross section is the sum of all interactions except elastic scattering. These quantities can both be measured directly even if all the partial cross sections constituting it are unknown. Moreover, they can serve as guidance

when different optical models all describe the same elastic scattering data well, but result in different rection cross sections.

Within HINDAS, we have performed measurements of elastic neutron scattering from a series of nuclei at 96 MeV. Previously, high-quality data have been available up to 65 MeV [1]. Thereby, the 96 MeV studies represent the highest energy where resolved elastic neutron scattering has been studied. Data on ^{12}C and ^{208}Pb have recently been published [2,3].

In the course of this project, an important side-effect has emanated. It turns out that the novel normalization technique developed for elastic neutron scattering data can provide information pertinent to one of the outstanding issues of fundamental nuclear physics; the debate on the absolute strength of the strong interaction. This paper is focused on this issue.

The absolute strength of the strong interaction

The np scattering cross section - in particular at 180 degrees (c.m.), which corresponds to proton emission at 0 degrees in the lab - is used to normalize measurements of other neutron-induced cross sections, i.e., it is the primary standard cross section. In addition, it plays an important role in fundamental physics, because it can be used to derive a value of the absolute strength of the strong interaction in the nuclear sector, commonly expressed as the pion-nucleon (πNN) coupling constant. (See Ref. [4] for a review.) Large uncertainties for such an important cross section are therefore unacceptable.

If np scattering were due to one-pion exchange only, the determination of the πNN coupling should be rather straight-forward. If no other processes were present, the cross section would be proportional to the square of the πNN coupling.

The differential cross section for np scattering decreases with increasing momentum transfer, i.e., with increasing angle, assuming the interaction to be mediated by the uncharged pion and the characteristic scale of how rapidly the cross section decreases is given by the pion mass. However, in addition to this pure scattering process, there is the possibility of charge exchange, where a charged pion is mediating the interaction, thus altering the identity of the two particles. This process has its minimum momentum transfer at 180 degrees in the centre-of-mass (c.m.) system, and should therefore to first order look like a mirror image of π^0 exchange. This simplified picture resembles reality, as illustrated in Fig. 1.

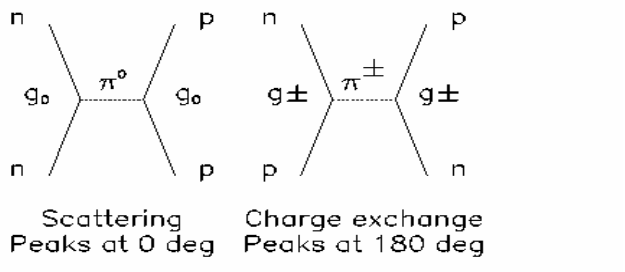

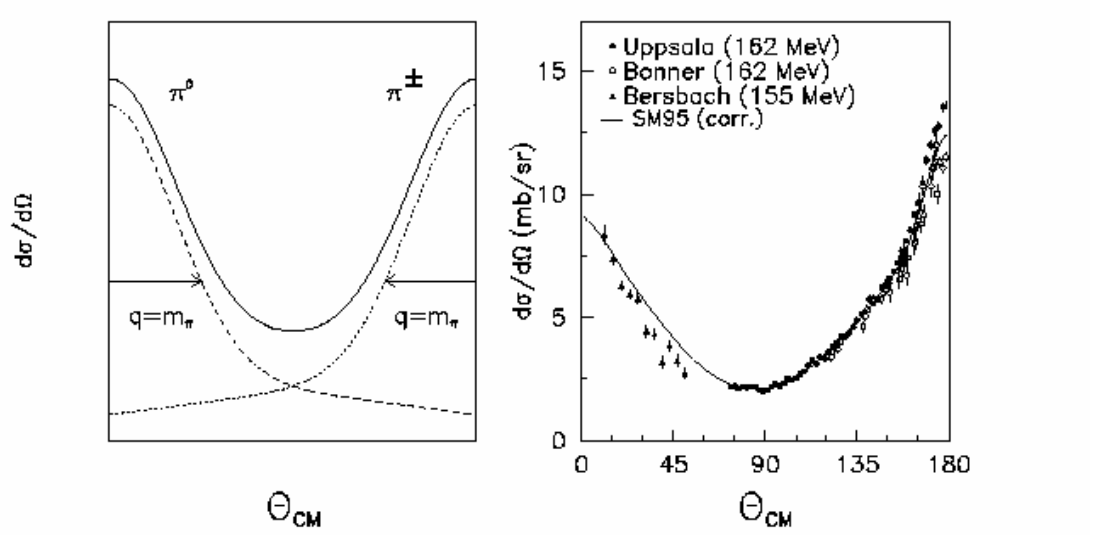

Fig. 1. Upper panel: Simplified diagrams of scattering and charge-exchange contributions to np scattering. Lower panel: Expected angular distributions due to one-pion exchange, and data close to 160 MeV.

Backward np scattering data have frequently been used to extract the pion-nucleon coupling [5]. In such extractions, both the shape and the normalization of the data contribute [6]. To first order, the coupling goes as the square root of the normalization. As can be seen in Fig. 1, the two backward data sets [7,8] differ by about 10 %, which translates to a 5 % difference in the extracted coupling constant.

The precise value of the πNN coupling constant has consequences for the quantitative discussion of a large number of phenomena in hadron and nuclear physics. For instance, its strength governs the properties of the deuteron to a very high degree. If all other nucleon-nucleon potential information were known, the value could be determined very accurately, because then a difference of only a few percent in its value would be sufficient to either unbind the deuteron or to produce a bound di-proton, in both cases with major consequences for the world as we know it.

It is difficult to overemphasize the importance of knowing the np scattering cross section precisely. Besides providing a testing ground for the pion-nucleon coupling constant, the np scattering cross section is of utmost importance for many applications of today, including medical applications [9], studies of electronics failures induced by cosmic-ray neutrons [10], and accelerator-driven transmutation of nuclear waste and energy production technologies. The reason is that this cross section is frequently used to normalize measurements of other neutron-induced cross sections.

Unfortunately, there are severe discrepancies in the data base on np scattering in the 100-1000 MeV range[6]. Uncertainties of 10 % or more are common, and thereby no other neutron-induced cross sections are known to better than that. Clearing up this mess should therefore be of high priority.

The black magic of absolute measurements of neutron-induced reactions

To measure a cross section, the intensity of the beam has to be known. A most notorious problem is how to determine the intensity of a neutron beam. This might sound like an innocent problem, but it is close to impossible to overcome it (!).

A charged particle interacts with the electrons of the atom. Thereby it is possible to build systems where *every* particle gives a signal when passing through a detector, and hence it is a relatively simple task to determine the beam intensity by just counting pulses. Another option is to stop particles via their energy loss - which is also an effect of interaction with the atomic electrons - and finally measure the collected charge. This is performed in every Faraday cup at every laboratory.

Neutrons interact by the strong interaction only, and they are uncharged. This means that there is no way you can build a device which produces a signal for each particle that passes, and you cannot stop neutrons in a controlled way. Detection of neutrons *always* has to proceed via a nuclear reaction, releasing charged particles, which can subsequently be detected. The problem is that there is no way to determine a nuclear cross section from theory only with a reasonable precision. This means we end up in circular reasoning.

Let us assume we want to use neutron-proton (np) scattering for neutron detection. Counting the protons emanating from a hydrogenous material is a simple task, but we need to know the cross section to derive the number of incoming neutrons. To measure that cross section, however, we need to know the number of incident neutrons. Are there no ways out of this vicious circle?

In fact, there are a few tricks which can be used, but they are all associated with large difficulties. The standard procedure is therefore to determine a single cross section using all these painstaking methods, and subsequently this cross section is used as *reference*, i.e., other cross section measurements are measured relative to it. The only three techniques available are presented below:

(1) Tagged beams

The methodologically simplest method is probably to use tagged beams, but this does not necessarily mean it is the simplest technique in real life. Neutrons do not exist freely in nature but have to be produced by nuclear reactions. For a few reactions, detection of the residual nucleus can be used to verify the neutron production. An example is the $D(d,n)^3He$ reaction. By detecting the kinetic energy and direction of the residual ^3He nucleus, the energy and angle of the neutron is known. In addition, the detection of a ^3He nucleus implies that there *must* be a neutron, i.e., the ^3He nucleus serves as a "tag" on the neutron. With this technique, "beams" of really low intensity, but with known intensity can be produced. This beam can subsequently be used for cross section measurements.

(2) Combination of total and differential hydrogen cross sections

The total cross section, i.e., the probability that a neutron interacts at all with a target nucleus, is a quantity that can be determined without knowledge of the absolute beam intensity. This integral cross section is related to the attenuation of a neutron beam, which means that a relative measurement of the beam intensity before and after a target is sufficient.

In the case of hydrogen, the total cross section is completely dominated by elastic np scattering, which accounts for more than 99 % of the total cross section. A relative measurement of the np scattering angular distribution can thereby be normalized to agree with the total cross section, and thus an absolute np cross section can be obtained.

(3) Combination of total, reaction and differential elastic cross sections

The differential elastic cross section of a nucleus can be determined absolutely by a combination of total and reaction cross section measurements, together with a relative measurement of the differential elastic cross section. Both the total cross section and the reaction cross section can be determined in relative measurements of beam attenuation. The only important difference is the geometry used. The integrated elastic cross section can then be derived as the difference of the total and reaction cross sections. The elastic differential cross section on almost any nucleus falls dramatically with angle. Thus, by covering a moderately wide range at forward angles, essentially all the elastic differential cross section is covered. Thereby, the differential cross section can be related to the integrated elastic cross section.

Cross-check of normalization procedures

Before the HINDAS project, only technique 1 and 2 were known, while method 3 is a result of the elastic neutron scattering project of HINDAS.

Returning to Fig. 1, the two backward data sets differ by about 10 %. It has been questioned whether this could be due to normalization problems. The Uppsala data have been normalized with method 2 [8], while the Bonner data were normalized with a method that is not purely experimental, i.e., it involves some theory presumptions [7].

Recently, a facility for measurements of tagged np scattering has been developed at the cooler storage ring at Indiana University Cyclotron Facility (IUCF) [11]. A circulating proton beam impinges on a deuterium gas-jet target. Neutrons are produced by the $D(p,n)^2He$ reaction, where ^2He denotes two unbound protons in a relative $^1S_0$ state. By detection of these two low-energy protons, the neutron energy and angle are determined, which makes absolute cross section measurements feasible. The results of the IUCF tagged experiment are still preliminary [12]. They do, however, seem to indicate a good agreement on the absolute scale with the Uppsala results.

The previous Uppsala results were obtained in an experiment covering 74-180 degrees. Since part of the angular distribution was not covered, NN models were used to correct the normalization result for the undetected angular range, resulting in a 2 % uncertainty. As has been mentioned above, if the entire angular range were known, it would have been possible to normalize the data to the total cross section directly by integration. This has motivated a recent experiment with on forward np scattering (0-84 degrees) to cover the missing part of the angular distribution. Subtraction of data obtained with CH_2 and carbon targets has been used to obtain the np differential cross section.

This method provides a second cross-check of the normalization techniques outlined above. By measuring CH_2 and carbon in the same experiment, the elastic cross section ratio of hydrogen versus carbon can be obtained. Since the elastic cross section of carbon can be determined absolutely by a combination of differential, total and reaction

cross section measurements, an independent absolute np cross section can be obtained. Results are expected early 2004.

Acknowledgments

This work was supported by the Swedish Natural Science Research Council, Vattenfall AB, Swedish Nuclear Fuel and Waste Management Company, Swedish Nuclear Power Inspectorate, Ringhals AB, the EU Council, and the Swedish Defence Research Agency. The present work was partly performed within the HINDAS project.

References

1. E. Hjort, et al., Phys. Rev. C 50 (1994) 275.
2. J. Klug, et al., Phys Rev C 67 (2003) 031601(R).
3. J. Klug, et al., accepted for publication in Phys. Rev. C.
4. Critical Issues in the Determination of the Pion-Nucleon Coupling Constant, ed. J. Blomgren, Phys. Scr. T87 (2000).
5. T.E.O. Ericson, Nucl. Phys. A 543 (1992) 409c.
6. J. Blomgren, N. Olsson, J. Rahm, Phys. Scr. T87 (2000) 33.
7. B.E. Bonner, et al., Phys. Rev. Lett. 41 (1978) 1200.
8. J. Rahm, et al., Phys. Rev. C57 (1998) 1077.
9. J. Blomgren and N. Olsson, Rad. Prot. Dos. 103 (2003) 293.
10. J. Blomgren, B. Granbom, T. Granlund and N. Olsson, Mat. Res. Soc. Bull. 28 (2003) 121.
11. T. Peterson, et al., accepted for publication in Nucl. Instr. Meth. A.
12. M. Sarsour, et al., in Proceedings of the 17th International IUPAP Conference on Few-Body Problems in Physics.

Appendix XII

Light-ion Production on Silicon and Electronics Reliability

U. Tippawan[a,b], S. Pomp[a,*], A. Atac[a], B. Bergenwall[a], J. Blomgren[a], A. Hildebrand[a], C. Johansson[a], J. Klug[a], P. Mermod[a], M. Österlund[a], K. Elmgren[c], N. Olsson[a,c], O. Jonsson[d], L. Nilsson[d], A.V. Prokofiev[d], P.-U. Renberg[d], P. Nadel-Turonski[e], S. Dangtip[a,b], V. Corcalciuc[f], Y. Watanabe[g], A. Koning[h].

[a]*Department of Neutron Research, Uppsala University, Sweden*
[b]*Fast Neutron Research Facility, Chiang Mai University, Thailand*
[c]*Swedish Defence Research Agency (FOI), Stockholm, Sweden*
[d]*The Svedberg Laboratory, Uppsala University, Sweden*
[e]*Department of Radiation Sciences, Uppsala University, Sweden*
[f]*Institute of Atomic Physics, Heavy Ion Department, Bucharest, Romania*
[g]*Department of Advanced Energy Engineering Science, Kyushu University, Japan*
[h]*Nuclear Research and Consultancy Group NRG, Petten, The Netherlands*

Abstract. Cosmic-ray neutrons create a reliability problem in modern electronics. A neutron can cause a nuclear reaction inside or near a chip, thus releasing free charge, which in turn could, e.g., flip the memory content or change the result of a logical operation. The magnitude of this problem is expected to increase in the near future.

For assessment of the problem, and for identifying possible solutions to it, improved knowledge of the underlying nuclear physics is of major importance. New data on light-ion production on silicon at 96 MeV, acquired with the MEDLEY setup at TSL Uppsala, are presented and compared with recent models.

I. Introduction

In recent years, the importance of cosmic radiation effects in microelectronic devices on board aircraft[1,2)] and satellites[3,4)] has been highlighted. At commercial flight altitudes, as well as at sea level, the most important particle radiation is due to neutrons, created in the atmosphere by cosmic-ray protons causing spallation of nitrogen and oxygen nuclei. The spallation neutron spectrum shows a typical 1/E dependence, extending to energies of several GeV. When a neutron collides with a silicon nucleus, light and heavy charged particles can be produced in a nuclear reaction. If the charge released by ionization passes a critical threshold, the memory content in a bit flips. This is called a single-event upset (SEU)[5,6)]. In some cases, two or more bits in a single memory word may flip, which is called single-word multi-bit upset (SMU)[7,8,9)].

Light charged particles (p, d, t, ^{3}He and α) are normally not considered in SEU calculations since the energy deposited by these particles within the sensitive volume is very small. The memory residing in highly integrated microchip devices are today formed by very small charges. With the expected advances in technology, the development towards higher scale integration includes reducing the operation voltage which also means that the critical threshold is decreased. For this reason, also the contribution from light ions, such as alpha particles, is expected to become significant for SEU, and it might also affect the SMU rate[7)].

In this paper, experimental double-differential cross sections (inclusive yields) for protons, deuterons, tritons, ^{3}He and alpha particles produced by 96 MeV neutrons incident on silicon are presented. Measurements have been performed at the cyclotron of The Svedberg Laboratory (TSL), Uppsala, using the dedicated MEDLEY experimental set-up[10)]. Spectra have been measured at 8 laboratory angles, ranging from 20° to 160° in 20° steps. Extrapolation procedures are used to obtain coverage of the full angular distribution and consequently energy-differential and production cross sections are deduced, the latter by integrating over energy and angle. The experimental data are compared to results of calculations with nuclear reaction codes and to existing experimental data.

* Corresponding author. E-mail address: stephan.pomp@tsl.uu.se

II. Experimental Methods

The neutron beam facility at TSL uses the $^{7}Li(p,n)^{7}Be$ reaction (Q = -1.64 MeV) to produce a quasi-monoenergetic neutron beam[11]. The lithium target was 26 mm in diameter and 8 mm thick in the present experiment and enriched to 99.98% in ^{7}Li. The 98.5 ± 0.3 MeV protons from the cyclotron impinge on the lithium target, producing a full energy peak of neutrons at 95.6 ± 0.5 MeV with a width of 3 MeV FWHM and containing 40% of the neutrons, and an almost constant low-energy tail containing 60% of the neutrons. The neutron beam is directly monitored by a thin-film breakdown counter (TFBC). Relative monitoring can be obtained by charge integration of the proton beam from the Faraday cup in the beam dump. The agreement between the two beam monitors was very good during the measurements.

The charged particles are detected by the MEDLEY setup[10]. It consists of eight three-element telescopes mounted inside a 100 cm diameter evacuated reaction chamber. Each telescope has two fully depleted ΔE silicon surface barrier detectors. The thickness of the first ΔE detector (ΔE_1) is either 50 or 60 μm, while the second one (ΔE_2) is either 400 or 500 μm, and they are all 23.9 mm in diameter (nominal). In each telescope, a cylindrical CsI(Tl) crystal, 50 mm long and 40 mm in diameter, serves as the E detector. The back-end 20 mm of the crystal has a conical shape, tapered off to 18 mm diameter, to fit the size of a read-out diode. To obtain a well-defined acceptance, a plastic scintillator collimator is placed in front of each telescope. The active collimators had an opening of 19 mm diameter and a thickness of 1 mm.

A Passivated Implanted Planar Silicon (PIPS) detector is used as an active target, without frame or other mounting assemblies. It has a 32x32 mm^2 quadratic shape and a thickness of 303 μm. It is suspended in a thin aluminium frame using threads and small springs. The dimensions of the frame have been chosen in such a way that it does not interfere with the incident neutron beam. Besides the energy deposited by the detected light ion, the active target recorded the energy deposition due to other products, like recoils, of the same event. This information was not used in the present analysis.

For absolute cross section normalization, a 25 mm diameter and 1.0 mm thick polyethylene $(CH_2)_n$ target is used. The n-p cross sections at 20° laboratory angle provides the reference cross section[12]. Background is measured by removing the target from the neutron beam.

The background is dominated by protons produced by neutron beam interaction with the beam tube and reaction chamber material, especially at the entrance and exit of the reaction chamber and in the telescope housings. Therefore the telescopes at 20° and 160° are most affected.

The time-of-flight (TOF) obtained from the radio frequency of the cyclotron (stop signal for TDC) and the timing signal from each of the eight telescopes (start signal), is measured for each charged-particle event.

The raw data are stored event by event for on-line monitoring and subsequent off-line analysis. Typical count rates for target-in and target-out runs were 10 and 2 Hz, respectively. The dead time of the system was typically 1-2 % and never exceeding 10 %.

III. Data reduction procedures

III.1 Particle identification and energy calibration

The ΔE-E technique is used to identify light charged particles ranging from protons to lithium ions. Good separation of all particles is obtained over their entire energy range therefore the particle identification procedure is straight forward (see Appendix I.1).

Energy calibration of all detectors is obtained from the data itself[13]. Events in the ΔE–E bands are fitted with respect to the energy deposited in the two silicon detectors. This energy is determined from the detector thicknesses and calculations of energy loss in silicon. The ΔE_1 detectors are further calibrated and checked using a 5.48 MeV alpha source. For the energy calibration of the CsI(Tl), two parameterizations of the light output versus energy of the detected particle[10] are used, one for hydrogen isotopes and another one for helium isotopes. Supplementary calibration points are provided by

transitions to the ground state and low-lying states in the H(n,p), $^{12}C(n,d)^{11}B$ and $^{28}Si(n,d)^{27}Al$ reactions. The energy of each particle type is obtained by adding the energy deposited in each element of the telescope.

Low-energy charged particles are stopped in the ΔE_1 detector leading to a low-energy cutoff for particle identification of about 3 MeV for hydrogen isotopes and about 8 MeV for helium isotopes. The helium isotopes stopped in the ΔE_1 detector are nevertheless analyzed and a remarkably low cutoff, about 4 MeV, can be achieved for the experimental alpha-particle spectra. These alpha-particle events could obviously not be separated from ^{3}He events in the same energy region, but the yield of ^{3}He is much smaller than the alpha-particle yield in the region just above 8 MeV, where the particle identification works properly.

III.2 Low-energy neutron rejection and background subtraction

Knowing the energy calibration and the flight distances, the TOF for each charged particle from target to detector can be calculated and subtracted from the registered total TOF. The resulting neutron TOF is used for selection of charged-particle events induced by neutrons in the main peak of the incident neutron spectrum (see Appendix I.2). The TOF cut reduces the background of charged particles produced by peak neutrons hitting the chamber and telescope housing since the flight paths are different, especially for the backward telescopes.

Background events, measured in target-out runs and analyzed in the same way as target-in events, are subtracted from the corresponding target-in runs after normalization to the same neutron fluence.

III.3 Absolute cross-section normalization

Absolute double-differential cross sections are obtained by normalizing the silicon data to the number of recoil protons emerging from the CH_2 target. After selection of events in the main neutron peak and proper subtraction of the target-out and $^{12}C(n,px)$ background contributions, the latter taken from a previous experiment, the cross section can be determined from the recoil proton peak, using n-p scattering data[12]. All data have been normalized using the n-p scattering peak in the 20° telescope.

IV. Corrections

Due to the thickness of the target and to the low-energy cut-offs in the particle identification, the measured low-energy charged particles are produced in fractions of the entire thickness of the target. Therefore, not only energy-loss corrections are needed but also particle-loss corrections. A FORTRAN program, TCORR[14], has been developed for correcting this effect by a folding method (see Appendix II).

Results from the correction method have been verified with an independent Monte-Carlo program called TARGSIM, based on GEANT[15]. This program simulates the measured spectra using the corrected spectra and the MEDLEY geometry as input. The simulation results are in agreement with the experimental data within the statistical errors over the whole energy region.

In addition, evaluated data[16] were chosen as input to check the reliability of our programs, obviously because validation with known “realistic” data is desirable. The latter have been simulated with the TARGSIM program to get pseudo-experimental data and have then been corrected with the TCORR program using the same conditions as in the experiment. The corrected results appear to reproduce the known “realistic” data well.

V. Results and discussion

Double-differential cross sections at laboratory angles of 20°, 40°, 100° and 140° for protons and alpha particles, compared to the calculations based on the GNASH[16,17] and TALYS[18] models, are shown in Figs. 1-2, respectively. In Appendix III, a description of the data set is given and the double-differential cross sections for deuterons, tritons and ^{3}He particles are shown.

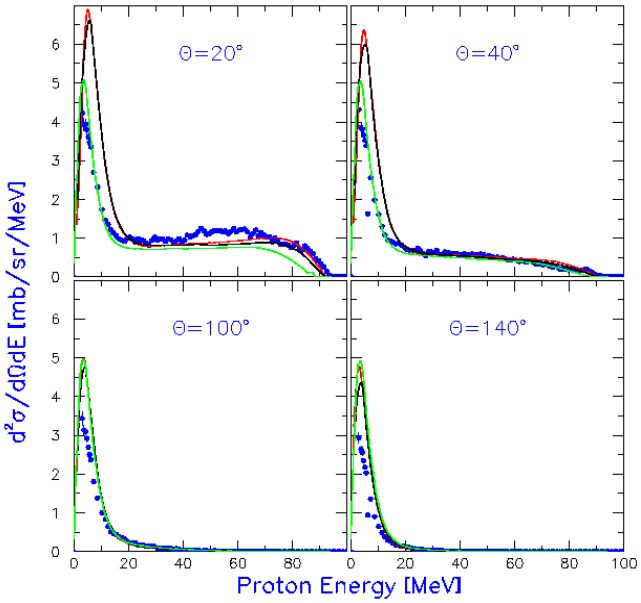

Fig. 1. Experimental double-differential cross sections (filled circles) of the Si(n,px) reaction at 96 MeV at four laboratory angles. The curves indicate theoretical calculations based on modified GNASH[16] (red), GNASH[17,19] (black) and TALYS[18] (green).

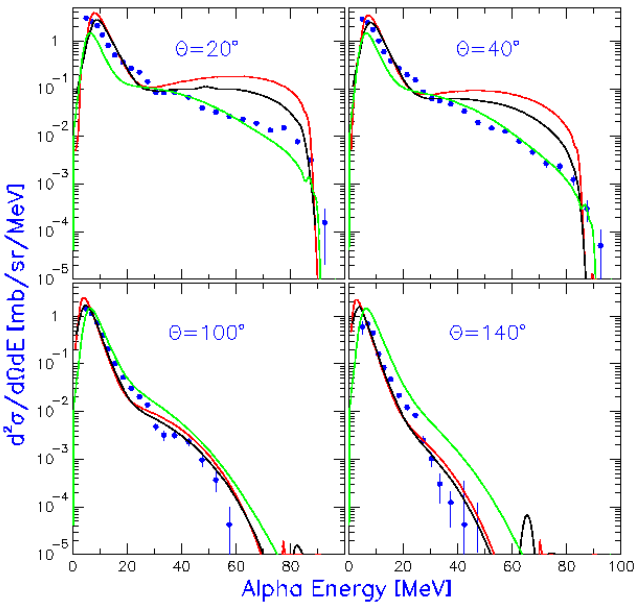

Fig. 2. Same as Fig. 1 for the Si(n,αx) reactions. Note the logarithmic scale.

For protons above 25 MeV, all calculations give a good description of the spectra. Below this energy, some differences can be observed, e.g., at forward angles TALYS gives a better description of the statistical peak than the GNASH calculations. The error bars represent statistical uncertainties only.

All the particle spectra have more or less pronounced peaks at low energies (below 10–15 MeV), the angular distributions of which are not too far from isotropy. All the spectra at forward angles have relatively strong intensity at medium-to-high energies. This intensity is strongly forward-peaked and hardly visible in the backward hemisphere. It is a sign of particle emission before statistical equilibrium has been reached in the reaction process.

The overall relative statistical uncertainties of individual points in the double-differential energy spectra at 20° are typically 3% for protons, 7% for deuterons, 20% for tritons, 20% for ^{3}He and 15% for alpha particles. As the angular distributions are forward-peaked, these values are increasing with angle. The systematic uncertainty contributions are due to thick target correction (1-20%), collimated solid angle (1-5%), beam monitoring (2-3%), the number of silicon nuclei (1%), CsI(Tl) intrinsic efficiency (1%), particle identification (1%) and dead time (<0.1%). The uncertainty in the absolute cross section is about 5%, which is due to uncertainties in the n-p scattering angle, as well as, in the contribution from the low-energy continuum of the ^{7}Li(p,n) spectrum to the n-p scattering proton peak (3%), the reference n-p cross sections (2%), statistics in the n-p scattering proton peak (2%), the carbon contribution (0.1%) and the number of hydrogen nuclei (0.1%).

V.2 Integrated spectra

For each energy bin of the outgoing light charged particle spectra, the experimental angular distribution is fitted by a simple two parameter formula[20],

$$\frac{d\sigma}{d\Omega} = a\exp(b\cos\theta) \qquad (1)$$

This allows extrapolation of double-differential cross sections to very forward and very backward angles. In this way coverage of the full angular range is obtained. By integration of the angular distribution, energy-differential cross sections (dσ/dE) are obtained for each ejectile which are shown in Fig. 3 together with the theoretical calculations. All calculations are in good agreement with the proton experimental data over the whole energy range. In the deuteron and alpha-particle cases, the models overpredict the high energy part of the spectra.

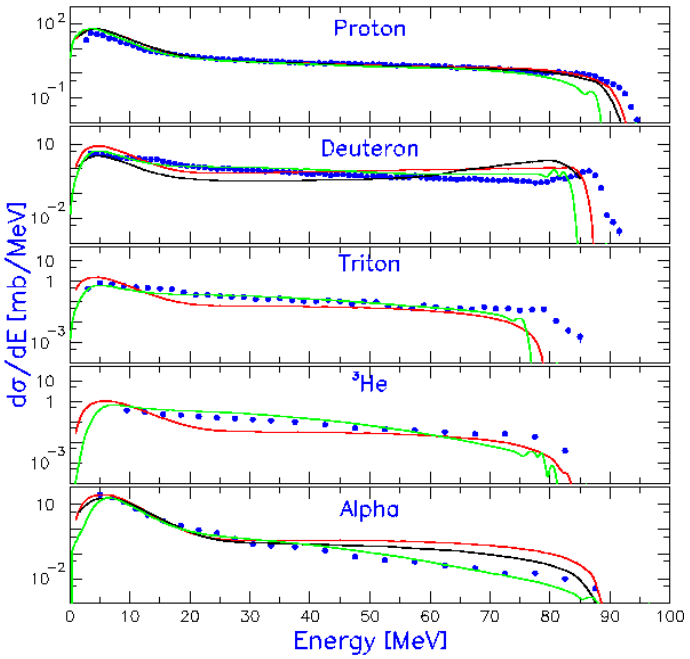

Fig. 3. Experimental energy-differential cross sections (filled circles) for neutron-induced p, d, t, ^{3}He and α production at 96 MeV. The curves indicate theoretical calculations based on modified GNASH[16] (red), GNASH[17,19] (black) and TALYS[18] (green).

The production cross sections (see Table 1) are deduced by integration of the energy-differential spectra. As explained above, the experimental values in Table 1 have to be corrected for the undetected cross section below the low-energy cutoff. This is particularly important for ^{3}He because of the high cutoff.

	Experiment	Experiment cutoff corrected	GNASH (Ref.19)	GNASH (Ref.16)	TALYS (Ref.18)
σ_{prod}(n,px) (mb)	458 ± 23	559	670.3	686.2	558.3
σ_{prod}(n,dx) (mb)	84 ± 4	95.8	77.0	126.5	107.6
σ_{prod}(n,tx) (mb)	15.2± 0.8	18.7	—	15.3	13.1
σ_{prod}(n, ^{3}Hex) (mb)	7.8 ± 0.5	12.6	—	10.1	14.5
σ_{prod}(n,αx) (mb)	152 ± 8	181	175.8	220.9	146.8

TABLE 1. Experimental production cross sections for proton, deuteron, triton, ^{3}He and alpha particles from the present work. Theoretical values resulting from GNASH and TALYS calculations are given as well. The experimental data in the second column have been obtained with cutoff energies of 2.5, 3.0, 3.5, 8.0 and 4.0 MeV for p, d, t, ^{3}He and alpha particles, respectively. The third column shows data corrected for these cutoffs, using the GNASH[16].

VI. Conclusions and outlook

In the present paper an experimental data set for light-ion production induced by 96 MeV neutrons on silicon[21] is reported. Experimental double-differential cross sections ($d^2\sigma/d\Omega dE$) are recorded at eight angles between 20° and 160°. Energy-differential (dσ/dE) and production cross-sections are obtained for the five types of outgoing particles. Theoretical calculations based on nuclear

reaction codes including direct, pre-equilibrium and statistical calculations give generally a good account of the magnitude of the experimental cross sections. For proton emission, the shape of the spectra for the double-differential and energy-differential cross sections are well described. The calculated and the experimental alpha-particle spectra are also in fair agreement with the exception of the high-energy part where the theory predicts higher yields than experimentally observed. For the other complex ejectiles (deuteron, triton and ^{3}He) there are important differences between theory and experiment in what concerns the shape of the spectra.

For the further development of the field, data at even higher energies are requested. The results suggest that the MEDLEY facility, which was used for the present work, should be upgraded to work also at 180 MeV, i.e., the maximum energy of the TSL neutron beam facility. At present, a new neutron beam facility is under commissioning at TSL, with a projected intensity increase of a factor five. This will facilitate measurements at higher energies than the present work.

The setup described in this paper comprises an active target, the information of which was not used in the analysis here but can provide valuable information on the kinetic energy transferred to the residual nucleus. This information might be crucial for SEU studies and it would therefore be of interest to compare this measurement with theoretical calculations.

Acknowledgements

This work was supported by the Swedish Natural Science Research Council, the Swedish Nuclear Fuel and Waste Management Company, the Swedish Nuclear Power Inspectorate, Ringhals AB, and the Swedish Defence Research Agency. The authors wish to thank the The Svedberg Laboratory for excellent support. One of the authors (U.T.) wishes to express his gratitude to the Thai Ministry of University Affairs and the International Program in the Physical Sciences at Uppsala University.

References

[1] H. Kanata *et al.*, Proc. IEEE 1999 Int. Conf. on Microelectronic Test Structures. **12**, 184 (1999).
[2] P. Hazucha and C. Svensson, IEEE J. Solid-State Circuits. **35**, 1422 (2000).
[3] V.F. Bashkirov *et al.*, Radiat. Meas. **30**, 427 (1999).
[4] S. Buchner *et al.*, IEEE Trans. Nucl. Sci. **47**, 705 (2000).
[5] Single-Event Upsets in Microelectronics, topical issue, eds. H.H.K. Tang and N. Olsson, Mat. Res. Soc. Bull. **28** (2003).
[6] S. Pomp *et al.*, paper in these proceedings (2003).
[7] K. Johansson *et al.*, IEEE Trans. Nucl. Sci. **46**, 1427 (1999).
[8] S. Satoh *et al.*, IEEE Electron Device Lett. **21**, 310 (2000).
[9] P. Hazucha and C. Svensson, IEEE Trans. Nucl. Sci. **47**, 2595 (2000).
[10] S. Dangtip *et al.*, Nucl. Instr. Meth. Phys. Res. A **452**, 484 (2000).
[11] J. Klug *et al.*, Nucl. Instr. Meth. Phys. Res. A **489**, 282 (2002).
[12] J. Rahm *et al.*, Phys. Rev. C **63**, 044001 (2001).
[13] U. Tippawan *et al.*, J. Nucl. Sci. Tech., Suppl. **2**, 1330 (2002).
[14] S. Pomp, Internal note (unpublished).
[15] GEANT, CERN Program Library Long Writeup W5013 (1993), Detector Description and Simulation Tool.
[16] Y.Watanabe, Internal note (unpublished).
[17] P. G. Young, E. D. Arthur, M. B. Chadwick, Los Alamos National Laboratory Report No LA-12343-MS (1992), GNASH-FKK version gn9cp0, PSR-0125.
[18] A. J. Koning, S. Hilaire , M.C. Duijvestijn (unpublished).
[19] ICRU Report 63, International Commission on Radiation Units and Measurements Bethesda, MD, March 2000.
[20] C. Kalbach, Phys. Rev. C **37**, 2350 (1988).
[21] U. Tippawan *et al.*, (to be published).

Appendix I. Data reduction procedures

Appendix I.1 Particle identification and energy calibration

The ΔE-E technique is used to identify light charged particles ranging from protons to lithium ions, which is illustrated in Fig. 1a. Good separation of all particles is obtained over their entire energy range. Since the energy resolution of each individual detector varies with the particle type, the particle identification cuts are defined to cover 3σ where σ is the standard deviation of the energy resolution of each particle type. Typical energy resolutions of the thin ΔE detectors are between 40 and 80 keV increasing with particle mass. The corresponding values for the thick ΔE detectors are between 150 and 550 keV and for the E detectors between 900 and 1200 keV. For the energy deposition in the E detector above 70 MeV in Fig. 1b, the two-dimensional cuts for protons, deuterons and tritons overlap slightly since the energy loss of the hydrogen isotopes in the ΔE_2 detector is rather small. This ambiguity is resolved by a two-dimensional plot (inset of Fig. 1b) of the deviations of the ΔE_1 and ΔE_2 signals from the calculated energy loss values in silicon (red lines in Fig. 1a). Particle identification is done by cutting along the minimum contour line, and thus possible misidentification should even out. This technique is also used to improve the separation between ^{3}He and alpha particles in some telescopes where the energy resolution is poor.

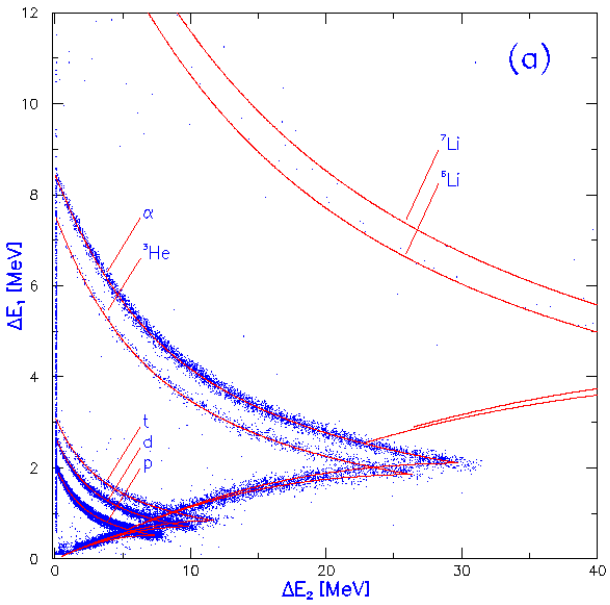

Fig. 1. a) Particle identification spectra at 20° for the ΔE_1 - ΔE_2 detector combinations. The red lines represent the calculations of energy loss in silicon. The straight line along the ΔE_1 axis represents low-energy charged particles which are stopped in the ΔE_1 detector.

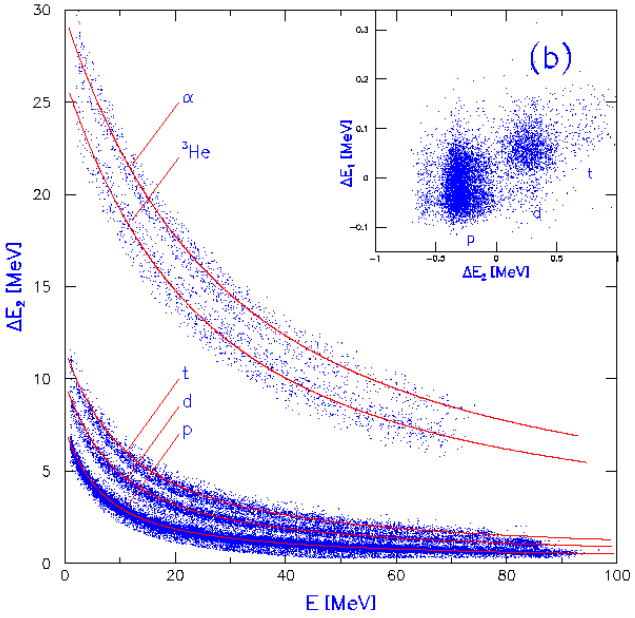

Fig. 1. b) Particle identification spectra at 20° for the ΔE_2 – E detector combinations. The red lines represent the calculations of energy loss in silicon. The inset figure illustrates the separation of high-energy protons, deuterons and tritons discussed above.

Energy calibration of all detectors is obtained from the data itself. Events in the ΔE–E bands are fitted with respect to the energy deposited in the two silicon detectors (red lines in Fig. 1). This energy is determined from the detector thicknesses and calculations of energy loss in silicon. The ΔE_1 detectors are further calibrated and checked using a 5.48 MeV alpha source. For the energy calibration of the CsI(Tl), two parameterizations of the light output versus energy of the detected particle are used, one for hydrogen isotopes and another one for helium isotopes. Supplementary calibration points are provided by transitions to the ground state and low-lying states in the H(n,p), ^{12}C(n,d)^{11}B and ^{28}Si(n,d)^{27}Al reactions. The energy of each particle type is obtained by adding the energy deposited in each element of the telescope.

Low-energy charged particles are stopped in the ΔE_1 detector leading to a low-energy cutoff for particle identification of about 3 MeV for hydrogen isotopes and about 8 MeV for helium isotopes (see Fig. 1a). The helium isotopes stopped in the ΔE_1 detector are nevertheless analyzed and a remarkably low cutoff, about 4 MeV, can be achieved for the experimental alpha-particle spectra. These alpha-particle events could obviously not be separated from ^{3}He events in the same energy region, but the yield of ^{3}He is much smaller than the alpha-particle yield in the region just above 8 MeV, where the particle identification works properly. That the relative yield of ^{3}He is small is also supported by the theoretical calculations in the evaporation peak region. In conclusion, the ^{3}He yield is within the statistical uncertainties of the alpha-particle yield for alpha energies between 4 and 8 MeV. A consequence of this procedure is that the ^{3}He spectra have a low-energy cutoff of about 8 MeV.

Appendix I.2 Low-energy neutron rejection and background subtraction

Knowing the energy calibration and the flight distances, the TOF for each charged particle from target to detector can be calculated and subtracted from the registered total TOF. The resulting neutron TOF is used for selection of charged-particle events induced by neutrons in the main peak of the incident neutron spectrum. The TOF cut reduces the background of charged particles produced by peak neutrons hitting the chamber and telescope housing since the flight paths are different, especially for the backward telescopes. The width of TOF cuts in all detectors is fixed to 3σ where σ is the standard deviation of the H(n,p) peak in the 20° telescope. Fig. 2a illustrates the selection procedure for deuterons at 20° laboratory angle. The red line is a kinematic calculation of the ground state peak in the deuteron spectra for each corresponding neutron energy. It provides a cross check of the energy and time calibration of the whole energy spectrum.

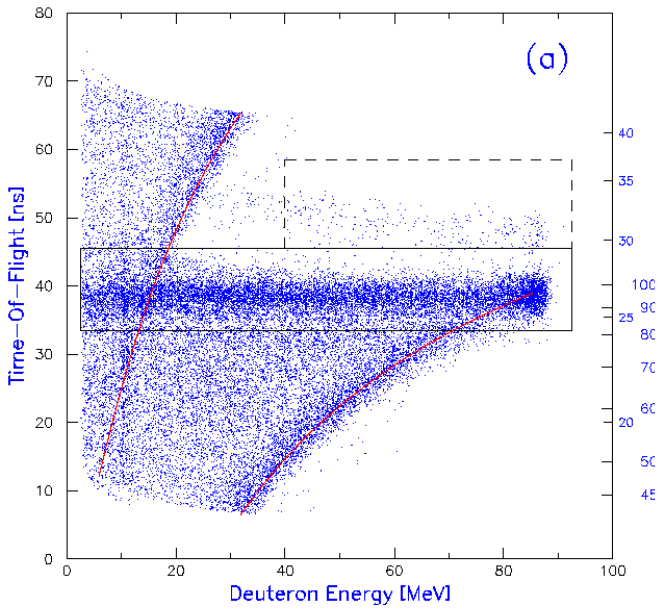

Fig. 2. a) Neutron TOF spectrum versus deuteron energy for the Si(n,dx) reaction at 20° and the selection of deuterons associated with the full-energy neutron peak. The neutron-energy scale is given to the right. The red line is a kinematic calculation of the ground-state energy as a function of the neutron energy. The lower rectangular cut is associated with neutrons in the full-energy peak, whereas the adjacent rectangular cut is used when correcting for the observed timing shift.

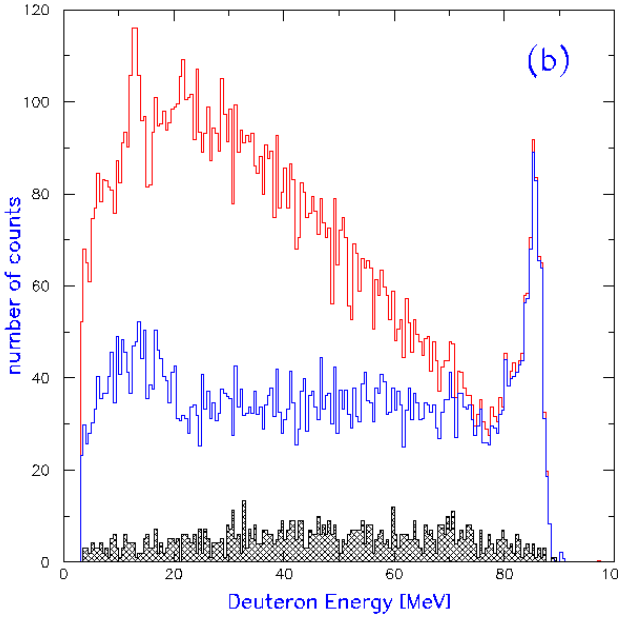

Fig. 2. b) Deuteron energy spectrum at 20° with (blue histogram) and without (red histogram) the full-energy neutron cut. The hatched histogram shows the target-out background.

Background events, measured in target-out runs and analyzed in the same way as target-in events, are subtracted from the corresponding target-in runs after normalization to the same neutron fluence. Fig. 2b shows the resulting spectrum of deuteron events at 20° induced by the main neutron peak. For comparison, the same spectrum without TOF cut is presented. Finally, the target-out background, obtained with the same TOF cut is shown. The signal-to-background ratio is about 4.

Appendix II. Corrections

Appendix II.1 Thick target correction

Due to the thickness of the target and to the low-energy cut-offs in the particle identification, the measured low-energy charged particles are produced in fractions of the entire thickness of the target. Therefore, not only energy-loss corrections are needed but also particle-loss corrections. Charged particles with the initial kinetic energy E_{init} have a well-defined range R in the target material. If $R(E_{init})$ is equal to or larger than the target thickness, all produced particles can escape from the target and no particle loss correction is required. If, on the other hand, $R(E_{init})$ is smaller than the target thickness, a correction for particles stopped inside the target is needed.

The adopted correction method employs an initial energy (E_{init}) distribution called the inverse response function for each measured energy. For the 303 μm silicon target used in the present experiment, a measured alpha particle of 4 MeV could either be due to a 4 MeV particle from the front surface of the target, a 27 MeV particle from the back surface of the target or anything in between. Therefore the content of the measured energy bin should be redistributed over the initial energy region from 4 MeV up to 27 MeV. A FORTRAN program, TCORR , has been developed which calculates the inverse response functions assuming, initially, an energy-independent cross section. Using these response functions, the measured spectrum is first folded to get the true initial energy spectrum including the correction for particle loss. The resulting spectrum is folded with the primary inverse response functions to get improved inverse response functions and the procedure is repeated. Resulting spectra from two successive iterations are compared by a Kolmogorov test to judge the convergence.

Results from the correction method have been verified with an independent Monte-Carlo program called TARGSIM, based on GEANT. This program simulates the measured spectra using the corrected spectra and the MEDLEY geometry as input. The simulation results are in agreement with the experimental data within the statistical errors over the whole energy region.

Obviously, the simulated spectra have much better statistics than the original experimental spectra and, therefore, the statistical fluctuations between neighboring energy bins are much smaller. In a sense, they are a fit to the experimental spectra. In order to estimate the systematic uncertainty introduced by the thick target correction, these simulated spectra are corrected with TCORR again and compared with the result of the first correction. The observed differences for individual energy bins are typically 5% and less than 10% in general. An extreme value of 40% was found in the lowest bin of the alpha spectrum at 140°. However, in all cases, except for protons where the statistical errors are very small, the deviations are within the statistical uncertainties of the original corrected data.

In conclusion, the systematic error of the target correction comes essentially from the statistical uncertainties. For protons and deuterons we estimate that this error is about 10% in the lowest two energy bins decreasing to only a few percent from 15 MeV and upwards. Due to less statistics and the increasing width of the inverse response functions, the uncertainty is larger for tritons, ^{3}He and alpha particles, where it is 20% in the lowest two bins decreasing to 10% above 25 MeV.

In addition, evaluated data were chosen as input to check the reliability of our programs, obviously because validation with known “realistic” data is desirable. The latter have been simulated with the TARGSIM program to get pseudo-experimental data and have then been corrected with the TCORR program using the same conditions as in the experiment. The corrected results appear to reproduce the known “realistic” data well.

Appendix II.2 Collimator correction

Active collimators have been placed in front of the telescope in order to define the solid angle. However, due to malfunctioning in the present experiment, the signal from these collimators could not be used to suppress events hitting them. Therefore, although the collimators actually work as passive collimators for helium particles below 35 MeV, their effect when particles punch through has to be corrected for. To this end, a FORTRAN program has been developed that, based on the measured spectrum of particles and an iteration procedure, estimates the shape and fraction of the energy spectrum of particles hitting the collimator. It has been found that the corrections in shape are rather small and under control in all cases. The systematic error related to this correction comes from the uncertainty in solid angle subtended by the silicon detectors, which is estimated to be 5% for the helium and the low-energy part of the hydrogen spectra. For the high-energy part of the hydrogen-isotope spectra this uncertainty vanishes due to the normalization procedure.

Appendix II.3 Other corrections

The 17 MHz repetition rate of the cyclotron beam pulse, which limits the TOF window to 58 ns, causes wrap-around problems. Thus, it is not possible to distinguish 96 MeV neutrons from those of 26 MeV created by the previous beam burst, since the latter have the same apparent TOF. This can be seen in Fig. 2a, where the bent band from the low-energy neutron tail crosses the straight band of the full-energy neutrons. Since the Q-value for the ^{28}Si(n,d) reaction is –9.4 MeV, this interference shows up as a bump below 20 MeV in Fig. 2b. A correction can be applied to the data by subtracting the average Si(n,d) cross section from 20 MeV to 30 MeV after normalizing with the ratio of neutron fluence at these energies and that at 96 MeV which is 6.3 %.

There is a TOF shift problem, seen as a band parallel to the main band in Fig. 2b. The reason for this is probably that the electronic timing module has not worked properly. This is corrected by extending the TOF cut with the dotted rectangle in the same figure, to include these events. This method could be applied only in the energy region where there is no interference from the low energy neutron tail. Therefore, the ratio of the number of events between the parallel and the main band is determined and then applied to the low-energy region as well. This ratio is 1.3 % in the worst case.

Albeit a majority of the neutrons appear in the narrow full-energy peak at 95.6 MeV, a significant fraction (about 25 %) are found in a tail towards lower energies remaining also after the TOF cut. The average neutron energy with these tail neutrons included is 92.4 MeV. This effect has been taken into account in the normalization of the data.

Minor corrections of a few percent are applied to the experimental spectra for the CsI(Tl) intrinsic efficiency and for the dead time in the data acquisition system.

Appendix III. Results and discussion

Double-differential cross sections at laboratory angles of 20°, 40°, 100° and 140° for deuterons, tritons and ^{3}He particles are shown in Figs. 3-5, respectively. All spectra for each particle type are plotted on the same cross section scale to facilitate the comparison of their relative intensity. The choice of the energy bin width is a compromise between the energy resolution in the experiment, the width of the inverse response functions and acceptable statistics in each energy bin. The error bars represent statistical uncertainties only.

From Figs. 3–5 it is obvious that the charged-particle emission from 96 MeV neutron irradiation of silicon is dominated by proton, deuteron and alpha particle channels. The spectra of the two other particle types studied in this work (tritons and ^{3}He) are more than an order of magnitude weaker. All the spectra have more or less pronounced peaks at low energies (below 10–15 MeV), the angular distributions of which are not too far from isotropy. This low-energy peak is not observed in the ^{3}He spectra due to the 8 MeV low-energy cutoff discussed above.

All the particle spectra at forward angles have relatively strong intensity at medium-to-high energies. This intensity is strongly forward-peaked and hardly visible in the backward hemisphere. It is a sign of particle emission before statistical equilibrium has been reached in the reaction process. In addition to this broad distribution of emitted particles, the deuteron spectra at forward angles show narrow peaks corresponding to transitions to the ground state and low-lying states in the final nucleus, ^{27}Al. These transitions are most likely due pick-up of weakly bound protons in the target nucleus, ^{28}Si.

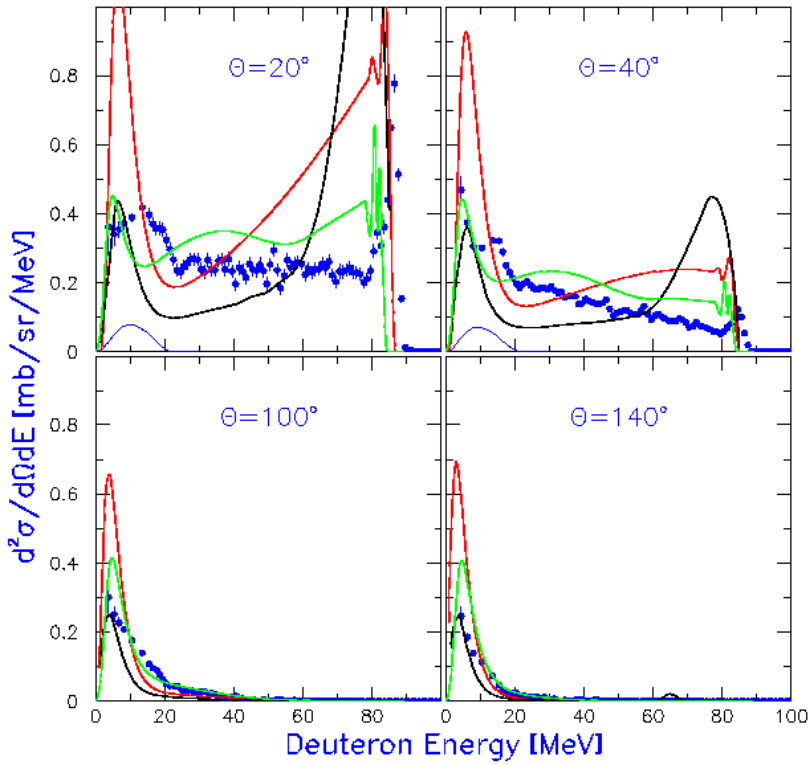

Fig. 3. Experimental double-differential cross sections (filled circles) of the Si(n,dx) reaction at 96 MeV at four laboratory angles. The curves indicate theoretical calculations based on modified GNASH[15] (red), GNASH[16] (black) and TALYS[17] (green). The blue line represent correction of the wrap-around effect.

There is another structure in the deuteron spectra at forward angles extending downwards from 20 MeV. This structure is due to the wrap-around effect discussed in Appendix II.3. In principle this effect is present in all spectra, but only visible for deuterons at forward angles due to the concentration of (n,d) intensity to low-lying states.

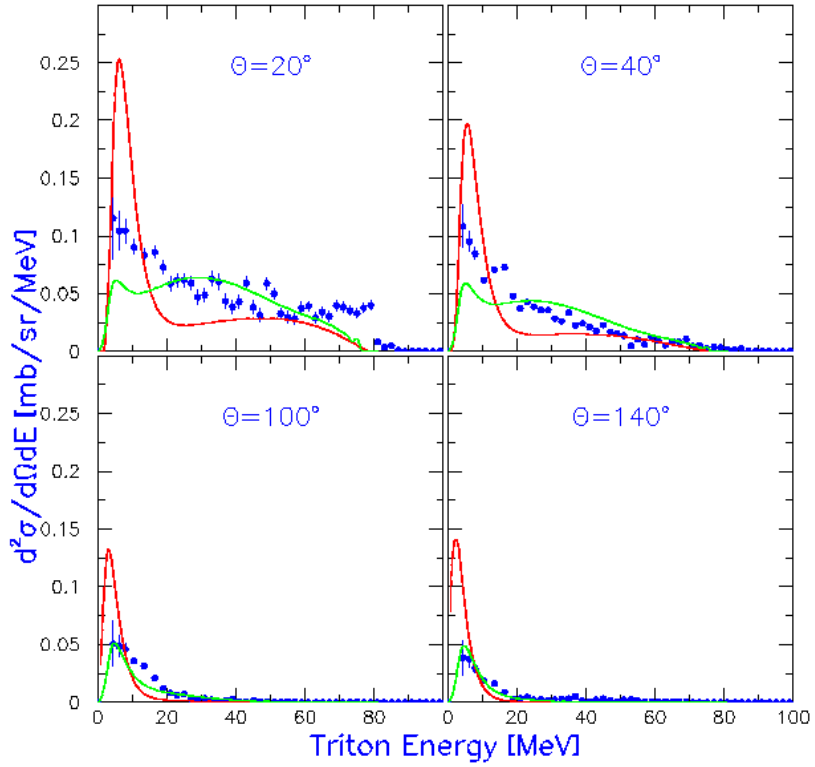

Fig. 4. Same as Fig. 3 for the Si(n,tx) reactions.

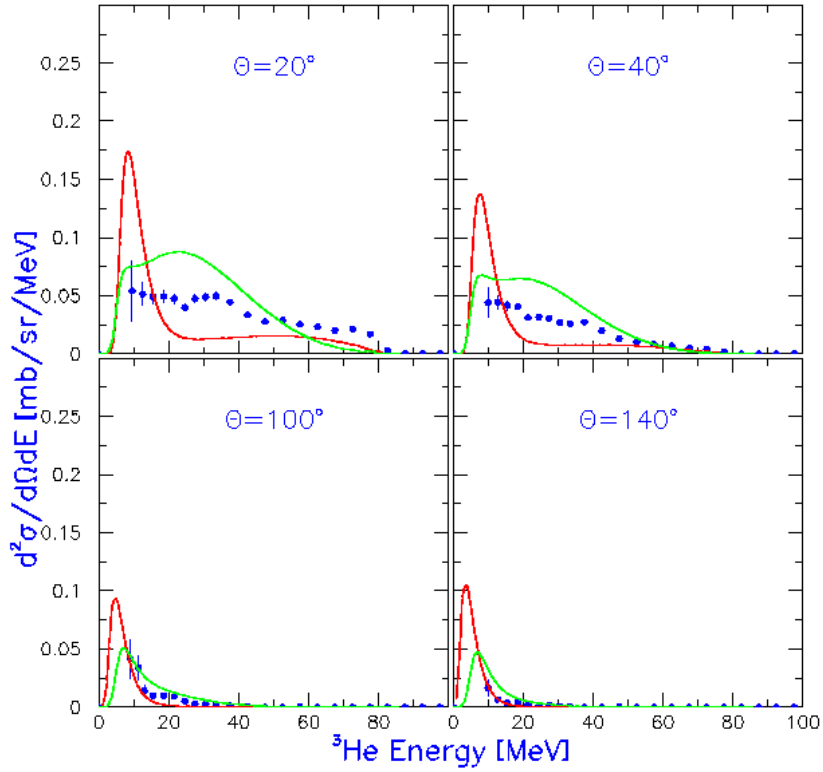

Fig. 5. Same as Fig. 3 for the Si(n, ^{3}Hex) reactions.

Appendix XIII

Nuclear Data for Medicine and Electronics

S. POMP[a*], J. BLOMGREN[a], B. BERGENWALL[a], S. DANGTIP[a,b], A. HILDEBRAND[a], C. JOHANSSON[a], J. KLUG[a], P. MERMOD[a], L. NILSSON[a], N. OLSSON[a,c], M. ÖSTERLUND[a], A.V. PROKOFIEV[d], P.-U. RENBERG[d], U. TIPPAWAN[a,b]

[a]*Department of Neutron Research, Uppsala University, Box 525, SE-751 20 Uppsala, Sweden*
[b]*Fast Neutron Research Facility, Chiang Mai University, Thailand*
[c]*Swedish Defence Research Agency (FOI), Stockholm, Sweden*
[d]*The Svedberg Laboratory, Uppsala University, Sweden*

Abstract. Fast-neutron cancer therapy is now routinely performed at about a dozen facilities worldwide. Typical neutron energies for treatment are up to 70 MeV. Lately, it has been recognized that cosmic-ray neutrons, with energies up to many GeV, give significant dose contributions to airplane personnel. In fact, airplane personnel are the category, which receives the largest doses in civil work. These cosmic-ray neutrons also create a reliability problem in modern electronics. A neutron can cause a nuclear reaction inside or near a chip, thus releasing free charge, which in turn could, e.g., flip the memory content or change the result of a logical operation. For all these applications, improved knowledge of the underlying nuclear physics is of major importance. The MEDLEY setup, which has been extensively used for ADS related work, has been used for measurements of cross sections related to biomedicine and electronics reliability. Simulations of single-event upsets are described as well as accelerated device testing activities at neutron beams.

1 Introduction

Recently, there has been increased attention on various applications where fast neutrons play a significant role. Two of these applications are nuclear medicine and single-event effects in electronics.

Conventional radiation treatment of tumours, i.e., by photons or electrons, is a cornerstone in modern cancer therapy. Some rather common types of tumours, however, cannot be treated successfully. For some of these, very good treatment results have been obtained with fast-neutron therapy[1)]. Furthermore, neutrons at commercial aircraft altitudes induce significant radiation doses to the airplane personnel[2)].

During the last few years, it has also become evident that electronics in airplanes suffer effects from cosmic-ray neutrons[3)]. For instance, a neutron can induce a nuclear reaction in the silicon substrate of a memory device, releasing free charge, which flips one or several memory units. This phenomenon is often referred to as single-event upset (SEU), a special case of single-event effects (SEE). Similar effects causing soft- and/or hardware damage have recently been identified also at ground level.

For both dosimetry and SEE, neutrons from cosmic rays are important. Although the cosmic-ray flux in space consists to 92% of protons and to 8% of alpha-particles and heavier atomic nuclei, most of these particles are absorbed in the atmosphere by atomic and nuclear interactions with nitrogen and oxygen nuclei. Sometimes, cascades of secondary particles, mainly neutrons and protons, are created. At typical aircraft flight altitudes (≈10 km) most of the secondary protons have, due to their charge, been stopped by atomic interactions with the atmosphere. Thereby, neutrons, having a total flux of the order of 10,000 $m^{-2} \cdot s^{-1}$, and showing a 1/E spectrum extending to several GeV of energy, dominate the relevant atmospheric radiation environment. At sea level, the neutron spectrum looks similar, although the intensity is about a factor of 100 lower.

For all these applications, an improved understanding of neutron interactions is needed for calculations of neutron transport and radiation effects. It should be emphasized that for these applications, it is beyond reasonable efforts to provide complete data sets. Instead, the nuclear data needed for a better understanding must come to a very large extent from nuclear scattering and reaction model calculations, which all depend heavily on nuclear models, which in turn are benchmarked by

* Corresponding author. E-mail address: stephan.pomp@tsl.uu.se

nuclear reaction cross-section data. However, for some applications data on specific nuclei can be of special importance. This is the case for both neutron therapy and SEUs.

Sections 2 and 3 briefly discuss fast-neutron therapy and single-event upsets, respectively. How the needed microscopic data can be measured is outlined in section 4. Turning the attention to SEUs, section 5 describes how the cross section can be simulated, while section 6 gives an outline of accelerated device testing in neutron beams. An outlook concludes this paper.

2 Fast-neutron therapy

Cancer treatment with fast neutrons is performed routinely at several facilities around the world, and today, it represents the largest therapy modality besides the conventional treatments with photons and electrons. Tumour types for which neutrons were found superior to conventional X-rays comprise salivary gland tumours, soft tissue sarcomas, prostatic adenocarcinomas and others[1)]. The rationale for using neutrons is their high linear energy transfer (LET) and hence the high relative biological effect (RBE). Due to a low oxygen enhancement ratio, fast neutrons are of an advantage for tumours with low oxygen content, so-called hypoxic tumours. In addition, the cell-cycle sensitivity is found to be less pronounced for irradiation with neutrons[4,5)].

However, there is clinical and radiobiological evidence that the accuracy required for clinical dosimetry for neutrons is at least as high as that in photon clinical dosimetry. In general, an accuracy on the level of 3.5% is required[6)].

In neutron therapy, the energy released per unit volume, *i.e.*, the dose, does not come directly from the neutron but from secondary charged particles produced by the neutron. The biological effects of the various charged particles produced by neutron interactions in the tissue are relatively well known. Not equally well known is the probability for the creation of charged particles and their energy and angular distributions. In other words, for the dose planning to be accurate enough, high-quality double-differential cross-section data for neutron-induced charged-particle production in the nuclei of the tissue are required[7)].

3 The single-event upset

When, e.g., an electronic memory circuit is exposed to particle radiation, the latter can cause a flip of the memory content in a bit, which is called a single-event upset (SEU). This induces no hardware damage to the circuit, but unwanted re-programming of memories, CPUs, etc., which can have consequences for the reliability, and ultimately for the safety of the system. Such software errors were in fact discovered by accident in a portable PC used at an airplane a few years ago, and later, the effect has been verified under controlled conditions, both in in-flight measurements[8,9)], as well as in the laboratory[10-12)].

The reason that the errors are referred to as SEUs is that they are induced by a single particle hitting the device. This is in contrast to radiation damage of electronics, a phenomenon caused by the integrated dose, which is normally delivered by a large quantity of particles.

Both neutrons and protons can be the source for SEUs. However, as described above, the relevant cosmic-ray flux at aircraft flight altitudes and below is dominated by neutrons. Therefore, similar to the case of fast-neutron cancer therapy, knowledge on neutron-induced production cross sections for charged particles in silicon and also on their energy and angular distributions is needed as a first step in order to obtain a full understanding of the SEU problem. Such experimental information is very scarce, and one has had to rely heavily on calculations based on nuclear models[13)]. Typically, nuclear spallation-reaction models, built on intranuclear-cascade processes and compound nuclear reactions have been used. Unfortunately, there are very few data to test these models, especially with

respect to production of particles heavier than alpha particles, and therefore the precision in the results is essentially unknown. More data exist on proton-induced reactions, but since the two particles differ both in charge and isospin, the corresponding cross sections can be quite different, especially in the range of 10 to a few hundred MeV. At higher energies, these cross sections are expected to be more similar.

One can estimate that, for typical memory devices produced a few years ago, an ionisation of around 1 MeV/μm is required in order to induce a SEU. This is with most standards a very high ionisation, and it is, therefore, evident that protons have no effect; they simply ionise too sparsely. Lithium and heavier ions can play a role, while alpha particles are on the margin. With increasing device densities, smaller geometries and decreasing critical charges, the sensitivity to radiation increases, and it is possible that also the alpha-particle spectrum can contribute to SEUs. Thus, detailed knowledge of basic nuclear data might allow the prediction of new sensitivity effects before they actually appear in commercial technology.

Experimental studies of the cross section for SEU induction have revealed that it has a threshold at about 10 MeV, rises almost linearly up to about 100 MeV and then saturates, or increases less rapidly[14]. Folding this cross section with the atmospheric neutron spectrum, which has a 1/E intensity distribution, the SEU rate in a real circuit as a function of neutron energy is obtained, resulting in a distribution that peaks around 100 MeV.

Once the production rates of various charged particles are known, the liberated charge and charge density from the stopping of the ion by the atomic electrons can be calculated using well-known physics. The second problem area of SEU is the interplay between the released charge and the pn-junction properties of the circuit. The circuit contains a large number of pn-junctions, often in complex geometry, in a scale comparable with the stopping length of the particles. It is, therefore, a complex task to evaluate the electrical effect of the deposited charge. One way to cope with this problem is to perform a simulation of the semiconductor, by simulating voltages and currents close to the pn-junctions, and their time dependencies, resulting from the charge deposition. An important aspect of such simulations is to find if a single particle affects several pn-junctions, as multiple correlated events may give rise to more severe system errors than single events.

The last step in the understanding is how the full circuit, or the system, is affected by the disturbance at one or several pn-junctions. Here, multiple correlated events may give rise to multiple errors, which are much harder to handle by error-correction codes than single errors. Because of the strong relation between particle-track geometry, pn-structure geometry, and circuit topology, all of the same scale, the full problem may not be easy to separate, leading to a very high complexity. One goal of the research should be to see to what extent the various problems could be separated. One necessary input are double-differential cross sections for neutron-induced reactions.

4 Measurements of neutron-induced cross sections

Light-ion production is at present motivated by theory development only, but, as mentioned above, it might be possible that such data can be of direct importance in a not so distant future. The MEDLEY detector setup[15] at TSL has been designed for measuring double-differential neutron-induced production cross sections of p, d, t, ^{3}He, and α data (and possibly also ^{6}Li and ^{7}Li) in the 50-130 MeV range. Such measurements have, *e.g.*, been performed for both carbon and silicon and are reported in Refs.[15-17]. Further measurements on carbon with improved statistics and on oxygen are currently under analysis.

As has been discussed above, the most important nuclear reactions causing SEUs in present technologies are probably neutron-induced production of heavy, low-energy recoils. Direct measurement of such cross sections with a neutron beam on a silicon target is in reality impossible with present technology, because these recoils have such low energies that an extremely thin target is needed if they should escape it. But then the luminosity becomes too small to obtain good statistics within a reasonable

time. This problem can be circumvented if using inverse kinematics. Such an experiment is under development at TSL[18].

5 Simulations

A common model applied by the device users, which usually do not have detailed technical informations about the device from the manufacturer, is the BGR method[19]. Here, some very preliminary simulation results from a BGR type of program currently under development at AerotechTelub/Saab are quoted[20]. The program uses stopping-power and range data from SRIM calculations[21], and neutron-silicon cross-section data calculated using the GNASH code by Chadwick *et al.*[22]. These cross-section data, which can be considered as state-of-the-art today, covers the neutron-energy range from 20 to 150 MeV, and include all ejectiles from hydrogen up to silicon, including all possible isotopes of each element.

Inputs to the calculations are the line-width and the sensitive thickness of the device. Typical values for 0.8 μm CMOS technology are 2.5 μm for the sensitive thickness, yielding a sensitive volume of about 80 μm^3, and a threshold for upsets of about 2 MeV. In this calculation only particles heavier than boron give contributions to the SEU cross section. The result of the calculation, scaled by a factor of 0.63 to give a charge collection efficiency (C) and volume (V) product of CV=50 μm^3, is shown in Fig. 1, together with the memories studied experimentally at TSL[14]. As can be seen, good agreement is obtained with these rather rough estimates of the input parameters. The simulation does neither include funnelling nor diffusion calculations of free charges. Though, funnelling and diffusion are probably effectively taken care of through the charge collection efficiency factor and the choice of the size for the sensitive volume.

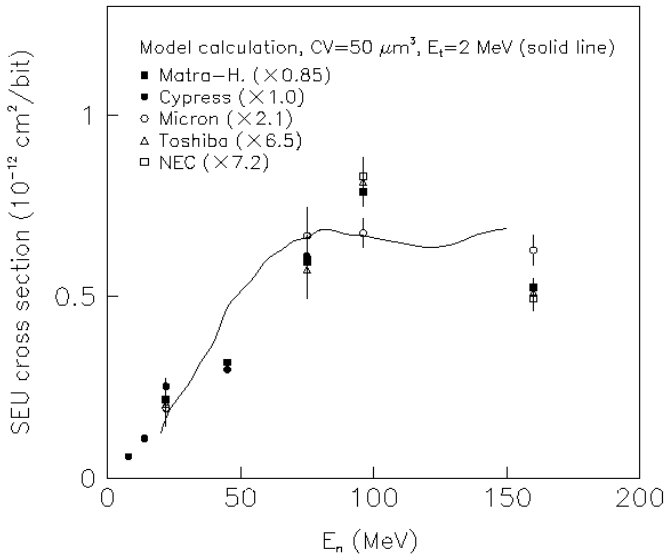

Figure 1. The SEU cross section for a few memory devices versus neutron energy. The line refers to a model calculation of the SEU cross section. See the text for details.

It is striking that this simple calculation translates, more or less directly, the nuclear cross sections into cross sections for SEU with a surprisingly good agreement. This illustrates the importance of fundamental nuclear data for a deep understanding of the SEU problem. As long as such an understanding has not been achieved, accelerated testing of the device prototypes at neutron-beam facilities is necessary.

6 Device testing activities

It is very time-consuming to use the natural flux of cosmic neutrons for testing of SEU effects in devices. Thus, it is of interest to perform accelerated testing, i.e., using a neutron flux far larger than the

natural one. This can be provided by neutron production using particle accelerators, where two major types of neutron beams are produced; white or mono-energetic.

White neutron beams have an intense neutron flux and typically a 1/E spectrum, strongly resembling the atmospheric neutron spectrum. Hence, if only the overall sensitivity of a specific device is required to be investigated, this would be the preferred technique. Although white neutron beams have a much larger total number of neutrons than mono-energetic ones, the difference is not profound for SEU studies. The reason is that the intensity of white beams falls dramatically with energy, while it is fairly constant for mono-energetic beam facilities[1], and SEU effects are to a large extent produced by rather high neutron energies. In addition white beams have a clear disadvantage when it comes to detailed studies of the origin of SEU effects, since they do not allow investigations of the SEU rate versus neutron energy. Mono-energetic neutron beams allow energy-resolved measurements, which, as has been demonstrated recently[23], can provide essential information. An example of such a facility is the neutron beam at TSL, mentioned above and described in detail in Refs.[24,25].

Results of energy-resolved measurements at TSL are presented in Ref.[14]. Several memory devices based on 4-transistor CMOS technology have been tested. It was found that the SEU sensitivity for different devices shows similar energy dependence, although the absolute magnitude differs. Furthermore, the cross-section curve seems to saturate, or even decrease slightly, at energies beyond 100 MeV. A similar behaviour has also been observed in proton measurements[26].

These findings are compatible with the discussion in section 3, where the critical charge seemed to suggest release of relatively heavy ions as the major source of the SEU effect. The energy dependence of neutron-induced heavy-ion production reactions strongly resembles the SEU data; there is a threshold at about 10 MeV, the cross section rises slowly with energy, and a maximum is reached in the 50-200 MeV range (the maximum differs for different ions produced).

In sum, to study the SEU phenomenon in some detail, one needs to perform both measurements and simulations. The measurements needed are energy-resolved neutron measurements, covering a wide energy range. For SEUs caused by the atmospheric neutron environment, the energy range from 10 to a few hundred MeV is especially interesting. While measurements at mono-energetic facilities obtain more information than at white beams, and are therefore preferred for detailed studies of the mechanisms behind the SEU phenomenon, measurements at white neutron sources can then be very valuable for an integral check, and to calibrate the absolute SEU rate in a realistic spectrum. Such a crosscheck has in fact been carried out. By folding energy-resolved data from the 20-180 MeV mono-energetic neutron beam at TSL with a white neutron spectrum, the SEU rates measured at TSL have been compared with corresponding data measured at the white source of the Weapons Neutron Research Facility (WNR) in Los Alamos. For devices that have been studied with both beams, the results are in agreement[27].

7 Outlook

It has been argued, that good double-differential cross sections for neutron-induced reactions are needed for applications in medicine and electronics. While the data should be used to develop nuclear reaction models, detailed data for a limited number of nuclei (carbon, oxygen and silicon) are of special importance.

One important reason for the development of precise and reliable simulation tools for SEUs is the limited availability of facilities for device testing. At present, less than ten neutron-beam facilities with relevant performance are available worldwide. Testing is so time-consuming that even if all

[1] This is due to the fact that the ^{7}Li(p,n) cross section is fairly constant with the energy of the incoming proton and that the proton-beam intensity is in general independent of the beam energy. The slight decrease with energy of the relative amount of mono-energetic peak neutrons compared to tail neutrons can be compensated by the use of a thicker ^{7}Li target without, due to the higher energy, loss in energy resolution.

facilities in the world were dedicated to SEU testing, only a small fraction of all devices introduced on the market could be investigated. Therefore, it can be anticipated that simulations will become the method of choice for the large bulk of devices, and in-beam testing will be performed for validation of the simulations. This scenario strongly suggests a dedicated campaign for cross-section measurements, because this represents the presently largest uncertainties in the simulation input.

For the further development of the field, data over a wide energy range are requested. The results of double-differential cross-section measurements obtained with MEDLEY suggest that this facility should be upgraded to work also at 180 MeV, i.e., the maximum energy of the TSL neutron-beam facility. The current commissioning of a new neutron-beam facility at TSL, with a projected intensity increase of a factor five, will facilitate this.

Acknowledgements

This work has been supported by the Swedish Natural Science Research Council and the Swedish Defence Research Agency. The authors wish to thank the technical staff of the The Svedberg Laboratory for enthusiastic and skillfull assistance.

References

[1] A. Wambersie, P. Pihet, H.G. Menzel, Radiat. Prot. Dosim. **31** (1990) 421.
[2] D.T. Bartlett, *et al.*, Radiat. Res. Cong. Proc. **2** (2000) 719. See also Radiat. Prot. Dosim. **86(4)** (1999).
[3] Single-Event Upsets in Microelectronics, topical issue, eds. H.H.K. Tang and N. Olsson, Mat. Res. Soc. Bull. **28** (2003).
[4] J. J. Broerse, *et al.*, Nuclear data for neutron therapy: Status and future needs, IAEA-TECDOC-992, Vienna (1997).
[5] Nordic Conference on Neutrons in Research and Cancer Therapy, Acta Oncol. **33(3)** (1994).
[6] B. J. Mijnheer, J. J. Battermann and A. Wambersie, Radioth. Onc. **8** (1987) 237.
[7] J. Blomgren and N. Olsson, Radiat. Prot. Dosim. **103(4)** (2003) 293.
[8] J. Olsen, *et al.*, IEEE Trans. Nucl. Sci. **40** (1993) 74.
[9] A. Taber and E. Normand, IEEE Trans. Nucl. Sci. **40** (1993) 120.
[10] E. Normand, *et al.*, IEEE Trans. Nucl. Sci. **41** (1994) 2203.
[11] C.A. Gossett, *et al.*, IEEE Trans. Nucl. Sci. **40** (1993) 1845.
[12] E. Normand, *et al.*, IEEE Trans. Nucl. Sci. **42** (1995) 1815.
[13] H.H.K. Tang, IBM J. Res. Develop. **40** (1996) 91.
[14] K. Johansson, *et al.*, IEEE Trans. Nucl. Sci. **45** (1998) 2519.
[15] S. Dangtip, *et al.*, Nucl. Inst. Meth. A452 (2000) 484.
[16] U. Tippawan, *et al.*, paper in these proceedings (2003).
[17] U. Tippawan, *et al.*, to be submitted to Phys. Rev. C.
[18] Y. Murin, private communication (2003).
[19] J. F. Ziegler and W. A. Lanford, Science **206** (1979) 776.
[20] T. Granlund, private communication (2003).
[21] J. F. Ziegler, J. P. Biersack, and U. Littmark, The Stopping and Range of Ions in Solids (Pergamon Press, New York, 1985).
[22] M.B. Chadwick, *et al.*, Med. Phys. **26** (1999) 974; and ICRU Report **63** (International Commission on Radiation Units and Measurements, Bethseda, MD, 2000)
[23] K. Johansson, *et al.*, IEEE Trans. Nucl. Sci. **46** (1999) 1427.
[24] H. Condé, *et al.*, Nucl. Instr. Meth. **A292** (1990) 121.
[25] J. Klug, *et al.*, Nucl. Instr. Meth. **A489** (2002) 282.
[26] C. Sanderson and C. Dyer, (private communication).
[27] T. Granlund and N. Olsson, A Comparative Study Between Two Neutron Facilities Regarding SEU, 7th European Conference on Radiation and its Effects on Components and Systems, Noordwijk, the Netherlands, September 2000.

A NEW FACILITY FOR HIGH-ENERGY NEUTRON-INDUCED FISSION STUDIES

A. Prokofiev[1,*], S. Pomp[2], U. Tippawan[2, 3], B. Bergenwall[2], L. Einarsson[1], C. Johansson[2], A. Hildebrand[2], P. Mermod[2], M. Österlund[2, 4], S. Dangtip[3], P. Phansuke[3], T. Germann[5], and J. Blomgren[2]

1 The Svedberg Laboratory, Uppsala University, Sweden
2 Department of Neutron Research, Uppsala University, Sweden
3 Chiang Mai University, Thailand
4 Jönköping University, Sweden
5 University of Konstanz, Germany

A new facility is constructed for measurements of neutron-induced fission cross sections in the absolute scale, i.e. versus *np* scattering cross section, which is adopted as the primary neutron standard. The advantage of the experiment compared to earlier studies is that the fission fragment detection and the neutron flux measurement via *np* scattering are performed simultaneously and at the same position in the beam, and therefore many sources of systematic errors cancel out. Further reduction of systematic errors is achieved due to "embedded" determination of effective solid angle of particle detectors using α-particles from the radioactive decay of the target nuclei. The performance of the facility is illustrated by first data obtained for angular distributions of fission fragments in the ^{238}U(n,f) reaction.

Introduction

Fission is one of the important processes that occur in the spallation target and in the reactor core. The fission channel contributes to the neutron production, to the radioactivity produced in the target, as well as to the chemical and radiological toxicity of the reaction products.

Furthermore, neutron-induced fission reactions of ^{235}U, ^{238}U, and ^{209}Bi are internationally recommended as standards for monitoring of high-energy neutron beams [1]. The ^{238}U(n,f) reaction is most widely used due to the compromise between the magnitude of the cross section, the insensitivity to the low-energy neutrons, and the availability of the target material. Monitors based on the ^{238}U(n,f) reaction are employed at many high-energy neutron facilities, *e.g.* at Los Alamos (USA) [2], Louvain-la-Neuve (Belgium) [3], NAC (South Africa) [4], JAERI (Japan) [5], and at TSL (Sweden) [6]. Schuhmacher *et al.* [3] have reported the use of the ^{238}U(n,f) reaction for neutron spectrum measurements as well.

It is still a long way towards a theory for high-energy fission that would give consistent description even for the simplest fission observables (total fission cross section, angular distribution of fragments) and that would be able to *predict* these quantities for an arbitrary unmeasured fission reaction. The reason of the difficulties in the theoretical description of fission is the great complexity of the fission process, which is concerned with alterations of the nuclear shape, and with reiterated redistribution of nuclear excitation energy between its different forms. An additional complication for high-energy fission stems from the fact that, for sufficiently large excitation energy, fission becomes energetically possible even after emission of a light particle. Thus, the fissioning nucleus in a given reaction is not unique, but belongs to a distribution on mass, charge and excitation energy.

During the last decade, great interest has been paid to dynamic effects in the fission process, *i.e.*, effects that are not taken into account in the statistical description of the process. An appropriate way to account for fission dynamics is to consider fission as a diffusion process over the fission barrier. In the framework of such an approach, suggested long ago by Kramers [7], the fission width, which serves as a measure of the fission probability, depends on a dissipation coefficient, which characterizes the viscosity of nuclear matter. In addition, formation of such a large-amplitude collective motion as the fission process requires a finite time, and fission will be suppressed during that time, while competing decay channels are active. Calculations of Grange and Weidenmüller [8] show that these effects grow rapidly with increasing excitation energy of the fissioning nucleus. Considering such effects has been found necessary for the description of nucleon-induced fission at intermediate energies (see, *e.g.*, an evaluation of Ignatyuk *et al.* [9]).

* Corresponding author. E-mail: Alexander.Prokofiev@tsl.uu.se

The particle that induces fission may leave a part of its linear momentum to the fissioning nucleus, or transfer the momentum completely, which corresponds to fission of the true compound nucleus. Due to this effect of linear momentum transfer (LMT), the folding angle between two complementary fission fragments is no longer equal to 180° in the laboratory frame, and fragments are preferentially emitted in the forward hemisphere. Measurements of LMT data are of interest not only in fission physics, but also for fundamental theories of nuclear reactions and nuclear matter. Another closely related effect is the anisotropy of the fission fragment angular distribution in the frame of the fissioning nucleus. The fact that more fragments are emitted at 0 and 180° than at 90° with respect to the incident beam direction is a consequence of the angular momentum transfer. The theory of anisotropy, developed by Halpern and Strutinsky [10], links the experimental observables to fundamental nuclear quantities, *e.g.*, the nuclear moment of inertia.

Despite the importance of the high-energy (n,f) cross-section data for theory and applications, there have been few attempts [4, 11-14] to measure them in the absolute scale, i.e. versus *np* scattering cross section, which is adopted as the primary neutron standard [1]. Only two studies [11, 13] have resulted in journal papers, and one of them [11] is in apparent disagreement with newer data above 20 MeV. The current standard ^{235}U and ^{238}U(n,f) cross-sections recommended by IAEA [1] are based on the data sets of Lisowski et al. [12]. The latter data have undergone a few revisions, but a publication is still awaited that would include the results and the thorough description of the experimental technique. The data of Newhauser et al. [14] have been superseded by newer data of the same group [4], not finally published either. Even fewer data sets are available for angular distributions of fragments from neutron-induced fission above 20 MeV [15-17].

In framework of the **FIRANDET** project (**Fi**ssion **R**esearch with **A**dva**n**ced **Det**ectors), a new facility is constructed for measurements of neutron-induced fission cross sections in the absolute scale. As a first step towards the cross-section measurements, we have obtained data on angular distributions of fission fragments from the ^{238}U(n,f) reaction.

Experimental Setup and Methods

The neutron beam

The facility makes use of the Uppsala neutron beam produced via the ^{7}Li(p,n) reaction by protons in the 20-180 MeV energy range. A thorough description of the facility may be found in a recent paper of Klug et al [6].

An example of the measured facility neutron spectrum is shown in Fig. 1, together with predictions of semi-empirical systematics of Prokofiev et al [18]. Satisfactory agreement is observed between the data and the systematics. The systematics gives correct prediction of the share of the high-energy peak neutrons in the spectrum (39.0% versus 37.8% for the experimental spectrum extrapolated to zero energy). This agreement confirms that the neutron spectrum is sufficiently well known and controlled.

The MEDLEY setup

An extensive description of the MEDLEY setup may be found in the paper of Dangtip et al. [19], and only a brief description is given below with the emphasize to the features that are specific to the studies of neutron-induced fission.

A photograph of the MEDLEY vacuum chamber is shown in Fig. 2. The chamber was situated at the distance of about 9.2 m. It has circular shape with a target assembly in the center and eight detector telescopes mounted at the angles of 20, 40, 60, 80, 100, 120, 140, and 160° relative to the beam direction.

The target assembly consists of two layers of $^{238}UF_4$, each about 1 mg/cm^2 thick, deposited on polyethylene backings, about 90 μm thick, and mounted back-to-back so that the angle between the target surface and the beam direction is 45°. The target assembly is 65 mm in diameter, and therefore it is fully covered by the central homogeneous area of the neutron beam.

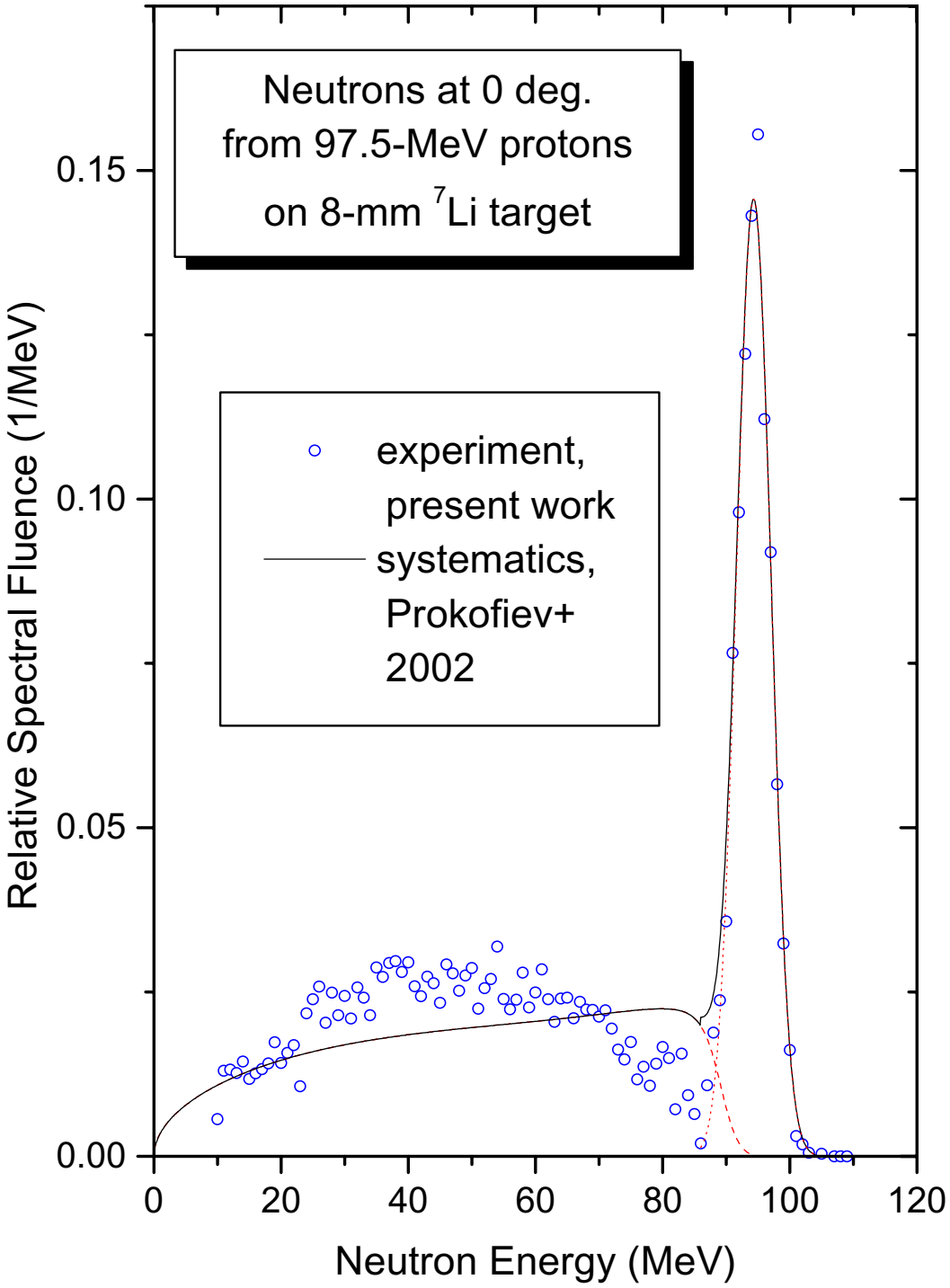

Fig. 1.
The neutron spectrum at 0º for 97.5-MeV protons incident on 8-mm thick ^{7}Li target. The symbols show data obtained in the present experiment. The curves represent the predictions of the systematics developed by Prokofiev et al [18]. The dotted, dashed and solid lines show respectively the predictions for high-energy peak, the low-energy tail and the sum of the two components. The width of the predicted high-energy peak component is adjusted to the experimental data. Both experimental and systematics data are normalized so that the area under the high-energy peak is unity.

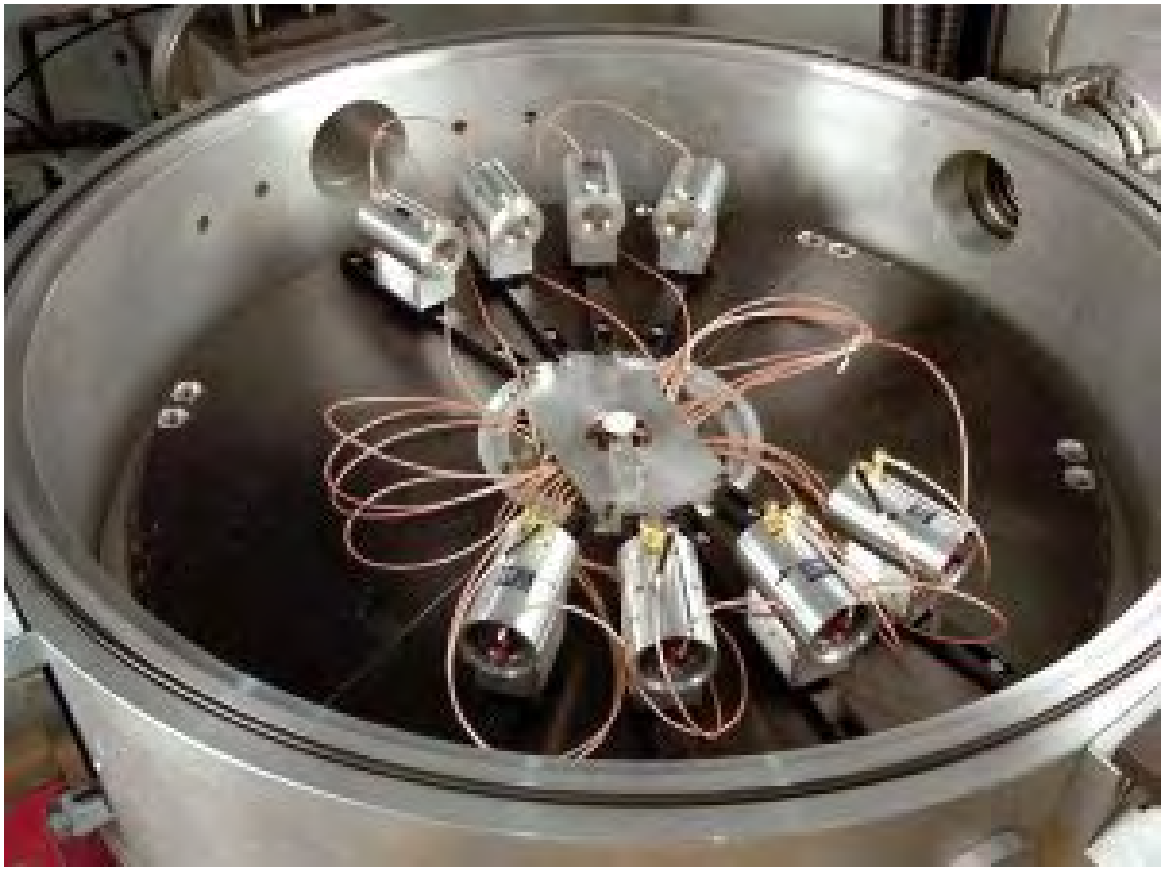

Fig. 2.
The view of the MEDLEY chamber. The neutron beam entrance is located at the right upper corner of the photograph. Eight telescope housings at different angles are seen. The location of the target assembly is in the center of the chamber. The assembly is mounted on the bottom side of the chamber lock and therefore is not seen on the photograph.

Each detector telescope consists of two surface barrier Si detectors, about 50- and 400-μm thick, and a 5-cm long CsI(Tl) scintillator crystal. Fission fragments are fully stopped and detected by the first Si detector, as well as α-particles from the radioactive decay of ^{238}U. Recoil protons, coming from the H(n,p) reaction with the hydrogen nuclei in the target backing, pass through both the Si detectors and deposit the most of their energy in the CsI(Tl) scintillator. The protons are discriminated against other charge particles using the ΔE-E techniques. Only information from the telescopes at 20 and 40° is useful for neutron beam monitoring, because of unwanted contribution of recoil protons from the ^{12}C(n,p) reaction at the other angle settings. Time-of-flight (TOF) techniques are employed to distinct fission and recoil proton events due to the high-energy peak and the low-energy tail in the neutron spectrum.

Data Analysis

An advantage of the experiment compared to earlier studies is that the fission fragment detection and the neutron flux measurement via *np* scattering are performed simultaneously and at the same position in the beam, and therefore many sources of systematic errors cancel out.

The counting rate of fission events induced by high-energy peak neutrons and registered by *i*-th detector is:

$$n_f(\vartheta_i) = \frac{\Omega_i}{2\pi} m \frac{N_A}{A} j_n \frac{d\sigma_f}{d\Omega}(\vartheta_i), \qquad (1)$$

where Ω_i is the solid angle subtended by *i*-th detector, ϑ_i is its angular coordinate, *m* is the mass of the fissile nuclide, N_A is the Avogadro number, *A* is the atomic mass of the fissile nuclide, j_n is the peak neutron flux through the target, and $\frac{d\sigma_f}{d\Omega}$ is the differential fission cross section.

The counting rate of α-particles from radioactive decay of target nuclei is:

$$n_\alpha(\vartheta_i) = m a_{spec} \frac{\Omega_i}{4\pi}, \tag{2}$$

where a_{spec} is the specific α-activity of the fissile nuclide. Combining Eqs. (1) and (2) gives:

$$\frac{d\sigma_f}{d\Omega}(\vartheta_i) = W(\vartheta) \frac{a_{spec} A}{2N_A} \frac{1}{j_n}, \tag{3}$$

where

$$W(\vartheta) = \frac{n_f(\vartheta_i)}{n_\alpha(\vartheta_i)} \tag{4}$$

is the relative angular distribution of fission fragments. Thus, the described procedure allows us to reduce the angular distribution measurement to the simple counting of fragments and α-particles, the latter being done either during the beamtime or in additional runs without the beam.

The second term in Eq. (3) includes only well-known physical constants, and the third one is the inverse neutron flux. Neither the mass of the fissile nuclide nor the solid angle subtended by the detector are present in Eq. (3). Thus, counting α-particles from radioactive decay of target nuclei provides "embedded" determination of effective solid angle of the detectors and allows one to reduce further the systematic errors. In particular, the described procedure is insensitive to possible inhomogeneity of the fissile target.

As it is known from the past studies (see e.g. the works of Tutin et al [15] and Ryzhov et al [16]), the fragment angular distribution from fission induced by high-energy neutrons may be expressed as:

$$W(\vartheta) = \frac{k_{norm}}{2\pi}(1 + B\cos^2\vartheta), \tag{5}$$

where *B* is the angular anisotropy factor and k_{norm} is a normalization constant. Combining Eqs. (3) and (5) and integrating over the angle ϑ gives the final expression for the fission cross-section:

$$\sigma_f = \frac{a_{spec} A k_{norm}}{N_A j_n}\left(1 + \frac{B}{3}\right). \tag{6}$$

Experimental Results

A few neutron beam runs have been performed at different neutron energies, and the data are being analyzed with the goal to deduce fission cross-sections and angular distributions of fission fragments. In order to illustrate the performance of the facility, we report angular distributions of fission fragments in the ^{238}U(n,f) reaction at quasi-monoenergetic neutrons with the peak energy of 21 MeV.

Sufficiently good separation between fission fragments and products of non-fission reactions is observed in the energy spectra for all detectors, and therefore the uncertainty in the fission count rate is virtually purely statistical. In Fig. 3, the fragment angular distribution is shown, obtained according to Eq. (4). As soon as TOF information has not been used yet, the shown angular distribution is a superposition of contributions from reactions induced by neutrons of any energy in the incident spectrum. The line in Fig. 3 represents the least squares fit of the data according to Eq. (5). It is seen that the distribution is successfully approximated by the fit. The deduced angular anisotropy factor *B*, related to the whole incident neutron spectrum, is 0.55±0.11.

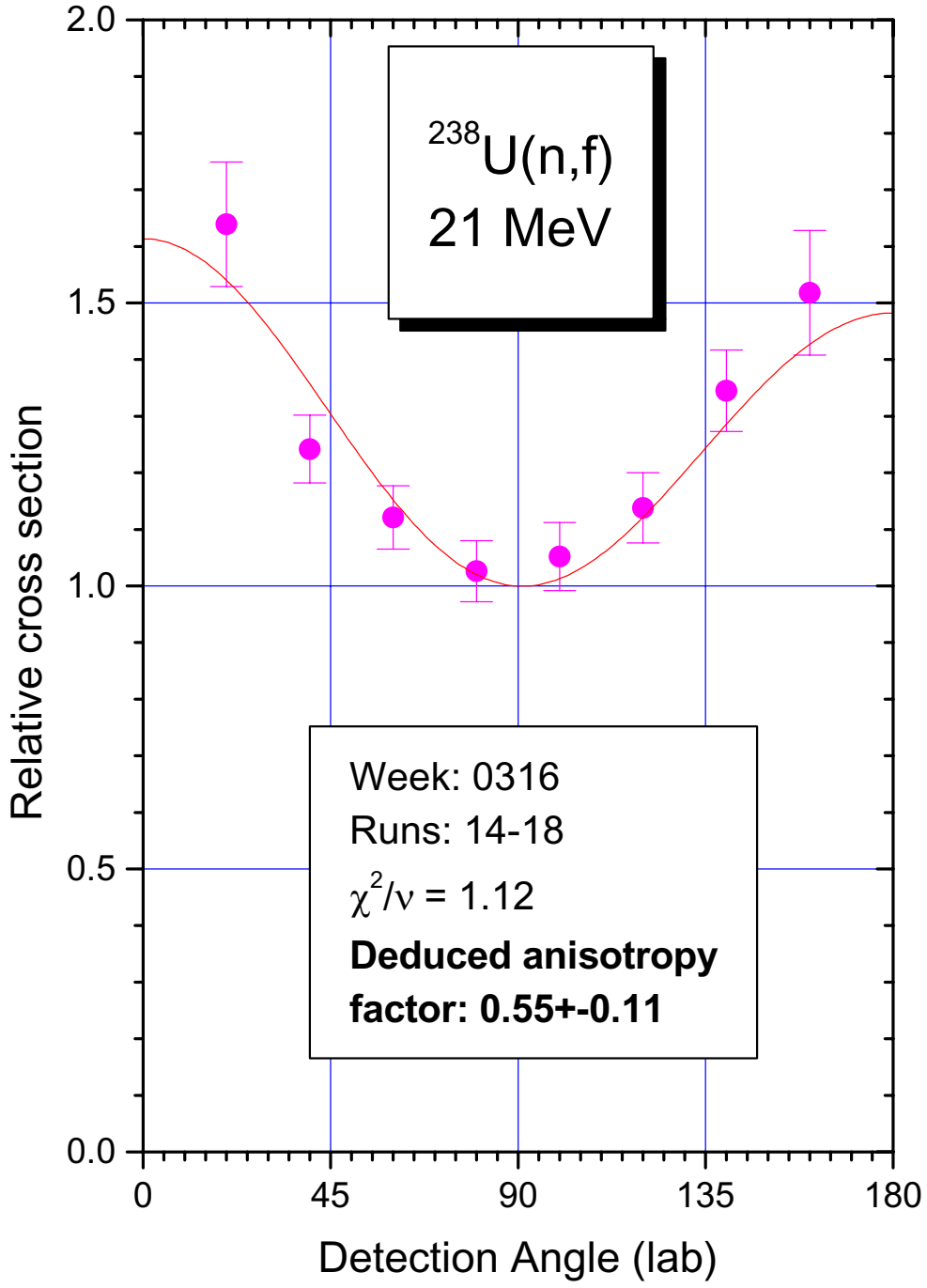

Fig. 3.
Angular distribution of fragments from fission of ^{238}U induced by quasi-monoenergetic neutrons with the peak energy of 21 MeV. No TOF selection is performed, and therefore the data correspond to the whole neutron spectrum. The shown uncertainties are solely due to statistical errors.

In order to deduce the angular anisotropy for the peak neutron energy, one has to correct for the contribution of reactions induced by low-energy tail neutrons. Such correction can be obtained either by application of the TOF cut to the experimental data or by a model calculation based on the data on incident neutron spectrum, the fission cross-section, and the angular anisotropy in the low-energy region. At the present work, only the second option is tried. The neutron spectrum from the ^{7}Li(p,n) reaction at 0° is taken from the evaluation of Mashnik et al [20] included in the LA150 library. The ^{238}U(n,f) cross-section data come from the ENDF-VI library (below 20 MeV) and from the evaluation of Carlson et al [1] (above 20 MeV). By folding the neutron spectrum and the fission cross-section, we obtain the distribution of fission events on neutron energy. The latter is folded with fission anisotropy calculated using the STAPRE-H code [17, 21] for the neutron energies below 20 MeV. The result is the contribution to the anisotropy due to the low-energy tail neutrons. Its comparison with the integral anisotropy factor gives the result for the anisotropy related to the high-energy peak neutrons:

$$B\ (E_n = 21\ \text{MeV}) = 0.69 \pm 0.19. \qquad (7)$$

The obtained result is shown in Fig. 4 together with other experimental data [22] and the model calculation using the STAPRE-H code [17, 21]. Good agreement is seen between the result of the present work and the one of Ryzhov [16, 17], as well as with the STAPRE-H calculation [17, 21].

Conclusions and Further Work

First experimental data from the FIRANDET project are reported. The obtained angular distributions of fragments from the ^{238}U(n,f) reaction are in good agreement with the past experimental results and theoretical calculations. This ensures adequacy of the performance of the experimental setup and the data analysis techniques.

Measurements and processing of the obtained experimental data will be continued in order to make use of the TOF information, to improve the statistics, and to cover the whole 20-180 MeV energy region with angular distribution and cross section data for the most important fission reactions.

Acknowledgement

The authors are grateful to R. Nolte and I. V. Ryzhov for valuable discussions and for sending us their results prior to publication. We are thankful to the staff of The Svedberg Laboratory for providing us with the beam and for other various help. The study was supported in part by The Swedish Foundation for International Cooperation in Research and Higher Education (STINT).

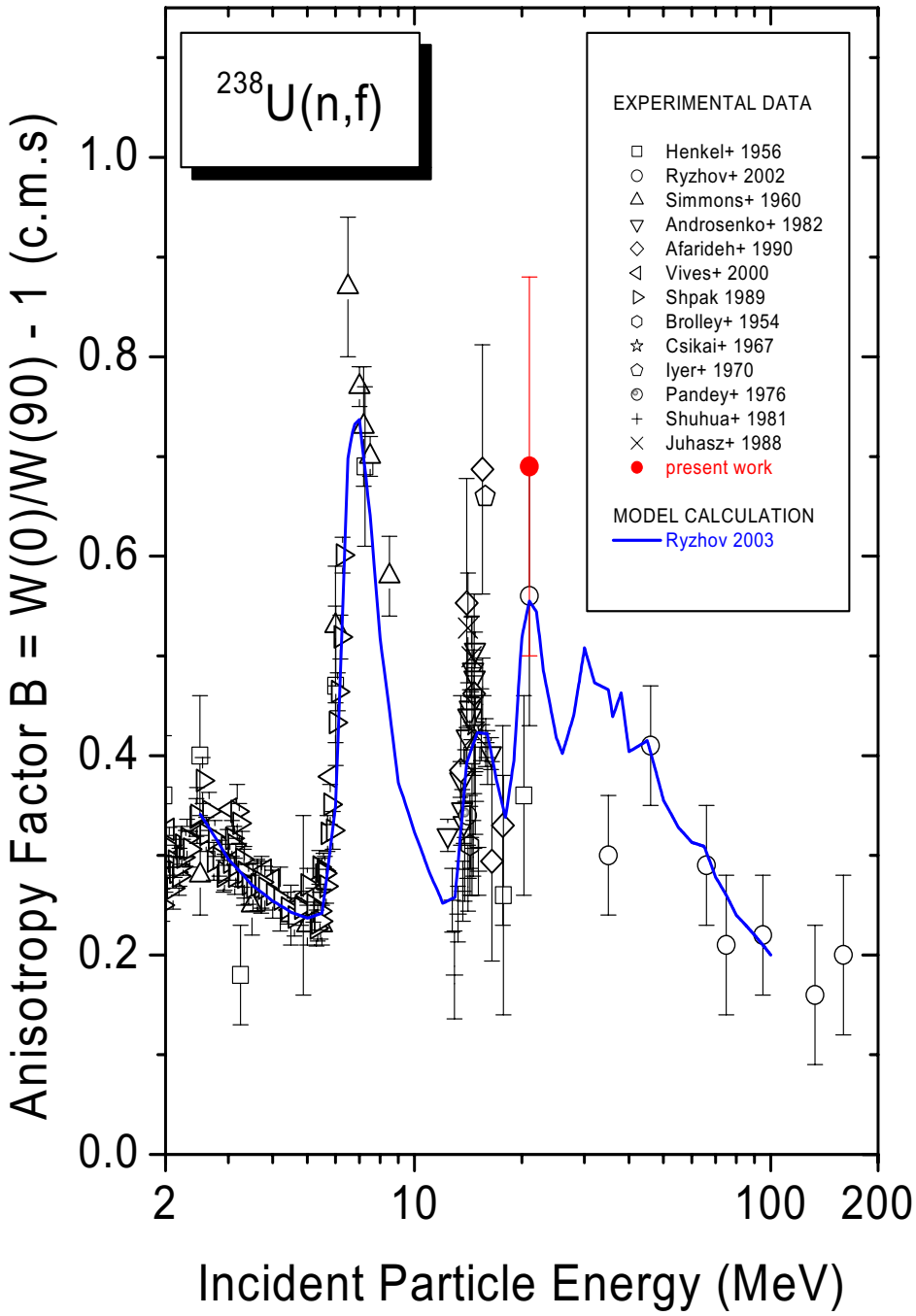

Fig. 4
Energy dependence of the anisotropy of neutron-induced fission of ^{238}U: experimental data [22] and theoretical calculations [17, 21]

References

[1] A.D. Carlson, S. Chiba, F.-J. Hambsch, N. Olsson, A. N. Smirnov, Proc. Int. Conf. on Nuclear Data for Science and Technology, Trieste, Italy, May 19-24, 1997, Part II, 1223-1229.

[2] S. A. Wender, S. Balestrini, A. Brown, R. C. Haight, C. M. Laymon, T. M. Lee, P. W. Lisowski, W. McCorkle, R. O. Nelson, W. Parker, and N. W. Hill, NIM A336, 226-231 (1993).

[3] H. Schuhmacher, H. J. Brede, V. Dangendorf, M. Kuhfuss, J. P. Meulders, W. D. Newhauser and R. Nolte, NIM A421, 284-295 (1999).

[4] R. Nolte, M. S. Allie, P. J. Binns, F. D. Brooks, A. Buffler, V. Dangendorf, K. Langen, J.-P. Meulders, W. D. Newhauser, F. Roos, and H. Schuhmacher, Journal of Nuclear Science and Technology, Supplement 2, 311-314 (2002).

[5] M. Baba, Y. Nauchi, T. Iwasaki, T. Kiyosumi, M. Yoshioka, S. Matsuyama, N. Hirakawa, T. Nakamura, Su. Tanaka, S. Meigo, H. Nakashima, Sh. Tanaka, N. Nakao, NIM A 428, 454-465 (1999).

[6] J. Klug, J. Blomgren, A. Atac, B. Bergenwall, S. Dangtip, K. Elmgren, C. Johansson, N. Olsson, A.V. Prokofiev, J. Rahm, O. Jonsson, L. Nilsson, P.-U. Renberg, P. Nadel-Turonski, A. Ringbom, A. Oberstedt, F. Tovesson, C. Le Brun, J.F. Lecolley, F.R. Lecolley, M. Louvel, N. Marie, C. Schweitzer, C. Varignon, Ph. Eudes, F. Haddad, M. Kerveno, T. Kirchner, C. Lebrun, L. Stuttge, I. Slypen, A.N. Smirnov, R. Michel, S. Neumann, U. Herpers. Nuclear Instruments and Methods in Physics Research A489, 282-303 (2002).

[7] H.A. Kramers, Physica 7, 284 (1940).

[8] D. Grange and H.A. Weidenmüller, Phys. Lett. B96, 26 (1980).

[9] A.V. Ignatyuk *et al.,* Nucl. Sci. Eng. 136, 340-356 (2000).

[10] I. Halpern and V.M. Strutinsky, In: Proc. 2nd Conf. on the Peaceful Uses of Atomic Energy. Geneva, 1958, v. 15, p. 408.

[11] V.M. Pankratov, Atomnaja Energija 14, 177 (1963) (in Russian).

[12] P.W. Lisowski, A. Gavron, W.E. Parker, J.L. Ullman, S.J. Balestrini, A.D. Carlson, O.A. Wasson, and N.W. Hill, Proc. of a Specialists' Meeting on Neutron Cross Section Standards for the Energy Region above 20 MeV, Uppsala, Sweden, May 21-23, 1991, OECD/NEA Report NEANDC-305 'U', 177-186.

[13] V.P. Eismont, A.V. Prokofiev, A.N. Smirnov, K. Elmgren, J. Blomgren, H. Condé, J. Nilsson, N. Olsson, T. Rönnqvist, and E. Tranéus, Phys. Rev. C53, 2911-2918 (1996).

[14] W.D. Newhauser, H.J. Brede, V. Dagendorf, W. Mannhart, J.P. Meulders, U.J. Schrewe, H. Schuhmacher, Proc. Intern Conf. on Nuclear Data for Science and Technology, May 19-24, 1997, Trieste, Italy, 1236-1238.

[15] G. A. Tutin, I. V. Ryzhov, V. P. Eismont, A. V. Kireev, H. Condé, K. Elmgren, N. Olsson and P. -U. Renberg, NIM A457, 646-652 (2001).

[16] I. V. Ryzhov et al., J. Nucl. Sci. Techn., Suppl. 2, 295-298 (2002);

[17] I. V. Ryzhov, Ph. D. thesis, V.G. Khlopin Radium Institute, St. Petersburg (2003) (in Russian).

[18] A.V. Prokofiev, M.B. Chadwick, S.G. Mashnik, N. Olsson, and L.S. Waters, Journal of Nuclear Science and Technology, Supplement 2, 112-115 (2002).

[19] S. Dangtip, A. Ataç, B. Bergenwall, J. Blomgren, K. Elmgren, C. Johansson, J. Klug, N. Olsson, G. Alm Carlsson, J. Söderberg, O. Jonsson, L. Nilsson, P. -U. Renberg, P. Nadel-Turonski, C. Le Brun, F. -R. Lecolley, J. -F. Lecolley, C. Varignon, Ph. Eudes, F. Haddad, M. Kerveno, T. Kirchner and C. Lebrun, *Nucl. Instr. and Meth.* **A** 452, 484-504 (2000).

[20] S. G. Mashnik, M. B. Chadwick, P. G. Young, R. E. MacFarlane, and L. S. Waters. LANL Report LA-UR-00-1067 (2000).

[21] M. Avrigeanu, M. Ivascu, V. Avrigeanu, Report NP-63 (1987).

[22] The CSISRS data base, http://www.nndc.bnl.gov/nndc/exfor.html

Forward-angle neutron-proton scattering at 96 MeV

C. Johansson[a], J. Blomgren[a1], A. Ataç[a], B. Bergenwall[a], S. Dangtip[e], K. Elmgren[b], A. Hildebrand[a], O. Jonsson[c], J. Klug[a], P. Mermod[a], P. Nadel-Turonski[d], L. Nilsson[a,c], N. Olsson[a,b], S. Pomp[a], A.V. Prokofiev[c], P.-U. Renberg[c], U. Tippawan[a,e], M. Österlund[a]

[a] *Department of Neutron Research, Uppsala University, Box 525, S-75120 Uppsala, Sweden*
[b] *Swedish Defence Research Agency (FOI), Stockholm, Sweden*
[c] *The Svedberg Laboratory, Uppsala University, Sweden*
[d] *Department of Radiation Sciences, Uppsala University, Sweden*
[e] *Department of Physics, Chiang Mai University, Thailand*

Abstract

The differential *np* scattering cross section has been measured at 96 MeV in the angular range $\theta_{\text{c.m.}} = 20^\circ - 76^\circ$. Together with an earlier data set at the same energy, covering the angles $\theta_{\text{c.m.}} = 74^\circ - 180^\circ$, a new data set has been formed in the angular range $\theta_{\text{c.m.}} = 20^\circ - 180^\circ$. This extended data set has been normalised to the experimental total *np* cross section, resulting in a renormalisation of the earlier data of 0.7 %, which is well within the reported normalisation uncertainty for that experiment. A novel normalisation technique has been investigated. The results on forward *np* scattering are in reasonable agreement with theory models and partial wave analyses and have been compared with data from the literature.

PACS numbers: 13.75.Cs, 25.40.Dn, 28.20.Cz

1 Introduction

The neutron-proton scattering cross section plays an important role in fundamental physics, since it can be used to derive a value of the absolute strength of the strong interaction between nucleons, i. e., the pion-nucleon coupling constant, $g^2_{\pi NN}$. The πNN coupling constant governs the properties of the two-nucleon system to such an extent that only a few percent difference in its value is sufficient to either unbind the deuteron or to produce a bound diproton, in both cases with major cosmological consequences. Moreover, its precise value is of crucial importance for the quantitative discussion of a large number of phenomena in hadron and nuclear physics.

[1] Corresponding author. Tel. +46 18 471 3788, *e-mail address:* jan.blomgren@tsl.uu.se

The actual value of the πNN coupling constant is quoted at the pion pole, where the square of the momentum transfer q^2 is equal to $-m_\pi^2$, where m_π is the pion mass. It is therefore not directly available from experimental data, but at 180° np scattering, the conditions are close to this limit. As a consequence, backward np scattering data have often been used to extract the charged coupling constant, $g^2_{\pi^\pm NN}$. In such determinations, both the absolute normalisation and the shape of the angular distribution close to 180° are of importance for the extracted value of $g^2_{\pi NN}$.

Unfortunately, there are severe discrepancies in the differential np scattering cross section data base in the energy region $100 - 1000$ MeV [1]. It is dominated by two large data sets, data from Los Alamos National Laboratory (LANL) (Bonner *et al.* [2], Evans *et al.* [3, 4], Jain *et al.* [5] and Northcliffe *et al.* [6]) and from Paul Scherrer Institute (PSI) (Hürster *et al.* [7], recently replaced by Franz *et al.* [8]). Until recently, the LANL data constituted almost 50 % of the data base. The recent publication of an extended PSI data set [8] means that these data now account for over 60 % of the statistical weight of the data base.

The two data sets are incompatible when only statistical uncertainties are considered. Above about 500 MeV, the angular distribution shapes of these two sets agree reasonably well, while at 200 MeV, the 150°/180° cross section ratios differ by as much as $10 - 15$ %. Unfortunately, the systematic uncertainties are not well known for the two data sets. It cannot be excluded that at least part of the discrepancies is related to systematic effects not taken into account [9].

These two large data sets can serve as an illustration of the problems, but these difficulties are not unique. There are a large number of other experiments that also differ significantly. It has been concluded that the np scattering cross section is hardly better known than to about 10 %, using experimental information only [1].

Besides shape differences, there also seem to be inconsistencies in the normalisation of np data, which is not surprising, because absolute measurements of neutron beam intensities are notoriously difficult [10]. This is because the only way to determine the number of neutrons in a beam is to detect charged particles produced in neutron-induced nuclear reactions, but to measure the cross section for those reactions, the beam intensity has to be known.

There are ways to circumvent this dilemma, but they are associated with painstaking efforts. Below the pion-production threshold at about 270 MeV, two methods have been used to determine the np scattering cross section absolutely.

One of the methods is tagging, i.e, neutrons are produced in a nuclear reaction where the detection of associated charged particles gives unambiguous information about the neutron. For instance, at low energies, the ^{2}H(d,^{3}He)n reaction has been used in measurements where determination of the energy and direction of the ^{3}He recoil gives information about the neutron energy and direction, and the mere presence of the ^{3}He recoil implies that a neutron has been produced. Thereby, this technique can be used to produce neutron beams of low, but well-known, intensity.

The second method is to combine a relative measurement of the np angular distribution with information about the total np cross section. The total cross

section can be determined without knowledge of the absolute beam intensity; a measurement of the relative beam attenuation in a target is sufficient, and therefore total cross sections are often known to about 1 %. Below the pion-production threshold, the inelastic channels in np interactions, i. e., capture and bremsstrahlung, are very weak and contribute far less than 1 % to the total cross section. Thus, the total and differential np cross sections are directly linked via the relation

$$\sigma_T = \int \frac{d\sigma}{d\Omega} d\Omega = \int_{0^\circ}^{180^\circ} 2\pi \sin(\theta) \frac{d\sigma(\theta)}{d\Omega} d\theta. \quad (1)$$

Previously, our group has studied np scattering in the backward angular range. At 96 MeV, data in the $74 - 180^\circ$ angular range have been published [11]. Since part of the total angular range was missing, the normalisation was obtained in a procedure where the undetected fraction of the angular distribution was obtained from partial-wave analyses and NN interaction models. This has motivated the present experiment on forward-angle np scattering. Extending the angular distribution to cover $20 - 180^\circ$ allows a purely experimental normalisation. The missing part $(0 - 20^\circ)$ gives very small contributions to the uncertainty in the normalisation, because the solid angle vanishes at zero degrees.

Recently, a novel technique for normalisation of neutron-induced cross sections has been presented [12]. In elastic neutron scattering from nuclei, the absolute scale can be provided with a method similar to the one of Eq. 1, with the difference that a relative angular distribution of elastic scattering is normalised to the total elastic cross section. The latter, in turn, can be derived from the difference between the total cross section and the reaction cross section. In a recent experiment on elastic neutron scattering from ^{12}C and ^{208}Pb, this technique was found to have an uncertainty of 3 %. Thereby, a measurement of the ^{12}C/^{1}H elastic neutron scattering cross section ratio could provide a new, independent normalisation of np scattering.

There are many applications that could benefit from better knowledge of the np cross section for normalisation purposes. Besides its importance for fundamental physics, the interest in high-energy neutron data is rapidly growing since a number of potential large-scale applications involving fast neutrons are under development, or have been identified. These applications primarily fall into three sectors; nuclear energy and waste management, nuclear medicine and radiation effects on electronics.

The recent development of high-intensity proton accelerators has resulted in ideas to use sub-critical reactors, fed by neutrons produced in spallation processes maintained by external proton beams, for transmutation of spent fuel from nuclear power reactors or incineration of nuclear weapons material. This might result in less problematic handling of fissile material. New nuclear data are needed for feasibility assessments of these techniques. The present work is linked to the EU project HINDAS (High and Intermediate energy Nuclear Data for Accelerator-driven Systems), which has been organised to meet this demand [13].

Conventional radiation treatment of tumours, i. e., by photons or electrons, is a cornerstone in modern cancer therapy. Some rather common types of tumours, however, cannot be treated successfully using these modalities. For some of these,

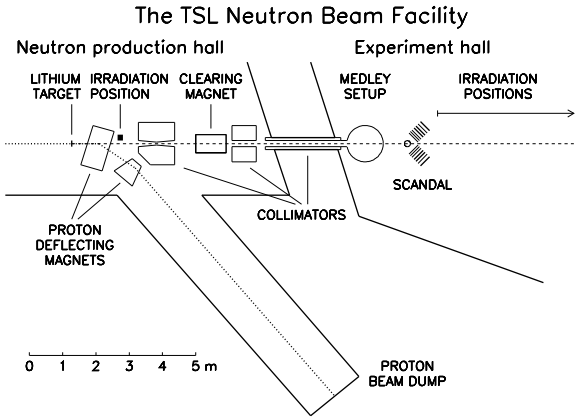

Figure 1: Overview of the TSL neutron beam facility.

good treatment results have been obtained with neutron therapy [14].

During the last few years, it has become evident that electronics in aircrafts suffer effects from neutrons generated by cosmic radiation interacting in the upper atmosphere [15, 16]. For instance, a neutron could induce a nuclear reaction in the silicon substrate of a memory device, releasing free charge, which could flip one or more memory units. Similar effects causing soft- and/or hardware damage have recently been identified also at ground level.

Finally, neutrons at commercial aircraft altitudes induce significant radiation doses to the crew [17].

For all the applications mentioned above, an improved understanding of neutron interactions is needed. Neutron cross sections are generally measured relative to the *np* cross section, and therefore the accuracy of most neutron data depend on how well the *np* cross section is known for various angles and energies.

2 Experimental arrangement

2.1 Neutron beam and detector setup

The neutron beam facility (Fig. 1) at the The Svedberg Laboratory, Uppsala, Sweden, has recently been described in detail [18], and therefore only a brief outline will be given here. Neutrons of 96 MeV were produced by the ^{7}Li(p,n)^{7}Be reaction when protons hit a neutron production target consisting of lithium enriched to 99.98 % in ^{7}Li. The Li target used in the present experiment had a thickness of 427 mg/cm^{2} and was bombarded with a proton beam of a few μA from the Gustaf Werner cy-

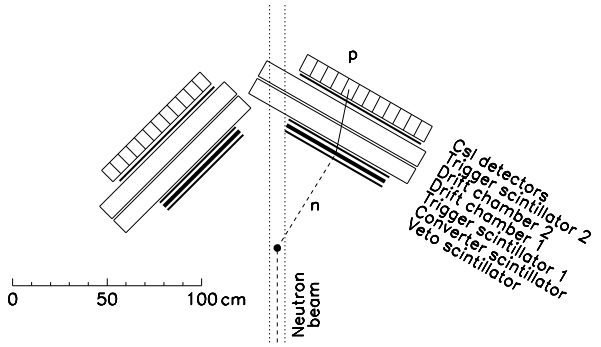

Figure 2: Schematic layout of the SCANDAL setup. In the present experiment, the converter scintillator consisted of two plastic scintillators on each arm. A typical event is indicated.

clotron. The resulting neutron spectrum consisted of a peak at 95.6 ± 0.5 MeV with an energy spread of 1.6 MeV (FWHM), and a low-energy tail which was suppressed by time-of-flight techniques. After the production target, the proton beam was bent into a well-shielded beam dump where the beam current was integrated in a Faraday cup. This procedure left the experimental area essentially background free.

Definition of the neutron beam was accomplished with a system of three collimators. At the scattering target position, the neutron beam was 9 cm in diameter, corresponding to a neutron beam solid angle of 60 μsr, and the yield was typically $4 \cdot 10^4$ s^{-1}cm^{-2}. Finally, the neutron beam was dumped in a tunnel about 10 m downstreams the experimental position.

The neutron beam was transported in a vacuum system which was terminated with a 0.1 mm thick stainless steel foil, 80 cm upstreams the scattering target position. Immediately after the foil, a fission detector for absolute monitoring of the neutron fluence, based on thin-film breakdown counters (TFBCs) [19], was mounted.

In the present experiment, the SCANDAL (SCAttered Nucleon Detection AssembLy) setup was used (Fig. 2). This detector setup, which has previously been described in Ref. [18], consists of two identical arms positioned on each side of the neutron beam, covering the angular ranges $10 - 50^\circ$ and $30 - 70^\circ$. In the present experiment, each arm consisted of a 2 mm thick veto scintillator for charged-particle rejection, two converter scintillators of 20 mm and 10 mm thickness for neutron-proton conversion, a 2 mm thick ΔE plastic scintillator for triggering, two drift chambers (DCH) for proton tracking, another 2 mm thick ΔE plastic scintillator which was part of the trigger, and an array of CsI detectors (12 on each arm) for energy determination of recoil protons produced in the converter by np scattering. The CsI detectors as well as the plastic scintillators are read out by photomultiplier (PM) tubes. The CsIs have one PM tube each, and the scintillators two each, mounted adjacent to each other on one of the longer, horizontal sides. This design has been chosen in order to allow the spectrometer arms to be placed close to the

beam.

The trigger, when detecting neutrons, was defined by a coincidence of the two trigger scintillators, with the most upstream scintillator acting as a veto. The total neutron energy resolution is different for individual CsI crystals, but is on average 3.7 MeV (FWHM). The variations between the crystals are due to internal properties of the detectors [18].

The SCANDAL setup has been tested using backward *np* scattering, i.e., by recoil proton detection at 96 MeV [18, 20]. Data from these tests are presented in Fig. 3, together with the Rahm et al. data obtained with the LISA magnetic spectrometer at the same energy [11]. As can be seen, the most backward data display larger uncertainties than data at more forward angles. This is because SCANDAL was run in a non-standard configuration very close to the neutron beam, resulting in pile-up problems. Additional studies of *np* scattering by proton detection with SCANDAL as well as another device, MEDLEY [21], are underway [22, 23].

2.2 Experimental procedure

The experiment was carried out during a two-week run with a beam calibration break after the first week of data taking. At the beginning of the campaign, calibration runs were performed by placing a thin CH_2 target in the beam and detecting recoil protons from *np* scattering. The CH_2 target consisted of several sheets of CH_2 mounted in a multi-target box, that allows up to seven targets to be mounted simultaneously, sandwiched between multi-wire proportional counters (MWPC). In this way it was possible to determine in which target the reaction took place, and corrections for energy loss in the subsequent targets could be applied. Two additional MWPCs, located upstreams the targets, acted as veto detectors for charged particles accompanying the neutron beam. A more detailed description of the multi-target box is given in Ref. [24].

In the multi-target box, two of the target positions were used for graphite targets, allowing a background spectrum of ^{12}C(n,p) to be recorded simultaneously. This background was subtracted in order to identify the recoil protons originating from hydrogen in the CH_2 target. The hydrogen peak is, however, already prominent in the CH_2 spectra before subtraction of carbon, since the ^{12}C(n,p) reaction has a Q-value of -12.6 MeV, which makes the *np* scattering peak kinematically separated from the carbon background at small angles.

During calibration runs, the trigger condition was changed to include the veto scintillator as well as the two plastic scintillators before and after the DCHs, thus accepting charged particles from the target. After the calibration runs, the trigger was again set for neutron detection, by using the most upstream plastic scintillator as a veto detector for charged-particle rejection. As mentioned earlier, the two detector arms covered the angular regions $10 - 50^\circ$ and $30 - 70^\circ$. The lower limit of this range, 10°, represents an arm position where the scintillator detectors barely avoid being hit by the neutron beam and it is the smallest angle where data can be collected with this detector setup. At the largest angle, 70°, neutrons due to *np*

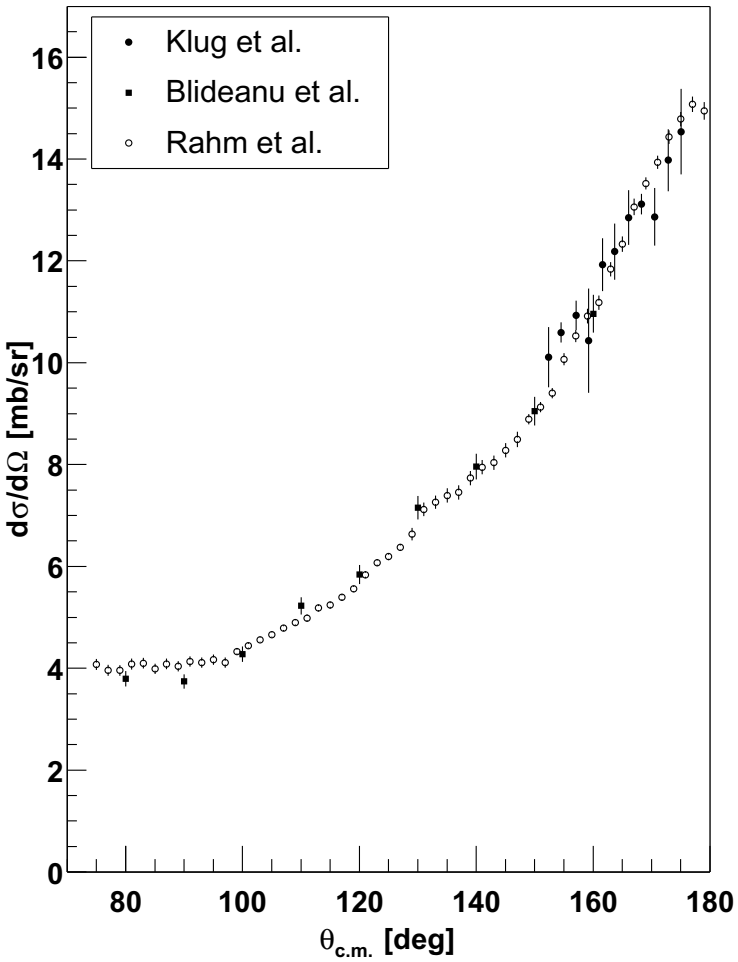

Figure 3: Data on *np* scattering at 96 MeV in the angular range $80 - 180°$ obtained with SCANDAL (Klug et al. [18], Blideanu et al. [20]). Data on the same reaction at the same energy, obtained with the LISA magnetic spectrometer (Rahm et al. [11]), are shown for comparison.

scattering have too low energy to induce triggers, and therefore no real events were expected in the outermost CsI detectors. The angular region covered by both arms, $30 - 50°$, allows studies of the consistency between the two arms.

In the (n,n) measurements, the multi-target box was placed empty upstreams the scattering target and used as an extremely thin charged-particle veto detector. It has, however, been shown that the contamination of charged particles in the neutron beam is very small.

As scattering targets, cylinders of graphite and CH_2 were used, where carbon was treated as a background to H(n,n) events in CH_2. The distribution of beam time between the CH_2 and graphite target was based on an estimation of the number of counts in the carbon background in the region of hydrogen peaks at different angles. The signal-to-background ratio varies dramatically with angle. Since all angles were measured simultaneously, a compromise in the distribution of beam time was necessary. To obtain good statistics in both CH_2 and graphite for all angles, about twice the beam time was spent on CH_2 as compared to graphite. The two target cylinders had the same size, 16 cm high with a diameter of 8 cm. The graphite cylinder was made of natural carbon with an isotopic composition of 98.9 % ^{12}C, and had a mass of 1225 g. The CH_2 target consisted of 14.4 % H (by mass), and 85.6 % C, with a mass of 748.2 g. During the experiment, background data (no target) were also recorded.

Some 80 cm upstreams the scattering target position, the vacuum termination foil and TFBC neutron monitor act as neutron scattering targets. This gives rise to a background of neutrons not originating from the real scattering target, but still triggering the detector setup. SCANDAL is triggered by protons coming from the neutron-proton converter scintillators, and cannot distinguish between neutrons coming from the scattering target, and neutrons from, e. g., the fission detector. To minimise this source of background neutrons, a lead collimator was installed on both sides of the neutron beam, between the multitarget box and the scattering target position. The collimator was constructed of 10 cm thick lead blocks, placed along the neutron beam.

Downstreams the target position, the neutron beam passes through the drift chambers of the arm located at the right hand side of the beam. The drift chambers contain very little material and are located such that it produces virtually no triggers. Thereby, the setup itself produces very little background. In fact, the background is consistent with elastic neutron scattering in the air surrounding the target.

While the experiment was running, on-line data were displayed for immediate inspection. Simultaneously, the data were written to tape for subsequent analysis. The dead time in the data acquisition system was around 18 %, 23 % and 3 % during CH_2, graphite and background runs, respectively.

3 Data analysis

3.1 Pre-sorting and calibration

In the off-line event-by-event analysis, data were analysed using the ROOT package from CERN [25]. The first pre-sorting procedure checked that the event was correctly written to tape, and that a number of basic criteria in the CsIs and the drift chambers were fulfilled. It was required that at least one CsI detector in the event had a pulse height (PH) above a certain threshold value. Another requirement was that each event had both vertical and horizontal drift chamber information in two points along the path.

In around 10 % of all events, the event contained more than four drift chamber wire hits, mostly due to cross talk between the wires. In those cases, the first firing wire was chosen, since signals induced by cross-talk come later in time. This procedure has been investigated earlier using four drift chambers for over-determination of proton tracks, and has proved to give the correct result in about 90 % of these cases. Hence, it can be estimated that of the order of 1 % of all events in a given DCH plane suffer from incorrect trajectory information due to problems with multiple hits in the drift chambers. These events can, however, to a large extent be removed by checking the trajectory versus hit in CsI.

Around 60 % of all recorded events were rejected during the pre-sorting procedure. The dominating reasons for event rejection was drift chamber inefficiency and too small energy deposition in the CsI crystals. As described in sect. 3.4, the total drift chamber efficiency, i.e., requiring all four drict chamber planes to give one unique position signal, was around 75 %. About 20 % of the events was rejected due to energy deposition in the CsI detectors below threshold. Thus, these two effects account for the entire loss in the pre-sorting. In addition, a small fraction (a few % at most) was rejected due to corrupt information due to malfunctioning of the data acquisition system. Partly, this seemingly large rejection fraction is due to a relatively relaxed trigger criterion. In this experiment, the count rate is rather low and therefore computer dead time was not a major problem. Therefore, a strategy with generous trigger criterions to minimize the loss of good events was adopted.

Once an event had been accepted in the pre-sorting, it was saved for further analysis. At this point, the conversion point in one of the two converters was calculated. The depth of the conversion (i. e., if the (n,p) reaction occurred in the upstream 20 mm converter or in the downstream 10 mm converter, and at what depth) was determined from pulse height information, and the conversion angle was calculated from DCH trajectory information. At the same time, the elastic neutron scattering angle in the target was calculated from the knowledge of the conversion point, presuming neutron scattering in the target centre.

The calibration of the CsIs was made detector-by-detector with (n,p) data from the calibration runs. In each detector it was possible to identify two calibration points; the pedestal channel and the *np* proton peak. The pedestal channel was associated with zero energy deposition, and the energy represented by the proton

peak was obtained by calculating the energy loss of the proton through the detector setup from the target to the CsI under consideration. The centroid channel was determined by a gaussian fit to the proton peak.

A linear relationship was assumed between PH and deposited energy. This should be a reasonably good assumption for CsI in the present application [21]. However, due to detector geometry and local variations in the light output within a CsI crystal, protons with the same energy give rise to different PH values along the vertical axis in the crystal. The reason for this vertical dependence is that the crystals have a rather elongated, trapezoidal shape; 30 cm high with a $7 \cdot 7$ cm^2 cross section area at the PM tube end, and a $5 \cdot 5$ cm^2 area at the other end. If not compensated for, this geometry effect would contribute up to half the intrinsic energy resolution in the CsI detectors. Therefore, when calculating the energy deposited in the CsI crystal, the coordinate of the vertical hit position in the detector was used to select the calibration PH value that correctly corresponds to the *np* proton peak energy.

After having calibrated the plastic scintillators (see below), the energy deposited by the protons in the CsI detectors was once again checked by subtracting the measured energy losses in the scintillators and the calculated energy losses in other material.

As described earlier, each plastic scintillator has two PM tubes attached to one of the longer horizontal sides. To calibrate them, a region in the centre of the scintillator was chosen to obtain a similar distance to both PM tubes. In this case it can be assumed that each PM tube detects half the light from the deposited energy. Also for the scintillators, the pedestal channel and the *np* proton peak (as defined by the CsI detectors) were used as calibration points. The pedestal channel was taken to represent zero deposited energy, and the energy of the proton peak centroid was obtained from the energy loss calculation in the detectors. A linear correspondence was assumed between PH and deposited energy, and the total deposited energy of a plastic scintillator (ΔE) was obtained by adding the contributions from the two PM tubes.

In the plastic scintillators, there are geometry effects causing protons with the same energy to give different ΔE signals depending on their location in the detector. This deviation of ΔE from the expected value was mapped over the detectors as a function of the location in the scintillator, both horizontally and vertically. The effect has been found to be caused to a large extent by the design of the detectors, with both PM tubes situated on the same side. For the 2 mm thick detectors, the effect is small on an absolute scale, and therefore a compensation was made only for the converter scintillators, with thicknesses of 20 mm and 10 mm.

To obtain the correct energy loss through the whole detector setup, it is necessary to calculate energy losses in parts of SCANDAL where the protons cannot be detected. Such parts are detector wrappings, drift chamber foils and air. A calculation of this "undetected" energy loss was based on the detected proton energies in the trigger scintillators and the CsI crystals.

Since there are no excited states in hydrogen, it might seem a bit strange to refer to the hydrogen excitation energy. The SCANDAL setup, however, and all

data analysis routines, were originally developed for elastic neutron scattering from heavier nuclei, where the excitation energy is a most relevant quantity. The same routines were used when analysing the present experiment, and therefore the excitation energy was calculated, meaning only that the hydrogen peak appears at zero energy in the analysed spectra.

In the last step of the calibration process, the total energy of the charged particle was calculated as the sum of all different contributions from the detectors and other material. In regular measurements, also the neutron energy at the conversion and the excitation energy were calculated using the scattering angle, the conversion angle and the total energy. This gave excitation-energy spectra for 24 different angles in the laboratory system, related to the position of the CsI crystal in which the proton was stopped.

3.2 Data reduction

Particle identification was achieved by a $\Delta E - E$ technique, where the sum of the detected energy losses in the two trigger scintillators was plotted against the energies in the CsI detectors. Other particles than protons (mostly deuterons) arise mainly in the converter scintillators, but they were rarely seen in the CsI detectors, since their energies are in general too low to penetrate the preceding material in the setup.

In the present experiment, each CsI crystal defined an angular bin, and it was considered important to associate every elastically scattered event with one specific CsI. Furthermore, energy determination for protons that passed through more than one CsI crystal was very poor due to large straggling effects in CsI wrapping material. Consequently, a position gate was applied on every crystal, ensuring that an accepted proton was stopped in a single CsI detector.

Events from the low-energy tail of the neutron spectrum were rejected using a cut on the neutron time of flight (TOF). The TOF was defined as the time difference between the first trigger detector and a signal from the cyclotron RF. There is, however, no background from low-energy neutrons in the energy region of the elastic peak. The reason is that a low-energy neutron, i. e., from wrap-around effects, cannot induce emission of a full-energy neutron from the scattering target. The TOF cut was therefore not important in this experiment.

The conversion of neutrons to protons in the converter scintillators can occur through the ^{12}C(n,p) reaction, besides the H(n,p) reaction, since the scintillators contain carbon as well as hydrogen. On the other hand, the Q-value for ^{12}C(n,p) is -12.6 MeV, meaning that at forward angles, an energy cut is sufficient to separate the two reactions. However, at a conversion angle of about 20°, the proton energies from the two processes overlap, and it cannot be determined whether *np* scattering or the ^{12}C(n,p) reaction is responsible for the conversion. To resolve this ambiguity, a maximum conversion angle criterion was applied, demanding that the conversion angle was less than 10°.

About two thirds of the events were found to have converted in the thicker upstream detector, as was expected. Later in the analysis, however, it proved difficult

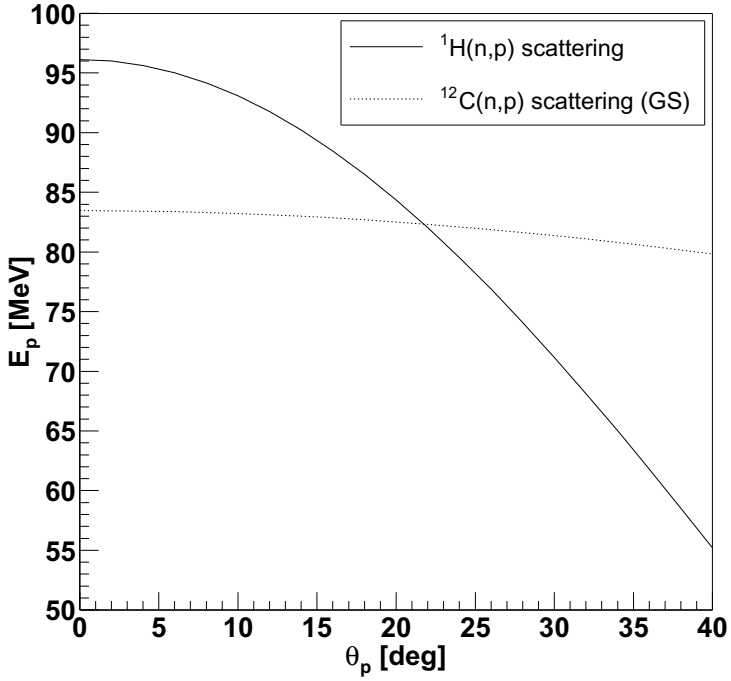

Figure 4: Laboratory system kinematics of proton emission from hydrogen and the carbon ground state. At small angles, the proton emission is kinematically well separated, while at about 20°, the two reactions coincide. An opening angle criterion of 10° was used in the analysis.

to use the events from the thick converter, since its energy resolution was poor (4 MeV compared to 2 MeV for the thinner converter), and since statistics was sufficiently good using only the thinner converter, the events from the thick one were discarded.

3.3 Extraction of elastic scattering events

So far the analysis had been done on event-by-event basis, and when all cuts had been applied the result was excitation-energy spectra at 24 angles (corresponding to the 24 CsI detectors) in the range $10 - 70^\circ$ in the laboratory system. It was, however, not possible to extract peaks for the largest angles, so in reality spectra were obtained for 12 angles between 10° and 38° in the laboratory system. Since the measurement was made with two detector arms, partly overlapping each other in angular range, two sets of data were obtained, one ranging from 10° to 38° and the other one from 26° to 38°.

All cuts were applied in the same way for CH_2, graphite and background (no target) runs. For all runs, the hydrogen mass was used in kinematics calculations when defining the excitation energy.

For the further analysis, the energy spectra were stored as histograms. Examples are shown in Fig. 5. By subtracting background and carbon from CH_2, hydrogen spectra were obtained. In a first step, background spectra were subtracted from both graphite and CH_2 for each CsI. Background and signal spectra were normalised to the same neutron fluence (given by the fission monitor) and corrected for dead time. In the second step, the carbon content was subtracted from CH_2, taking the contents of carbon nuclei in the two samples into account.

A fact to consider when subtracting carbon from CH_2 is the difference in attenuation in the two target samples. The targets have the same dimensions, but different densities and chemical compositions. In the graphite target, the attenuation is due to nuclear reactions in carbon. In the CH_2 target, on the other hand, both the hydrogen and carbon nuclei are of importance, and here all hydrogen interactions are considered as attenuation, since a neutron scattered from hydrogen essentially always loses enough energy to be regarded as lost from the flux of the incoming neutrons. Attenuation correction coefficients, calculated from the carbon reaction cross section and the hydrogen total cross section, were applied to the spectra before subtraction. These coefficients were estimated from an assumption of the mean path travelled in the sample by the neutrons before and after scattering, based on a Monte Carlo simulation [26]. Since the attenuation is energy dependent, different correction coefficients were applied for different CsI detectors.

Due to the relatively large scattering targets used in this experiment, it was necessary to investigate the effects of multiple scattering due to carbon in the targets. The graphite and CH_2 targets were of the same size, but their carbon contents were quite different, resulting in a larger fraction of multiple-scattered events from the graphite sample. To investigate the effect, a Monte Carlo code [26] was used to simulate the multiple scattering of neutrons from carbon in the two scattering targets.

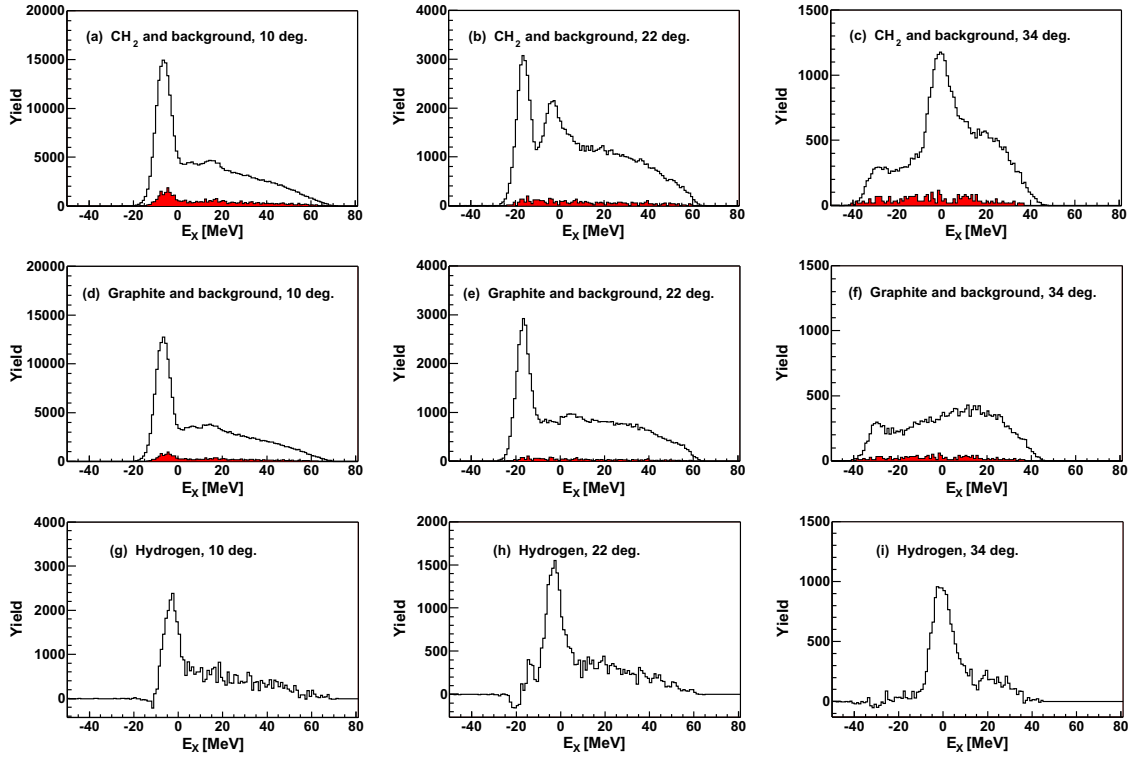

Figure 5: Energy spectra for CH_2, graphite and hydrogen shown at three different angles in the laboratory system; 10°, 22°, and 34°. In the upper panels, CH_2 spectra are presented together with background (no target) spectra. In the middle panels, graphite and background spectra are shown, and in the lower panels the hydrogen spectra. The tails in the hydrogen spectra are due to the low-energy neutron beam continuum.

This gave an estimate of how much the cross section changes for every angular bin due to multiple scattering, and spectra were multiplied by these coefficients before the carbon subtraction. The effect was found to be of importance only at the two most forward CsI detectors (at angles 10° and 14° in the laboratory system). At 10° the correction for multiple scattering was around 5 % in CH_2 and 7 % in graphite.

In parallel with signal histograms, variance histograms were obtained by performing the corresponding operations. These histograms were used for calculation of the statistical uncertainties.

3.4 Cross section determination and normalisation

When determining the angular distribution of the elastic neutron scattering cross section, the number of scattering events in every CsI was obtained from the hydrogen histograms, the number of neutrons in the beam given by either the fission counter or the integrated proton beam current, and the number of target nuclei calculated from the density, volume, and chemical composition of the scattering target.

The solid angle for protons detected in the CsI crystals is different from detector to detector, depending on different distances to the scattering target and individual sizes of the accepted regions (position hit gates) of each crystal. Also, the neutron energy (which varies with neutron angle) is of importance, since it affects the conversion probability in the converter as the *np* cross section is energy dependent. These effects give rise to an individual effective solid angle for every CsI detector, which is due to both the geometrical solid angle for that CsI crystal and the probability that a conversion proton hits the crystal. To calculate these solid angles, a computer code which has recently been described [12], was used. The same code was used to calculate the average elastic neutron scattering angle associated with each CsI detector, and the angular range covered.

The proton detection efficiency has components from the drift chamber efficiency, the efficiency of selecting the correct DCH wire in multiple hit events, and the CsI response. The drift chambers consist of four detection planes on each arm, with a combined efficiency that has previously been measured to 0.75 ± 0.10 (from an average of 0.93 per plane). The efficiency of selecting the correct wire has been measured to 0.93 (from 0.98 per plane). No energy dependence in the DCH efficiencies has been found for a given set of detector parameters. The CsI response varies with energy and gives different detection efficiency for crystals at different angles. This is due to the fact that some protons undergo nuclear reactions before coming to rest in the CsI, resulting in loss of light [18].

The low-energy continuum originating from the ^{7}Li(p,n) reaction gives a contribution to the full-energy *np* peaks, and hence to the ground state peaks in the excitation-energy spectra. This effect is different for different CsIs, because of the variations in energy resolution. The contribution from the low-energy neutrons is a function of the peak width [27], and has been determined using experimental neutron spectra for the ^{7}Li(p,n) reaction measured by Byrd and Sailor [28]. These correction factors were then used in the cross section calculations. For some CsIs,

the effect was quite large (up to 20 %), while a more normal value of the correction was between 6 % and 11 %.

The number of elastic scattering events at each angle was obtained by integrating the corresponding peaks in a region of $\pm\Gamma$ around the peak centroid, where Γ is the full width at half maximum (FWHM). The centroid of the peak and the width Γ were obtained from a gaussian fit to the peak.

When all corrections had been taken into account, the final angular distribution for the forward *np* scattering cross section was obtained. The absolute scale was given by the TFBC neutron monitor which in itself has an uncertainty of more than 10 %, making further normalisation necessary.

The data were normalised to the total *np* cross section in the following way. As described in Sect. 3.3, the present data consist of two subsets from the two SCANDAL detector arms, i. e., SCANDAL left and SCANDAL right. These two sets were to be combined with the earlier data by Rahm *et al.* using the LISA magnetic spectrometer [11] to form one data set covering the angular interval $20^\circ - 180^\circ$ in the centre of mass (c.m.) system. To obtain a single relative distribution, the three subsets were internally normalised using the Nijmegen partial wave analysis PWA93 [29]. The two SCANDAL data sets were normalised to PWA93 in the angular region where the arms overlap, i. e., in the range $50^\circ - 76^\circ$, and the LISA data were normalised to PWA93 in an equally large angular range, $75^\circ - 101^\circ$. The factors used in this procedure were 1.02, 1.08, and 1.03 for SCANDAL left, SCANDAL right, and LISA, respectively. A final normalisation of the combined data set to the total *np* cross section measured with high precision by Lisowski *et al.* [30] was then made, using Eq. 1. The normalisation factor needed this time was 0.978.

Note that the SCANDAL arms needed renormalisation of 0 % ($1.02 \cdot 0.978$) and 6 % which is satisfactory considering that the uncertainty in the neutron monitoring alone is around 10 % [18]. The renormalisation of the Rahm data is 0.7 %, which is well within the normalisation uncertainty of 1.9 % stated in [11].

The original Rahm data were normalized in a procedure where the fraction of the total cross section due to *np* scattering in the studied angular range ($74 - 180$ ∘) was deduced from a set of partial-wave analyses and potential models [11]. This fraction was estimated to 61.3 ± 1.5 %. In the present work, such a procedure is no longer necessary, but the resulting data set can be used to inspect this previously estimated fraction. In the present data set, 61.8 % of the total cross section is accounted for by the differential *np* cross section in the $74 - 180$ ∘ range, i.e., the result is in good agreement with the previous estimate.

Other methods of normalisation were also attempted. From the CH_2 spectra, it was possible to analyse elastic neutron scattering from carbon and compare it to elastic neutron scattering from hydrogen at the same laboratory angle. For five CsIs where the peaks are prominent and resolved, the ratios between the number of counts in the carbon and hydrogen peaks were extracted and related to the expected ratios in cross sections. From knowledge of the carbon cross section for a specific angle, the expected hydrogen cross section was calculated, and compared to the

actual measured cross section for that CsI. As carbon reference cross section, the fit to the ^{12}C(n,n) data in Fig. 5 of Klug *et al.* [12], was used. The fit to the data was made using a parametrisation by Koning and Delaroche [31]. The ratio between the reference hydrogen cross section and the measured one, was on average $0.94 \pm 0.03 \pm 0.11$, where the first uncertainty is the statistical error, and the second is the systematic error of the method. The latter was estimated from the standard deviation of the spread in results between the five CsIs.

Thus, on average this normalisation technique deviates from normalisation to the total cross section by 6 %, with a 3 % statistical error. The ^{12}C(n,n) reference cross section has been estimated to have a 3 % uncertainty [12]. Thus, the average deviation is in reasonable agreement with what can be expected from those uncertainties only. The systematic uncertainty (11 %) is, however, significantly larger than the statistical error, and therefore it seems more correct to assign an uncertainty to this method of at least 10 %. The reason for the larger systematic uncertainty is at least partly due to the different behaviour of the angular distributions of elastic neutron scattering from ^{12}C and ^{1}H. The former has a very steep angular distribution, where the cross section changes by about 20 % per degree, while the *np* scattering cross section changes much less (typically 2 % per degree). Hence, the obtained systematic uncertainty of 11 % corresponds to an uncertainty in the absolute angle of around 0.5°, i. e., less than the angular uncertainty of the present experiment.

The method above relies on only a few data points. Still, the possibility that a better normalisation might result from a larger set of data should be investigated. Therefore, the full angular distribution of ^{12}C(n,n) was extracted from the graphite target data. This angular distribution was then used to derive a value of the total elastic cross section, resulting in a value 18 % lower than the experimental value derived from the difference of the total and the reaction cross sections.

It might seem surprising that relative normalisation of ^{12}C versus ^{208}Pb can be performed with a 3 % uncertainty while normalisation of ^{12}C versus ^{1}H results in discrepancies of 10 % or more. The properties of these normalisation techniques can be understood from the information displayed in Fig. 6. In the upper panel, the differential cross sections for neutron scattering from ^{1}H, ^{12}C and ^{208}Pb are shown in parametrised form. As can be seen, the cross sections for ^{12}C and ^{208}Pb have a similar overall slope, but the ^{208}Pb data display more structure. Compared with scattering from these nuclei, the *np* scattering angular distribution is much flatter. In the middle panel, the cross section ratios C/H and Pb/C are displayed, and in the lower panel, the relative change of these ratios per degree scattering angle is illustrated.

As can be seen in Fig. 6, the Pb/C ratio fluctuates significantly, but if integrated over a wide angular range, these oscillations more or less cancel. Thus, if normalising in a single point, the result could be significantly off, but if using the entire angular distribution for normalisation, like in Ref. [12], it is rather likely that a small mismatch in angle will be compensated for. The C/H ratio is more difficult to use for normalisation, because there is no "built-in" compensation. Over the entire $10° - 60°$ range, a 1° error in absolute angle results in a cross section ratio

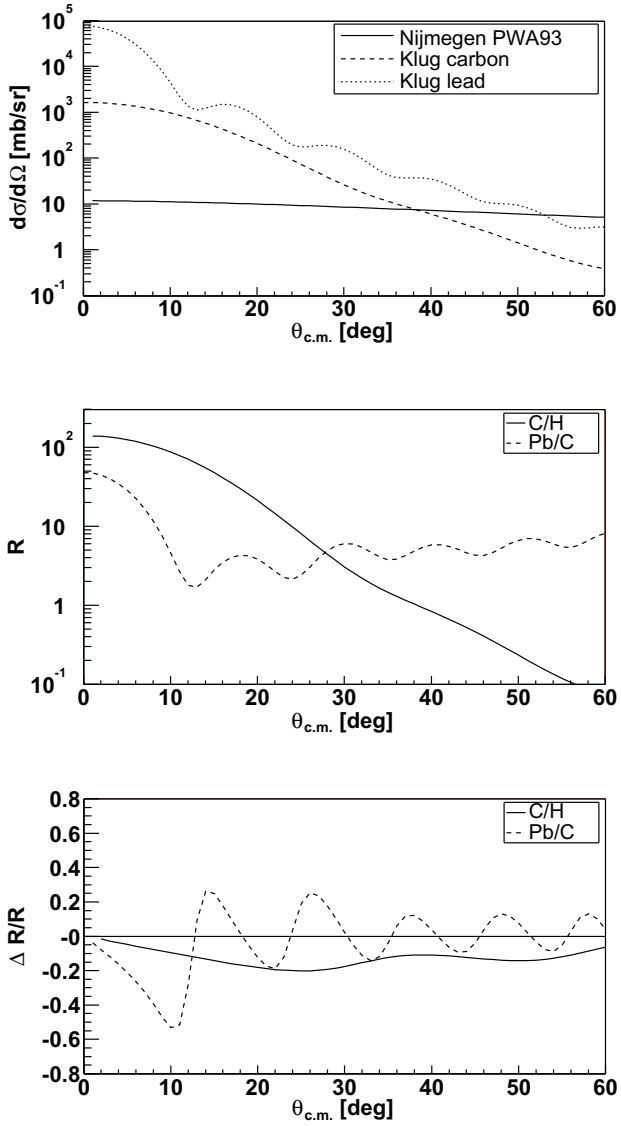

Figure 6: In the upper panel, predictions of angular distributions of elastic neutron scattering from hydrogen, carbon and lead at 96 MeV are shown. The lead (dotted line) and carbon data (dashed line) are fits to the data of Klug *et al.* [12] using the optical model parametrisation by Koning and Delaroche [31], and the solid line is the Nijmegen partial wave analysis PWA93 [29]. In the middle panel, the ratio between the carbon and hydrogen cross sections is shown together with the ratio between the lead and carbon cross sections, and in the lower panel the relative changes in these ratios per degree scattering angle are shown. See the text for further details.

$10 - 15$ % different from the expected, and integration over a wider angular range does not remedy the problem. Thus, to employ the C(n,n) cross section as reference for normalisation of *np* scattering to a precision of 2 %, i. e., similar to what can be obtained with normalisation to the total *np* cross section, an absolute angular uncertainty of less than 0.2° is required. With the experimental techniques of today, this would require smaller targets and larger distances to the detector which would demand very long experimental runs.

3.5 Estimation of experimental uncertainties

In the present experiment, the relative differential cross section was measured and then normalised using independent information. Uncertainties that affect all angles equally (e. g., drift chamber inefficiencies, neutron monitoring, and computer dead time) are therefore taken care of by the normalisation procedure. Other uncertainties, however, are angle dependent and must somehow be quantified, since they can affect the shape of the angular distribution. Some of these effects can easily be modelled and corrected for, such as the different energy losses through the SCANDAL setup due to its geometry.

Among the corrections that vary with angle is the contribution to the *np* scattering peak from the low-energy continuum of the ^{7}Li(p,n) spectrum. This contribution gives an uncertainty in the peak content, which varies with peak width. Assuming the uncertainty to be 10 % of the correction, this effect induces an error in cross section of up to 2 % in the worst case. For most angles, however, the uncertainty is around 1 % or smaller.

Another uncertainty comes from the procedure of determining integration limits by fitting gaussians to the elastic scattering peaks. By varying the gaussian fits and thereby the integration intervals within the uncertainties, it was found that the total resulting uncertainty in the cross section was around 2 % for all angles.

The subtraction of carbon from CH_2 induces an angle-dependent uncertainty which has several contributions. First of all is the random error due to counting statistics which affects different CsIs differently since the signal-to-background ratio depends strongly on angle. At small angles, where the carbon and hydrogen peak overlap in energy, the statistical error in hydrogen is as large as 3.5 %.

Another effect which is correlated to the subtraction is the correction for attenuation in the targets. In order to get the subtraction coefficients correct, the attenuation correction has to be done first. Its uncertainty has a large impact on the resulting hydrogen spectra at forward angles, where the cross section results from the subtraction of two large numbers. It was assumed that the uncertainty in attenuation was at most 10 % of the correction, coming from uncertainties in the involved cross sections and calculation of the mean path travelled by neutrons in the targets. The attenuation in graphite and CH_2 are however correlated, since the carbon reaction cross section enters in both cases, as well as the calculation of the mean path. Taking this into account, the uncertainty in the resulting experimental *np* cross section was estimated to be around 0.5 % except at the smallest angles

where the effect was significantly larger (up to 6 %).

Finally, the subtraction uncertainty depends on the uncertainty in the correction for multiple scattering, which was again taken to be 10 % of the correction itself. This correction was made for the two smallest angles only, but since the corrections for graphite and CH_2 were treated as uncorrelated, it had a large impact on the resulting *np* cross section. For the smallest angle, the uncertainty in the final result due to the uncertainty in the multiple scattering correction was 10 %.

The solid-angle calculation depends on several factors, such as the size of the target and the accepted area on the CsI detectors. The latter depends on the position uncertainty in the drift chambers, resulting in an area uncertainty of typically 3.2 % [18]. This uncertainty affects individual CsI detectors differently.

The average angle seen by each CsI detector, is the mean of a distribution with r.m.s. values around 1.9°. To be able to extract the angular distribution of the cross section, it is important to know the angles at which the detectors were situated. The inherent angular uncertainty has been estimated to be about 0.5°, having components from the uncertainty in the position of the target, the drift chambers, and the detector arms. These effects result in an equal shift of all detector angles on the same detector arm. In addition, each drift chamber contains many drift cells that act as independent detectors with an uncertainty in position information of around 0.5 mm, resulting in a negligible uncertainty in the present experiment. Presuming that the centroid of a distribution can be determined with an accuracy of 0.5 σ, the uncertainty in angle due to the extension of the target is close to 1.0°. With the inherent angular uncertainty of the setup added in quadrature, the resulting total angular uncertainty is estimated to 1.1°.

In the present measurement of forward *np* scattering, different normalisation factors were needed for the data points from the two detector arms, i. e., SCANDAL left and SCANDAL right. The normalisation factor for SCANDAL left was 1.00, and the factor for SCANDAL right was 1.06. The fact that two detection systems were used allows some further investigation of the systematic uncertainties in the present experiment. In the normalisation procedure, it was found that the absolute scale of the two SCANDAL arms differ by 6 %. In this comparison, all uncertainties related to drift chamber inefficiencies come into play. This means that a 1 % uncertainty in the efficiency per plane can easily account for the entire difference.

A second test is provided by four pairs of data points, measured at about the same angle but with different SCANDAL arms. After normalisation of both arms, internal differences in these pairs beyond statistical errors (which are small) should reflect the systematic uncertainties involved. The average pairwise difference is 7.7 %, while the expected difference from the estimated systematic uncertainties is 5.9 %. Thus, the difference is in reasonable agreement with expectations.

4 Results and discussion

The results of the present work consist of two parts; firstly the forward-angle *np* data measured in the present experiment and presented in Table 1, and secondly

Table 1: Differential cross sections for forward *np* scattering at 96 MeV. The first error is the statistical and the second the estimated systematic excluding normalization uncertainty.

$\theta_{c.m.}$	$\mathrm{d}\sigma/\mathrm{d}\Omega$	$\Delta\mathrm{d}\sigma/\mathrm{d}\Omega$ statistical	Δrel.	$\Delta\mathrm{d}\sigma/\mathrm{d}\Omega$ systematic	Δrel.	SCANDAL arm
(deg.)	(mb/sr)	(mb/sr)	(%)	(mb/sr)	(%)	(L or R)
19.9	10.68	0.37	3.5	1.31	12.3	R
27.0	9.82	0.32	3.3	0.65	6.6	R
34.2	7.39	0.17	2.3	0.31	4.2	R
42.5	7.63	0.13	1.7	0.30	3.9	R
50.0	5.70	0.11	1.9	0.23	4.0	R
51.6	6.31	0.16	2.5	0.25	4.0	L
58.2	5.08	0.09	1.8	0.21	4.1	R
58.9	4.54	0.12	2.6	0.18	4.0	L
66.5	4.33	0.11	2.5	0.18	4.2	L
66.9	4.48	0.08	1.8	0.18	4.0	R
74.6	4.28	0.10	2.3	0.18	4.2	L
75.6	4.03	0.07	1.7	0.18	4.5	R

the backward-angle *np* data previously reported in [11], and now renormalized and presented in Table 2. For the forward-angle data, the table gives the statistical as well as the systematic errors separately, while for the backward angle data, total errors are given as the quadratic sums of the statistical and systematic uncertainties. Errors due to normalization are not included. Neither are other uncertainties that affect the data points equally since they vanish with the adopted normalization method.

Together, these two data sets cover an angular range of 160° in the c.m. system, i. e., the angles $20° - 180°$. The results are shown in Fig. 7, where the upper panel presents the angular distribution of the two data sets together with Nijmegen PWA93 [29], and the lower panel shows the same information multiplied by the solid angle element to illustrate the importance of each data point in the normalization to the total hydrogen cross section.

The upper panel of Fig. 8 shows data from the present experiment together with other forward *np* scattering data at $90-100$ MeV from the literature, i. e., data from Chih *et al.* [32], Griffith *et al.* [33], Bersbach *et al.* [34], and Scanlon *et al.* [35]. In the same panel the partial wave analyses Nijmegen PWA93 [29] and SAID SP03 [36] are shown. The lower panel of Fig. 8 compares data with three potential models, the Nijm93 [37], CD Bonn [38, 39], and Paris [40] potentials. In this panel, data are plotted both with statistical errors and the total errors (statistical and systematic errors, excluding the overall normalization errors, added in quadrature).

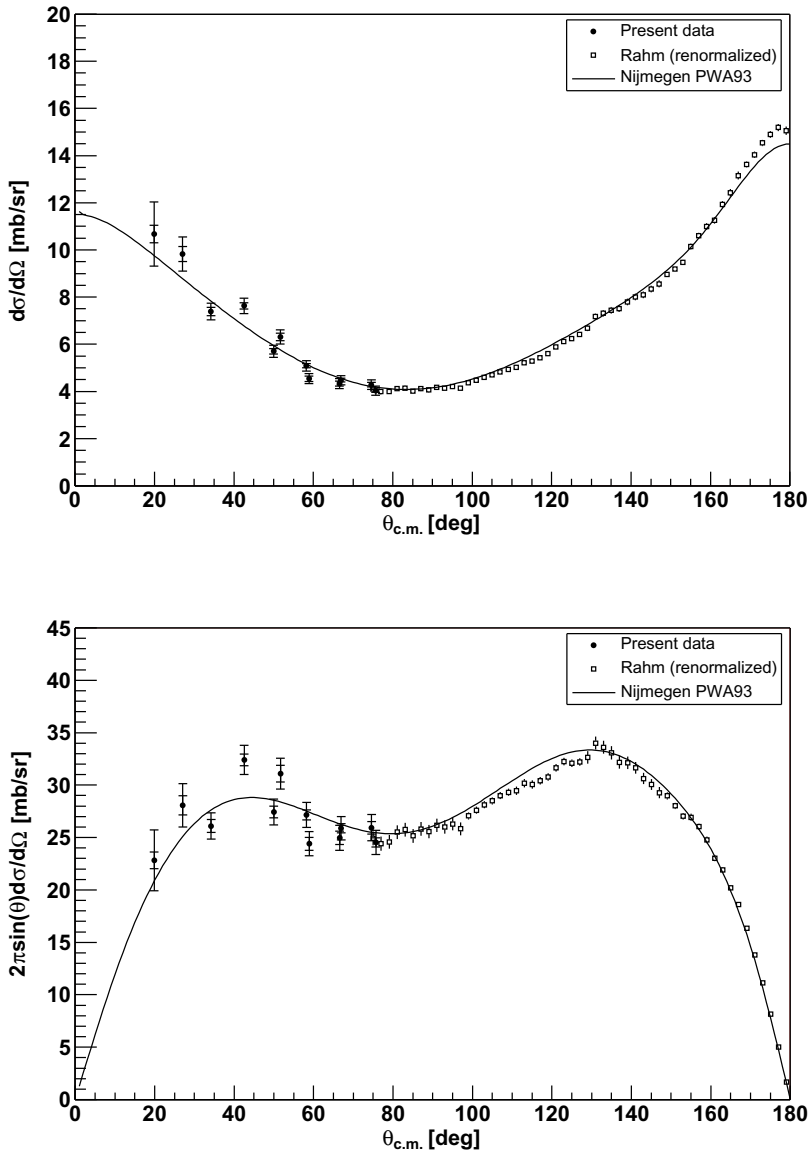

Figure 7: Angular distributions of *np* scattering cross sections at 96 MeV. Filled circles represent the present data and open squares are the renormalized Rahm *et al.* data [11], i. e., the data of Table 2. In the upper panel, experimental differential cross sections are shown together with the Nijmegen partial wave analysis PWA93 [29]. In the lower panel, data and PWA93 have been multiplied with the solid angle element $2\pi sin\theta$ to illustrate the relative weight in the normalization to the total cross section. In both panels, the present data are shown with double error bars; the inner bars representing the statistical error, and the outer the statistical and systematic errors, excluding normalization errors, added in quadrature.

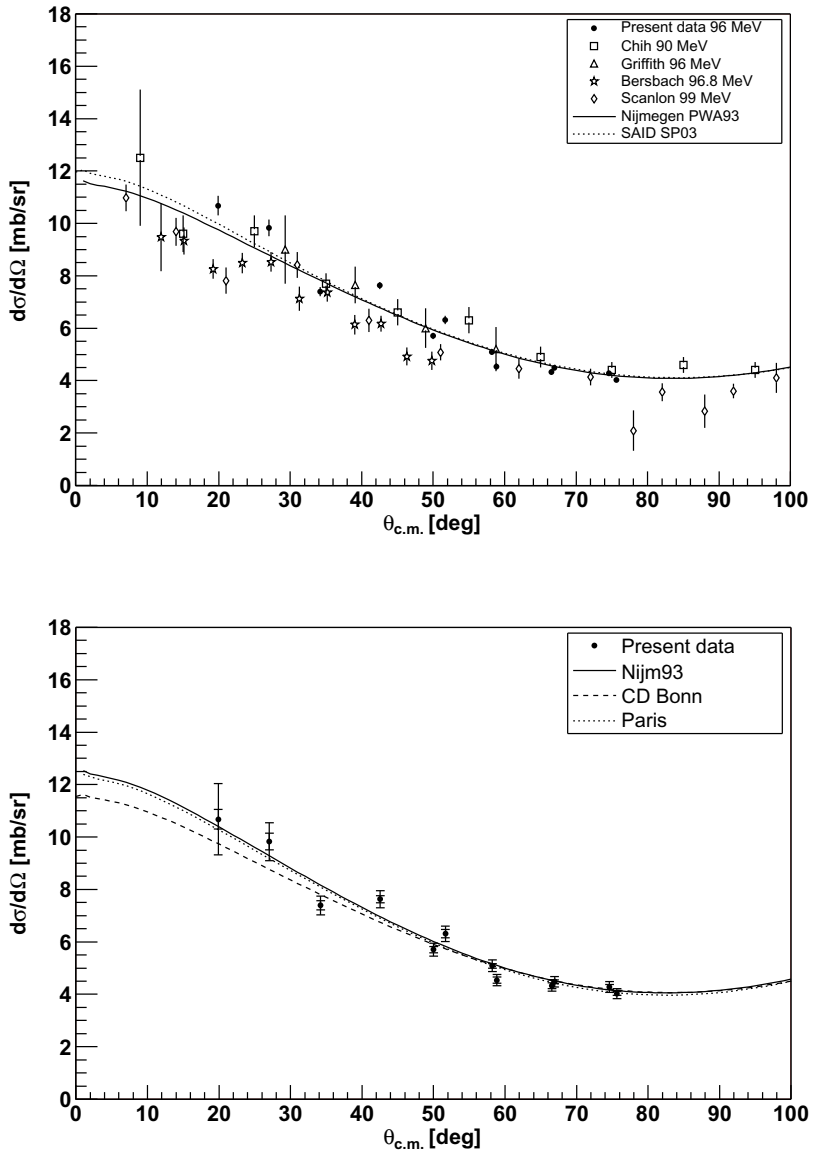

Figure 8: Differential scattering cross sections of the present work (filled circles). In the upper panel, data are shown together with the Nijmegen PWA93 [29] and SAID SP03 [36] partial wave analyses and with experimental data from the literature in the energy region 90 – 100 MeV [32, 33, 34, 35]. In the lower panel, the present data are compared with the Nijm93 [37], CD Bonn [38, 39], and Paris [40] potentials. In the lower panel, both the statistical errors (the inner error bars) as well as the statistical and the systematic errors, excluding normalization errors, added in quadrature (the outer error bars) are shown.

Table 2: Renormalized differential cross sections for backward *np* scattering at 96 MeV. Original data are from Rahm *et al.* [11].

$\theta_{c.m.}$ (deg.)	$d\sigma/d\Omega$ (mb/sr)	$\Delta d\sigma/d\Omega$ (mb/sr)	Δrel. (%)	$\theta_{c.m.}$ (deg.)	$d\sigma/d\Omega$ (mb/sr)	$\Delta d\sigma/d\Omega$ (mb/sr)	Δrel. (%)
75	4.10	0.11	2.7	129	6.68	0.12	1.8
77	3.99	0.11	2.8	131	7.17	0.13	1.8
79	3.99	0.11	2.8	133	7.31	0.13	1.8
81	4.11	0.11	2.7	135	7.44	0.14	1.9
83	4.13	0.11	2.7	137	7.51	0.14	1.9
85	4.02	0.10	2.5	139	7.70	0.14	1.8
87	4.11	0.10	2.4	141	8.01	0.14	1.7
89	4.07	0.10	2.5	143	8.10	0.14	1.7
91	4.16	0.10	2.4	145	8.34	0.14	1.7
93	4.14	0.10	2.4	147	8.55	0.15	1.8
95	4.20	0.10	2.4	149	8.95	0.10	1.1
97	4.14	0.10	2.4	151	9.19	0.10	1.1
99	4.36	0.06	1.4	153	9.47	0.10	1.1
101	4.47	0.06	1.3	155	10.14	0.12	1.2
103	4.59	0.06	1.3	157	10.60	0.12	1.1
105	4.69	0.06	1.3	159	11.00	0.14	1.3
107	4.82	0.06	1.2	161	11.26	0.14	1.2
109	4.93	0.06	1.2	163	11.92	0.14	1.2
111	5.02	0.07	1.4	165	12.42	0.15	1.2
113	5.22	0.07	1.3	167	13.15	0.16	1.2
115	5.28	0.07	1.3	169	13.62	0.12	0.9
117	5.43	0.06	1.1	171	14.04	0.13	0.9
119	5.60	0.06	1.1	173	14.53	0.13	0.9
121	5.88	0.07	1.2	175	14.89	0.14	0.9
123	6.12	0.07	1.1	177	15.19	0.15	1.0
125	6.24	0.07	1.1	179	15.05	0.17	1.1
127	6.41	0.07	1.1				

A simple check of the data is provided by Wick's limit [41, 42]. It can be derived from very fundamental quantum mechanics relations [43] that the differential cross section at 0° must exceed a value related to the total cross section,

$$\frac{d\sigma(0^\circ)}{d\Omega} \geq \left(\frac{\sigma_T}{4\pi\lambda\!\!\!^{-}}\right)^2 . \qquad (2)$$

Since the total cross section is very well known, this can provide a very stringent test of the data. For *np* scattering at 96 MeV, Wick's limit is 9.09 ± 0.09 mb/sr. As can be seen from Table 1 and in Figs. 7 and 8, the differential cross section clearly

Table 3: χ^2 per degree of freedom for the present data compared to various PWAs and NN potentials. Results are shown when the statistical error only is considered and when both the statistical and systematic uncertainties, excluding normalization errors, are taken into account.

Potential or PWA	χ^2/N statistical error	χ^2/N total error
PWA93	9.48	1.98
SP03	9.73	2.07
Nijm93	8.04	1.80
CD Bonn	9.34	1.94
Paris	7.67	1.70

exceeds this value, and thus obeys the relation.

In Table 3, χ^2/N values for the forward np data compared with the different PWAs and potentials are presented. χ^2/N was calculated both with only statistical errors in the data and with statistical as well as systematic errors. Generally, using only the statistical uncertainties result in a high χ^2/N (around 9), while including the systematic uncertainties pushes the χ^2/N down to around 2.

These results seem to corroborate our previous conclusion that the statistical errors are not dominating. Instead, the systematic uncertainties are in general more important. When including these, the χ^2/N values are dramatically reduced, down to reasonable values.

It is interesting to note that the data do not seem to favour any particular potential model or partial wave analysis; they all result in very similar χ^2/N values. As can be seen in Fig. 8, a significantly improved data quality would be needed to distinguish between these theory models. It is notable that no experiment in the $90 - 100$ MeV range is even near the precision required to favour one model over another in the forward angular range. Since the limiting factors in the present experiment are systematic effects that hardly can be improved significantly upon, it can be concluded that a fundamentally different experimental approach is needed to reach such a precision.

A novel approach in experimental studies of np scattering has recently been attempted at IUCF [44]. Neutrons are produced by the ^{2}H(p,n)^{2}He reaction, where ^{2}He denotes two correlated protons. Thus, by coincident detection of two low-energy protons, a beam of "tagged" neutrons can be produced, as was discussed in sect. 1. This beam has low – but well-known – intensity, and can be used to measure the np scattering cross section. The aim has been to reach an uncertainty of a few percent, i. e., resembling the quality of experiments using the total np cross section for normalization. Preliminary results of a measurement at 190 MeV have been presented recently [45] and further data analysis is in progress. The technique as

such could in principle be used also at the energy of the present work.

Assessment of the resulting total uncertainty in the overall normalization is not straightforward. With the adopted method, there is an uncertainty contribution from the uncertainty in the total cross section, which is assumed to be 1.0 % at the present energy. In addition, there is a contribution due to the uncertainty in absolute energy in the present experiment, because the total cross section changes with energy. The latter contribution is estimated to 0.6 % based on an analysis of the total cross section slope in the present region. These two effects added in quadrature results in a 1.1 % normalization uncertainty [11].

If the shape of the differential cross section were perfectly measured, there would be essentially no additional uncertainties involved, since the statistical uncertainty in the data would be negligible. If, however, there are distortions of the shape of the angular distribution, this could lead to a normalization error. This possibility has been investigated as described below.

The Rahm et al. data at backward angles were obtained by a technique where data from a number of overlapping angular regions were added to a joint data set. This allowed an estimation of the uncertainty in the 90/180° cross section ratio, based on the statistical errors in the overlap regions, which was found to be 2.2 %. In the present work at forward angles, the 20/75° ratio has a 3.9 % statistical uncertainty. The systematic uncertainty is larger, but to some extent correlated. If we use the full experimental data set, ranging from 20 to 180°, but distorting the shape of it and subsequently normalizing it with the prescription described in this paper, we arrive at slightly different values of the differential cross section. We used a distortion which increases the 0° and 180° differential cross sections before normalization with 2 %, while keeping the 90° differential cross section unchanged, and all other cross sections modified with a linear function, i.e., a distortion function looking like the letter "V". With such an approach, the differential cross sections change from 1.0 to 1.5 % depending on angle.

It should be pointed out that the *np* data presented are not the only important results, but also the investigations of measurement techniques and normalization methods. The present experiment has reached a very high level of accuracy, given the fact that it deals with neutrons both in the incident and exit channel. Two independent detector systems of equal design agree absolutely on the overall scale to within 6 %, and the spread in individual data points using either one or the other is about 8 %. Moreover, the two detection systems do not only agree internally to a few percent, but also absolutely. After analysis and corrections, the two arms needed renormalization of 0 and 6 %, which are remarkably small numbers for this type of experiment.

With the present data in the $20° - 75°$ range, the normalization of the previous data by Rahm *et al.* [11] in the $74° - 180°$ range could be cross-checked. This resulted in a renormalization of these data of 0.7 %, i. e., within the reported uncertainty of 1.9 %.

A novel technique for absolute scale normalization has been tested and found to have about 10 % uncertainty for the present purpose, i. e., normalization of *np*

scattering data using ^{12}C(n,n) data as reference. With the present uncertainties of about 10 % in the *np* scattering data base, a normalization method should have uncertainties significantly smaller than that to provide useful guidance. Thus, it can be concluded that the new method is not very decisive in the quest for the *np* scattering cross section.

Acknowledgements

We wish to thank the technical staff of the The Svedberg Laboratory for enthusiastic and skillful assistance. This work was supported by Vattenfall AB, the Swedish Nuclear Fuel and Waste Management Company, the Swedish Nuclear Power Inspectorate, Barsebäck Power AB, Ringhals AB, the Swedish Defence Research Agency and the Swedish Research Council.

References

[1] J. Blomgren, N. Olsson, J. Rahm, Phys. Scr. **T87**, 33 (2000).

[2] B.E. Bonner, J.E. Simmons, C.L. Hollas, C.R. Newsom, P.J. Riley, G. Glass, Mahavir Jain, Phys. Rev. Lett. **41**, 1200 (1978).

[3] M.L. Evans, G. Glass, J.C. Hiebert, Mahavir Jain, R.A. Kenefick, L.C. Northcliffe, B.E. Bonner, J.E. Simmons, C.W. Bjork, P.J. Riley, H.C. Bryant, C.G. Cassapakis, B. Dieterle, C.P. Leavitt, D.M. Wolfe, D.W. Werren, Phys. Rev. Lett. **36**, 497 (1976).

[4] M.L. Evans, G. Glass, J.C. Hiebert, Mahavir Jain, R.A. Kenefick, L.C. Northcliffe, B.E. Bonner, J.E. Simmons, C.W. Bjork, P.J. Riley, H.C. Bryant, C.G. Cassapakis, B. Dieterle, C.P. Leavitt, D.M. Wolfe, D.W. Werren, Phys. Rev. **C26**, 2525 (1982).

[5] Mahavir Jain, M.L. Evans, G. Glass, J.C. Hiebert, R.A. Kenefick, L.C. Northcliffe, B.E. Bonner, J.E. Simmons, C.W. Bjork, P.J. Riley, H.C. Bryant, C.G. Cassapakis, B. Dieterle, C.P. Leavitt, D.M. Wolfe, D.W. Werren, Phys. Rev. **C30**, 566 (1984).

[6] L.C. Northcliffe, Mahavir Jain, M.L. Evans, G. Glass, J.C. Hiebert, R.A. Kenefick, B.E. Bonner, J.E. Simmons, C.W. Bjork, P.J. Riley, Phys. Rev. **C47**, 36 (1993).

[7] W. Hürster, Th. Fischer, G. Hammel, K. Kern, M. Kleinschmidt, L. Lehmann, H. Schmitt, L. Schmitt, D.M. Sheppard, Phys. Lett. **B90**, 367 (1980).

[8] J. Franz, E. Rössle, H. Schmitt, L. Schmitt, Phys. Scr. **T87**, 14 (2000).

[9] B. Bonner, private communication (1999).

[10] J. Blomgren, in Proceedings of Workshop on Nuclear Data for Science & Technology: Accelerator Driven Waste Incineration, Trieste, Italy, Sept. 10-21, 2001, eds. M. Herman, N. Paver, A. Stanculescu, ICTP lecture notes **12**, 327 (2002).

[11] J. Rahm, J. Blomgren, H. Condé, S. Dangtip, K. Elmgren, N. Olsson, T. Rönnqvist, R. Zorro, O. Jonsson, L. Nilsson, P.-U. Renberg, A. Ringbom, G. Tibell, S.Y. van der Werf, T.E.O. Ericson, B. Loiseau, Phys. Rev. **C63**, 044001 (2001).

[12] J. Klug, J. Blomgren, A. Ataç, B. Bergenwall, A. Hildebrand, C. Johansson, P. Mermod, L. Nilsson, S. Pomp, U. Tippawan, K. Elmgren, N. Olsson, O. Jonsson, A.V. Prokofiev, P.-U. Renberg, P. Nadel-Turonski, S. Dangtip, P. Phansuke, M. Österlund, C. Le Brun, J.F. Lecolley, F.R. Lecolley, M. Louvel, N. Marie-Noury, C. Schweitzer, Ph. Eudes, F. Haddad, C. Lebrun, A.J. Koning, X. Ledoux, Phys. Rev. **C68**, 064605 (2003).

[13] A. Koning, H. Beijers, J. Benlliure, O. Bersillon, J. Blomgren, J. Cugnon, M. Duijvestijn, Ph. Eudes, D. Filges, F. Haddad, S. Hilaire, C. Lebrun, F.-R. Lecolley, S. Leray, J.-P. Meulders, R. Michel, R.-D. Neef, R. Nolte, N. Olsson, E. Ostendorf, E. Ramström, K.-H. Schmidt, H. Schuhmacher, I. Slypen, H.-A. Synal, R. Weinreich, J. Nucl. Sci. Tech., Suppl. **2**, 1161 (2002).

[14] A. Wambersie, P. Pihet, H.G. Menzel, Radiat. Prot. Dosim. **31**, 421 (1990).

[15] H.H.K. Tang, IBM J. Res. Develop. **40**, 91 (1996).

[16] J. Blomgren, B. Granbom, T. Granlund, N. Olsson, Mat. Res. Soc. Bull. **28**, 121 (2003).

[17] D.T. Bartlett, R. Grillmaier, W. Heinrich, L. Lindborg, D. O'Sullivan, H. Schraube, M. Silari, L. Tommasino, Radiat. Res. Cong. Proc. **2**, 719 (2000). See also the entire issue of Radiat. Prot. Dosim. **86(4)**, (1999).

[18] J. Klug, J. Blomgren, A. Ataç, B. Bergenwall, S. Dangtip, K. Elmgren, C. Johansson, N. Olsson, S. Pomp, A.V. Prokofiev, J. Rahm, U. Tippawan, O. Jonsson, L. Nilsson, P.-U. Renberg, P. Nadel-Turonski, A. Ringbom, A. Oberstedt, F. Tovesson, V. Blideanu, C. Le Brun, J.F. Lecolley, F.R. Lecolley, M. Louvel, N. Marie, C. Schweitzer, C. Varignon, Ph. Eudes, F. Haddad, M. Kerveno, T. Kirchner, C. Lebrun, L. Stuttgé, I. Slypen, A. Smirnov, R. Michel, S. Neumann, U. Herpers, Nucl. Instr. Meth. Phys. Res. **A489**, 282 (2002).

[19] A.N. Smirnov, V.P. Eismont, A.V. Prokofiev, Rad. Meas. **25**, 151 (1995).

[20] V. Blideanu, F.R. Lecolley, J.F. Lecolley, T. Lefort, N. Marie, A. Ataç, G. Ban, B. Bergenwall, J. Blomgren, S. Dangtip, K. Elmgren, Ph. Eudes, Y. Foucher, A. Guertin, F. Haddad, A. Hildebrand, C. Johansson, O. Jonsson, M. Kerveno, T. Kirchner, J. Klug, Ch. Le Brun, C. Lebrun, M. Louvel, P. Nadel-Turonski,

L. Nilsson, N. Olsson, S. Pomp, A.V. Prokofiev, P.-U. Renberg, G. Rivière, I. Slypen, L. Stuttgé, U. Tippawan, M. Österlund, Phys. Rev. C. **70**, 014607 (2004).

[21] S. Dangtip, A. Ataç, B. Bergenwall, J. Blomgren, K. Elmgren, C. Johansson, J. Klug, N. Olsson, G. Alm Carlsson, J. Söderberg, O. Jonsson, L. Nilsson, P.-U. Renberg, P. Nadel-Turonski, C. Le Brun, F.R. Lecolley, J.F. Lecolley, C. Varignon, Ph. Eudes, F. Haddad, M. Kerveno, T. Kirchner, C. Lebrun, Nucl. Instr. Meth. Phys. Res. **A452**, 484 (2000).

[22] P. Mermod, J. Blomgren, B. Bergenwall, A. Hildebrand, C. Johansson, J. Klug, L. Nilsson, N. Olsson, M. Österlund, S. Pomp, U. Tippawan, O. Jonsson, A.V. Prokofiev, P.-U. Renberg, P. Nadel-Turonski, Y. Maeda, H. Sakai, A. Tamii Phys. Lett. **B 597**, 243 (2004).

[23] P. Mermod, J. Blomgren, B. Bergenwall, A. Hildebrand, C. Johansson, J. Klug, L. Nilsson, N. Olsson, M. Österlund, S. Pomp, U. Tippawan, O. Jonsson, A.V. Prokofiev, P.-U. Renberg, P. Nadel-Turonski, Y. Maeda, H. Sakai, A. Tamii to be published.

[24] H. Condé, S. Hultqvist, N. Olsson, T. Rönnqvist, R. Zorro, J. Blomgren, G. Tibell, A. Håkansson, O. Jonsson, A. Lindholm, L. Nilsson, P.-U. Renberg, A. Brockstedt, P. Ekström, M. Österlund, F.P. Brady, Z. Szeflinski, Nucl. Instr. Meth. Phys. Res. **A292**, 121 (1990).

[25] R. Brun and F. Rademakers, Nucl. Instr. Meth. Phys. Res. **A389**, 81 (1997). See also http://root.cern.ch/.

[26] B. Holmqvist, B. Gustavsson, T. Wiedling, Ark. Fys. **34**, 481 (1967). Modified version by N. Olsson (unpublished).

[27] J. Rahm, J. Blomgren, H. Condé, S. Dangtip, K. Elmgren, N. Olsson, T. Rönnqvist, R. Zorro, A. Ringbom, G. Tibell, O. Jonsson, L. Nilsson, P.-U. Renberg, T.E.O. Ericson, B. Loiseau, Phys. Rev. **C57**, 1077 (1998).

[28] R.C. Byrd and W.C. Sailor, Nucl. Instr. Meth. Phys. Res. **A264**, 494 (1989).

[29] V.G.J. Stoks, R.A.M. Klomp, M.C.M. Rentmeester, J.J. de Swart, Phys. Rev. **C48**, 792 (1993).

[30] P.W. Lisowski, R.E. Shamu, G.F. Auchampaugh, N.S.P. King, M.S. Moore, G.L. Morgan, T.S. Singleton, Phys. Rev. Lett. **49**, 255 (1982).

[31] A.J. Koning and J.P. Delaroche, Nucl. Phys. **A713**, 231 (2003).

[32] C.Y. Chih and W.M. Powell, Phys. Rev. **106**, 539 (1957).

[33] T.C. Griffith, A.P. Banford, M.Y. Uppal, W.S.C. Williams, Proc. Phys. Soc. **71**, 305 (1958).

[34] A.J. Bersbach, R.E. Mischke, T.J. Devlin, Phys. Rev. **D13**, 535 (1976).

[35] J.P. Scanlon, G.H. Stafford, J.J. Thresher, P.H. Bowen, A. Langsford, Nucl. Phys. **41**, 401 (1963).

[36] R.A. Arndt, I.I. Strakovsky, R.L. Workman, Phys. Rev. **C62**, 034005 (2000).

[37] V.G.J. Stoks, R.A.M. Klomp, C.P.F. Terheggen, J.J. de Swart, Phys. Rev. **C49**, 2950 (1994).

[38] R. Machleidt, Adv. Nucl. Phys. **19**, 189 (1989).

[39] R. Machleidt, Phys. Rev. **C63**, 024001 (2001).

[40] M. Lacombe, B. Loiseau, J.M. Richard, R. Vinh Mau, J. Côté, P. Pirès, R. de Tourreil, Phys. Rev. **C21**, 861 (1980).

[41] G.C. Wick, Atti. R. Accad. Naz. Lincei, Mem. Cl. Sci. Fis. Mat. Nat. **13**, 1203 (1943).

[42] G.C. Wick, Phys. Rev. **75**, 1459 (1949).

[43] G.R. Satchler, Introduction to Nuclear Reactions, (Macmillan Education Ltd., 1990), p. 118.

[44] T. Peterson, L.C. Bland, J. Blomgren, W.W. Jacobs, T. Kinashi, A. Klyachko, P. Nadel-Turonski, L. Nilsson, N. Olsson, J. Rapaport, T. Rinckel, E.J. Stephenson, S.E. Vigdor, S.W. Wissink, Y. Zhou, Nucl. Phys. **A663&664** (2000) 1057c.

[45] M. Sarsour, T. Peterson, M. Planinic, S.E. Vigdor, C. Allgower, B. Bergenwall, J. Blomgren, T. Hossbach, W.W. Jacobs, C. Johansson, J. Klug, A.V. Klyachko, P. Nadel-Turonski, L. Nilsson, N. Olsson, S. Pomp, J. Rapaport, T. Rinckel, E.J. Stephenson, U. Tippawan, S.W. Wissink, Y. Zhou, Measurement of the Absolute Differential Cross Section for np Elastic Scattering Near 190 MeV, 17th International IUPAP Conference on Few-Body Problems in Physics, Durham, NC, USA, June 5-10, 2003 (accepted).

Appendix XVI

European Nuclear Education Network

Blomgren, J.
Swedish Nuclear Technology Center and Department of Neutron Research,
Uppsala University, Box 525, S – 751 20 Uppsala, Sweden
Tel. + 46 18 471 3788, Fax + 46 18 471 3853, Jan.Blomgren@tsl.uu.se

Moons, F
Studiecentrum voor Kernenergie•Centre d'étude de l'Energie Nucléaire,
SCK•CEN, Boeretang 200, B – 2400 Mol, Belgium,
Tel. +32 14 332596, Fax +32 14 338936, Frans.Moons@sckcen.be

Safieh, J.
Commissariat à l'Energie Atomique, Institut Nationales des Sciences et Techniques
Nucléaires, Saclay, Bât. 395, F – 91 191 Gif sur Yvette Cedex, France,
Tel. +33 1 69 08 69 94, Fax. +33 1 69 08 99 50, jsafieh@cea.fr

on behalf of the
European Nuclear Education Network

Abstract

In most countries within the European Union that relies to a significant extent on nuclear power, neither the undergraduate nor the PhD education is producing a sufficient number of engineers and doctors to fill the needs of the industry. Moreover, in many countries reactor physics and technology are being reduced or even removed from the academic curriculum. This has motivated an EU-supported project, aiming at finding means for raising the interest in nuclear technology among university students.

As a result of this process, a new education organisation, European Nuclear Education Network (ENEN), has recently been established. This is an organisation that will issue a special certificate in nuclear engineering. Students will be registered at various universities and get their exams from their respective alma mater, just as today. If the student fulfills some criteria on the total amount and type of courses, ENEN will issue an additional certificate stating that the student meets the standards for a European master of nuclear engineering. Thus, accreditation of courses is an important aspect of the work of ENEN.

At present, the process of harmonising nuclear education in Europe has progressed into a second stage. A new EU project, Nuclear European Platform of Training and University Organisations (NEPTUNO), was launched in January 2004. The project has two main foci; the practical implementation of ENEN and harmonisation of training activities. The latter refers to the training of personnel in industry, which is commonly being performed by utility-owned companies. A leading thought behind these efforts is that if more similar procedures are implemented within EU, mobility of personnel could increase, which in turn might make a career in the nuclear power industry more tempting.

Introduction

The need to preserve, enhance or strengthen nuclear knowledge is worldwide recognised since a couple of years. Among others, "networking to maintain nuclear competence through education and training", was recommended in 2001 by an expert panel to the European Commission [1].

It appears that within the European university education and training framework, nuclear engineering is presently still sufficiently covered, although somewhat fragmented. However, it has been observed that several areas are at risk in the very near future including safety-relevant fields such as reactor physics and nuclear thermal-hydraulics. Furthermore, in some countries deficiencies have been identified in areas such as the back-end of the nuclear fuel cycle, waste management and decommissioning.

To overcome these risks and deficiencies, it is of very high importance that the European countries work more closely together. Harmonisation and improvement of the nuclear education and training have to take place at an international level in order to maintain the knowledge properly and to transfer it throughout Europe for the safe and economic design, operation and dismantling of present and future nuclear systems. To take up the challenges of offering top quality, new, attractive and relevant curricula, higher education institutions should cooperate with industry, regulatory bodies and research centres, and more appropriate funding from public and private sources. In addition, European nuclear education and training should benefit from links with international organisations like IAEA, OECD-NEA and others, and should include world-wide cooperation with academic institutions and research centres.

The first and central issue is to establish a European Master of Science in Nuclear Engineering. The concept envisaged is compatible with the projected harmonised European architecture for higher education defining Bachelors and Masters degrees. The basic goal is to guarantee a high quality nuclear education in Europe by means of stimulating student and instructor exchange, through mutual checks of the quality of the programmes offered, by close collaboration with renowned nuclear-research groups at universities and laboratories. The concept for a nuclear master programme consists of a solid basket of recommended basic nuclear science and engineering courses, but also contains advanced courses as well as practical training. Some of the advanced courses also serve as part of the curricula for doctoral programmes.

A second important issue identified is Continued Professional Development. The design of corresponding training courses has to respond to the needs of industry and regulatory bodies, and a specific organisation has to be set up to manage the quality assessment and accreditation of the Continued Professional Development programmes.

In order to achieve the important objectives and practical goals described above, the ENEN Association, a non-profit association under French law, has been formed. This international association can be considered as a step towards the creation of a virtual European Nuclear University symbolising the active collaboration between various national institutions pursuing nuclear education.

Based on the concepts and strategy explained above, and with the full co-operation of the participating institutions, it may be possible that the intellectual erosion in the nuclear field can be reversed, and that high quality European education in nuclear sciences and technology can be guaranteed.

Background

The need to preserve, enhance or strengthen nuclear knowledge has been recognised worldwide since a couple of years.

"Although the number of scientists and technologist may appear sufficient today in some countries, there are indicators, e.g., declining university enrolment, changing industry personnel profiles, dilution of university course content, and high retirement expectations, that future expertise is at risk." [2]

"Today, the priorities of the scientific community regarding basic research lie elsewhere than in nuclear sciences. Taken together, these circumstances create a significantly different situation from three to four decades ago when much of the present competence base was in fact generated. In addition, many of the highly competent engineers and scientists, who helped create the present nuclear industry, and its regulatory structure, are approaching retirement age. These competence issues need to be addressed at Community level and a well designed Community research and training programme should play a role that is more important than ever before. This is an area where the concept of a European research area should be further explored." [1]

"In September 2002, the (IAEA) General Conference noted that the need to preserve, enhance or strengthen nuclear knowledge arises irrespective of the future expansion in the applications of nuclear technologies, and requested the Director General to note the high level of interest of Member States in the range of issues associated with preserving and enhancing nuclear knowledge in the process of preparing the Agency's programme." [3]

Thus, decreasing student enrolment, professors retiring without successors, shrinking resources to academic nuclear engineering – such descriptions of the present situation in nuclear engineering education have been commonplace in many European countries during the last decade. Can something be done about it?

ENEN – European Nuclear Engineering Network

Within the 5th Euratom research and training programme on nuclear energy (1998-2002), the European Commission supported a project on European nuclear engineering education. 22 academic institutions and research laboratories participated [4].

Within the project, the major elements for a European master of science in nuclear engineering have been defined, pilot sessions on nuclear engineering education have been performed, the ENEN-association has been established and a process of re-vitalization of nuclear education and training in Europe has been initiated. The project contributed towards farther reaching objectives, e.g., the conservation of nuclear knowledge and expertise, the creation of a European higher education area and the implementation of the Bologna declaration and the enlargement of the European Union.

It should be emphasized that ENEN was created based on a bottom-up approach. It has been formed without governmental or other types of high-level initiatives. Instead, the starting point was a number of active professors in nuclear engineering and related areas that saw a necessity – and possibility – of taking action. The absence of a strong leadership imposed from above has meant that the major properties of the project had to be agreed upon by a majority of its members. This has obviously made decision sometimes somewhat time-consuming, but on the other hand, when a decision has finally been reached, the implementation of it has been relatively straight-forward.

Since ENEN is not an organisation with power to overrule universities, the strategy adopted to promote nuclear engineering had to be based on a voluntary basis. This has resulted in the following approach. The basic organization of the university studies is unchanged. Like today, students are enrolled at their respective university, and they get their degrees from it, like before.

If the exam of the student fulfils the ENEN criteria, an additional certificate is issued, stating that the student is also awarded a European master of nuclear engineering.

There are presently major changes of the educational systems in many European countries motivated by the Bologna process. There is an ongoing process to harmonize essentially all the university education system in the EU countries into a 3+2+3 year education system. In this system, three years should be mandatory to obtain a bachelor's degree. A two-year addition would then result in a master's degree, followed by three years of research to get a PhD.

To diminish some confusion on the meaning of ENEN, it has to be mentioned already here that the acronym ENEN actually refers to two different meanings. The EU project ENEN (European nuclear Engineering Network) was active during 2002-2003. This project resulted in the establishment of the association European Nuclear Education Network, also abbreviated ENEN. Although all the partners of the ENEN project are now members of the ENEN network, the latter also has additional members. The change of the name, from "nuclear engineering" to "nuclear education", was suggested by the EU commission, with the motivation that this would facilitate a future expansion into activities related to nuclear engineering, like radiation protection. Below, the major components of the ENEN project are outlined.

European master of science in nuclear engineering

Based upon a year-long exchange of views between the partners of ENEN, consisting of a representative cross section of nuclear academic institutions and research laboratories of the EU-25, a coherent and practicable concept for a European Master of Science in Nuclear Engineering has emerged. The concept is compatible with the Bologna philosophy of higher education for academic engineers in Europe (a Bachelor of Science after 6 full-time semesters, and a Master of Science after a further 4 full-time semesters). In addition, the approach to the European Master of Science in Nuclear Engineering, can accommodate the presently existing variety of educational systems in the EU-25 members and candidate-member states, as well as the Bologna implementation in some countries, where Master degrees will be granted after a 2-semester program beyond the Bachelor.

The full curriculum leading to the degree of Master of Science in Nuclear Engineering is composed of course units formally recognized by ENEN. A Master of Science in Nuclear Engineering can only be granted after having obtained a full-time load of ten semesters beyond secondary level or in other words 300 credits engineering academic level studies. One credit amounts to a student load of about 30 hours and a full semester corresponds to 30 credits or about 900 load hours [5].

A minimum of two semesters equivalent or 60 credits must be obtained in strictly nuclear subjects composed of a set of core-curriculum courses complemented with nuclear electives and a project work/thesis in a nuclear domain (see figure 1).

European Master of Science in Nuclear Engineering

Minimal Requirements for EMSNE:

- At least 300 ECTS university-level study
- At least 60 ECTS purely nuclear engineering (NE) oriented
- At least 30 ECTS in other ENEN institution than "home institution"

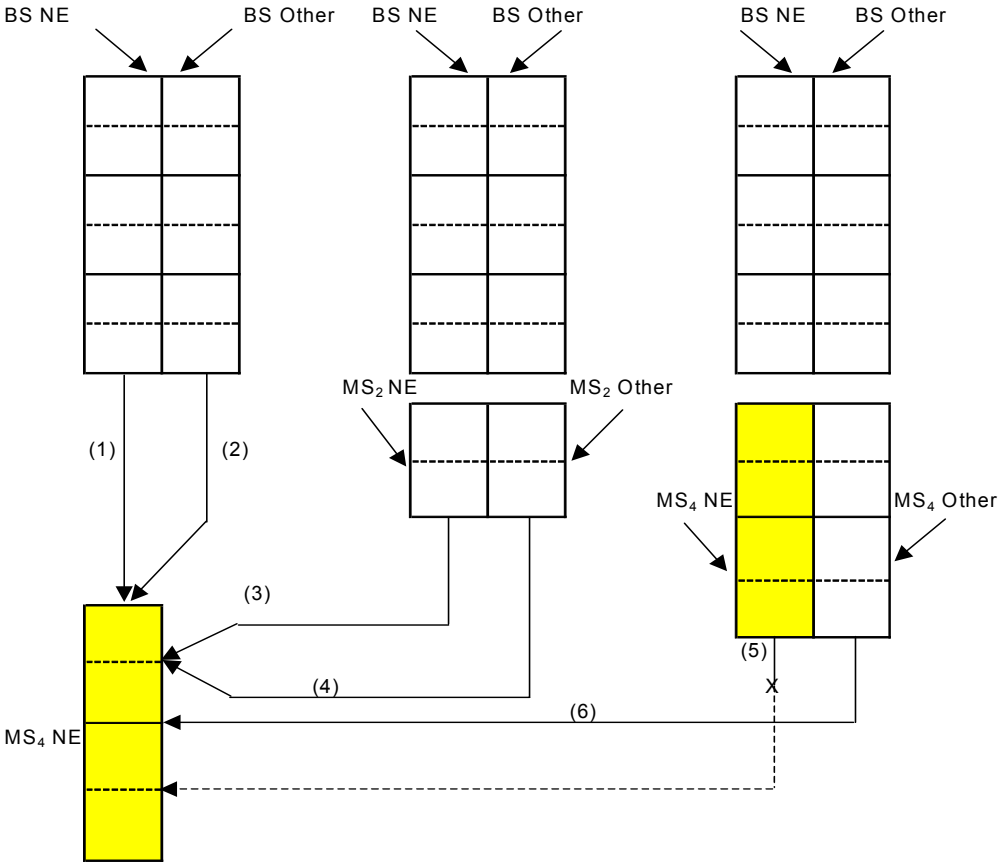

(1) 48-60 ECTS non NE; 48-60 ECTS NE (partly tradeable); 12-24 ECTS Thesis (NE)
(2) 48-60 ECTS non NE; 48-60 ECTS NE; 12-24 ECTS Thesis (NE)
(3) 24-30 ECTS non NE; 48-54 ECTS NE (partly tradeable); 12-18 ECTS Thesis (NE)
(4) 24-30 ECTS non NE; 48-54 ECTS NE; 12-18 ECTS Thesis (NE)
(5) only for "European" quality label; extra 30 ECTS "abroad"
(6) 42-48 ECTS NE; 12-18 ECTS Thesis

Figure 1. Typical full program variations.

Students register in one ENEN-accredited "home" institution and acquire the required credits in ENEN-institutions of their choice. The home institution grants the formal degree of Master of Science in Nuclear Engineering, based upon the formal recognition of credits, very much similar to the ERASMUS philosophy. ENEN, on behalf of its members, grants the quality label European Master of Science in Nuclear Engineering if a substantial amount (some 20 or 30) of credits have

been followed at an ENEN-member institution other than the home institution. Typically these credits might be obtained by performing "abroad" the project work or master thesis, and taking there also some related advanced courses.

The first European masters in nuclear engineering are expected to graduate after the 2005 summer semester.

Because of the different meaning of the words "undergraduate, graduate and post-graduate" in UK and US contexts, these terms are preferentially not used in the ENEN terminology. It is advised to talk about Bachelor, first Master, additional Master always with the number of credits or full-time semesters required, mentioned.

Pilot sessions on nuclear engineering education

To demonstrate the feasibility of European nuclear education schemes, a three weeks course, called "Eugene Wigner" course for nuclear reactor physics experiments, was successfully organized from April 28 to May 16, 2003. Some 20 postgraduate students from about 10 different European, including accession countries, participated in nuclear reactor physics experiments, organized jointly by four universities. Students performed reactor physics experiments on research and training reactors in respectively Vienna, Prague and Budapest. One week of theoretical lecturing at Bratislava University introduced or refreshed the knowledge to perform the nuclear reactor physics experiments. The ENEN partners rated the course between 6 to 8 credits or an equivalent student load of some 180 to 240 hours. Students got a certificate of participation. Individual marks are transmitted to the home professors.

Because of the success of the first edition, the course is organised for the second time from April 27 to May 15, 2004. The main organiser is the Institute of Nuclear Techniques at the Budapest University of Technology and Economics [6].

This course has fulfilled many of the ENEN underlying principles. It has a European dimension, since it involves four countries in the organization. Moreover, by joining forces among these partners, an added value is produced that could not have been provided by a single partner. At the time when the course was conceived, one country was already an EU member, while three were candidate countries, all of which are now EU members. Thus, this course also had a moment of integration of candidate countries. Finally, it has to be mentioned that clever use of existing infrastructure is a cornerstone in the EU research and education policy, a policy that was obviously adhered to.

The courses on Nuclear Thermal Hydraulics, 6 credits and Nuclear Reactor Theory, 8 credits, both part of the Belgian interuniversity program on nuclear engineering, were respectively organised October 20-31, 2003 and November 17-28, 2003. The former course was attended by 20 students and the latter by 10. In both, about half of the students were "foreign" students. Respectively on November 21 and December 19, 2003, the students were subjected to a written examination at the respective home university. The examination assignments, devised by the course staff, were mailed to the home professors. The home professors supervised the respective written examination sessions and mailed back the examination manuscripts to the course staff. The quotas, assigned by the course staff, were finally transmitted to the home professors. Although the data do not allow definite conclusions, both courses appeared to give evidence of a high academic standard.

The Belgian "additional master" program in nuclear engineering (BNEN) is organised in a highly modular way and taught in English to facilitate and exchange participation of foreign students. The program extensively uses the laboratory and lodging facilities of the Belgian Nuclear Research Centre. The BNEN calendar for the upcoming academic year is even more modularly structured to facilitate and enhance participation of foreign students and professors [7].

The pilot sessions on nuclear engineering education performed within the Euratom ENEN-project evidenced processes of qualification, mutual recognition and mobility. The pilot sessions fully subscribed the objectives of the 1999 Bologna agreement on higher education and used instruments such as the European Credit Transfer System.

The ENEN association

Pursuing the sustainability of the concept, the ENEN partners organized themselves in September 2003 in a non-profit-making legal association called ENEN, European Nuclear Education Network. The first general assembly was held on November 11, 2003 in Luxemburg, with representatives from the European Commission, the Nuclear Energy Agency of the Organisation of Economic Cooperation and Development and the International Atomic Energy Agency.
The main objectives of the ENEN association are:

- To deliver a European master of science degree and promote PhD studies in nuclear engineering,
- To promote exchange of students and teachers participating in the network,
- To establish a framework for mutual recognition,
- To foster and strengthen the relationship with research laboratories, industry and regulatory bodies.

The *ENEN association* consists of effective and associated members. The effective members are academic institutions providing high-level scientific education in the nuclear field. The associated members have a firmly established tradition of relations with members in the field of nuclear education, research and training. The Board of Governors recommends new member applications to the General Assembly. The organization is illustrated in figure 2.

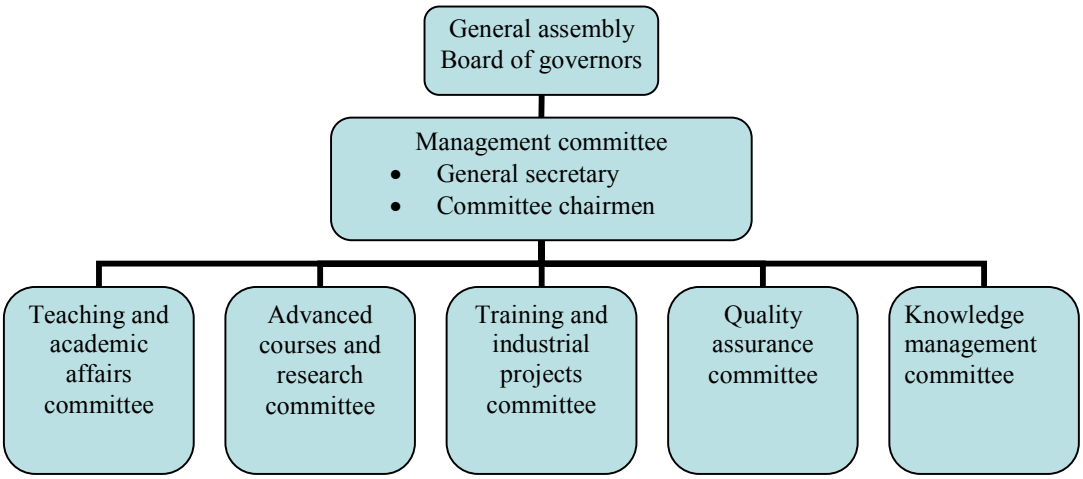

Figure 2. Simplified organizational chart of the ENEN association.

The *General Assembly* is composed of all effective and associated members. The Board of governors has six effective and two associated members, elected by the General Assembly for

four years. A reasonable geographical representation is strived for in the Board membership. The General Secretary is responsible for the day-to-day management. He chairs the Management Committee composed of the sub-committee chairmen.

The *Management Committee* examines the affiliation of a new member to the ENEN association. The decision is taken by the General Assembly.

The *teaching and academic affairs committee* defines the way to implement the degree of "European master of science in nuclear engineering", this means amongst others to establish the equivalence between the curricula in nuclear engineering education and credits (ECTS units), to approve the equivalence of admission criteria and to define the mandatory courses corresponding to the students' background.

The *advanced courses and research committee* ensures the link between ENEN members and research laboratories. It identifies in research centers and industry topics for internship leading to the preparation of a master's thesis. This constitutes a step to encourage and fund mobility of students through the European countries. The committee also participates in the organization of summer schools and advanced courses, identifies collaboration and sources of funding and recommends research projects. The committee establishes a list of PhD topics and creates incentives and facilities to PhD students.

The *training and industrial projects committee* identifies the industrial needs for continued professional development and organizes corresponding training sessions and courses. The committee facilitates the mobility of professors from different institutions participating as lecturers and to raise funding for this purpose. The committee organizes access to large nuclear structures.

The *quality assurance committee* examines the practices adopted in each affiliated institution concerning quality assurance. It establishes the accreditation of the European Masters in Nuclear Engineering and monitors the quality of current and proposed members.

The *knowledge management committee* identifies and monitors deficiencies in scientific knowledge relevant to nuclear technology and safety. It has to prepare, maintain and implement an action plan by academia in order to ensure that vulnerable scientific knowledge is not lost. To meet this objective, the committee has to, amongst others, publish books on relevant subjects for students and engineers working in the nuclear field. The committee also ensures efficient use of information and communication technology to support teaching and learning, e.g., elaborated Web server, simulators, electronic books and e-learning.

Moreover, although being in early youth, the ENEN association is recognized as a strong partner in nuclear power technology education by the Asian Network for Education in Nuclear Technology (ANENT). The ENEN association chairs and co-chairs the working groups on curriculum design and on inter-university cooperation of the World Nuclear University (WNU) initiative. The ENEN association submitted an Expression of Interest to provide consultancy services in connection with specific education and training activities proposed in projects of the Euratom research and training program on nuclear energy. The ENEN association advises the International Atomic Energy Agency on the preparation for and the organization of the International Conference on Nuclear Knowledge Management to be held from 7 to 10 September 2004 in Saclay, France.

Recently, the ENEN association has also resumed a role as research coordinator. In the Euroatom 6^{th} framework programme, a proposal on accelerator-driven transmutation research, EUROTRANS, has recently been submitted. The EUROTRANS proposal outlines a four-year project that amounts to 31.5 MEUR. In EUROTRANS, a large number of universities as well as national research centres, business companies and other types of organizations are involved. ENEN will coordinate the participating universities in the EUROTRANS project, and represent them in the EUROTRANS management committee.

NEPTUNO - Education and training in nuclear engineering and safety

Within the 6th Euratom research and training programme on nuclear energy (2002-2006), the European Commission supports the project: "Nuclear European Platform of Training and University Organisations, NEPTUNO". 35 partners from industry, training centres, academic institutions and research laboratories participate in it [8].

The ENEN project objective, "to preserve, enhance and strengthen nuclear knowledge", is continued and developed in the NEPTUNO project. However, as the former concentrated on higher education, the latter strives for education and training in the perspective of Continued Professional Development. The rationale is based on internationalisation and globalisation of the nuclear industry and nuclear energy production requesting for mobility, accreditation and recognition of qualified licensed staff. Within NEPTUNO, proposals are formulated for best practices for mobility, accreditation and recognition of qualified licensed staff and in general all staff needing some form of education, schooling or training before operating in the nuclear industry. The ongoing trends towards co-operation between training organisations, research institutes and academia are facilitated. Amongst others, attention is also given to the re-training of trainers and to the modular schemes for staff not requiring the full academic education program, in other words contributing to life-long learning schemes. "Training" is the terminology used in the NEPTUNO initiative to describe the schooling activities other than the regular academic education schemes. The NEPTUNO project strives for training (technicians, engineers) and education (master, PhD, post-doctoral) on equal terms of quality.

Re-inspiration of nuclear education and training

The present day reflections on nuclear knowledge management and the different initiatives taken, definitely catalyse networking in the nuclear education and training domain, internally in several countries as well on inter-academic level as between academia, research centres, regulatory bodies and utilities. The approach stimulates in an organic fashion, the process of identifying centres of excellence in the different disciplines of nuclear education and training. The approach also stimulates related disciplines, e.g., radiation protection to develop similar strategies and policies.

Conclusions

In the late nineties, the need to preserve, enhance or strengthen nuclear knowledge was widely recognised. Within the 5th Euratom research and training programme on nuclear energy, the European Commission supported a project on European Nuclear Engineering Education. Within the project, the major elements for a European master of science in nuclear engineering were defined, pilot sessions on nuclear engineering education were performed and the ENEN association was formed. The ENEN association is a non-profit-making legal association with as main objective to foster high-level nuclear education. Within the 6th Euratom research and training programme on nuclear energy (2002-2006), the European Commission supports the NEPTUNO project. The former concentrated on higher education, while the latter strives for education and training in the perspective of Continued Professional Development.

The present-day reflections on nuclear knowledge management and the different initiatives taken definitely catalyse networking in the nuclear education and training domain. However, the key question still remains: Do we attract more of the better students? Although the process is still in a premature stage to allow solid conclusions to be drawn, preliminary observations indicate a positive evolution, in quantity as well as in quality of students.

Acknowledgements

The ENEN project work was sponsored by the European Commission through contract n° FIR1-CT-2001-80127-ENEN. The NEPTUNO project work is sponsored by the European Commission through contract n° FI6O-CT-2003-508849.

References

1. EUR 19150 EN, "Strategic issues related to a 6th Euratom Framework Programme (2002-2006)". Scientific and Technical Committee Euratom. Pag.14.
2. OECD/NEA, "Nuclear education and training: Cause for Concern?, OECD 2000, ISBN 92-64-18521-6
3. IAEA 2003. "Strengthening the Agency's Activities related to Nuclear Science, Technology and Applications". IAEA. GOV/2003/53-GC(47)11, August 11, 2003.
4. ENEN. http://www.sckcen.be/ENEN
5. ECTS. http://europa.eu.int/comm/education/programmes/socrates/ects_en.html
6. Eugene Wigner. http://www.reak.bme.hu
7. BNEN. http://www.sckcen.be/BNEN
8. NEPTUNO. http://www.sckcen.be/NEPTUNO

ANNEX

ENEN partners:

Belgian Nuclear Research Centre (B)
Budapest University of Technology and Economics (HU)
Check Technical University (CZ)
Institut "Josef Stefan" (SI)
CEA-INSTN (F)
Kungliga Tekniska Högskolan (S)
K.U.Leuven Research and Development (B)
Consorzio Interuniversitario per la Ricerca Tecnologica Nucleare (I)
Universiteit Gent (B)
Slovak University of Technology (SK)
Swiss Federal Institute of Technology Zürich (CH)
Delft University of Technology (NL)
Helsinki University of Technology (SF)
Atominstitut der Österreichischen Universitäten (A)
Université Catholique de Louvain (B)
University of Birmingham (UK)
University Politehnica of Bucharest (RO)
Universidad Politecnica de Madrid (E)
National Technical University of Athens (EL)
Technische Universität München (D)
Ustav jaderného vyzkumu REZ (CZ)
Centre of Technology and Engineering for Nuclear Projects (RO).

NEPTUNO partners:

Belgian Nuclear Research Centre (B)
Budapest University of Technology and Economics (HU)
Check Technical University (CZ)
Institut "Josef Stefan" (SI)
CEA-INSTN (F)
Kungliga Tekniska Högskolan (S)
K.U.Leuven Research and Development (B)
Consorzio Interuniversitario per la Ricerca Tecnologica Nucleare (I)
Universiteit Gent (B)
Slovak University of Technology (SK)
Swiss Federal Institute of Technology Zürich (CH)
Delft University of Technology (NL)
Helsinki University of Technology (SF)
Atominstitut der Österreichischen Universitäten (A)
Université Catholique de Louvain (B)
University of Birmingham (UK)
University Politehnica of Bucharest (RO)
Universidad Politecnica de Madrid (E)
National Technical University of Athens (EL)
Technische Universität München (D)
Ustav jaderného vyzkumu REZ (CZ)
Centre of Technology and Engineering for Nuclear Projects (RO)
Tecnatom (E)
University of Stuttgart (D)
VTT Technical Research Centre of Finland (SF)
Lappeenranta University of Technology (SF)
Instituto Tecnologico e Nuclear (P)
Nuclear Department, HMS Sultan (UK)
Uppsala University (S)
Technical University of Sofia (BG)
University of Ljubljana (SI), ISaR Institute for Safety and Reliability (D)
Paks Nuclear Power Plant (HU)
GfS Gesellschaft für Simulatorschulung (D)
PENTRAC Pan-European Nuclear Training Centers Association (HU)
University of Manchester (UK)

Appendix XVII

Education for the nuclear power industry – Swedish perspective

Blomgren, J.

Swedish Nuclear Technology Centre
and
Department of Neutron Research, Uppsala University, Box 525, S – 751 20 Uppsala, Sweden
Tel. + 46 18 471 3788, Fax + 46 18 471 3853
Jan.Blomgren@tsl.uu.se

Abstract

In Sweden, about 50 % of the electricity is produced by nuclear power. The nuclear power industry hires about 50 people per year on a masters or PhD level. Of these, very few have a deep education in reactor technology. Instead, essentially all of them have their background in other areas of physics or engineering. In addition, the industry is hiring a comparable number of engineers on a bachelor's level for reactor operation positions.

To educate the staff, the nuclear power industry has formed a joint education company, Nuclear Training and Safety Center (KSU). KSU provides education and training programs for all levels of professional skills. Reactor operators undergo an extended training program over many years, where training in simulators constitutes an important part. In addition, courses aiming at a deeper theoretical understanding of reactor physics and thermohydraulics are provided. The latter types of courses are given in collaboration with Uppsala University.

To ensure that nuclear competence will be available also in a long-term perspective, the Swedish nuclear power industry and the Swedish Nuclear Power Inspectorate (SKI) have formed a joint center for support of universities, the Swedish Nuclear Technology Center (SKC). SKC has established collaboration with three Swedish universities, where undergraduate and PhD education is undertaken. Besides financial support, SKC also acts as a coordinator between the universities. One example is that SKC organizes courses for graduate students in such a way that they are open to all PhD students of the country.

Below, the activities of these organizations, and their impact on the competence development for the nuclear power industry, will be outlined.

Swedish nuclear power – an introduction

About 50 percent of the Swedish electricity is produced by nuclear power. This puts Sweden among the top five countries when it comes to percentage of nuclear power in the electricity production. Counted by installed power per capita, Sweden is the number one nuclear power country in the world.

Twelve light-water reactors were connected to the power grid between 1972 and 1985. Of these, nine boiling water reactors (BWRs) were produced in Sweden and the remaining three reactors are pressurised water reactors (PWRs) originating from the USA.

Nuclear power has had a political dimension in many countries, but Sweden has in some aspects an especially complicated relation between politics and nuclear power. In 1978, a three-party coalition government resigned from office because of disagreement on nuclear power. To my knowledge, this is the only event anytime, anywhere where a government has resigned because of nuclear power.

In 1980, an advisory referendum was held on the future of nuclear power in Sweden, a referendum that can be described as an aftermath of the Three Mile Island (TMI) accident the year before. In this referendum, three alternatives were on the ballot, neither of which indicated operation of nuclear power indefinitely. One alternative was closure within ten years, and the other two, which were to a large degree identical, suggested operation of the already built or planned reactors, i.e., the twelve finally taken into operation, to be run "for their technical lifetime", after which no new reactors should be built. The votes for latter two alternatives were considered merged by the Swedish parliament. The technical lifetime was assumed to be 25 years by the parliament. Since the last reactor should go critical in 1985, this meant that nuclear power should be phased out by 2010, which was thereby set to be the final date of Swedish nuclear power.

Over time, the perception of nuclear power by the general public has become dramatically more positive. All recent polls indicate that a large majority, 60-80 % of the population, would like to continue running the existing reactors as long as they fulfil the safety criteria. About 20-30 % of the population would prefer new reactors to be built in favour of deployment of fossil fuel-based electricity generation, and only about 20 % would like to see a rapid phase-out of nuclear power [1].

By now, it is clear that the technical life span of these reactors is more than 40 years, and operation for 60 years is seriously considered. With the preset closure in 2010 approaching, it became increasingly clear that a nuclear power phase-out would be very expensive, and it would be detrimental to the environment. This resulted in a new parliamentary decision in 1997 to withdraw 2010 as closing date. Instead, it was decided to close two reactors within two years, not because of safety reasons but to prove that the government was serious in its strive to phase out nuclear power. The remaining ten reactors should be "phased out with even time intervals", but the exact time interval was never defined. In spite of the decision to close two reactors quickly, only one has actually been taken out of operation, although it is kept in such a shape that it can easily be re-started. The other one has been identified, but a condition that the replacement power should not be more costly or cause increased environmental problems has so far lead to repeated postponements of the closure. At present, no date has been fixed.

Recently, the liberal political party has suggested the entire ban on new nuclear power to be lifted, and it has been suggested that installation of new reactors should be investigated. Restart of the already closed reactor was also suggested.

All these political maneuvers have resulted in a situation where nuclear power has for a long time been considered a no-future industry. Not surprisingly, it has not been a prime career choice for young people. As a consequence, the enrolment in nuclear engineering studies has dwindled to very small numbers, and a few years ago, less than ten students in the whole country graduated in nuclear engineering from the technical institutes. This perception has, however, changed dramatically in a rather short time lately. Nuclear power is no longer politically incorrect among young people. On the contrary, it is generally seen as environmentally friendly and economically sound. Moreover, the collapse of the information

technology boom in year 2000 has resulted in massive lay-offs from the computer and telecom businesses, which in turn has resulted in that many engineers look for more stable industry jobs. The general perception is that nuclear power is such a safe haven, in spite of the political talk about closure in an undefined future.

These backgrounds are necessary to understand the current situation. For the last twenty years, investments in the reactor park have been hampered by the decision to close them, and the lack of attraction among young people has led to that nuclear engineering has almost vanished from the curriculum of Swedish universities. Because of this, the industry had a difficult time getting its personnel needs satisfied by the universities. Instead, the industry had to hire other types of engineers, often relatively mature in age, and to educate them at work.

Training and education in the industry

The Swedish nuclear power industry employs 30-50 new people per year for duties where knowledge of nuclear physics and engineering is required. Of these, only a minor fraction (less than 10 %) has reactor physics or engineering in their curriculum. The vast majority have engineering degrees with specialization in other fields, with electrical engineering, machine technology and engineering physics being the most common.

This category can roughly be divided into two subgroups, operators and others. A majority of the reactor operators today have high-school education only. There is, however, a strong trend that the newly employed operation staff typically has a three-year engineering education beyond high school, i.e., corresponding to a bachelor's level degree. There is a many-year career track to become an operator. A period of at least three but typically five years as general technical support at the power plant is required before education to become an operator is initiated. During this first phase, the staff undergoes an education programme of typically two years. For promotion to operator, an additional education programme of one year is mandatory. There are, however, two categories of operators, turbine and reactor operators. These fulfil different duties in the control room during regular operation, and are recognized as different positions. The turbine operator education always comes first and some continue to the second step to become reactor operator. Each of these two levels requires one year full-time education.

This education is composed of regular teaching as well as training in simulators. For all reactors, there are corresponding simulators. Until a few years ago, the simulators were located at the Studsvik site south of Stockholm, which then served as a central hub in the education. Recently, most of the simulators have been moved to the power production sites to increase the accessibility for the personnel.

Finally, there is an educational programme to become operative leader of the production (shift manager), which comprises about half a year. This programme is mostly focused on leadership aspects, organization, etc., but it also involves some technical education.

It is required by the nuclear power inspectorate that an operator undergoes education and training of at least ten days per year, whereof simulator training for at least five days per year. It is not uncommon that a person has dual competence, e.g., both as reactor and turbine operator, and therefore has to spend twice this time per year in simulator training. In reality, personnel with only a single competence, i.e., as turbine operator, nevertheless spends ten days on training.

In addition to the simulator training and the education targeting direct aspects of daily operation, there is teaching on more fundamental understanding of the underlying physics of reactors. The TMI accident in 1979 was the starting point for this type of education. It was a general conclusion that part of the reason for the TMI accident was inadequate education of the staff. They lacked a general understanding of the physics of reactors, which made them poorly suited to handle a situation far from the standard drift scenarios. The Chernobyl accident seven years later further stressed the need for education of the operational personnel, beyond training.

Besides reactor operators, there is a large category working with tasks that require advanced knowledge of reactors for purposes then direct operation. Good examples are core and drift planning, i.e., core simulations to optimise the use of fuel, and staff involved in reactor instrumentation. They do not undergo simulator training, but need general reactor physics and technology, often beyond the needs of operators. In contrast to the operators, which have many years of employment and significant practical experience before going to general reactor physics, the latter category need this education at the beginning of their employment.

To meet the educational demands, the power utilities have jointly formed a dedicated education company, called Nuclear Safety and Training Centre (KärnkraftSäkerhet och Utbildning AB in Swedish, abbreviated KSU) [2]. KSU is owned by the utilities with proportions roughly corresponding the share of the total nuclear electricity production. The company is non-profit in the sense that the employers are charged for the course participation of their staff, such that KSU neither makes profit nor loss when integrated over a few years. Due to this construction, the KSU courses are open to participants also from non-owner organizations, because the fees are set to cover the full costs for the education.

KSU owns and operates the simulators, and provides the regular teaching near practical operation. The courses on general understanding of reactor-relevant physics, from hereby referred to as higher education, is provided by the Department of Neutron Research (Institutionen för neutronforskning, INF) of Uppsala University [3]. This cooperation is based on a six-year contract, where KSU grants a fixed support to INF, and in return KSU can demand a specified teaching volume.

Education at universities

Until only a few years ago, nuclear engineering education and research were undertaken at two universities only, the Chalmers Institute of Technology (CTH) in Gothenburg [4] and the Royal Institute of Technology (KTH) in Stockholm [5]. Chalmers has two chairs, one in reactor physics and one in nuclear chemistry directed towards partitioning (separation of spent fuel). KTH had four chairs, in reactor physics, nuclear chemistry directed towards geological repositories, nuclear engineering and nuclear power safety. All these professors were scheduled for retirement at about the same time a few years ago, and the prospects of replacement were not very positive.

To promote long-term sustainability of reactor-relevant research and education at Swedish universities, the Swedish Centre for Nuclear Technology (Svenskt Kärntekniskt Centrum, SKC) has recently been established [6]. The center is financed by the power plants in proportional to their installed power, with added contributions from Westinghouse (Nuclear Fuel production in Västerås) and the Swedish Nuclear Power Inspectorate (Statens KärnkraftInspektion, SKI), i.e., the governmental regulatory body [7].

The fact that the inspectorate contributes might call for an explanation. There is a long-term tradition in Sweden that the inspectorate primarily acts proactively. Thus, instead of just inspecting and handling the judicial aspects after possible incidents, the inspectorate involves itself in a continuing discussion with industry with the aim to guarantee or even raise the security. The inspectorate has a mission issued by the political sphere to promote nuclear security. This has been interpreted to also encompass support to education and research, because such activities are viewed as crucial to uphold a high security standard. Thus, SKI finances about one third of SKC.

SKC has long-term collaboration agreements with three universities, the Royal Institute of Technology (Kungliga Tekniska Högskolan, KTH) in Stockholm, Chalmers Institute of Technology (Chalmers Tekniska Högskola, CTH) and Uppsala University (UU). As part of these agreements, the universities have committed themselves to open reactor-relevant positions, which are then financially supported by SKC. In addition, SKC supports research projects where scientists of any university can apply. Besides projects on reactor technology in traditional sense, SKC also supports reactor-relevant research in areas like materials

science (properties of zircalloy, quantum mechanical modelling of neutron-induced materials damage), chemistry (iodine chemistry in severe accidents) and man-machine-organization interface problems.

These long-term collaboration agreements have resulted in that the chairs above will all continue. Without this support, it is likely that very little activities – if any – would have prevailed. Moreover, nuclear power relevant education and research has recently been established at Uppsala University, which has very little previous tradition in the field.

Recently, SKC has initiated a graduate school on nuclear power technology. The background is that the limited enrolment in PhD studies at Swedish universities makes it difficult to uphold a large volume of courses for the PhD students at each university. Instead, courses are re-organized in such a way that students from all universities can attend them. This means in reality that courses have to be concentrated in time, like summer schools. A typical course is therefore organized with full-time teaching for about a week. For a longer course, there could be several separate study weeks.

This type of organization makes the courses suited also for foreign participants. Since the studies are concentrated in time, essentially any student in Europe can attend them. It is notable that at about the time SKC initiated the new organization of its PhD courses, a similar activity began in the entire EU. A large number of European universities have recently formed the European Nuclear Education Network, ENEN [8]. The driving force behind ENEN has been to re-organize nuclear engineering education in Europe to increase the attraction in nuclear engineering careers. Part of the work has been spent on providing courses with a structure similar to the SKC courses, i.e., concentrated in time to allow participation from more than the local students. With the fairly short travel time and modest travel costs in Europe, such an organization can facilitate a significantly increased total education volume, combined with an improved quality. The ENEN initiative is described in detail in a separate contribution to these proceedings, and is therefore not described further here.

One particular aspect needed to understand the structure of the research and education is the absence of research institutes. Besides the Swedish Defence Research Agency, there are essentially no research institutes in Sweden. Instead, industry-oriented research is either carried out in industry itself or at the universities.

A consequence of this strategy is that only a minor fraction of the industry-oriented research at Swedish universities is financed by government grants. Instead, the large majority is financed by external industry grants to the universities, and nuclear engineering is no exception from this rule. In fact, essentially all the research and PhD education is financed via industry grants. Only the undergraduate education is to a significant degree government-funded, but this is also a truth with qualification. There is a system to finance teaching that barely covers the costs for the actual teaching, but if no other funding was at hand, the teacher would have to work full time on teaching only just to cover the own salary costs. In reality, this would be impossible because it is out of question to fill the agenda so efficiently. Therefore, some additional funding must be present just to have the teaching capability available, and this is possible thanks to the industry support.

Synergy effects

With the organization outlined above, it has been possible to achieve a fairly efficient utilization of limited resources, especially when two organizations collaborate.

As has been described above, the KSU courses for industry personnel have been designed for newly employed personnel. A pre-requisite for such courses to be useful for the industry is that they are concentrated in time. This requirement, however, also makes them well suited for PhD students. Accordingly, an agreement has been reached between KSU and SKC that whenever there are free seats available during a KSU course, PhD students from any Swedish university can participate. This has resulted in a marked increase in the total course volume. Moreover, the fact that course participants come from different backgrounds have resulted in increased student activity in the courses, simply because of the need to explain various

concepts across professional barriers, and because questions are being asked from a wider range of perspectives.

Up to now, this collaboration has been established in general courses on nuclear power technology for newly employed industry personnel. The content of these courses is essentially basic reactor physics and thermo-hydraulics, with moments of nuclear power safety. Thus, these courses are giving a broad introduction to nuclear power, but they do not go deeply into the subject. Thereby, they are useful to PhD students working in areas related to nuclear power, but where the focus is not on reactor technology. A good example is nuclear chemists working with partitioning. For them, a broad view of nuclear power is useful to put their work into a larger perspective, but their cutting edge knowledge has to be in chemistry. Other examples are nuclear physicists, PhD students working with reactor applications like neutron scattering for materials investigations, boron-neutron capture therapy (BNCT), etc.

This student category is fairly large. In loose terms, it comprises about 50 PhD students in Sweden. For the students in more reactor-oriented research, however, these courses are not sufficiently deep. Therefore, more specialized courses have to be taught. Recently, an example of synergy effects also in more specialized education has materialized. A two-week course on probabilistic safety analysis (PSA) will take place during autumn 2004, where about half the participants come from academia and half from industry and the regulatory body. The course is provided by a commercial company that performs PSA studies on demand. Neither participant category is sufficiently large to carry the costs for such a course, but by joining forces, the total number of participants is sufficiently large to make the cost per participant realistic.

Recently, the cross-disciplinary collaboration has been taken a step further. As described above, in the introductory KSU industry-oriented courses above, PhD students have been accepted as participants for a few years. Since these courses are nowadays taught at a university, they are now available also to undergraduate students. For simple geographic reasons, up to now mostly local students have taken the chance to follow the course whenever there are available seats. This has resulted in a number of new aspects of this teaching. First and foremost, this has allowed an expansion of the total volume of nuclear power education at a university hitherto not involved in the field. Because of this teaching, a faculty staff of five young professors has emanated, and suitable teaching material has been developed. This has opened new opportunities for other courses, targeting undergraduate education on nuclear engineering. Second, it has rapidly become popular among undergraduate students to follow these courses because of the unusual format. The students strongly appreciate the presence of industry personnel, because they benefit from their knowledge, and it makes the education feel more realistic. A common student complaint on undergraduate education is that it is poorly linked to industrial reality. Therefore, taking a course originally intended and designed for industry and where half the participants work in industry is perceived as an utterly positive experience.

Outlook

Sweden is a country with a small population on a relatively large area. This has to a considerable degree prompted the solution that courses within a relatively small subject, like advanced nuclear engineering, are organized in such a way that students and teachers meet full time during a relatively short period (one or a few study periods of 1-2 weeks each). With such an organisation, the education is already well suited for integration into a larger European perspective. The time and cost to travel is not dramatically different within Sweden and within Europe. Belgium has already re-organized its nuclear engineering education with a similar course structure, however for other reasons [9]. Moreover, in Belgium this has also been done for undergraduate education. Within ENEN, similar organisational changes are underway in many European countries. Recently, a similar harmonisation process has been initiated on industrial training via the NEPTUNO project [10].

We are presently facing a major change of the educational system in many European countries through the Bologna process. There is an ongoing process to harmonize essentially all European university education system into a 3+2+3 year education system. In this system, three years should be mandatory to obtain a bachelor's degree. A two-year addition would then result in a master's degree, followed by three years of research to get a PhD. In this report, I have distinguished undergraduate engineering courses and PhD student studies, but in a few years, this will no longer be a valid distinction. Instead, we are entering a situation where what today is last-year specialization undergraduate courses and PhD courses will become the same, i.e., part of the master's programmes. Referring to the discussion above, this means that ENEN can have a large impact on the master's education level.

I believe it is possible that nuclear engineering education can increase both in popularity and quality, even in a short time perspective. Even if that happens, however, I do not foresee that this will lead to that industry can fill even half their vacant employment positions with well-educated nuclear engineers or doctors. Nuclear power is nowadays a mature technology, and in all mature technologies the required competence is primarily built by hiring people with general technology skills, and then educate them for their particular duties through training programs. This has long been the situation in the paper and pulp industry, in forestry, mining, etc., i.e., mature industries. Because of this, training and education in industry is not likely to diminish even if the undergraduate education situation improves.

Sweden is such a small country that we simply cannot afford duplication in the long run. In this report, I have given a few examples of how synergy effects have been possible to achieve through cross-disciplinary activities during the last few years. I do not believe that all possibilities of collaboration for clever use of resources have been exhausted. On the contrary, I foresee increased synergetic activities. Last but not least, it should be stressed that efficient use of resources is not the only benefit that can be obtained through cross-disciplinary initiatives. Such approaches are also important because they have a potential to improve the quality. When people from various environments meet, new challenges and opportunities emanate, and this provides – more or less intrinsically – quality assurance.

References

1. See, e.g., http://www.analys.se/engsite/engopin.html
2. KSU. www.ksu.se
3. Department of neutron research, Uppsala University. www.inf.uu.se
4. Department of reactor physics, Chalmers Institute of Technology, Gothenburg. www.nephy.chalmers.se
5. Department of nuclear and reactor physics, Royal Institute of Technology, Stockholm. www.neutron.kth.se
6. Swedish Centre for Nuclear Technology, www.nuclear-tech-centre.org
7. Swedish Nuclear Power Inspectorate, www.ski.se
8. ENEN. http://www.sckcen.be/ENEN
9. BNEN. http://www.sckcen.be/BNEN
10. NEPTUNO. http://www.sckcen.be/NEPTUNO

Appendix XVIII

For Official Use **NEA/SEN/NSC(2004)3**

Organisation de Coopération et de Développement Economiques
Organisation for Economic Co-operation and Development **19-Jul-2004**

English - Or. English

NUCLEAR ENERGY AGENCY
NUCLEAR SCIENCE COMMITTEE

NEA/SEN/NSC(2004)3
For Official Use

SUMMARY RECORD OF THE FIFTEENTH MEETING OF THE NUCLEAR SCIENCE COMMITTEE

Château de la Muette, Paris
9th – 11th June 2004

English - Or. English

JT00167584

SUMMARY RECORD OF THE FIFTEENTH MEETING OF THE NUCLEAR SCIENCE COMMITTEE

9th – 11th June 2004

1. The Chair, T. Lefvert, Sweden, opened the meeting and welcomed the delegates. The following two new members of the committee were announced: Riku Mattila Finland (replacing A. Tanskanen) and David Simister, UK (replacing D. Edens). N. Ramamoorthy, director in the IAEA division of physical and chemical sciences, participated for the first time.

2. B. Briggs, chairman of the Working Party on Nuclear Criticality Safety (WPNCS) and D. Hill, chairman of the Working Party on Scientific Issues in Partitioning and Transmutation (WPPT) were invited to present proposed new mandates for the respective Working Parties. M. Silari and W.D. Newhauser were invited as experts for the in-depth discussion on "Shielding and dosimetry for accelerators". F. Baron was invited to present the Euratom integrated project PERFECT.

3. Apologies for absence had been received from H. Leeb, Austria, R Mattila, Finland, and N. Olsson, Sweden. The complete list of participants is given in Annex 1.

Introduction by the Director General

4. L. Echavarri, Director General of NEA, informed the committee of recent events within the OECD and the NEA. He mentioned specifically the on-going discussions within OECD of the budget for 2005-2006, which seemed to be pointing towards a zero nominal growth with some compensation for inflation. He also informed the committee that the new Strategic Plan for NEA had in principal been approved at the last NEA Steering Committee meeting and that it would be followed by a revision of the mandates of all NEA standing technical committees. These committees would also be invited to make a self-evaluation of their meetings and assess the usefulness of the outputs of the committee's programme of work.

5. L. Echavarri announced that the NEA would act as the technical secretariat for the Generation-IV International Forum (GIF). This work would be supported by extra voluntary contributions and would not affect the normal programme of work. He also mentioned that the NEA had started an internal activity to review methods and means to preserve information (knowledge) produced by the NEA committees, Working Parties and Expert Groups.

Adoption of the Agenda (NEA/SEN/NSC(2004)1/REV1)

6. The proposed agenda was adopted with minor modifications to the order in which the points were taken.

Approval of the Summary Record of the 14th Meeting (NEA/SEN/NSC(2003)3)

7. The summary record of the fourteenth meeting of the NSC was approved without modifications.

Renewal of the NSC mandate

8. T. Dujardin informed the committee that, after the formal approval of the new NEA Strategic Plan, it would be necessary to review the mandate of all NEA Standing Technical Committees. The present committee mandates, having a 5-year duration, would expire in 2005. The time-schedule for the renewal of the NSC mandate would be the following: the final version of the new NEA Strategic Plan would be distributed in July 2004. The consistency between this new Strategic Plan and the existing NSC mandate should be reviewed and comments or proposed changes to the mandate should be sent to the NEA secretariat before mid October. The NSC bureau would then discuss the proposals and prepare a new version of the NSC mandate in December 2004 to be approved by the committee by written procedure during January 2005. The final version of the NSC mandate would then be forwarded to the NEA Steering Committee and its bureau meeting in February 2005.

Status of Committee Projects (NEA/SEN/NSC(2004)2)

Review of progress and renewal of mandates of the NSC Working Parties

Working Party on the Physics of Plutonium Fuels and Innovative Fuel Cycles (WPPR)

9. K. Hesketh, chairman of WPPR, presented the proposed new mandate of the Working Party. He recalled the evolution of the activities of the Working Party and suggested that the new name of the Woking Party would be the Working Party on Reactor Systems (WPRS).

10. Considering the close relation between this proposal and the proposed new mandate for the Woking Party on Scientific Issues in Partitioning and Transmutation (WPPT), the committee agreed to postpone the discussion of the proposed new WPPR mandate until after having listened to the presentation from the WPPT.

Working Party on Scientific Issues in Partitioning and Transmutation (WPPT)

11. D. Hill, chairman of WPPT, started by presenting the progress of the Working Party's on-going programme of work. The four subgroups on accelerators, chemical partitioning, fuels and materials, and physics and safety, would all finalise their state-of-the-art reports by autumn 2004. A few longer term or recently started activities, such as the Lead-Bismuth Eutectic Handbook, a study on fuel cycle separations criteria and a review of fuel cycle transition scenarios would be transferred to a proposed new Working Party.

12. A proposal for a new Working Party was presented. The scope of the Working Party would be to deal with scientific issues in various existing and advanced nuclear fuel cycles, including fuel cycle physics, associated chemistry and flowsheets, development and performance of fuels and materials, and accelerators and spallation targets. The name of the new Working Party was proposed to be the Working Party on Scientific Issues of the Fuel Cycle (WPFC).

Discussion and decision of the new Working Party mandates

13. The committee members thoroughly discussed the two proposed new Working Party mandates. It was generally felt that both mandates needed to be revised in order to avoid potential duplication, both in between the Working Parties and also with other NEA activities. The secretariat was asked to continue the

discussions with K. Hesketh and D. Hill, taking into account the comments expressed by committee members, and to present revised proposals at the end of the meeting.

14. The committee reviewed the revised mandates presented at the last day of the meeting. The mandates were approved for a three-year period starting from 11 June 2004. The secretariat would contact OECD delegations to solicit nomination of members to these new Working Parties. The adopted mandates for the new Working Parties on Scientific Issues of Reactor Systems (WPRS) and on Scientific Issues of the Fuel Cycle (WPFC) can be found in Annex 2 and Annex 3 respectively.

Working Party on Nuclear Criticality Safety (WPNCS)

15. B. Briggs, chairman of WPNCS, presented a summary of the Working Party activities during the last year, including the outcome of the International Conference on Nuclear Criticality (ICNC 2003), held in Tokai-Mura, Japan, in October 2003. The need for critical and near critical experiments with low-moderated MOX fuels had been identified by the WPNCS subgroup on experimental needs and the issue was discussed at a workshop held in Paris, France in April 2004. The workshop concluded with the following two recommendations to the NSC:

- Investigate the possibility of releasing and evaluating unpublished experimental data (e.g. ERASME/S and BFS-49).
- Define a framework and method for the selection and performance of new experimental program(s) of interest.

16. The committee strongly supported the first recommendation above and asked the chairman to approach the respective laboratories/institutes with a request for the release of the data. Concerning the second recommendation, the committee suggested the Working Party to review the necessary criteria and then make a more detail proposal to the NSC.

17. A new three-year mandate for the WPNCS was proposed. The committee approved the new mandate, which can be found in Annex 4.

Working Party on International Nuclear Data Evaluation Cooperation (WPEC)

18. A. Koning informed the committee about the status of the WPEC activities. New versions of the ENDF and JEFF libraries were expected in 2005 (ENDF/B-VII and JEFF-3.1), whereas the latest version of the JENDL library (JENDL-3.3) had been released in May 2002 and work on the new version (JENDL-4) had just started and was expected to be released in 2009-2010.

19. The High Priority Request List for nuclear data was being revised and an improved version would be available at the NEA website in autumn 2004. Four of the five short-term subgroups would complete their work and publish final reports in late 2004 or early 2005. A number of suggestions for new subgroups were reviewed and would be decided upon at the next meeting of the Working Party in spring 2005.

Follow-up to recent NSC organised workshops and meetings

Third Information Exchange Meeting on basic Studies in the Field of High-temperature Engineering

20. The third information exchange meeting on Basic Studies in the Field of High-Temperature Engineering was held at JAERI Oarai, Japan in September 2003. The main topics discussed at the meeting comprised high temperature engineering research activities, behaviour of irradiated graphite/carbon & their composites and material properties at high-temperature irradiation.

21. The information exchange meeting recommended to the NSC to establish an expert group to review the present capability of computer codes to predict property change in irradiated graphite at high temperatures. The expert group would produce a state-of-the-art report on the current understanding and to make recommendations for further work. A proposal, which had been developed in consultation with the University of Manchester, was presented.

22. The committee approved the proposal, with the suggestion to extend the scope of the study to cover also interests expressed within the Generation-IV International Forum project.

Second Information Exchange Meeting on Nuclear Production of Hydrogen

23. The second information exchange meeting on Nuclear Production of Hydrogen was held at Argonne National laboratory, USA, in October 2003. The 60 participants discussed different processes considered for the production of hydrogen and noted a substantial progress since the last meeting three years earlier, especially what concerns the number of papers presenting experimental results.

24. It was proposed to organise a third information exchange meeting in 2005, possibly in Japan. The IAEA had expressed interest to co-sponsor such a meeting in 2005 and has asked if the NSC would be interested to co-sponsor an IAEA conference on the same subject in 2007.

25. The committee approved the proposal to organise a meeting on Nuclear Production of Hydrogen in Japan in 2005. The NSC welcomed the proposal from IAEA to co-sponsor the NEA meeting in 2005 and agreed to co-sponsor the proposed IAEA conference in 2007.

Tenth International Conference on Radiation Shielding (ICRS-10)

26. P. Vaz presented the outcome of the 10th International Conference on Radiation Shielding (ICRS-10) and the joint Radiation Protection conference (RPS-2004). The conferences attracted 333 participants from 33 countries and were held on the Madeira Island, Portugal in mid May 2004. Three tutorials had also been held, covering "big challenges in Monte Carlo calculations (from physics to biology)", an introductory course in proton cancer therapy and radiation shielding for diagnostic radiology and radiation therapy. The next International Conference on Radiation Shielding (ICRS-11) is planned to be held in Atlanta, USA in 2008.

Fourth International Workshop on Utilisation and Reliability of High Power Proton Accelerators

27. The fourth international workshop on Utilisation and Reliability of High Power Proton Accelerators was held in Daejeon, Korea in mid May 2004. More than 120 participants from 12 countries and 2 international organisations attended the meeting, which comprised the following five technical

sessions: Accelerator reliability, Target, window and coolant technology, Sub-critical system design and ADS simulations, Safety and control of ADS, and ADS experiments and test facilities.

28. The committee supported a proposal to organise a fifth workshop in Europe in spring 2006 and noted that coordination with the EC IP-EUROTRANS project would be assured.

Seminar on Pellet-Clad Interaction in Water Reactor Fuels (PCI-2004)

29. An international seminar on Pellet-Clad Interaction in Water Reactor Fuels was held in Aix-en-Provence, France on 9-11 March 2004. The meeting was organised by CEA Cadarache and was attended by 140 participants from 20 countries, representing 46 different organisations, including research laboratories, fuel vendors, NPP operators, nuclear safety institutions and consultancy firms. The aim of this third seminar on basic performance in fuel behaviour was to draw up a comprehensive picture of the current understanding of pellet clad interaction and its impact on the fuel rod, under the widest possible conditions. A summary of the meeting has been issued with the reference NEA/NSC/DOC(2004)8.

Short review of NSC expert groups and task forces

Preservation of Reactor Physics Experiments (IRPhE)

30. Last year the NSC approved the mandate and a three-year programme of work for the preservation of reactor physics experiments (IRPhE), following the successful completion of the initial pilot evaluations. The following types of measurements are included in the IRPhE project: fundamental mode lattice experiments, heterogeneous core configurations, power reactor start-up data, and specific applications experiments, such as fission product integral data and irradiation experiments.

31. Progress has been made in adding new evaluations in spite of the difficulties encountered in finding expertise available to work on the project. Voluntary contributions from member countries, especially Japan and Korea, have been extremely valuable for the advancement of the work. The IRPhE project will be presented at the “Nuclear Knowledge Management” conference in Saclay, France in September 2004. The next technical group meeting of the project will be held in October 2004

Reactor-based Plutonium Disposition

32. P. D’Hondt presented the status of the different MOX fuel behaviour issues and benchmarks related to the physics of MOX fuelled systems, which are managed by the task force on Reactor-based Plutonium Disposition. At the NSC bureau meeting in December 2003, it was questioned whether or not this task force be discontinued and the different activities be incorporated in the proposed new Working Parties WPRS and WPFC. Following discussions at the task force meeting in February 2004, it was proposed to continue the task force as a separate activity and a new two-year mandate was proposed for approval to the NSC.

33. The committee approved the proposed two-year mandate of the task force, taking into account that a close collaboration between the task force and the newly established Working Parties WPRS and WPFC would be continued.

Basic Phenomena in Fuel Behaviour

34. W. Wiesenack reported on the fuel behaviour activities, especially the development of the database on International Fuel Performance Experiments (IFPE) and the cooperation with the IAEA FUMEX activity. New editions of the IFPE data had been issued in October 2003 and April 2004. Nine new experiments, comprising data for 83 new rods, had been incorporated in the last year. Some of these experiments had been released to the IAEA coordinated FUMEX-II exercise on fuel modelling at extended burn-up.

Reactor Stability and LWR Transient Benchmarks

35. J.M. Aragones presented the status of the on-going reactor stability and transient benchmarks. The PWR main line steam break benchmark had been completed and 4 volumes had been published. The reports of the BWR Turbine Trip benchmark were being finalised and the VVER-1000 coolant transient benchmarks were being pursued. The final specifications of the NUPEC BWR Full-Size Fine-Mesh Bundle Test benchmark were in preparation and the CRISSUE-S (Critical Issues in Nuclear Reactor Technology) reports were being edited for publication in mid 2004.

Radiation Shielding

36. P. Vaz reported from the 7th meeting of the task force on Shielding of Accelerators, Targets and Irradiation facilities (SATIF). The meeting was held in Lisbon, Portugal on 17-18 May 2004. The task force review on-going work and discuss future directions, including new application areas, such as medical radiation applications, dosimetry-related calculations, shielding of transmutation facilities and applications involving "high" energy radiations. The next meeting of the task force is planned to be held in Korea on 22-24 May 2006.

37. The database of radiation shielding experiments (SINBAD) contains presently 67 experiments in the areas of reactor shielding and pressure vessel dosimetry, fusion blanket neutronics, and accelerator shielding. Nine data sets were added in 2003 and nine data sets are scheduled to be added in 2004. The NEA cooperation with the EU-Concerted Action QUADOS (Quality Assurance for Numerical Dosimetry) was presented and it was proposed that a synthesis report be written to announce the NSC support to medical applications.

38. The first phase of the deterministic MOX Fuel Assembly Radiation Transport benchmark has been completed. This phase covered 2-D and 3-D geometries and the results, which showed good agreement with Monte Carlo reference calculations, were published in May 2004. The specifications for the second phase, a 3-D case without spatial homogenisation, had been distributed in the beginning of May 2004.

39. A proposal for a skyshine benchmark, based on experimental data from a research reactor in Kazakhstan, was presented. The data have been released by the ISTC and the Research and Development Institute of Power Engineering (NIKIET) in Moscow, Russia. The model and the results of the benchmark will be incorporated in the SINBAD database.

40. The committee approved the skyshine benchmark.

High burn-up fuel

41. K. Hesketh informed the committee on the status of the planned state-of-the-art report on Very High Burn-up Fuel Cycles in LWRs, to provide utilities and fuel vendors with a guide as to the technical feasibility of extending LWR discharge burn-up well beyond current levels. The first meeting of the expert group in charge of the project was held in January 2004. At this meeting, the group agreed on an outline of the report and assigned writing responsibilities. The draft chapters would then be discussed by E-mail during early autumn 2004 and the next meeting of the group will be held on 21-22 November 2004. A summary of the first expert group meeting is available with the reference NEA/NSC/DOC(2004)3.

R&D needs in Nuclear Science

42. A. Hasegawa presented a follow-up proposal to the NSC activity on R&D Needs in Nuclear Science. The new proposal concerned the setting up a new expert group, which would mainly focus on reviewing the status of research and test facilities worldwide and clarifying future requirements for research facilities in the field of nuclear science. The group would collaborate very closely with similar activities in other NEA technical committees, especially the NDC and CSNI.

43. J. Reig, head of the NEA Nuclear Safety Division, presented a related CSNI activity called SFEAR (Support Facilities for Existing and Advanced Reactors). The aim of this activity is to assess facilities needed to support safety for current and advanced reactors. A first meeting of the group was held in March 2004 and the next meeting is scheduled for November 2004. J. Reig proposed to establish a close collaboration between the SFEAR group and the potential new NSC group.

44. T. Dujardin informed the committee about the NDC expert group on International Collaboration to Achieve Nuclear Support Excellence, whose objective is to identify mechanisms and policies for promoting international collaboration in the area of nuclear education and R&D. The report would be published in mid 2004 and could serve as background information to the other mentioned activities.

45. The committee discussed the proposal by A. Hasegawa and agreed to set up an expert group according to the suggested scope and objectives. It was noted that the NSC main lines of the programme of work for 2005-06 needed to be updated and approved by the NEA Steering Committee before the group could formally be constituted. J. Reig invited the new expert group to send a few members to participate in the next meeting of the SFEAR group.

Future NSC organised workshops and meetings

ARWIF-2004

46. E. Sartori informed the committee about the forthcoming third workshop on Advanced Reactors with Innovative Fuels (ARWIF-2004), which will be held on 15-17 September 2004 in Oak Ridge, USA. The items discussed will cover design and performance of innovative fuels as well as reviews of different advanced or projected reactor systems. Panel discussion in the closing session of the workshop will discuss "international co-operation to facilitate the introduction of new reactor systems".

Information Exchange Meeting on Actinide and Fission Product Partitioning and Transmutation

47. B-C. Na presented the preparations for the 8th information exchange meeting on Actinide and Fission Product Partitioning and Transmutation, which is organised jointly by NSC and NDC. This time the NDC has the main responsibility. The meeting will be held in Las Vegas, USA on 9-11 November 2004 in cooperation with the EC and the IAEA. Special emphasis will this time be given to the role of P&T in the future of nuclear energy, especially its impacts on waste management policies. The next meeting in this series will most probably be held in Europe in autumn 2006.

Workshop on R&D needs in Actinide Chemistry

48. C. Madic informed the committee that this planned NSC meeting had not been possible to organise due to different factors. It was initially planned for April 2003, but had to be postponed due to the geopolitical situation at that time. The back-up date of October 2003 had not attracted enough people to merit a meeting. It would now be difficult to justify organising a meeting in 2005, as there will be a large conference (Actinides 2005) organised in Manchester in July 2005 on the same subject. The committee agreed to temporarily abandon the idea to organise a workshop on actinide chemistry.

ND-2007

49. A. Zaetta presented the plans for the organisation of the next International Conference on Nuclear Data for Science and Technology (ND-2007), which will be hosted by CEA and held in France in 2007, preferably in spring. The choice of location and exact dates for the meeting will be decided later in 2004, hopefully before the ND-2004 conference, which will be held in Santa Fe, USA at the end of September 2004.

50. The committee approved the proposal to organise the next large nuclear data conference in France in 2007.

Other NSC co-sponsored conferences

51. S. Qaim informed the committee on the 6th International Conference on Nuclear and Radiochemistry to be held on 29 August to 3 September 2004 in Aachen, Germany.

52. J. Aragones notified the committee about the next meeting on Mathematics and Computation (M&C 2005), which will be held in Avignon, France on 12-15 September 2005. More information about the meeting can be found at http://mcavignon2005.cea.fr/.

53. Two new proposals for NSC co-sponsorship were presented by P. D'Hondt and S. Qaim. It concerned the 12th International Conference on Emerging Nuclear Energy Systems (ICENES 2005) to be held in Brussels, Belgium on 21-26 August, 2005 and the 7th Topical Conference on Nuclear Applications of Accelerator Technology (AccApp05) to be held in Venice, Italy on 28 August to 1 September 2005.

54. The committee approved co-sponsorship of both conferences mentioned in the paragraph above.

In-depth discussions

Shielding and dosimetry for accelerators

55. P. Vaz introduced the subject Shielding and Dosimetry for Accelerators by highlighting the on-going NSC activities in the field and outlined the number of accelerators and their different application areas. He also presented the associated scientific and technical issues and described the recent development in shielding designs.

56. M. Silari made a presentation entitled "Induced radioactivity and accelerator decommissioning". He described the origins of the induced radioactivity and the experiences from the dismantling of the LEP facility at CERN. He also stressed the need for a continuous development of advanced MC codes to calculate induced radioactivity from e.g. transport of heavy ions, future accelerators like e+/e-linear collider, and high-power facilities.

57. An overview of proton beam cancer therapy and a simple cost/benefit analysis for new activities in radiation shielding was presented by W.D. Newhauser. In comparing photon/electron therapy with proton therapy it was noted that the former therapy is more cost effective. However, proton therapy have demonstrated or shown promise in improving patient outcomes, i.e., reducing morbidity and mortality costs and can therefore also be considered cost effective. W.D. Newhauser's analysis showed that significant cost reductions could be obtained by improving and optimising the shielding associated with proton beam cancer therapy installation.

58. The committee expressed its appreciation of the very informative and interesting presentations and regretted that there was no time available for further discussions, due to the very tight schedule of the meeting.

Prospective of LWRs to reduce minor actinide inventories

59. R. Chawla introduced the second subject for in-depth discussion and gave the floor to the two speakers, A. Zaetta and J. Herczeg.

60. A. Zaetta presented the French transmutation scenario studies towards Generation-IV systems. The scenario covered the transition from the present PWR reactors to the Generation-IV fast systems, using EPRs as intermediate transmutation systems. The possibility to recycle minor actinides in PWRs and the impact on safety, fuel fabrication, and reprocessing was discussed. The calculated future mass inventory for different scenarios was also presented.

61. J. Herczeg outlined the US long-term strategy for nuclear energy development and focused on the transmutation studies within the Advanced Fuel Cycle Initiative (AFCI) project. Irradiation experiments involving oxide, nitride, metal and dispersion fuels, containing minor actinides, would be undertaken and fabrication and characterisation questions related to these fuels would also be studied.

62. The committee concluded that there was presently no specific action to be taken on this subject. However, it was suggested that the WPRS and WPFC jointly discuss the issue, identify the underlying scientific issues and write a concise review report.

Reports from other NEA Divisions and other International Organisations

Report from the 13th meeting of the NSC Executive Group

63. P. D'Hondt presented a short summary of the meeting of the Executive Group that was held in the morning of 9th June 2004. The report is given in Annex 5.

64. T. Dujardin complemented the report by informing the committee that, although the potential cooperation between the NEA Data Bank and the EC would be easier within the 6th framework programme, there were still a number of legal questions to be solved. The NEA secretariat will continue to pursue these questions.

65. The committee endorsed the presented programme of work and budget for the NEA Data Bank for 2005 and 2006.

The NEA Nuclear Development, Nuclear Safety and Radiation Protection divisions

Nuclear Development

66. K-S. Lee, NEA Nuclear Development Division, presented two activities in the proposed NDC programme of work for 2005-06 for which the NDC is inviting the NSC to cooperate. It concerns the activities on "Innovations in Nuclear Technology" and on "Management of Recycled Fissile Materials". In the first case, the objective of the study is to examine the drivers behind nuclear innovation systems, to investigate innovative performance and experience in the nuclear sector and to delineate policy implications for member governments. In the second case the objective is to review alternative options for recycling various fissile materials, to assess difficulties, advantages and drawbacks of different options, and to identify strategic aspects of interest to policy makers. In both cases the NSC is invited to comment on the scope and objectives of the studies and to send experts to the ad-hoc groups.

67. The committee welcomed the proposals and strongly recommended the WPFC to cooperate with the NDC activity on the "Management of Recycled Fissile Materials". In the case of "Innovations in Nuclear Technology", the committee recommended that a few delegates from the newly approved NSC group on the needs for R&D facilities in nuclear science participate in the NDC activity.

Nuclear Safety

68. M. Hrehor gave an overview of activities in the NEA Safety Division of interest to the NSC. He briefly enumerated the workshops organised in 2003, and the on-going and planned separate funded projects. Two collective opinion statements, one on Closure Criteria and Good Practice for Safety Research and one on Safety Research Capabilities and Expertise in Support of Efficient and Effective Regulation of NPPs were presented, as well as the cooperation with the NEA Data Bank on the archiving of safety data.

Radiation Protection

69. T. Lazo, NEA Waste Management and Radiation Protection Division, outlined the content of the new recommendations from the International Committee on Radiological Protection (ICRP). He also informed the committee that these recommendations would be sent out for review to all NEA committee

members in the beginning of July 2004. Any comments should reach the NEA secretariat before 1st October 2004, for subsequent transmission to the ICRP.

The EC, including the NURESIM proposal and the PERFECT project

70. P. Rullhusen gave an overview of the EC framework programmes (FP) of interest to the NSC. Within the 5th framework programme (FP5) was mentioned the ADOPT (Advanced Options for Partitioning and Transmutation) network and the n_TOF nuclear data measurement facility at CERN. A few of the FP6 programmes, such as EUROPART (PARTitioning of minor actinides from high active waste) and IP EUROTRANS (EUROpean Research Programme for the TRANSmutation of High Level Nuclear Waste in an Accelerator Driven Systems).

71. D. Cacuci presented the EU-FP6 integrated project proposal NURESIM (NUclear REactor SIMulation), which has as an objective to prepare, on a common platform, a new generation of highly qualified reference physical models and software by improving the operational prediction capabilities of codes used in reactor physics calculation through the introduction of more physics in the models and less ad hoc phenomenology.

72. F. Baron, EdF, informed the committee that the three main objectives of the EC integrated project PERFECT were: to develop multi-scale numerical tools simulating the effects of irradiation on mechanical and corrosion properties of materials, to use these tools to solve issues related to pressure vessels and internal structures, and finally to disseminate the information. He also mentioned that the project started on 1st January 2004 and will run for 4 years. The EU financial support will be of the order of 7.5 M€.

73. The committee welcomed a proposal from F. Baron to organise a small meeting between representatives from the NSC and the IP-PERFECT. It was proposed to hold a one-day meeting sometime in October – November 2004. Interest from USA, Hungary and Sweden were noted.

The IAEA

74. N. Ramamoorthy, director at IAEA, briefed the committee about relevant IAEA activities with a special focus on the activities of the Nuclear Data Section (NDS). He gave an overview of the international coordination of nuclear data activities and highlighted the on-going co-ordinated research projects (CRPs). He also stressed the good cooperation and complementarity between the IAEA NDS and the NEA Data Bank.

Next NSC meeting

Date of next meeting

75. It was agreed to hold the next meeting of the committee on 8-10 June 2005, in Paris, France. The NSC bureau will meet on 30 November 2004.

Topics for in-depth discussion

76. The NSC confirmed that last year's proposal by K. Hesketh to discuss the "performance of the JEFF-3 data library" had been postponed and would be one of the subjects for in-depth discussion in 2005. Two additional proposals were forwarded. J.M. Aragones proposed to discuss "uncertainty analysis in modelling" and R. Chawla suggested to discuss "progress of advanced reactor concepts" to guide the newly established Working Parties.

77. The committee took note of the proposals and encourage the members to communicate additional proposals in time for the final decision by the NSC bureau at the end of November 2004.

Self-evaluation of committee meetings

78. T. Dujardin reminded the committee of the request from the OECD for a self-evaluation of the committee meetings and an assessment of the usefulness of the NSC work. A few of the NEA Standing Technical Committees had already performed such a self-evaluation using a questionnaire.

79. It was agreed that the Secretariat would prepare such a questionnaire for distribution to committee members before the next NSC meeting.

Election of Committee Officers

80. The chair was handed over to T. Dujardin, who, considering that two of the bureau members had recently been appointed, suggested to re-elect the chairman and vice-chairmen for one more year. As no other proposals were forwarded, the committee unanimously re-elected the bureau for one year.

Any other business

81. No other items were raised.

ANNEX 1

LIST OF PARTICIPANTS

BELGIUM

D'HONDT, Pierre Joseph
Director Reactor Safety
SCK-CEN
200 Boeretang
B-2400 MOL

Tel: +32 14 33 22 00
Fax: +32 14 32 15 29
Eml: pdhondt@sckcen.be

CZECH REPUBLIC

MACH, Rostislav
Nuclear Physics Institute
Academy of Science
250 68 Rez

Tel: +420 (2) 66172136
Fax: +420 (2) 20941002
Eml: mach@ujf.cas.cz

DENMARK

NONBOEL, Erik
Radiation Research
Risoe National Laboratory
Postbox 49
DK-4000 ROSKILDE

Tel: +45 4677 4923
Fax: +45 4677 4977
Eml: erik.nonboel@risoe.dk

FINLAND

ANTTILA, Markku
VTT Processes
P.O. Box 1604
FIN-02044 VTT

Tel: +358 9 456 5012
Fax: +358 9 456 5000
Eml: Markku.Anttila@vtt.fi

FRANCE

GUERIN, Yannick
DEN/DEC/SESC
CEA Cadarache
Bat. 151
F-13108 St. Paul-lez Durance Cedex

Tel: +33 4 4225 7914
Fax: +33 4 4225 4747
Eml: yannick.guerin@cea.fr

JACQMIN, Robert
CEA Cadarache
DEN/SER/SPRC - Bat 230
F-13108 St.-Paul-lez-Durance

Tel: +33 4 4225 3136
Fax: +33 4 4225 4849
Eml: robert.jacgmin@cea.fr

MADIC, Charles
CEA/Saclay
Direction de l'Energie Nucléaire
DEN/SAC/DIR, Bat. 523
F-91191 Gif-s-Yvette

Tel: +33 1 6908 8207
Fax: +33 1 6908 7990
Eml: charles.madic@cea.fr

ZAETTA, Alain
CEA - DEN/DER/SPRC
Cadarache
Bat. 230 - B.P. 1
13108 St.-Paul-lez-Durance

Tel: +33 (0) 4 42252761
Fax: +33 (0) 4 42254849
Eml: alain.zaetta@cea.fr

BARON, Frédéric
EDF R&D Grands Projets
Avenue des Renardières
Ecuelles
77818 MORET SUR LOING CEDEX

Tel: +33 1 60 73 67 30
Fax: +33 1 60 73 67 21
Eml: frederic.baron@edf.fr

GERMANY

CACUCI, Dan Gabriel
Forschungszentrum Karlsruhe GmbH
Institut fuer Reaktorsicherheit
Hermann von Helmholtz Platz 1
D-76344 Eggenstein-Leopoldshaven

Tel: +49 7247 82 2550
Fax: +49 7247 82 3718
Eml: cacuci@irs.fzk.de

QAIM, Syed M.
Inst. fuer Nuklearchemie
Forschungszentrum Juelich
Postfach 1913
D-52425 JUELICH

Tel: +49 (2461) 613282
Fax: +49 (2461) 612535
Eml: s.m.qaim@fz-juelich.de

HUNGARY

GADO, Janos
Director
KFKI Atomic Energy Research Institute
P.O.Box 49
H-1525 Budapest

Tel: +36 1 395 9159
Fax: +36 1 395 9293
Eml: gado@sunserv.kfki.hu

ITALY

MENAPACE, Enzo
E.N.E.A. C.R. E. Clementel
Division for Advanced Physics Technology
Via Don G. Fiammelli 2
I-40128 BOLOGNA

Tel: +39 051 60 98 239
Fax: +39 051 60 98 359
Eml: enzo.menapace@bologna.enea.it

JAPAN

HASEGAWA, Akira
Deputy Director
Department of Nuclear Energy System
Japan Atomic Energy Research Institute
2-4 Shirakata, Tokai-mura, Naka-gun
Ibaraki-ken 319-1195
Tel: +81 29 282 6929
Fax: +81 29 282 6122
Eml: hasegawa@ndc.tokai.jaeri.go.jp

MORI, Takamasa
Research Group for Reactor Physics
Department of Nuclear Energy System
Japan Atomic Energy Research Institute
Shirakta-shirane, Tokai-mura, Naka-gun
Ibaraki-ken, 319-1195
Tel: +81 29 282 5360
Fax: +81 29 282 6122
Eml: mori@mike.tokai.jaeri.go.jp

TAKEUCHI, Ei
First Secretary
Permanent Delegation of Japan
to the OECD
11, Avenue Hoche
75008 PARIS
Tel: +33 (0)1 53 76 61 81
Fax: +33 (0)1 45 63 05 44
Eml: takeuchi@deljp-ocde.fr

KOREA (REPUBLIC OF)

KIM, Young-Jin
Director, HANARO Utilization
Technology Development Division
Korea Atomic Energy Research
Institute
P.O. Box 105, Yuseong,
Tel: +82 42 868 2985
Fax: +82 42 861 3642
Eml: youkim@kaeri.re.kr

NETHERLANDS

KONING, Arjan
NRG Nuclear Research and
Consultancy Group
Building 34.213
Westerduinweg 3, P.O. Box 25
NL-1755 ZG PETTEN
Tel: +31 (224) 56 4051
Fax: +31 (224) 56 8490
Eml: koning@nrg-nl.com

VAN DER HAGEN, Tim
IRI - Interfaculty Reactor
Institute/Delft University
of Technology
Mekelweg 15
NL-2629 JB DELFT
Tel: +31 15 278 2105
Fax: +31 15 278 6422
Eml: hagen@iri.tudelft.nl

NORWAY

WIESENACK, Wolfgang
Project Manager
OECD Halden Reactor Project
Institutt for Energiteknikk
Os Alle 13 - P.O. Box 173
N-1751 HALDEN

Tel: +47 69 21 2347
Fax: +47 69 21 2201
Eml: wowi@hrp.no

PORTUGAL

VAZ, Pedro
Instituto Tecnologico e Nuclear/DPRSN
Estrada Nacional 10
P-2686-953 SACAVEM

Tel: +351 21 994 62 30
Fax: +351 21 994 19 95
Eml: pedrovaz@itn.mces.pt

SLOVAK REPUBLIC

BAHNA, Jan
VUJE
Dept.01900
Kruzna 5
918 64 TRNAVA

Tel: +421 33 599 1197
Fax: +421 33 599 1157
Eml: bahna@vuje.sk

SPAIN

ARAGONES BELTRAN, Jose Maria
Dpto. Ingenieria Nuclear
ETSI-Industriales
Univ. Politecnica de Madrid
Jose Gutierrez Abascal 2
E-28006 MADRID

Tel: +34 91 336 3108
Fax: +34 91 336 3002
Eml: arago@din.upm.es

PENA GUTIERREZ, Jorge
Desarrollo de Aplicaciones
Computing Centre
Consejo de Seguridad Nuclear
C/ Justo Dorado, 11
28040 MADRID

Tel: +34 91 346 0123
Fax: +34 91 346 0275
Eml: jpg@csn.es

SWEDEN

LEFVERT, Tomas
Director, Swedish Center for Nuclear Tech
Dept. of Physics.
Royal Institute of Technology
Center for Astronomy, Physics and
Biotechnology
SE-106 91 Stockholm

Tel: +46 8 55 37 82 25
Fax: +46 8 20 80 76
Eml: tomas@physics.kth.se

SWITZERLAND

CHAWLA, Rakesh
Laboratory for Reactor Physics
and Systems Behaviour
Paul Scherrer Institute
CH-5232 VILLIGEN PSI
Tel: +41 56 310 23 26
Fax: +41 56 310 23 27
Eml: Rakesh.Chawla@psi.ch

SILARI, Marco
C.E.R.N.
TIS-RP
CH-1211 GENEVE 23
Tel: +41 (22) 767 3937
Fax: +41 (22) 767 9360
Eml: marco.silari@cern.ch

UNITED KINGDOM

HESKETH, Kevin
British Nuclear Fuels plc
Nuclear Science and Technology Services
B709 Springfields
Salwick Preston
Lancashire PR4 OXJ
Tel: +44 1772 76 23 47
Fax: +44 1772 76 24 70
Eml: Kevin.W.Hesketh@bnfl.com

SIMISTER, David
Health and Safety Executive
Nuclear Installations Inspectorate
Room 616, St. Peter's House,
Stanley Prec Bootle
Merseyside, L20 3LZ
Tel: +44 (151) 951 3664
Fax: +44 (151) 951 3942
Eml: david.simister@hse.gsi.gov.uk

UNITED STATES OF AMERICA

HERCZEG, John W.
US Department of Energy
Office of Nuclear Energy, NE-20
1000 Independance Ave SW
Washington DC 20585
Tel: +1 301 903 1175
Fax: +1 301 903 5057
Eml: john.herczeg@nuclear.energy.gov

BRIGGS, Blair
Idaho National Engineering
& Environmental Laboratory
P.O. Box 1625, MS-3860
2525 North Fremont
IDAHO FALLS, ID 83415-3860
Tel: +1 (208) 526 7628
Fax: +1 (208) 526 2930
Eml: bbb@inel.gov

HILL, David
Associate Laboratory Director
Energy and Engineering Sciences
OAK RIDGE NATIONAL LABORATORY
PO BOX 2008 MS6228
OAK RIDGE TN 37831-6228
Tel: +1 (865) 574 9599
Fax: +1 (865) 576-6118
Eml: hilldj@ornl.gov

NEWHAUSER, Wayne D.
M. D. Anderson Cancer Center
Department of Radiation Physics
Proton Therapy Group, Box 94
1515 Holcombe Blvd
Houston, Texas 77030

Tel: +1 713 745 0048

Eml: wnewhaus@mail.mdanderson.org

INTERNATIONAL ORGANISATIONS

IAEA

RAMAMOORTHY, N.
Director
Division of Physical and Chemical Science
Dept. of Nuclear Sciences and Application
IAEA
P.O. BOX 100
AUSTRIA

Tel: +43 1 2600 21700
Fax: +43 1 26007
Eml: n.ramamoorthy@iaea.org

European Commission

RULLHUSEN, Peter
EC - JRC - Institute for Reference
Materials and Measurements
Joint Research Center
Retieseweg 111
B-2440 GEEL

Tel: +32 (14) 57 14 76
Fax: +32 (14) 57 18 62
Eml: peter.rullhusen@cec.eu.int

Nuclear Energy Agency (NEA)

DUJARDIN, Thierry
Deputy Director, Science and Development

Tel: +33 1 45 24 10 06
Eml: thierry.dujardin@oecd.org

NORDBORG, Claes
Head of Nuclear Science Section

Tel: +33 1 45 24 10 90
Eml: nordborg@nea.fr

YAMAGISHI, Isao
Nuclear Science Section

Tel: +33 1 45 24 11 52
Eml: yamagishi@nea.fr

GALAN, Juan
Data Bank

Tel: +33 1 45 24 10 08
Eml: galan@nea.fr

HREHOR, Miroslav
Nuclear Safety Division

Tel: +33 1 45 24 10 58
Eml: miroslav.hrehor@oecd.org

KODELI, Ivo
IAEA representative at the NEA Data Bank

Tel: +33 1 45 24 10 74
Eml: kodeli@nea.fr

LAZO, Ted
Radioprotection Division

Tel: +33 1 45 24 10 42
Eml: lazo@nea.fr

LEE, Kwang-Seok
Nuclear Development Division
Tel: +33 1 45 24 10 25
Eml: Kwang-Seok.Lee@oecd.org

NA, Byung-Chan
Data Bank
Tel: +33 1 45 24 10 91
Eml: na@nea.fr

NOURI, Ali
Data Bank
Tel: +33 1 45 24 10 84
Eml: nouri@nea.fr

REIG, Javier
Head of Nuclear Safety Division
Tel: +33 1 45 24 10 50
Eml: javier.reig@oecd.org

SARTORI, Enrico
Data Bank
Tel: +33 1 45 24 10 72
Eml: sartori@nea.fr

ANNEX 2

Mandate for a

Working Party on Scientific Issues of Reactor Systems (WPRS)

SCOPE

Under the guidance of the Nuclear Science Committee the Working Party will deal with reactor physics, fuel cycle, fuel behaviour, thermal hydraulics and dynamics/safety of present and future nuclear power systems.

OBJECTIVES

To provide the Member Countries with up-to-date information to preserve knowledge on and develop consensus regarding:

- Reactor physics, fuel behaviour, thermal hydraulics and dynamics/safety issues associated with innovative fuels in present and future nuclear power systems.

  Reactor physics aspects considered include:
  - Reactivity characteristics
  - Core power/flux distributions
  - Core kinetics and reactivity control
  - Reactivity coefficients
  - Safety / system dynamics
  - Vessel dosimetry

- Fuel cycle aspects considered will focus on fuel loading and discharge requirements, fission product and minor actinide inventories and radiotoxicity profiles versus time.

- Fuel behaviour, thermal hydraulics and kinetics/safety will be considered insofar as they impinge on the reactor performance.

Reactor types considered include, but are not limited to the following:

- Present generation LWRs with advanced and innovative fuels, evolutionary LWRs and innovative LWRs
- Novel reactor systems (Gen IV Systems)
- Accelerator driven (sub-critical) and critical systems for waste transmutation

To liaise closely with other relevant NEA working groups, especially those operating under the guidance of the NDC and CSNI, to ensure the respective work programmes are complementary and to provide advice and support where required and undertake common work where appropriate. Particularly close working relationships will be maintained with the Working Party on the scientific issues in Fuel Cycle (WPFC) and with the Task Force on Reactor-based Plutonium Disposition (TFRPD).

To provide advice to the nuclear community on the developments needed to meet the requirements (data and methods, validation experiments, scenario studies) for different reactor systems.

DELIVERABLES

- Publication of Volume VIII – Benchmark exercise on kinetics parameters based on comparison with experimental results from the CROCUS facility – Late 2004
- Publication of Volume IX – High temperature reactor core physics benchmark - Mid 2005
- Depletion calculation benchmark, Late 2005
- Publication of Volume X – Physics benchmarks for Gen IV reactor cores - Early 2006
- MOX-core control rod ejection benchmark – Early 2006

Meeting frequency: 9 months

ANNEX 3

Mandate for a

Working Party on Scientific Issues of the Fuel Cycle (WPFC)

SCOPE

Under the guidance of the Nuclear Science Committee, the Working Party will deal with scientific issues in various existing and advanced nuclear fuel cycles, including fuel cycle physics, associated chemistry and flowsheets, development and performance of fuels and materials, and accelerators and spallation targets.

OBJECTIVES

- To provide the Member Countries with up-to-date information on and develop consensus regarding:
  - Separations science;
    - Develop a scientific basis for optimisation of the use of future nuclear waste repositories
    - Establish a methodology for evaluating impacts of various existing and advanced fuel cycle scenarios on potential storage and repositories.
    - Provide a means for the development and evaluation of advanced processing concepts, including design bases for future reprocessing plants.
  - Fuel cycle scenarios;
    - Assemble and organise scientific information critical to the understanding of the issues involved in transitioning from current fuel cycles to future fuel cycles
    - Provide scientific bases for fuel cycle deployment strategies
  - Chemical partitioning;
    - Keep updated information on separation technologies, including advanced aqueous and pyrochemical processing issues
    - Perform a detailed scientific study of separations processes for different fuel cycle scenarios
  - Fuels and materials;
    - Undertake studies needed for development of fuels and materials for implementing advanced nuclear fuel cycles
    - Deal with performance and behaviour of advanced fuels
    - Publish a handbook on lead-bismuth eutectic (LBE) technology
  - Accelerators and targets;
    - Deal with accelerator reliability issues
    - Target performance, including spallation products
    - Window performance, including thermal stress and radiation damage
- To liaise closely with other relevant NSC Working Parties and NEA Standing Technical Committees, especially the Nuclear Development Committee (NDC) and the Radioactive Waste Management Committee (RWMC), to ensure the respective work programmes are complementary and to provide

advice and support where required and undertake common work where appropriate. Particularly close working relationships will be maintained with the Working Party on scientific issues of Reactor Systems (WPRS) and with the Task Force on Reactor-based Plutonium Disposition (TFRPD).

- To provide advice to the nuclear community on the developments needed to meet the requirements for implementing advanced long-term sustainable nuclear fuel cycles, including partitioning and transmutation.

DELIVERABLES

Chemical partitioning:

- State-of-the-art report on national programmes in partitioning in June 2005

- WG on detailed flowsheet study: Final report in June 2006

Fuel cycle scenarios:

- WG on Fuel Cycle Transition Scenarios Studies: Final report in June 2006

Accelerators utilisation:

- Organise the 5th HPPA workshop in Europe in 2006

Separations science:

- WG on Separations Criteria Studies: Final report in June 2007

Fuels and materials:

- WG on LBE Technology: Publication of an LBE Handbook in June 2007

ANNEX 4

Mandate for a

Working Party on Nuclear Criticality Safety (WPNCS)

Chair:	J. Blair Briggs (USA)
Members:	All NEA Member countries
Observers	Representatives from the IAEA, the Russian Federation and PR of China
Date of creation:	June 1996
Duration:	3 years starting on June 2004.
Mandate:	Agreed at the 7th Meeting of the Nuclear Science Committee (NSC), 29-30 June 1996 [NEA/SEN/NSC(96)3], extended at the 11th meeting of NSC in June 2000, extended at the 15th meeting of the NSC in June 2004.

SCOPE

Under the guidance of the Nuclear Science Committee, the Working Party will deal with technical and scientific issues relevant to criticality safety. Specific areas in interest include, but are not limited to investigations concerning static and transient configurations encountered in the nuclear fuel cycle such as fuel fabrication, transport and storage. Areas of activities include:

- Evaluation of available experimental data;
- Assessment of experimental needs;
- Code and data inter-comparison;
- Development of codes and models;
- Development of criticality methodologies and data;
- Establishment of technical bases for the application of burnup credit.

OBJECTIVES

- Exchange of information on national programs in the area of criticality safety.
- Guide, promote and co-ordinate high priority activities of common interest to the international criticality safety community, establish co-operations.
- Monitor the progress of all activities and report to the NSC.
- Publish databases, handbooks, and reports.
- Facilitate communications within the international criticality safety community through relevant Internet sites.
- Co-ordinate the ongoing series of International Conferences on Nuclear Criticality Safety (ICNC), to be held every four years.
- Co-ordinate WPNCS activities with other working groups within the NEA and in other international frameworks to avoid duplication of activities.
- Provide a technical basis for other international activities (e.g. ISO, IAEA).

DELIVERABLES

- New editions of the International Handbook of Criticality Safety Benchmark Evaluation Project (2004, 2005 and 2006).
- Report of a study on the effect of axial burn-up profile asymmetry on criticality calculation (2004).
- Report of a study on the effect of absorbers on burn-up credit (2005).
- Report summarising the findings of the Expert Group on Burn-up Credit and lessons learned (2005).
- Report on the study of source convergence issues through the analysis of four inter-comparison exercises (2004).
- Report on the assessment of statistical methods for source convergence detection and application in Monte-Carlo criticality safety codes (2006).
- Report compiling and comparing minimum critical data for a selection of fissile media (2004).
- Report on inter-code comparisons for the calculation of criticality transient experiments (2005).
- Web-based information resources on burn-up credit, criticality excursions and source convergence issues.
- Status reports of the progress of ICNC 2007

ANNEX 5

Report to the Nuclear Science Committee from the Thirteenth Meeting of the Executive Group

Pierre D'Hondt

Introduction

1. Fifteen delegates attended the meeting, including the representatives from the EC and from the IAEA. David Simister, UK and N. Ramamoorthy, IAEA participated for the first time.

2. Thierry Dujardin informed the Executive Group about recent staff changes in the NEA. He also mentioned the current budget situation, the development of a new strategic plan for the NEA, the subsequent need to revisit the mandates of all NEA standing technical committees and the request from the OECD council for a self-evaluation of all committees.

Progress report and programme of work

Computer program services

3. Enrico Sartori informed the Group that the computer program services celebrated its 40th anniversary in May 2004 and had during these years distributed in total about 67 000 programs upon request. Last year, the Data Bank had acquired 70 new or revised versions of computer codes. It had distributed slightly over 1 900 programs, which was somewhat less than in recent years. The distribution of integral data set was however higher than normal in 2003, bringing the total number of dispatches to over 4 400, a figure which was well in line with the two preceding years. The Data Bank had also issued five electronic newsletters and one new edition of the program abstracts on CD-ROM. Five training courses and two workshops, covering the most sought after computer codes, had been organised in 2003.

4. Ivo Kodeli presented the computer program distribution to non-OECD countries, which in 2003 had been slightly less than in 2002. It was also noted that 31 computer codes (23 from IAEA) had been received from non-OECD members in 2003, compared to only 9 in 2002.

5. The Executive Group noted that the acquisition of new or revised versions of computer codes had been rather low in 2003, partly because of the interruption in the exchange of codes with the US during the negotiation of a new cooperation agreement between the US DOE and the NEA Data Bank. The Group expressed hope that the new agreement would soon be in place.

Nuclear data services

6. The nuclear data services were presented by Ali Nouri. The compilation of bibliographic and experimental nuclear data had proceeded as planned in 2003 with more than 250 new experiments entered into the EXFOR database and close to 3 300 bibliographic references entered into the CINDA database. Concerning the on-line nuclear data services to member countries, the Data Bank has noted a considerable increase in the demand for experimental and evaluated data, since the abolition of password protections of the databases in 2002. The NEA Data Bank will send out a questionnaire to find out the real need for continuing to produce a printed version of CINDA, considering that the CINDA database is available both on CD-ROM and on-line through the Web.

7. A new version of the nuclear data-plotting software JANIS (JANIS-2.0), developed at the Data Bank, was released in January 2004. This extended and improved version now includes bibliographical data (CINDA), experimental data (EXFOR) and evaluated data (EVA). The software has become very popular in the nuclear community and the stock of 1 000 copies were distributed during the first two months.

8. The development of the JEFF project is progressing in-line with the revised mandate adopted by the Executive Group in June 2003. Studies performed at several participating institutes are providing feedback on the JEFF-3.0 library. Extensive processing and validation studies have been undertaken and have highlighted files which are in need of revisions. In parallel, evaluation work is progressing with the aim of providing new or revised evaluations for inclusion in the JEFF-3.1 library. It is planned to issue the JEFF-3.1 library in late spring 2005.

9. Federico Mompean presented the status of the separately funded Thermochemical database (TDB) project. An update to earlier reviews of thermochemical data for U, Np, Pu, Am, and Tc had been published in 2003. Reviews of data for Zirconium, Selenium, Nickel and selected organic compounds are underway and are expected to be published in 2004 and 2005. A new phase of the project was started in 2003 covering evaluation of inorganic complexes and compounds of Thorium, Iron, Tin and Molybdenum.

Computational methods

10. Two proposals for possible future activities within the framework of the computer program services have emerged from different seminars and workshops. The first proposal concerned a one year pilot phase to develop a first version of **G**eneral **E**nvironment for **R**adiation **A**nalysis and **D**esign (GERALD), intended to create a unifying software environment where the user can define, solve and analyse a nuclear radiation transport problem using available numerical tools seamlessly. The other proposal concerned the further development of tools for the analysis and estimation of sensitivities and uncertainties in calculations, or their propagation through complex computational schemes, used for example in the field of neutronics and thermal hydraulics.

11. The Executive Group adopted both proposals, under the condition that all Data Bank member countries could benefit from the activities, especially the non-European members, in case the NEA Data Bank entered in partnerships with the European 6th framework programme. In addition, it was agreed the projects be limited in time to profit from current Data Bank expertise and that the legal aspects be considered.

In-house computer system

12. Pierre Nagel described the Data Bank's in-house computer system. It was especially noted that the Data Bank had improved the overall security of the installation in relation to the Internet, by using separate firewall switches for the web and mail servers. Special filters had also been installed to identify spam e-mail.

Proposed budget

13. Claes Nordborg presented the Data Bank expenditure in 2003. As this year was the first of the new biennial (2003 - 2004) budget process, the final balance will be provided next year. The 2004 budget had been approved by the OECD Council in December 2003 on the basis of a 1.8% nominal increase from that of 2003. The recently adopted salary increases provoked a net shortfall in the 2004 budget, which will have to be compensated by savings in other budget lines. A proposed budget for 2005 and 2006, based on a slightly less than zero growth budget compared to 2004, was presented. This budget was still provisional as the NEA had not yet received any detailed instructions from the OECD Management.

Conclusions and recommendations

14. The Executive Group expressed its appreciation of the excellent services provided by the Data Bank, both what concerned the quantity and quality of the services.

15. The Executive Group approved the proposed Data Bank budget and programme of work for 2005 and 2006 and recommends the Nuclear Science Committee to endorse the approval.